PRESSURE INSTRUMENTATION IN EXPLOSIVE FORMING: THE NON-LINEAR TRANSIENT DISPLACEMENT OF A CIRCULAR PLATE

A thesis presented for the Degree of

Doctor of Philosophy in Mechanical Engineering

in the University of Canterbury,

Christchurch, New Zealand

by

J. S. SMAILL, B.E. (Hons)

University of Canterbury,

April 1984.

ACKNOWLEDGEMENTS

My sincere thanks are due to Mr F.W. Fahy, Professor D.C. Stevenson and Professor H. McCallion who have supervised the work. Their guidance and encouragement throughout the duration of the project has been much appreciated.

The support and interest of Professor L.A. Erasmus is gratefully acknowledged as is that of my colleagues, the staff of the Department of Mechanical Engineering. Many members of the academic, technical and secretarial staff have assisted in the project and, in particular, my thanks go to Miss J. Shelton for her care in the presentation of many graphs and diagrams and the secretaries, Mrs P. Dowell, Mrs N. Jones and Mrs J. Percival for their help in the preparation of the thesis. Appreciation is also due to Mrs C. McEntee for her typing of the equations.

Gratitude is also due to the staff of the Computer Centre and Engineering Library for their help and co-operation.

The financial support of the Mercer Memorial Scholarship and Todd Motors Scholarship in the initial stages of the project is appreciated.

Finally, the continual encouragement, support and assistance of my Wife, Merilyn, and family, has enabled me to undertake and complete this study.

ABSTRACT

The use of explosive forming for small production runs has been considered suitable for New Zealand manufacturing.

A literature review of the explosive forming process establishes the need for instrumentation that enables the loading of the workpiece to be determined, particularly that associated with the workpiece/energy transfer medium interaction. Because of the magnitude of the initial shock wave the development of a pressure transducer based upon the non-linear deflection of a circular clamped plate or plate/dielectric foundation is considered.

A modal analysis of the linear response of a clamped plate or plate/foundation system with viscous damping and subject to a transient loading is derived. The Winkler and Pasternak models were used to represent the foundation behaviour. To determine the non-linear response of both a rigidly fixed edge and a simply supported immovable edge plate for similar conditions to those applied to the modal analysis a numerical program is developed. The spatial domain is modelled by central finite differences with a time element method giving a resultant recurrence scheme which is used in the time domain. An analysis of the effect of viscous damping on the stability of a range of three point schemes is derived for a single degree of freedom system and the results presented.

For a range of transient loads a strong correlation was obtained between the linear deflection results determined from the numerical program and the modal analysis. The dynamic non-linear deflection of the plate and plate/foundation system is presented for step loads and a transient exponentially decaying load.

CONTENTS

Page

Page

CHAPTER FIVE MODAL ANALYSIS OF PLATE/FOUNDATION COMBINATION

LIST OF FIGURES

LIST OF TABLES

NOMENCLATURE

Note:

Subscripts i, j — pivotal points

m, n, r — summation

Dot denotes derivative with respect to time.

Symbol	Description
a	Radius of plate
a_m	Constant for the mth modal shape
a_r	Radius of gas bubble
a_1	Integration limit for impulse
A_e	Explosive constant
A_g	Area of guarded active transducer plate
A_m	Coefficients for modal pollution
A_t	Area of transducer plate
A_o	Initial area of blank normal to incident pressure
A_1	Explosive constant
A^*	Material constant
ΔA	Imposed change in area
b	$\frac{1}{\sqrt{2}\ \text{Standard deviation}}$
B_e	Explosive constant
B_m	Coefficients for modal solution
B^*	Material constant
c	Charge energy available
c_m	Yield stress/density
c_o	Velocity of sound
C	Capacitance
C_e	Explosive constant
C_i	Viscous damping corresponding to the i^{th} eigenvalue
C_1	Constant in modal shape equation
$\underline{C}$	Matrix of viscous damping value
d	Depth of forming

Symbol	Description
D	Flexural rigidity or plate stiffness
D_e	Explosive constant
D_o	Die opening diameter
D_1	Constant in modal shape equation
e	Energy available at explosive charge
E	Modulus of elasticity for plate material
E_e	Explosive energy
E_f	Energy flux density
E'_f	After-flow energy flux density
E_m	Orthonormal constant for m^{th} mode
E_p	Potential energy of energy transfer medium
E_1	Constant in modal shape equation
$f( )$	Function
f	Explosive constant (Floral)
f_f	Frequency of plate/foundation
f_p	Frequency of plate
$\underset{\sim}{f}_t$	Load vector at t
$\underset{\sim}{f}$	Sum of load vectors
F	Excess of dynamic stress over the static yield
$\underset{\sim}{F}$	Load vector
$F(w)$	Foundation reaction
F_e	Explosive constant
F_1	Constant in modal shape equation
$\underset{\sim}{F}_1$	Vector of pseudo-loads containing the non-linear terms
$\underset{\sim}{F}'_1$	Vector of pseudo-loads containing the non-linear terms
$F'_1( )$	Frequency equation for non-linear modal analysis
$\underset{\sim}{F}_2$	Vector of pseudo-loads containing the non-linear terms
$F'_2( )$	Radial boundary condition equation for non-linear modal analysis
$\underset{\sim}{F}'_2$	Vector of pseudo-loads containing the non-linear terms
$F^*(\alpha)$	Non-dimensional foundation reaction

Symbol	Description
g	Function for given eigenvalue
G	Pasternak foundation constant
G_m	Orthonormalisation constant for m^{th} mode
G^*	Non-dimensional Pasternak foundation constant
h	Plate thickness
h_f	Final thickness
h_i	Instantaneous thickness
H	Head of transfer medium
$H(\tau)$	Heaviside step function
H_1, H_2, H_3	Function in solution for root of non-linear modal analysis
i	* see initial note
I	Impulse
I_n	Bessel function of the modified first kind and the n^{th} order
j	* see initial note
J_n	Bessel function of the first kind and n^{th} order
J_2'	Second stress deviatoric
k_f	Non-dimensional Winkler foundation constant
k_i	Eigenvalue
k_s	Yield stress in simple shear
k_v	Viscous damping coefficient of plate vertical
k^*	Non-dimensional Winkler foundation constant
$\underline{K}$	Matrix of coefficients
$\underline{K}'$	Matrix of coefficients for slope
K_m	Bessel function of the modified second kind and n^{th} order
K_o	Material constant
K_1, K_2	Explosive constants associated with gas bubble behaviour

Symbol	Description
K_3	Constant
$\underline{K}_\alpha$	Matrix of coefficients for vertical deflection of plate
$\underline{K}'_\alpha$	Matrix of coefficients for vertical deflection for plate/foundation combination
$\underline{K}_\zeta$	Matrix of coefficients for radial deflection
K_θ	Explosive decay constant
ℓ	Function for given eigenvalue
L	Distance from explosive
$\underset{\sim}{L}$	Load vector
$\underset{\sim}{L}'$	Load vector
m	Density of plate
m_o	Density of energy transfer medium at ambient pressure
m_t	Density of energy transfer medium
$\underline{M}$	Mass matrix
M_r	Radial bending moment/unit length of circumference
M_t	Tangential bending moment/unit length of circumference
n	Strain hardening exponent
N_r	Radial membrane force/unit length of circumference
N_t	Tangential membrane force/unit length of circumference
p_f	Force parallel to the plate surface
p_i	Constant dependant on i^{th} eigenvalue
P	Pressure
P(t)	Pressure acting on diaphragm
P_e	Efficient pressure
P_m	Maximum pressure
P_o	Static yield pressure
P_s	Static collapse load

Symbol	Description
P_t	Pressure at time t
$P_1(t)$	Pressure due to incident shock wave
P^*	Material constant
$q(r,t)$	Load intensity
q_c	Change in capacitor
q_i	Constant dependant on i^{th} eigenvalue
q_n	Force normal to plate surface
$q_1(t)$	Co-ordinate of constraint motion to ensure uniform thinning of undeformed material
Q	Shear stress/unit length of circumference
Q_n	Stress resultant normal to the deformed surface
r	Radius
R	Radius of die-opening
$\underline{R}$	Matrix of co-efficients for foundation reaction
R_e	Explosive charge radius
R_m	Maximum gas bubble radius
R_1	Distance from explosive
s_{ij}	Stress deviator
S	Stand-off of explosive charge
t	Time
$t(r)$	Time at which hinge circle passes through r
t_c	Plate separation
t_f	Time at completion of plastic deformation
t_m	Time at completion of deformation
t_{me}	Time at centroid of pulse
t_y	Time at onset of plastic deformation
T	Elapsed time since incidence of shock front
T_e	Elapsed time for integration
T_o	Pulsation time for gas bubble
T_r^*	Chebyshev polynomial

Symbol	Description
u	Radial deflection
u_o	Initial radial position
u_v	Velocity of energy transfer medium
U	Shock front velocity
U_o	Initial velocity
U_s	Strain energy
U_1	Radial displacement after Hudson
v	Voltage
v_o	Initial normal velocity
V	Volume
w	Vertical deflection
W	Weight of explosive charge
$W(t)$	Function to describe dynamic plastic deflection
W_i	Length of Cordtex in mm
Y	Primary yield stress
Y_n	Bessel function of the second kind and n^{th} order
z	Tangent plane
Z_c	Central deflection of plate in analysis of explosive forming

Symbol	Description
α	Non-dimensional vertical displacement parameter
α_1	Explosive constant
α_2	Constant associated with shock front velocity
$\bar{\alpha}_m(\rho)$	Orthonormal modal shape
$\alpha'(\rho)$	Vertical deflection as a function of radius only
$\underset{\sim}{\alpha}$	Vector of vertical non-dimensional deflection
α^*	Material constant
β	Coefficient for time recurrence relationships
β_o	Hinge circle radius
β_1	Explosive constant
δ	Non-dimensional radius to thickness ratio
$\delta_{(max)}$	Central deflection (Krajcinovic)
δ_o	Central deflection (Florence)
δ_1	Explosive constant
δ_1'	Explosive constant
δ'	Order of power series
∇	Backwards difference operator
∇^4	Non-dimensional biharmonic operator $(\frac{\partial^4}{\partial\rho^4} + \frac{2}{\rho}\frac{\partial^3}{\partial\rho^2} - \frac{1}{\rho^2}\frac{\delta^2}{\partial\rho^2} + \frac{1}{\rho^3}\frac{\partial}{\partial\rho})$
$\bar{\nabla}^4$	Biharmonic operator $(\frac{\partial^4}{\partial r^4} + \frac{2}{r}\frac{\partial^3}{\partial r^3} - \frac{1}{r^2}\frac{\partial^2}{\partial r^2} + \frac{1}{r^3}\frac{\partial}{\partial r})$
ε	Non-dimensional load parameter
ε_c	Field strength between capacitance plates
ε_h	Hoop strain
$\dot{\varepsilon}_{ij}$	Strain rate
ε_m	Strain at centre
ε_o	Permittivity
ε_r	Relative permittivity
$\bar{\varepsilon}$	Effective plastic strain
$\dot{\varepsilon}_i$	Instantaneous strain rate
η	Coefficient for time recurrence relationships
η_t	Energy transfer coefficient

Symbol	Description
γ	Coefficient for time recurrence relationship
γ'	Constant following Berger's assumption
γ_o	Viscosity constant
γ_1, γ_θ	Explosive constant
γ^*	Non-dimensional constant following Berger's assumption
λ, λ_1, λ_2	Eigenvalue
λ^*	Spectral root
θ	Decay constant
θ'	Constant for representation of time domain
θ_d	Diffraction time
θ_p	Characteristic time
θ_i^*	Function for i^{th} eigenvalue
σ_n	Membrane stress in diaphragm
σ_r	Radial stress
σ_t	Tangential stress
σ_y	Static yield stress
$\bar{\sigma}$	Effective Stress
$\bar{\sigma}^*$	Capacitance charge density
ζ	Non-dimensional radial displacement parameter
$\underset{\sim}{\zeta}$	Vector of radial non-dimensional deflections
ρ	Non-dimensional radial parameter
τ	Non-dimensional time parameter
τ_1	Lapsed time after diffraction wave arrived at the surface of the blank
τ_m^*	Effective elapsed time in non-linear modal analysis
$\Gamma(\tau)$	Function in time domain

Symbol	Description
χ	Non-dimensional vertical viscous damping parameter
χ_i	Fraction of initial damping for i^{th} eigenvalue
χ_m	Fractional viscous damping coefficient
χ_s	Instantaneous strain rate
ω_m	Undamped circular natural frequency for the m^{th} mode
ω_o	Work hardening rate
Ω_m	Damped circular natural frequency (under-damped case) for the m^{th} mode
Ω'_m	Damped circular natural frequency (over-damped case) for the m^{th} mode
ψ	Angle between the radial direction and the radial tangent to the deformed middle surface of the plate
ν	Poisson's ratio for plate material
μ	Parameter: Schmidt's analysis of non-linear elastic deflection
ϕ	Slope, $\frac{\partial w}{\partial r}$
ϕ_o	Power function of dynamic stress over static yield
Φ	Stress function

CHAPTER ONE

INTRODUCTION

1.1 HIGH ENERGY RATE FORMING

One of the newer metal forming techniques which received considerable attention in the last fifteen years was the development of the High Energy Rate Forming (HERF) or High Velocity Forming (HFV) processes. The main distinction between the conventional and the High Energy Rate Forming processes was the rate of energy transfer to the workpiece and the resultant strain rates achieved during forming as illustrated in Fig. 1.1, page 2 .

The High Energy Rate Forming processes involve the transmission of energy to the workpiece as a large amplitude impulse with a total duration ranging from microseconds to milliseconds, rather than the long duration, constant amplitude energy transfer associated with the conventional metal forming technique.

1.2 EXPLOSIVE FORMING

Explosive forming was considered to justify a study in depth because of the advantages of low capital and tooling costs that were economic for short or one-off production runs. These were in addition to the following advantages claimed [1.2] for High Energy Rate Forming processes by comparison with conventional forming methods, which were to;

(1) Reduce the size of the equipment required to form large parts,

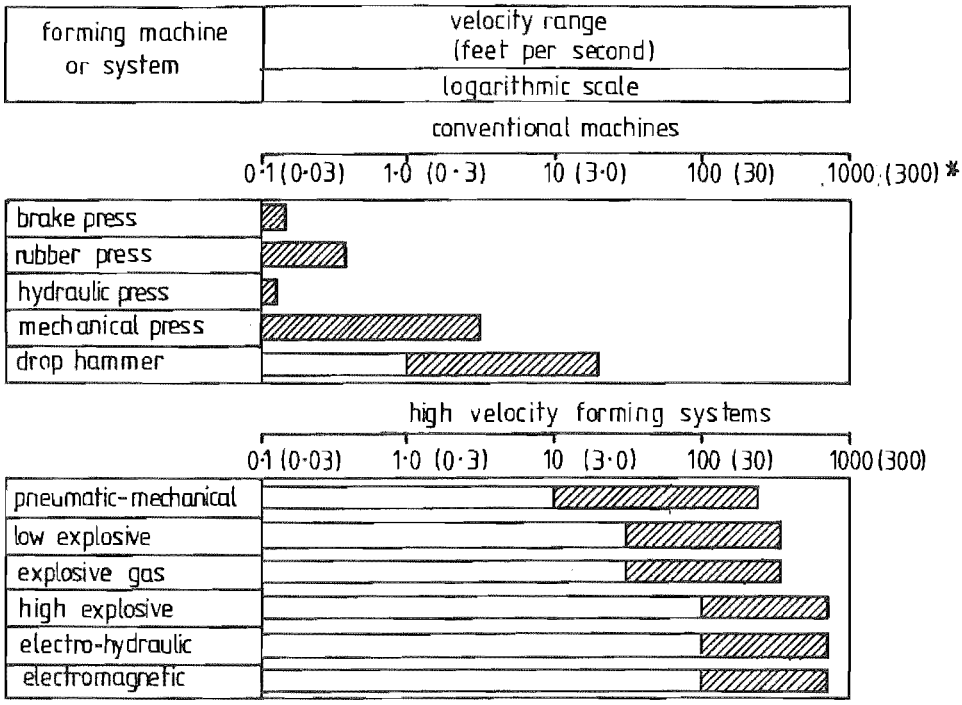

FIG 1·1 DEFORMATION VELOCITY RANGES FOR SEVERAL CONVENTIONAL MACHINES AND HIGH VELOCITY FORMING SYSTEMS [1·1] * m/s

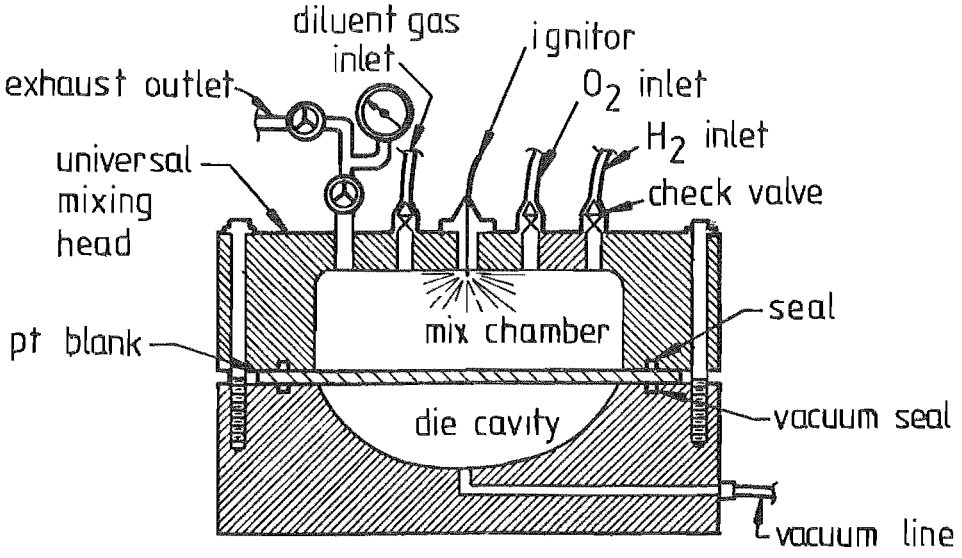

FIG 1·2 SCHEMATIC OF TYPICAL GAS FORMING ARRANGEMENTS [1·1]

(2) Facilitate the making of parts from certain materials not easily formed by conventional methods,
(3) Make parts which are not producible by other methods because of size, material characteristics, or both,
(4) Improve dimensional tolerances,
(5) Lower production costs,
(6) Reduce cost in the fabrication of "one-off" parts.

The lower capital cost of Explosive Forming by comparison with other High Energy Rate Forming processes was due to the inexpensive permanent installation used to transmit the energy from the energy source to the workpiece. The cost of the dies was relatively low because often a female die only was required and inexpensive die materials such as concrete, cast iron, plastic or low carbon steels could be used which resulted in simple tooling requirements. Also the size of workpiece was limited only by the strength of the container restraining the energy transmission media while the versatility of the process was such that all the following forming operations could be carried out using explosives as the energy source; namely sizing, drawing, embossing, engraving, flanging, compacting and cutting.

The limitations that existed for the explosive forming process were:

(1) A short production run because it was a labour intensive operation.
(2) Noise and vibration when associated and sited with other production facilities or in residential areas.
(3) Storage of explosives and detonators to comply with local dangerous goods regulations.
(4) Qualifications required by personnel to meet local regulations governing industrial usage of explosives.
(5) Modification of material properties.

Because of these limitations the explosive forming processes

must be considered complimentary to conventional forming techniques rather than replacing them.

In spite of these limitations it was felt that for New Zealand engineering and manufacturing conditions which often involved low volume or one-off production runs this process was ideal and allowed the cheap utilization of the advantages associated with High Energy Rate Forming. For these reasons this project was concentrated on the Explosive Forming process.

The Explosive Forming process was divided into three distinct classifications: Closed Deflagration, Contact Detonation and Stand-off Detonation. These classifications were dependent upon the energy source and the method of energy transmission from the source to the workpiece or metal blank to be deformed.

1.2.1. CLOSED DEFLAGRATION

The energy source was obtained by combustion of either a slow burning propellant explosive or gaseous mixtures. Because of the relatively slow pressure rise and low peak pressures due to either the containment of the products of combustion or the combination of containment and the impinging of the combustion front on the workpiece, Fig. 1.2, page 2 , the deflagration processes lent themselves to close control of the pressure impulse as well as being the most suitable explosive forming technique to initially automate. [1.2]

Preliminary investigations on this forming method using an oxygen/ acetylene gaseous mixture were conducted at the Mechanical Engineering Department, University of Canterbury [1.3] but discontinued because of the danger of pre-ignition with this particular gaseous mixture.

Because of the requirement to contain the products of

combustion, the size of the workpiece was limited and the capital cost higher than for the equivalent explosive detonation forming process.

1.2.2 CONTACT DETONATION

The high explosive in this process was detonated in contact with the workpiece, which resulted in very rapid stress rises in the material, and high maximum stresses associated with the detonation front in the explosive. This process was used for explosive welding, powder compaction, engraving, hardening and cutting. The major variables in this method were detonation velocity and configuration of the explosive with respect to the workpiece, which influenced both the final deformation and the material properties of the product.

1.2.3 STAND-OFF DETONATION

This explosive forming operation, Fig. 1.3, page 6 , relied upon the transmission of the energy from the high explosive charge to the metal blank to be formed by a shock wave moving through the transmission medium such as air or water.

Hence the stand-off of the explosive charge from the blank surface, and its size and shape were major variables because they controlled the geometric form and the intensity of the shock wave impinging upon the blank surface. Other major variables were the transmission medium, the required product shape and workpiece material. The hold-down force or method of draw wrinkle control also influenced the final product shape and strain distribution.

All these variables were interdependent and therefore optimization was usually based upon experience and experimentation,

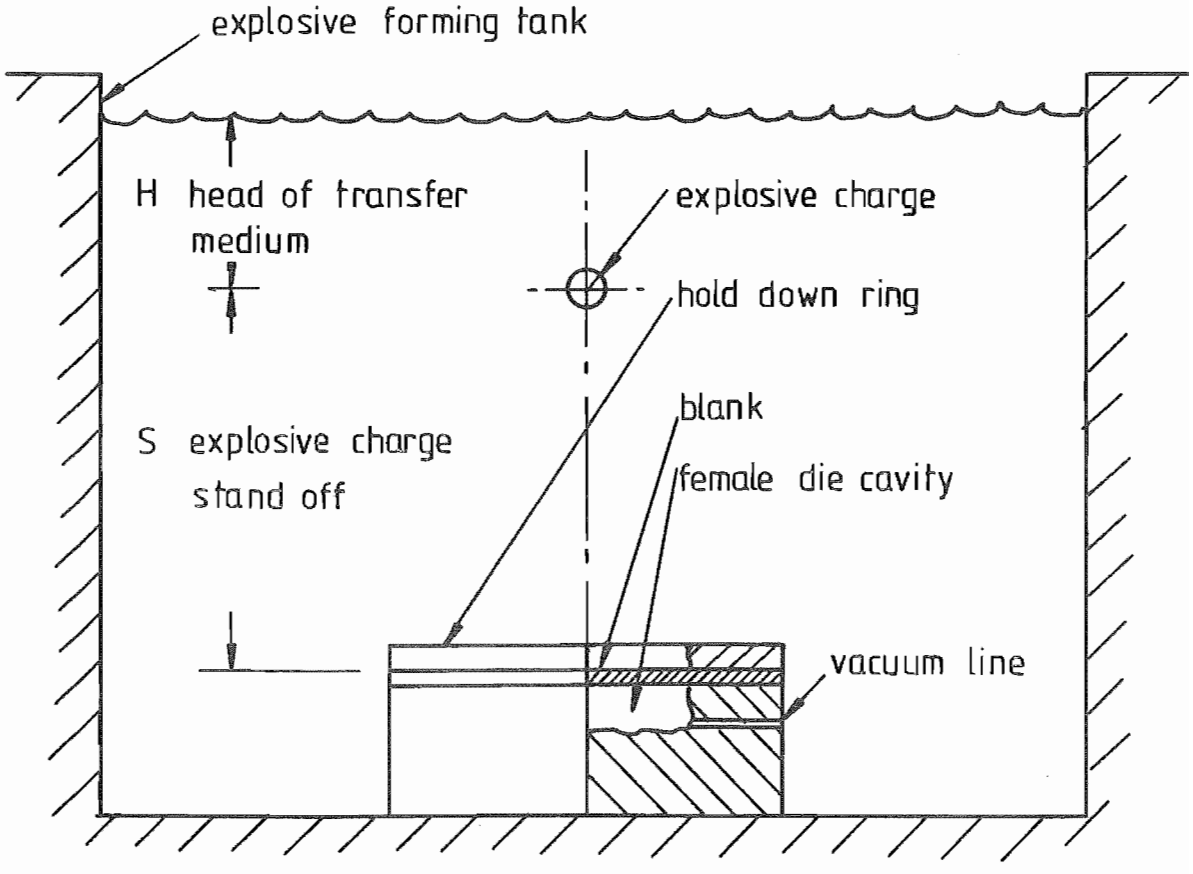

FIG 1·3 STAND-OFF EXPLOSIVE DIE FORMING

and although some analytical research work [2.4, 2.5] has been carried out the majority of the research work has been restricted to emperical analysis. [2.6, 2.7, 2.8].

Stand-off detonation techniques were further divided into two categories of die forming and free forming.

1.2.3.1 STAND-OFF EXPLOSIVE DIE FORMING The explosive charge was placed above the workpiece, as shown in Fig. 1.3, page 6 , and detonated. The energy released was transmitted through the transfer medium as a shock wave to the blank or workpiece which was located over the female die of the required final shape. The cavity between the blank and die was evacuated because the rate of deformation of the blank resulted in 'quasi-adiabatic' compression of any trapped residual air. This compression could produce local gas temperatures sufficient to weld [2.9] the blank to the die or otherwise damage the workpiece and die surface by overheating or 'burning'. Also any residual air prevented the blank from bottoming on the die and therefore resulted in incomplete forming.

If evacuation of the air was complete the workpiece deformed into the die and took up the shape of the die.

1.2.3.2 STAND-OFF FREE FORMING The metal blank, as shown in Fig. 1.4, page 8 , was supported by a draw ring which functioned in conjunction with the hold-down ring to control draw wrinkling and gave the peripheral diameter of the final shape.

This process had limited application and could only be used for very basic operations such as bulging and the development of simple symmetric shapes, although there were some techniques which allowed an element of control of the final shape.

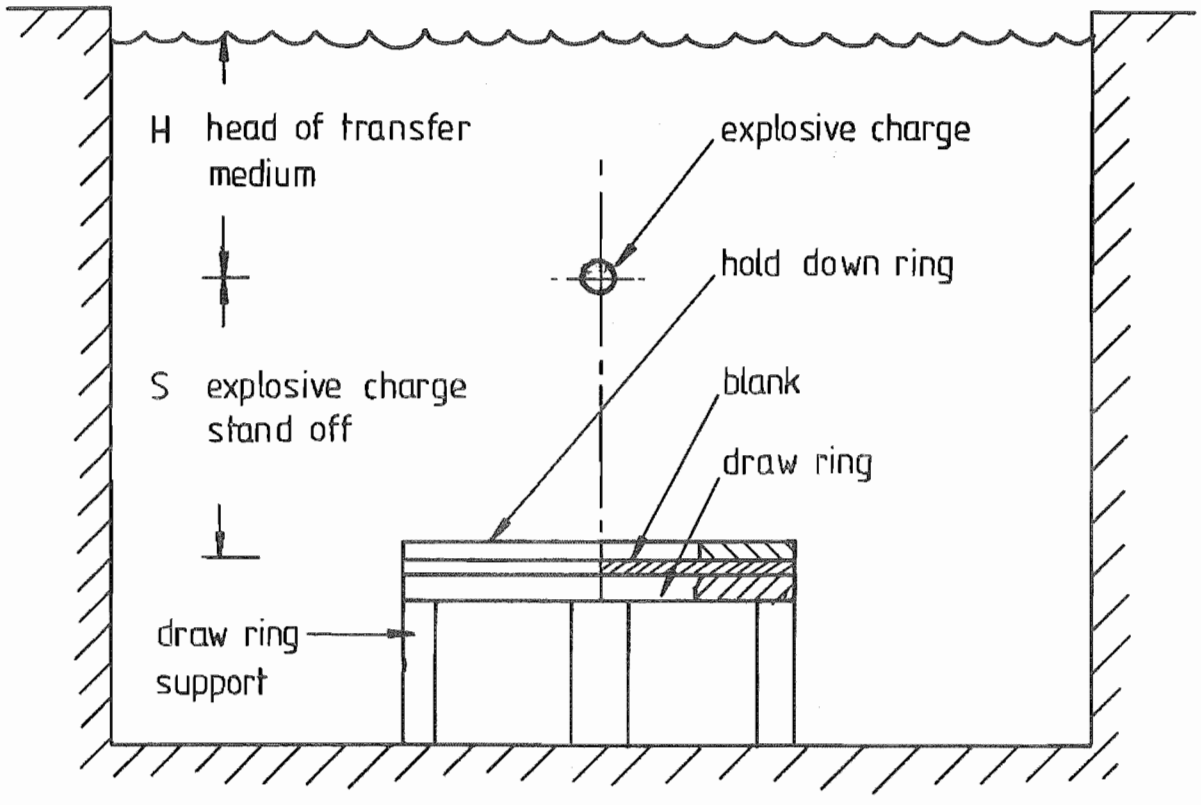

FIG 1·4 STAND-OFF EXPLOSIVE FREE FORMING

1.3 SCOPE OF PROJECT

The aim of the project was to investigate the explosive forming process and to consider the energy transfer mechanism and associated instrumentation.

Chapter Two contains a general review of the literature on stand-off explosive forming in which the specific processes of free forming and die forming are presented. In considering under water explosions and the subsequent energy transfer to the workpiece it became apparent that considerable effort has been put into the study of the detonation, primary pressure pulses and subsequent behaviour of the gaseous products of large homogeneous explosive charges (0.2 - 100 kgm) and the associated energy transfer to the water. However, the explosive has been located at distances of 10 - 100 m below the free surface of a semi-infinite body of water and the resultant pressure measurements were made at distances of 1 - 10 m from the charge which precludes the direct use of the data in typical explosive forming processes. In explosive forming operations the energy source is often non-homogeneous being some arrangement of a detonating fuse such as Cordtex, with a point source detonation. Usually these forming operations are carried out in a tank or finite body of water and therefore the distances between the explosive charge and the free surface are in the order of 0.1 - 3 metres while for energy efficiency the charge is in close proximity to the workpiece with stand-off distances of 0.025 - 0.300 m being common.

The deformation of plates subject to impulsive loading is reviewed because the close proximity of the explosive charge to the deforming blank is considered to interact with the secondary energy transfer associated with behaviour of the gaseous products of deformation. There is evidence that this secondary loading is significant in this forming process.

Energy transfer in the explosive forming process is also reviewed and this information is mainly based on the measurement of

the subsequent plastic deformation and equating this to the energy available from the explosive. Some pressure measurements have been carried out during the explosive forming process but the transducer used has been located away from the region of the workpiece.

From the review of the explosive forming literature it became apparent that the majority of explosive forming research has involved experimentation and the collection of data for specific formed product shapes, specific materials or modified free forming processes.

While some empirical relationships have been developed there was a need to better understand the interaction between the blank deformation and the energy transfer so that the deformation mechanisms could be adequately described. This pointed to the requirement for a pressure transducer which could be located in the energy transfer medium in the immediate region of the workpiece. It would have to withstand and record the primary pressure pulse while having sufficient sensitivity to record the reloading phase as well as being of such a size that it did not interfere with the energy transfer.

Therefore a review of instrumentation for deformation and pressure measurement is contained in Chapter Three with emphasis on pressure transducers which would be capable of operating in the region immediately adjacent to the deforming blank. High pressure and shock tube pressure measurement techniques are the main areas reviewed although conventional strain gauging techniques as well as use of a range of standard components which exhibit pressure sensitivity are considered. Following the review it became apparent that to record the pressure in the region adjacent to the blank a miniature transducer is required based on a plate/dislocation crystal. Because of the requirement to withstand and produce information on the incident initial shock wave as well as the reloading phase of the explosive forming process, the development of a pressure transducer which operates in the non-linear deflection mode for the primary shock wave and the linear deflection mode for the reloading phase is considered. Because of the difficulty

associated with accurately calibrating the transducer for the proposed operating regime the decision was made to numerically analyse the behaviour of the proposed design under the anticipated pressure loading conditions.

To achieve the requisite sensitivity in the reloading phase, the deflection of the transducer would exhibit geometrically non-linear behaviour during the initial incident shock wave and therefore the analysis had to describe the non-linear response of the plate/ foundation combination to impulsive transient loading. Chapter Four gives the development of the dynamic form of the Von Karman equations and the required boundary conditions to describe the non-linear dynamic behaviour of a plate/foundation system with a fixed edge boundary.

To establish the accuracy of the spatial numerical model for the plate prior to studying the transient non-linear behaviour of the plate/foundation combinations, a modal analysis is presented in Chapter Five, which satisfies the given boundary conditions and describes the linear dynamic response of the plate/foundation loading. This gave a basis for the verification of the accuracy of the numerical modelling of the transducer response in the linear range as well as allowing a comparison of the alogirithms available to describe the time domain. The modal analysis is extended by the application of quasi-linearisation and the use of an effective elapsed time parameter to give an approximate response to the transient loading in the non-linear deflection regime. Hence the non-linear deflection determined by the numerical analysis, described in Chapter Six, could be compared with the approximate deflection from the non-linear modal analysis.

After consideration of a range of methods of solution a central finite difference scheme is used to describe the spatial domain. The Winkler and Pasternak foundation models were implemented in the spatial numerical scheme.

The geometric non-linearity is considered to act as a pseudo load and at each time step iteration is carried out to converge on

the resultant non-linear deflection. A time-stepping solution based upon a three or four point recurrence scheme is applied to the time domain and the stability of the three point scheme for viscous damping conditions is investigated and the resultant spectral radii presented.

The results of the numerical investigation into the time domain recurrence schemes response for a multi-degree of freedom system, subject to a rectangular pulse load are contained in Chapter Seven. The comparison between the results from the linear modal analysis and the numerical program are presented for the plate and plate/ foundation system to verify the spatial and time numerical representation.

The non-linear dynamic transient deflection for the plate and plate/foundation with a simply supported immovable edges and the rigid clamped edge is presented in Chapter Seven and compared with the information available in the literature. The quasi-linearisation technique applied and the spatial representation used in the only published data for the non-linear plate/foundation combination is discussed. For fixed edge boundary conditions and particularly the Pasternak foundation model there is a major discrepancy in the published results. The design performance of the transducer is shown for the anticipated exponentially decaying transient load.

Chapter Eight contains the conclusions from this work as well as recommendations for subsequent development and testing of the pressure transducer and further research into non-linear transient deflection.

CHAPTER TWO

LITERATURE REVIEW

2.1 INTRODUCTION

The large volume of literature associated with explosive forming ranged from the descriptions of the development of specific components, such as submarine end closures[2.1] with their associated problems and methods of overcoming these problems, to the theoretical analysis of the deformation of the metal blank for explosive forming and its interaction with the energy transfer[2.2]

Therefore the literature review for explosive forming was considered under the following headings of general, energy transfer, deformation mechanisms and energy transfer/deformation interaction.

Although the major developments in the application of High Energy Rate Forming techniques have occurred within the last twenty years, explosive forming was first suggested as a metal working process in 1888 when C.E. Munroe[2.3] described a method of metal engraving using gun cotton as the energy source.

Of the general introductory texts in High Energy Rate Forming that have subsequently become available, the reference by Dr. A. A. Ezra[2.4] contained a comprehensive collection of results of both analytical and experimental research work in explosive forming up to 1972, as well as explosive data of particular application to explosive forming and welding. This book was an excellent introductory text, particularly with respect to explosive forming as it considers the mechanism of energy transfer,explosive forming of domes, scaling laws for model studies, expansion of rings by explosives, explosive forming dies, analysis and design of explosive forming facilities, explosives and the effect of explosive forming on material properties, to quote relevant chapter topics.

Another general introductory reference, 'High-Velocity Forming of Metals'[2.5] gave 'a concise yet intensive treatment of the mechanics, principles, equipment and methods employed in the forming of metals by the explosive, electro-hydraulic, magnetic pulse and pneumatic-mechanical processes'. J.S. Rinehart et al[2.6] have produced a comprehensive general reference for practical explosive forming techniques and gave methods of overcoming the problems facing the engineer installing this metal working process.

Work carried out in the Department of Mechanical Engineering at the University of Birmingham, is reported in the reference for high speed metal forming, written by R. Davies et al [2.7], while a critical evaluation of explosive forming methods was given by H.G. Baron et al[2.8]

2.2 GENERAL

Reviews of the state of the local application of explosive forming were presented at the First International Conference of the Centre for High Energy Forming, 1967, for Belgium, France, Germany, Japan and Norway.

The paper presented by Pietteur[2.9] gave an overview of the work carried out at the Centre National De Recherces Metallurgiques, Belgium, investigating the deep drawing of a range of materials and the manufacturing of specialised shapes difficult or impossible to produce by conventional techniques. The conclusions presented suggested that deep drawing could be profitably applied in the forming of product shapes involving large dimensions, with a suggested lower size limit of approximately two metres diameter, and a diameter:thickness ratio (D/h) which satisfied the relationship $20<(d/h)<190$, and if the risk of draw wrinkling was accepted, it could be increased to $20<(D/h)<235$. Also the economic production of specialised shapes such as components for aeronautical applications

was investigated, as well as the forming of high strength and stainless steels.

Frey's paper[2.10] briefly described the range of products manufactured by Secathen, a French company which was formed to use the explosive forming techniques as a primary production method, particularly involving stainless steels, light alloys such as the aluminium-magnesium alloys or specialised metals such as titanium. A point of interest in this paper was the mention of the discrepancy between the earlier optimistic technical reports on explosive forming and the subsequent experience of the company in the application of this forming method to the manufacture of specific products.

This point was reinforced by Simmler[2.11] in his review of the implementation of High Energy Rate Forming in Germany. Exploratory tests carried out both within German industry and Technical Institutes found that the areas of the explosive forming technique requiring more research prior to industrial acceptance of the process were;

(a) Scaling relationships to allow reliable small scale experimentation for large component manufacture.
(b) The determination of explosive properties and characteristics in methods more appropriate to their application in this forming technique.
(c) A knowledge of the interaction between the explosive and energy transmission media for distances of less than 0.3 metres from the charge.
(d) An understanding of draw wrinkling at high deformation velocities.
(e) The study of the energy transfer to the blank, the influence of the gas bubble following detonation and the resultant effect of these factors upon the material properties following forming.

(f) The development of techniques to take advantage of the characteristics of high energy rate forming; improvement of the preparation and charging times, as well as making large dies more economic to produce.

Subsequent research was conducted within Germany and Holland on developing suitable instrumentation, deriving scaling laws to utilise small scale experimental results in industrial production and determining the effects of this forming method on 'fatigue, ductility, brittle fracture and corrosion resistance'. As a result of this work, and to reduce charge sizes and hence associated vibration and shock wave amplitudes, a contact explosive forming technique was developed using specially produced low brisance explosives with prolonged pressure-time characteristics.

Nemitz[2.12] described the results of one aspect of the German research into the cold forming of high strength steels in the hardened condition by the use of contact explosives as well as the development of improved dies. A general review of the products manufactured by Japanese industry using High Energy Rate Forming was presented by Kiyota[2.13]

By considering the case histories of the application of explosive forming to a range of manufactured products, Haegland[2.14] further highlighted the difficulties experienced in the industrial application of the process in a small country such as Norway. The experience of Berman et al[2.15] in the commercial application of explosive forming showed the feasibility of the use of small stand-offs of the explosive charges so that the energy available at the blank surface was appropriate for deformations that were non-uniform. This enabled the energy distribution to be related to the required deformation.

The description of the manufacturing history of a range of products such as end closures for a research submarine[2.1], domes[2.16,2.17,2.18] and fuel tank caps for aerospace products such as for the Saturn V C rockets[2.19] indicated the extent of commercial application of the explosive forming process in America. It was pointed out by Simmler[2.11] that the majority of reported American applications involve production in the large aerospace industry.

As has been described[2.5] the major areas of research into the explosive forming process has concerned the energy release and transmission to the workpiece, the resultant behaviour of the workpiece and the material properties of the product manufactured by this forming method. While considerable effort has been expended particularly in the latter two areas, much of the energy transfer research has been either qualitative or the modification of results obtained for large charge sizes based upon Naval research[2.20]. This research has been conducted into studying the destructive capability or performance of explosive charges. Since explosive forming involved relatively small charges in close proximity to the deforming workpiece, it was considered that the energy transfer associated with stand-off explosive forming was an area requiring a better understanding. This was because of the interaction and dependence of the workpiece behaviour on the engergy transfer.

2.2.1 FREE FORMING

This process,described in section page ,involved only a limited number of variables by comparison with explosive die forming, and therefore a considerable section of fundamental investigation into explosive forming has been based upon the free forming technique. As Sag[2.21] suggested, the initial impetus for the current interest in utilization of explosive energy for metal forming was the result of the many investigations into the effect of underwater explosions carried out during and following the Second World War. While these investigations mainly considered the damage

caused to a structure by an underwater explosion as a function of charge size and distance from the charge, results associated with deformation gauges[2.22,2.23,2.24] could be applied to explosive free forming, thus further concentrating research into this method rather than the die forming process. An example of this was the UREL[2.24] diaphragm gauge which resulted in interest in the deformation of a circular diaphragm subjected to explosive loading before the advent of commercial explosive forming.

N.N. Ida et al[2.25] discussed the advantages and limitations of the process, as well as economic auxiliary methods aimed at overcoming the limitations of

'(1) excessive thinning of the material at the apex of the sheet,
(2) a tendency for extensive buckling to occur at the mouth of the formed shape,
(3) inability to form shapes other than fourth order paraboloids of revolution.
(4) the formability curves of the materials commonly used for missile parts in conjunction with the thickness specified, severely restricts the depth to which the domes can be formed.'

The auxiliary techniques used to obtain the maximum economic advantages of the die-less forming process and to overcome the disadvantages, were the plug cushion technique, the sandwich technique, the removal of surface oxides and the carriage principle.

2.2.1.1 PLUG CUSHION TECHNIQUE The plug cushion technique ,Fig. 2.1 page 19 , relied upon the placing of a pad of material such as lead or rubber on the upper surface of the blank and hence the energy was transmitted through the plug cushion to the blank.

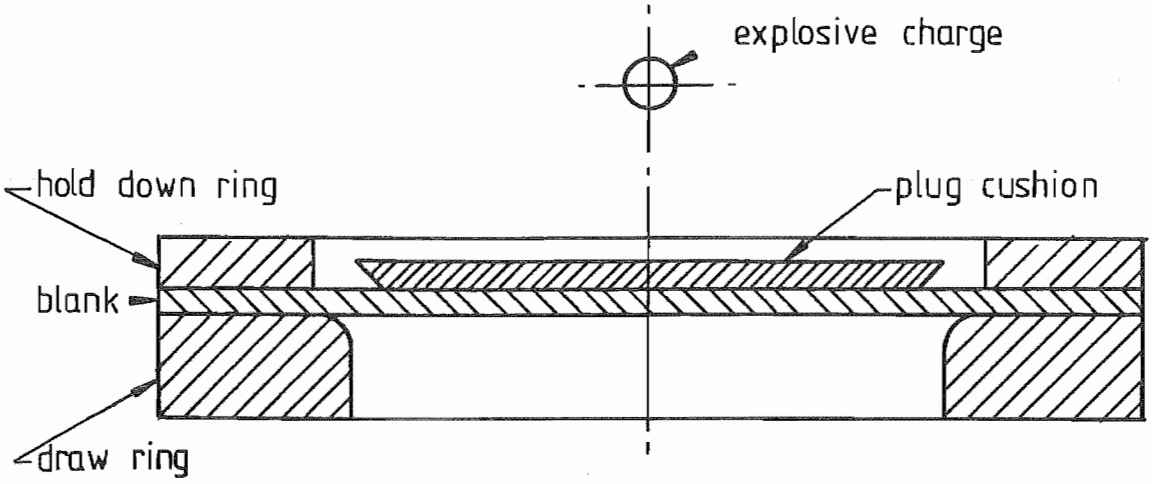

FIG 2·1 PLUG CUSHION TECHNIQUE

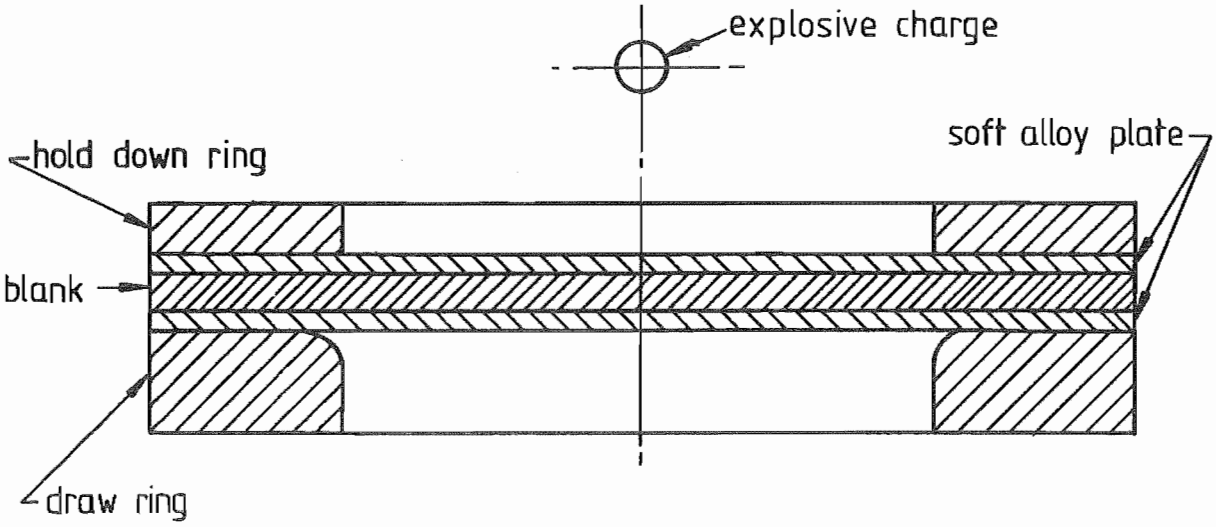

FIG. 2·2 SANDWICH TECHNIQUE

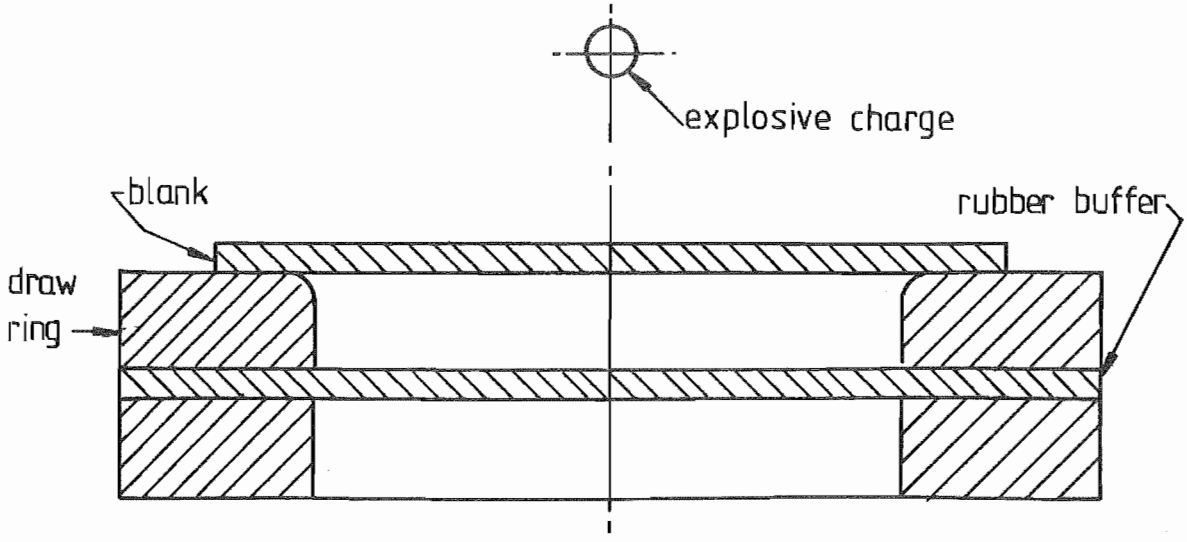

FIG 2·3 CARRIAGE TECHNIQUE

By variation of the plug cushion thickness, profile and material, along with the other parameters associated with the free forming process, considerable control was possible on shape, thickness strain distribution and draw wrinkling.

Johnson et al[2.26] did preliminary investigations into the influence of the following parameters associated with free forming;

'(i) charge weight,
(ii) plug cushion thickness and peripheral angle,
(iii) blank thickness,
(iv) die profile radius
(v) the effect of the clearance between the blank and the clamping ring,
(vi) the strain distribution resulting from these operations.'

For these investigations the plug material was lead and the desired product shape was a drawn hemi-spherical cup. Subsequent work by Johnson et al[2.27] gave the results of an investigation into the influence of the hydrostatic head and stand-off upon deep drawing using the plug cushion. Also in this reference, the velocity of deformation was measured using the pin contactor method* to determine the effect of the plug cushion upon the energy transfer.

The displacement velocity of the blank was similar to that exhibited in the free forming of a blank without a plug cushion[2.28], the kinetic energy of the blank being developed in two well defined phases. In the case of the plug cushion, the two proposed possible mechanisms of energy transfer were due to the primary shock wave impinging on the surface of the plug, while the second phase energy transfer was due either to the bubble pulse action and/or a water hammer effect following the collapse of cavitation, or a separation of the blank-plug interface under the primary shock wave and a transfer of kinetic energy at the

subsequent re-establishment of the interface contact from the plug to the blank.

2.2.1.2 SANDWICH TECHNIQUE The sandwich technique,Fig 2.2 page 19 , of explosive free forming was an extension of the plug cushion method, which obtained similar results by sandwiching the blank to be formed between layers of a softer alloy. The softer alloy would attenuate the applied loading as well as control the blank profile by the blank/alloy plate interface friction and the interaction of the deformation of the layers and the blank.

2.2.1.3 OXIDE REMOVAL It was claimed that by removing the surface oxide on aluminium blanks immediately prior to explosive forming, the resultant deformation profile was modified by comparison with aluminium blanks for which oxide removal was not carried out. However the oxide would reform immediately on exposure to air or water.

2.2.1.4 CARRIAGE PRINCIPLE The carriage principle,Fig 2.3 page 19 , allowed the blank to "bottom" on a thick rubber sheet which modified the final deformation by generating a force opposing the explosive generated pressure wave, as the blank and hence the rubber sheet deformed. This technique according to Ida[2.25] applied a cupping action which resulted in the advantages associated with the plug cushion method.

2.2.1.5 RESULTS OF FREE FORMING RESEARCH The work of Johnson and Sowerby[2.29] suggested that for free forming an optimum hydrostatic head existed dependent upon the charge weight and stand-off, but in agreement with other results [2.27],[2.30], above two feet(300mm) the influence of hydrostatic head was negligible. It was thought that this phenomenon resulted from the control the hydrostatic head had upon the migration of the bubble of gaseous products of detonation and/or the venting of such a bubble to atmosphere during the initial expansion. Subsequent work was done

using the contactor pin method to determine the blank deformation velocity throughout the forming process, and therefore obtain an indication of the energy transfer. It was found that in the range of hydrostatic heads up to three feet(900mm), the time taken for the blank to reach rest was less than that for the secondary pressure pulse, due to the gas bubble oscillations, to reach the blank surface. Hence it was assumed that the bubble pulsation had a negligible influence upon the final deformed shape. Therefore the second stage of kinetic energy exhibited by the blank was possibly derived from either water hammer following the collapse of cavitation, or gas bubble migration to the blank surface. Also the initial velocity of deformation and the velocity- deformation relationship was of interest, because of the dependence of most analytical models of impulsive deformation on an assumed initial velocity distribution. Tests were also conducted on the influence of charge size and stand-off upon the deformation.

Finally the influence of a tank air curtain and the use of air cells to obtain water hammer were studied. It was found that the water hammer effect due to the collapse of the air cell did result in an increase of the deflection for a given charge size and stand-off, while the air curtain interference gave a decrease in the deflection obtained.

Watts et al[2.31] also carried out some free forming experimental work, mainly to study the obtainable elongations under high velocity forming conditions for various metals. Velocity measurements were taken and an attempt was also made to measure the temperature.

Free forming of circular blanks was studied by Johnson et al [2.32] with particular interest being taken in the following aspects;

(i) The use of a rigid baffle plate surrounding the blank to increase the efficiency of the energy transfer,

(ii) The use of a reflecting plate above the

charge to obtain a further improvement in the efficiency of the process,

(iii) The influence of orientation of the die and explosive assembly to the free surface of the water in the forming tank,

(iv) The use of air cells to improve the efficiency of the energy transfer.

Miscellaneous influences were also studied, such as the effect of eccentricity in the locating of the explosive charge with respect to the blank, and eccentricity in the placing of the assembly in the forming tank.

At the University of Birmingham considerable work has been done on the development of an explosive forming machine with the initial studies being based upon free forming [2.24,2.33, 2.34,2.35,2.36]. After an initial study of the suitability of shock reflectors, a parabolic reflector was used, with the charge placed at the focal point to obtain the maximum efficiency in energy utilisation. Instrumentation based upon the pin contactor system and streak photography was used to measure the velocity of deformation and deformation history, while the pressure in the region of the reflector was measured using piezoelectric transducers. The locality of the pressure transducer resulted in the measurement of the energy reflected by the walls of the machine and difficulty was encountered with the overloading of the transducers. A satisfactory correlationship was obtained between the streak photography method of velocity measurement and the pin contactor system. A theoretical study was conducted into the reflection of the shock wave from the reflector surface.

A development of importance associated with free forming was that of scaling laws or process equations, so that the experimental checks on the feasiblity of forming of large components by model studies were relevant. Erza et al[1.6] did a dimensional analysis of the parameters involved in explosive free forming. The results obtained for 2024 Aluminium alloy in various heat treated states

showed that for 'the following conditions of similitude an adequate scaling law was operable;

(1) Geometrical similitude must be provided;
(2) The mechanical properties of the metal blank before explosive forming must be the same for model and full scale,
(3) The kind and shape of explosive charge must be the same for model and prototype.'

The dimensionless parameter was $\frac{e}{\sigma_y h^3}$ and within test limits was not influenced by changes in transfer medium viscosity, mass of the draw ring die or the hold-down force of the blank. Where

e = the energy of the explosive charge.
σ_y = the static yield stress of the metal blank before explosive forming.
h = the thickness of the metal blank.

J.M. Boswell[1.8] worked upon the development of a process equation giving the relationship between the main parameters in the free forming of aluminium.

$$z_c = 1.6938 \frac{(W)^{.6806} (D_o)^{.7325}}{(100h)^{.8831} (S)^{.6707}}$$

where z_c = polar deflection
W = weight of the explosive charge
D_o = the die opening diameter
h = the blank thickness
S = the stand-off of the explosive charge

Work was also carried out to determine the profile and strain distribution across the deformed blank.

Experimental investigation into the free forming of various metals by D.E. Baguley[1.7] obtained an empirical formula to determine the depth of deformation which was given by

$$W_i = K_o \left(\frac{d}{S}\right)^{\alpha_*} R^{1.68}\, h^{1.43}$$

where
- W_i = amount of charge in mm of Cordtex
- K_o = constant governed by the material used
- d = depth of forming
- α_* = a material constant
- R = the radius of the die opening

as well as the appropriate symbols from the previous representation.

S.E. Corbett[2.37] studied the profile of the blank during free forming, using a high speed camera and photographing in silhouette. Hence the deformation and bending wave velocity were determined and it was found that the deformation process fell into four stages;

(1) After the arrival of the shock wave, there is a delay of the order of 100 microseconds before any movement is observable.

(2) The diaphragm then very quickly accelerates to a constant velocity perpendicular to the initial plane of the diaphragm.

(3) The diaphragm moves substantially as a flat plate but the peripheral restraint very quickly brings the edges to rest; this effect is transmitted radially inwards so that successive annular elements are tilted and brought to rest, until the shape is substantially a cone with a rounded tip.

(4) A much slower rounding-out process occurs

in the arrested material. This is sometimes accompanied by a small decrease in central deflection. The final profile is a more gently rounded contour.'

The typical initial deformation profile for the first three of the proposed stages of deformation were as in Fig 2.4 page 27.

Ezra and Malcolm[2.38] carried out an experimental program to study the effect of explosive stand-off and it was found that the influence of the stand-off on the final product was complex.Optimization of stand-off involved a compromise between charge size, strain distribution, blank pull-in, draw depth, draw uniformity and free form shape, as was pointed out by Beck et al[2.17]*

While Ezra et al found that increasing stand-off resulted in a change in the final form from an ellipsoidal profile to a parabolic profile, it was noted by Beck et al, that the decreasing of the stand-off distance, below an "optimum" value gave rise to a "peaked" profile rather than an ellipsoidal profile. Although the results appear to be at variance, it should be noted that Beck's work considered a range of stand-off distance:die opening diameter of 0.01-0.20 while Ezra considered the range 0.083-0.500, and hence the non-uniform distribution of energy at the blank, due to the smaller stand-off, would give rise to localised central deformation observed by Beck et al. Again there was a conflict of results involving the influence of stand-off on uniformity of draw, with Beck et al suggesting that increasing stand-off resulted in decreasing uniformity, while Ezra et al found that an optimum stand-off:die opening diameter was obtained by increasing the stand-off outside Beck's experimental range to 0.333. Finally both works found that increasing stand-off decreased draw and hence adversely affected strain distribution. Beck et al suggested that

---

* Footnote: Beck et al. worked on die forming however their consideration of stand-off was applicable to either free or die forming.

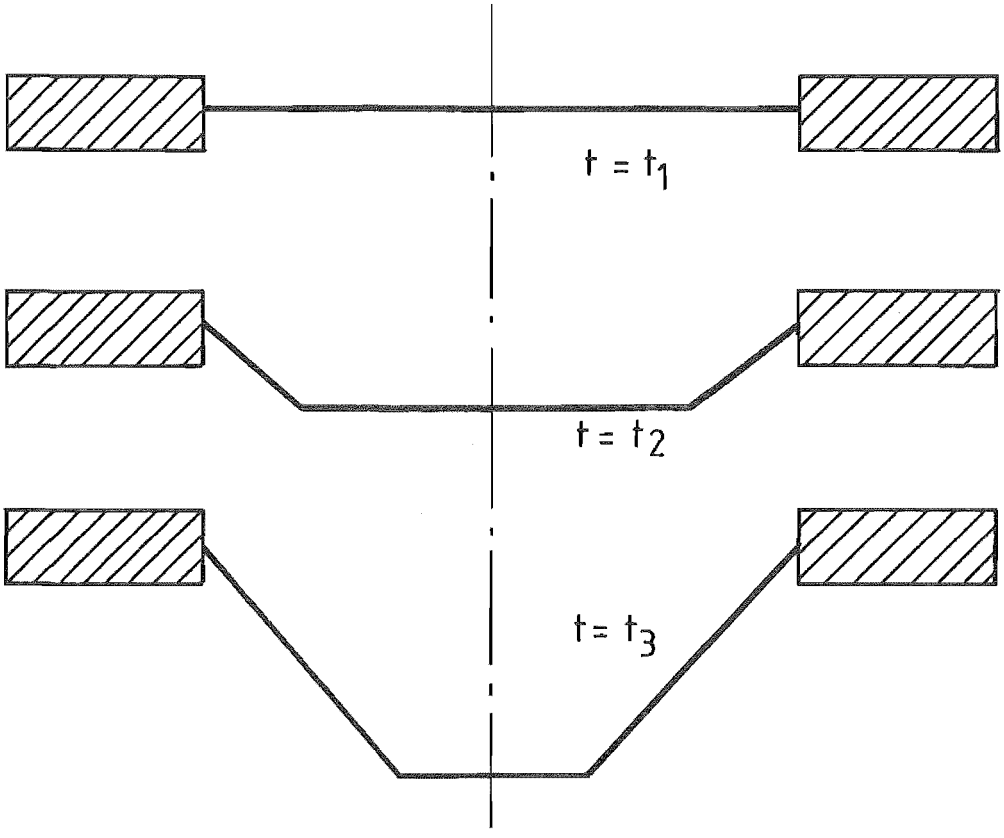

where $t_1 < t_2 < t_3$ and $t_1 < 100$ microseconds

FIG 2·4 DEFORMATION PROFILES IN FREE FORMING

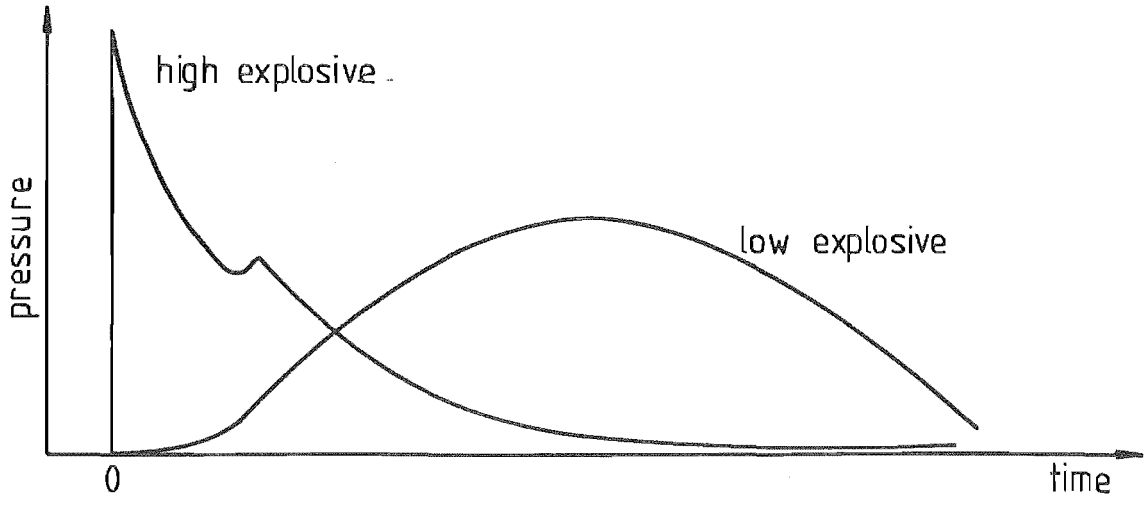

FIG 2·5 SCHEMATIC PRESSURE-TIME CURVES FOR LOW AND HIGH EXPLOSIVES

this was due to the reinforcing of the hold-down pressure by the explosive force on the hold-down ring as the stand-off increased and therefore stretching of the blank resulted before the final shape was taken up with the resultant thinning.

While the use of explosive free forming was limited to symmetrical simple thin shapes, its economic advantages has resulted in research aimed at extending the range of application such as the investigation into the free forming of thick steel domes by Wittrock[2.39] and the expansion of tubes[2.40,2.41] and rings[2.42].

2.2.2 DIE FORMING

As explained in section 1.2.3.2, explosive die forming involved a large number of variables and hence was not used as the basis of much of the reported experimental work into the fundamentals of explosive forming.

The main factors under consideration for the die forming method were springback and the final strain distribution; the springback determining the dimensional accuracy, and the strain distribution limiting the shapes and depth of draw obtainable with this forming process.

Originally it was claimed that all H.E.R.F. processes resulted in the virtual elimination of springback[1.1] but this was disproved by Watts et al[2.31] and the conclusion reached was that 'springback is not eliminated with the application of high strain rates.' Also Agricola et al[2.43] studied springback and reached the following conclusions relevant to springback;

'(1) Explosive forming of partially restrained, nonaxisymmetric blanks causes modification in springback behaviour.

(2) Least metal springback is achieved by using

sheet explosive.

(3) Close explosive stand-offs using sheet explosive yield lower metal springback than the use of high explosive stand-offs.

(4) Large blank coverage, achieved by using sheet explosive is desireable both from the standpoint of reduced springback and uniform strain distribution across the blank.

(5) Increasing the clamping and the hold-down ring roughness decreases the springback.

(6) Springback amounts decrease as blank thickness increases.

(7) Lubrication of the die entrant radius causes an increase in blank springback.

(8) When using nonaxisymmetric die shapes, changes in die entrant radii and the depth of draw do not appreciably modify springback behaviour if partial blank restraint used.'

Boes[2.44] showed that, within limits, increasing the charge weight decreased the springback.

2.2.2.1 DIE MANUFACTURE AND MATERIALS A factor having considerable influence on the economics of explosive die forming and the resultant feasibility of the explosive forming process was the manufacturing cost and durability of the dies. The limited production runs associated with this forming technique resulted in investigations into the use of a range of die materials and die configurations.

While the general references in explosive forming [2.4, 2.5,2.6] gave qualitative guidelines for the design of simple dies, it was obvious that the difficulty of predicting the die performance was having a major effect on industrial acceptance[2.11,2.14,2.16] of this forming process. The die design technique was still a function of intuition, empirical formula[1.2,2.8] and experimental

development[2.16,2.45] rather than accurate quantitative analysis.

Experience in the use of concrete as a die material was reported by a range of workers, examples being Nemitz[2.12], Giannoccolo[2.1] and the report of Haegland[2.14]. Nemitz described the use made of a concrete die with a steel draw and hold-down ring, while Giannoccolo used a glass fibre lined concrete die supported by a steel containment ring for the single shot manufacture of submarine end closures. Haegland found that fibre epoxy resin lined concrete dies were only suitable for production of a limited number of components because of the deterioration of the die linings. Also described briefly in this paper was the use of particle board as a die material. Berman et al[2.15,2.46] presented interesting papers discussing the commercial manufacture of dies, particularly the preparation of simple profiles by fabrication rather than machining and involving relatively cheap materials.

The use of a thin fibre glass shell die on a shock absorber mounting with a steel draw and hold-down rings to manufacture ten foot diameter domes was investigated by Ezra et al[2.16]. Initial experiments were conducted on one fifth scale models and using the scaling laws developed by Ezra, the production die was prepared. The major difficulty reported was in scaling the characteristics of the shock absorbers which may have contributed to the discrepancy between an average mean production run of twelve shots between die failures for the model, and failure occurring after each shot for the production die. The definition of failure was the inability to maintain vacuum and hence the application of epoxy resin between shots was used to increase the die life, but not to the number of shots predicted by the model study.

A further investigation into the design of water backed thin shell dies to produce domes was presented in a paper by Kulkarni et al[2.47], and was based upon a membrane analysis to describe the behaviour of the die under explosive forming conditions. An experimental program based upon dynamic strain measurement confirmed the analytically predicted results and allowed a calculated comparison of peak strain and stress levels for the water backed and

unbacked thin shell dies.

Measurement of elastic die strains were also obtained by Bourma[2.48] in a study of energy transfer and dynamic strain in the deforming blank.

A low cost method of die manufacture was suggested by Lieberman et al[2.49] using ice as the die material. A die was cast for each forming shot from a mould, in the shape of the required product. The resultant die was destroyed during the explosive forming operation. However it was claimed that the transfer of energy from the blank to the die which preceded the die failure ensured that the blank underwent no further plastic deformation following the bottoming in the die. The advantages claimed for the process were the low material and manufacturing costs of the die and a greater dimensional accuracy for the production of a run of components. This final advantage was due to the fact that the wear on the mould used in producing the ice dies was considerably less than that on the high strength die being subjected to typical explosive forming loads.

2.2.3 INFLUENCE OF EXPLOSIVE FORMING ON MATERIAL PROPERTIES

The influence of explosive forming on material properties has been the subject of research investigation for the following reasons.

The dynamics of the high velocity forming methods gave rise to residual stress distributions in the final product which varied markedly from those obtained by conventional forming methods for the similar product shape. This modified residual stress distribution was considered to be due to a combination of the variation in the final strain distribution between the forming techniques, and the effect of the workpiece velocity when it impacted the die in the

case of die forming. Since the material properties such as ultimate tensile strength, fatigue strength, stress corrosion susceptability and impact strength were influenced by residual stressing, researchers have compared the residual stress affected properties for products formed by both conventional and explosive forming techniques.

Also the dynamic strain rates, (400-600)/sec, associated with the forming processes were considered to result in plastic deformation mechanisms which differ significantly from those associated with the lower strain rates, (0.01-20)/sec, of conventional forming processes. Hence the material properties influenced by plastic deformation were modified when products were manufactured by the explosive forming technique, as opposed to those anticipated from conventional forming techniques.

Finally, since the high velocity forming methods were capable of manufacturing components from materials with properties which prevented or restricted their working by conventional techniques, there was considerable interest[2.50,2.51,2.31] in the effect of the forming on their properties.

2.2.3.1 RESIDUAL STRESSES Stone[2.52] using a split tube deflection method showed that the residual stress in an explosively formed 316 stainless steel hexagonal tube was compressive, while a cold drawn round tube of the same material exhibited a tensile residual stress. The maximum residual stress was observed at the corners of the hexagonal profile where workpiece/die impact was greatest, suggesting that volumetric strain due to the shock impact was significant in contributing to the residual stress in explosive die forming.

This confirmed work by Orava et al[2.53] involving comparison between explosively die formed and explosively free formed 316 stainless steel in which subsequent tensile tests exhibited a 29.6% increase in yield strength for the explosively die formed steel, as compared to a conventionally formed steel, while only a 3.4%

increase was observed for an explosively free formed steel with strain energy absorption similar to that for both the conventional and explosively die formed product.

Van Wely[2.54] also carried out residual stress measurements on five foot pressure vessel ends manufactured by cold pressing and explosive forming low carbon AISI 304-L and HY100 steels. The residual stresses were determined by both the back scattering X-ray technique and the strain gauge method involving placing strain gauges on the point of interest and locally relieving the residual stresses by drilling a hole. Both methods allowed the radial and tangential residual stresses to be measured. Some difficulty was encountered with the X-ray technique because of the localised surface nature of the measurement with the back scattering occuring only from a 10 micron outer layer of the material. The general conclusion was that the explosive die forming gave rise to a residual compressive stress, while the cold pressing method of manufacturing gave residual tensile stress.

2.2.3.2 PLASTIC DEFORMATION MECHANISMS It has been postulated[2.55] that since the peak pressure of the incident shock wave associated with explosive forming can be such that it may exceed the dynamic yield strength of the material to be formed, the deformation mechanisms were modified to allow the redistribution of the applied loading.

A modification which has been reported to occur as a function of the dynamic strain rate, was an increase in the proportion of twins observed[2.56] for the given strain magnitude and ambient temperature. This would result in a greater re-orientation of the lattice towards more favourable slip conditions and the possible increased concentration of mobile dislocations within the lattice. Also, increased concentration of point defects due to the lattice shock loading has been suggested[2.55].

Two further modifications have been discussed: firstly, the fracture of inclusions, as a function of the rate of dislocation propagation due to the dynamic load application, and the second being the presence of different dislocation structures or distributions following deformation than would be anticipated from conventional forming.

The observations on changes to the plastic deformation mechanisms have been basically uncorroborated and there exists a number of contradictory reports in the literature on this aspect of the effect of explosive forming on material properties.

The majority of observations currently available giving detailed examination of the dynamic deformation mechanisms either involve high pressure, short duration,(0-5 microseconds) contact explosive loading situations [2.51,2.57,2.58], or the development and operation of dynamic stress-strain rigs[2.59,2.60] used in work aimed at deriving constitutive equations to describe the material behaviour at high strain rates. While the results from these investigations may be applicable in certain specific stand-off explosive forming operations, care must be taken in equating these results to phenomena observed in stand-off explosive forming experiments.

The modification of properties has been used to reinforce observations involving a suggested deformation mechanism in a limited number of cases such as the accelerated ageing reported by Otte[2.61] for aluminium alloy. The accelerated ageing was attributed to increased diffusion rates within the lattice which were a function of the excess concentration of vacancies resulting from the non-conservative motion of edge jogs on screw dislocations. Also increased embrittlement and corrosion behaviour have been attributed to the modified plastic deformation mechanisms.

Optical[2.62] and Electron Microscopy[2.51,2.55] have been used in a limited number of studies to verify these modifications for a specific material or loading condition, but again contradictory information has resulted.

2.2.3.3 MATERIAL PROPERTY EFFECTS There exists in the literature a large number of unrelated descriptions of research carried out on the effect of explosive forming on material properties[2.50,2.54,2.55,2.56,2.62].

The most relevant review paper was that of R.N. Orava et al [2.53] which considered 'The effect of High Rate Forming on the Terminal Characteristics of Materials.' While this survey was restricted to cases where a comparison could be made between a high energy rate formed component and a conventionally formed component with similar deformation, it gave a comprehensive collection of the results of the significant research into this field up until 1969.

The majority of research into material effects was carried out during this period and hence, while recognising that work has been subsequently done, the conclusions of this review were still applicable.

2.3 UNDERWATER EXPLOSIONS

The feature which uniquely identified these methods of metal forming was the energy source and the technique of transmitting the energy from that source to the blank or 'workpiece' to be deformed or modified.

While a range of energy transmission media such as 'air, water, oil, gelatin, talc and liquid salts' have been mentioned for stand-off forming operations by Rinehart et al[1.1] and research has been carried out into the efficiency of plasticine, sand and water,sand and oil[2.63] as transfer media, it was considered that this investigation should be restricted to the stand-off explosive forming process using water as the energy transfer media.

The selection of this media was based upon its common usage, increased relative safety and industrial acceptability. The major safety aspect was the comparatively high transfer efficiency resulting in a smaller charge size for a given amount of plastic deformation when compared with other media. Also the containment effect of the water reduced the required safety distances for shot firing by preventing debris such as detonator casings attaining high velocities.

Another advantage of the reduced charge and the water energy transfer media was the lessening of noise and vibration problems associated with this manufacturing method, and hence reducing the restrictions on the siting of the forming installation.

Finally, water generally has an advantage of low cost, availability and ease of handling.

The energy source used in this forming method was high explosive charges as opposed to a low explosive charge. The distinction between high and low explosives is shown in Fig 2.5 page 27 .

The high explosive involved a shock or detonation wave, the chemical reaction occurring within this discontinuity which propagated through the explosive, while the low explosive reacted by deflagration. Although the rate of chemical reaction or deflagration increased with pressure, and the pressure was related to the chemical reaction rate giving rise to an explosion, the resultant rate of reaction was usually a few tenths of one per cent of that in the detonation wave[2.64]

2.3.1 DETONATION

The quantitative description of the detonation of solid explosives has, and continues to be the subject of considerable research[2.65,2.66] and is still not understood completely. The study of detonation in underwater explosions has been restricted to research carried out with respect to large charges, greater than one kilogram of TNT or its equivalent, mainly in support of naval research and weapons development[2.20,2.67,2.68].

The detonation and subsequent behaviour of the detonation products has a most significant influence on the mode of energy transfer to the surrounding media. The detonation wave impinging on the explosive/media interface gives rise to the primary shock wave and the subsequent non-homogenous behaviour of the gaseous products particularly at the interface determines the further energy transfer and decay characteristics of the primary shock wave. Finally, the media-gaseous detonation products interaction provides the mechanism controlling the final stages of the energy transfer. While the significance was recognised it was considered impractical to attempt to correlate the detonation in the charge to the resultant energy transfer.

This decision was taken because the energy source used in this investigation was Cordtex, consisting of a waterproof flexible cord containing a charge of granular pentaerythritol tetranitrate (P.E.T.N.) of weight 10.4 gms/metre wrapped around a No. 6 electric detonator in an approximation to a sphere. This arrangement of charge made the location of detonation and its subsequent propagation indeterminant. Although it was feasible to analyse detonation in line-charges of Cordtex, since they were non-uniform in their pressure, impulse and energy distribution, line charges were not suitable for the stand-off free forming operation under consideration. Also the common representation of shock waves for explosive forming[2.69] involved the assumption of either an acoustic approximation or alternatively, incompressible hydrodynamics because the charge size and resultant peak pressures

were not sufficiently large to require the finite amplitude approach. Hence a knowledge of the detonation and non-homogenous behaviour of the gaseous products of detonation immediately following passage of the detonation was not so significant.

It should be noted finally that while analyses of limited accuracy [2.65,2.70] were available to describe the detonation, studies into the shock wave behaviour in the energy transfer media were usually based upon an assumption simplifying the detonation/media interaction, such as adiabatic explosion at a constant volume[2.70]. Although these simplifications were general, work by S. A. Berger et al[2.68] did analytically described the detonation front of pentaerythritol tetranitrate and the resultant shock wave until it had travelled approximately 7 charge radii from the charge centre,allowing for nonisentropic behaviour of the detonation products behind the main shock wave, and before the secondary shock wave.

2.3.2 SHOCK WAVES

Experimental measurements for large explosive charges, unaffected by boundaries, give a general pressure history for the shock wave generated in water by a spherical charge, shown in Fig 2.6 page 39 after Cole[2.70] and Schauer[2.69]

An important experimentally derived result from the point of view of the usefulness of the explosive for plastic deformation of structures was the impulse available from the passage of the shock wave. A typical graph derived from pressure recording equipment, used in the investigation of the performance of large charges, is given in Fig 2.7 page 39 after Cole[2.70] for a fixed point in sea water twenty feet (6.1m) away from a 300 pound (136 Kgm) charge.

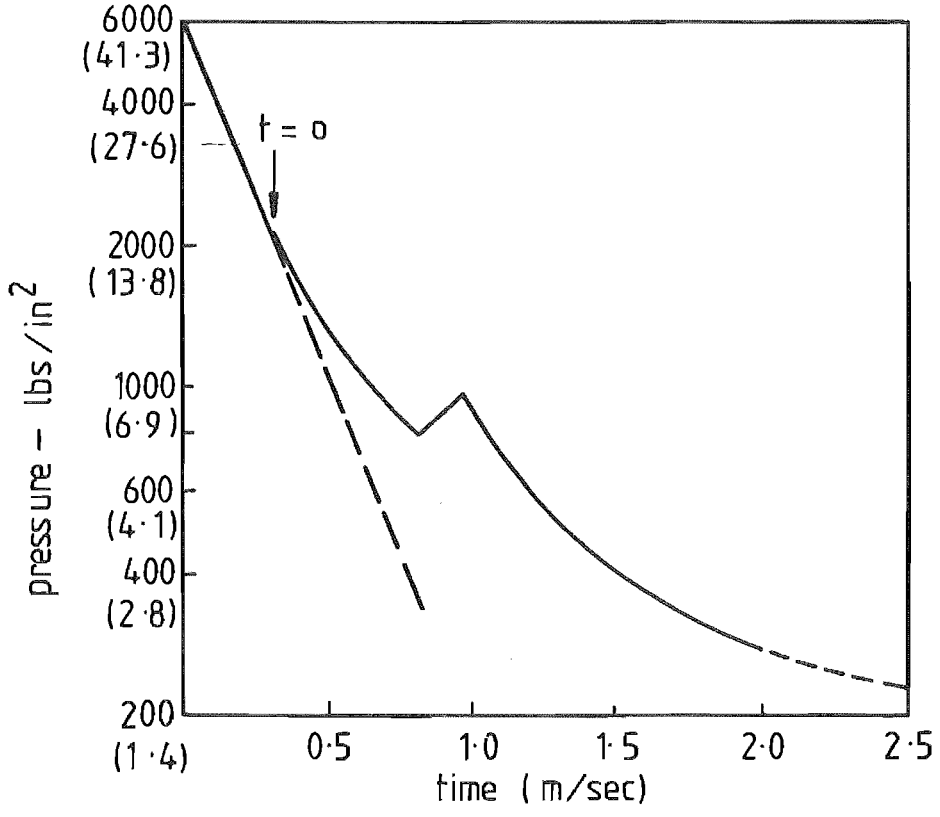

FIG 2·6 SEMILOGARITHMIC PLOT OF PRESSURE AGAINST TIME. (14FT [4·3m] FROM AN 80 POUND [36·3kgm] 50/50 PENTOLITE CHARGE) [2·70]

* pressure in megaPascals

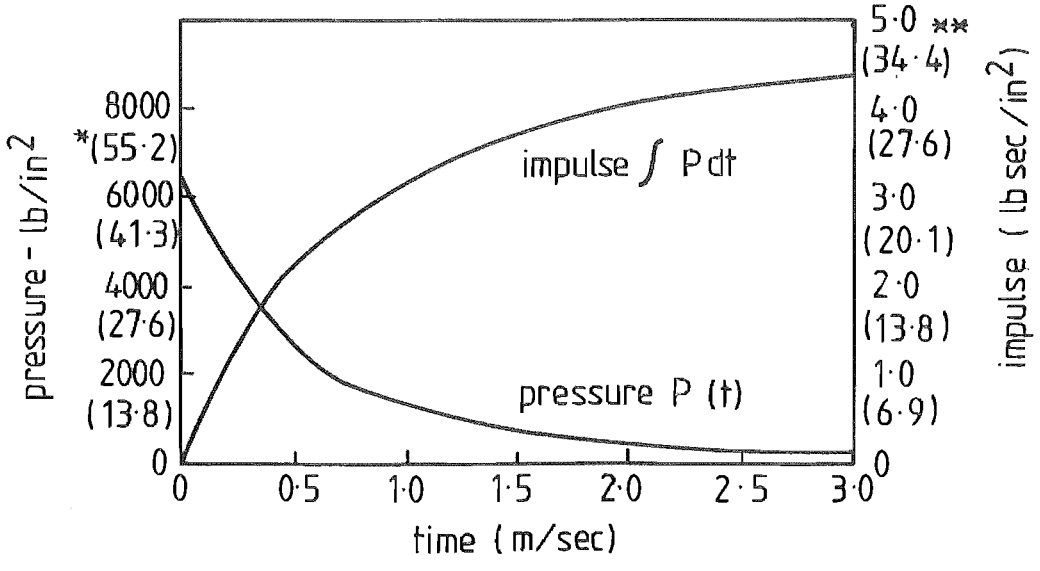

FIG 2·7 INCREASE IN IMPULSE FROM LATER PORTIONS OF THE SHOCK WAVE (PRESSURE 20FT [6·1m] FROM A 300 POUND [136·1 kgm) CHARGE) [2·70]

* pressure in megaPascals

** impulse in kN sec/m²

From the typical experimental results obtained, for large charges in effectively infinite bodies of water, it was found for a fixed point within the medium that the initial section of the pressure profile could be empirically represented by the equation

$$P_t = P_m \exp(-T/\theta) \qquad 2.1$$

where T = time elapsed since the incidence of the shock front

P_m = peak pressure of the shock front at the fixed point

θ = exponential time decay constant

P_t = instantaneous pressure at time due to the shock wave.

Also from experimental work[2.71] and similarity studies[2.70] it could be shown that

$$P_m = A_e \left(\frac{W^{1/3}}{R_1}\right)^{\alpha_1} \qquad 2.2$$

$$I = B_e W^{1/3} \left(\frac{W^{1/3}}{R_1}\right)^{\beta_1} \qquad 2.3$$

$$E_e = C_e W^{\frac{1}{3}} \left(\frac{W^{1/3}}{R_1}\right)^{\gamma_1} \qquad 2.4$$

represented the peak pressure P in psi (MP), Effective Unit Impulse (I) in lb-sec/in (KN-sec/M) and Effective Unit Energy Flux Density E_e in in-lb/in (KN/m) passing through unit area surface located at the fixed point, distance R_1 in feet (m) from the spherical charge weight W in lb (Kgm), and the surface being normal to the incident shock wave propagation direction. The constants A_e, B_e, C_e, α_1, β_1, γ_1 were obtained from the Table 2.1[1.2] for a limited range of explosives

Explosive	Density	Peak Pressure		Impulse		Energy		Integr-ation Time
	gm/cc	P_m		I(t)		E(t)		sec
		A_e	α_1	B_e	β_1	C_e	γ_1	
TNT	1.52	21,600 (52.4)*	1.13	1.46 (5.75)	0.89	2410 (82.5)	2.05	7.6θ
Loose Tetryl	0.93	21,400 (51.0)	1.15	1.73 (6.26)	0.98	3000 (98.1)	2.10	5.0θ
Pentolite	1.60	22,500 (54.6)	1.13	2.18 (7.40)	1.05	3270 (105.0)	2.12	6.7θ

Table 2.1 Explosive Constants after Cole[2.70]

* The constants for SI units based on the dimensions in brackets

Finally the value of the exponential decay time constant for a given explosive type, charge weight and stand-off could be obtained. Either from a graph of $\theta / W^{1/3}$ vs $W^{1/3}/R_1$ for the particular explosive or alternatively if the graph could be approximated to a straight line in the region of the conditions applying, then the relationship

$$\theta = D_e W^{1/3} \left(\frac{W^{1/3}}{R_1}\right)^{-\delta'_1} \qquad 2.5$$

enabled the decay constant θ to be calculated where D_e and δ were appropriate constants.

Erza[2.4] gave an alternative relationship for the decay constant

$$\theta = K_\theta W^{1/3} \left(\frac{W^{1/3}}{L}\right)^{\gamma_\theta}$$

where L was in in(m) and the constants were obtained from the table 2.2.

Explosive	$K_\theta \times 10^6$	γ_θ
TNT	38.4 (92.3)	-0.18
Pentolite	38.4 (92.3)	-0.18

Table 2.2 Explosive Constants for Decay Constant.

It should be realised that these empirical relationships were approximations to experimental results for idealised conditions of a homogenous spherical charge, spherical detonation wave and an infinite body of water. Unfortunately this information was available for a limited number of explosive types and only applied for stand-offs greater than seven to ten times the radius of the spherical charge. Also, as can be seen from Fig 2.6 page the representation of the pressure profile, equation 2.1 by an exponential decay was only valid for a pressure range to 30% of the peak pressure. While this often represented the limit of accurate pressure measurement for the shock wave phenomenon

during these experiments, because of the slower decay rates of the 'tail', these pressures contributed to the impulse available for deformation. It was suggested [2.70] that while the pressure profile was diverging from exponential decay at times 1.2θ, a realistic value of impulse due to the shock wave would be obtained by the integration

$$I = \int_o^{a_1} P_t \, dt \qquad 2.6$$

where a_1 was between 5θ and 6.7θ.

The energy flux associated with the passage of the shock wave could be found for the exponential decay section of the pressure profile as follows[2.70,2.71].

The expression for the energy flux density to time T_e after the arrival of the shock wave was given by

$$E_f = \int_o^{T_e} m_t \, u_v \, \Delta\left[E_p + \tfrac{1}{2}u_v^2 + \frac{P_t}{m}\right] dt \qquad 2.7$$

where $\Delta[E_p + \tfrac{1}{2}u_v^2]$ was the increase in potential and kinetic energy for a unit volume of the energy transfer medium, P_t was the pressure, m_t the density and u_v the velocity of the medium.

Considering finite amplitude waves and applying the Rankine-Hugoniot conditions for the shock wave, the equation became

$$E_f = \frac{1}{m_o} \int_o^{T_e} \frac{P_t^2}{U - \frac{P_t}{m_o U}} \, dt \qquad 2.8$$

and when the approximation $U = c_o(1 + \alpha_2 P)$ described the shock front velocity, then by expanding powers of P and substituting for the exponential decay pressure profile, the energy flux was given by

$$E_f \doteqdot \left(\frac{1}{m_o c_o}\right)\left\{1 - \frac{2}{3}\left(\alpha_2 - \frac{1}{m_o}\frac{c_o^2}{}\right)P_m\right\} \int P_t^2 \, dt \qquad 2.9$$

(where c_o = velocity of sound)
for the pressure range 0 - 40,000 psi (275 MP). Alternatively, for acoustic waves of infinitesimal amplitude, it has been established that the energy flux was given by

$$E_f \doteqdot \frac{1}{(m_o c_o)} \int P_t^2 \, dt \qquad 2.10$$

The divergence of the shock wave profile from the exponential decay could be attributed to the interaction at the explosives/energy transfer medium interface following the impingement of the detonation wave. As shown by S.A. Berger et al[2.67,2.68], the density of the water caused a second shock wave to implode into the centre of the products of detonation and therefore re-propagated as a reflected or refracted wave outwards, behind the main shock wave as a secondary pressure pulse. Also the interaction of the detonation waves and the subsequent expansion of the bubble of gaseous products following detonation contributed to this secondary pressure pulse or peak, which according to Cole[2.70] was intrinsically an explosive characteristic and could be used to identify the explosive type.

2.3.3 GAS BUBBLE BEHAVIOUR

Following the propagation of the shock wave away from the medium/gas interface, the gaseous products of detonation remained in a condition of high temperature and high pressure P_t where $P_t \gg P_o$ the ambient pressure. This high energy condition caused, as has been observed[2.70], a rapid expansion of the gas bubble with an outflow of water and the resultant radial velocity of the water was such that when the gas pressure equalled the ambient water pressure, the kinetic energy of the water caused the continued expansion at a decreasing radial velocity, until the work done against the pressure difference $(P_o - P_t)$ was sufficient to counteract the radial kinetic energy in the water adjacent to the gas bubble.

Subsequently, the pressure difference gave rise to an inward radial water velocity which overshot the radius for which the ambient and gas pressure were equal, and therefore the gas bubble underwent a number of dynamic oscillations about an equilibrium radius, with a decreasing radial amplitude of oscillation as the energy was transferred to the surrounding medium both as kinetic energy or after-flow and a discrete pressure pulse.

A typical experimental observation[2.70] was shown in Fig 2.8 page 46 and it was noted that for charges particularly at considerable depths in an infinite body of water, the bubble remained approximately symmetrical and that it retained its identity irrespective of the dynamic radial behaviour and the bubble's vertical motion.

Obviously the gravitational forces caused the bubble to rise and it was observed[2.69] Fig 2.9 page 46, that the upward migration occurred mainly as the bubble approached its minimum radius.

Finally, the Fig 2.10 page 46 shows the resultant pressure profile for the bubble pulsation, and it was noted that for the recorded pressure amplitudes involved, the acoustic assumptions such as incompressibility of water, were valid in the analysis of the gas bubble behaviour.

On the basis of the experimental work the following empirical relationships could be used to describe the gas bubble behaviour, as a function of depth, explosive weight and explosive type

$$T_o = K_1 \frac{W^{1/3}}{(H + 33)^{5/6}} \qquad 2.11$$

$$R_m = K_2 \frac{W^{1/3}}{(H + 33)^{1/3}} \qquad 2.12$$

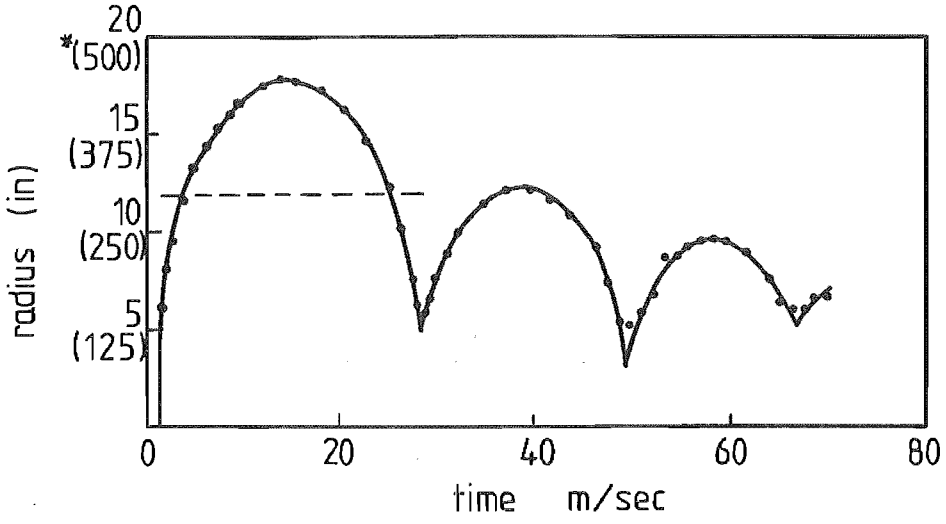

FIG 2·8 RADIUS OF THE GAS BUBBLE AS A FUNCTION OF TIME FOR A 0·55 POUND (0·25kgm) TETRYL CHARGE 300 FEET (91·4m) BELOW THE SURFACE. AFTER COLE [2·70]

*millimeters

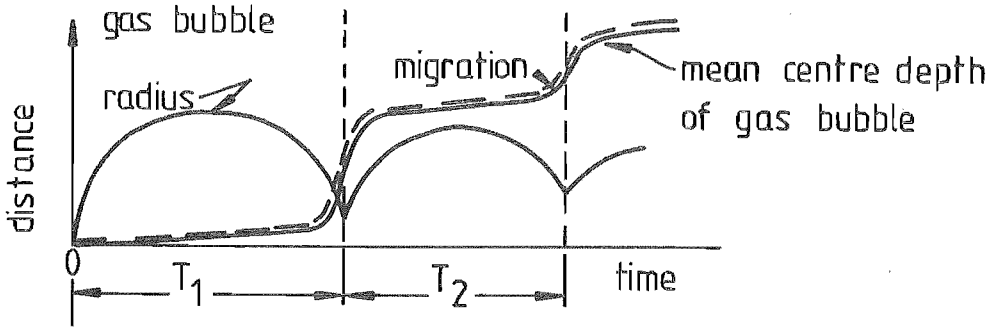

FIG 2·9 SCHEMATIC OF GAS BUBBLE RADIUS AND MIGRATION AS A FUNCTION OF TIME. AFTER SCHAUER [2·69]

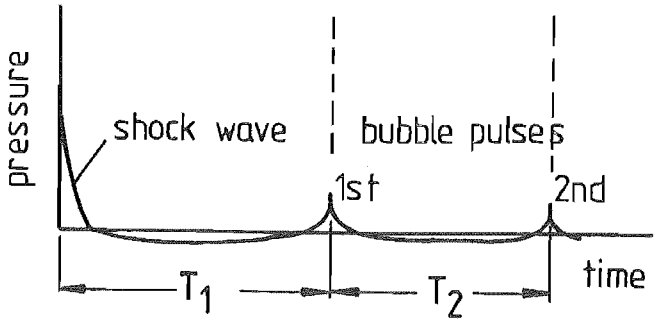

FIG 2·10 SCHEMATIC OF PRESSURE HISTORY AFTER SCHAUER [2·69]

where T_o was the pulsation time for the first bubble minimum, R_m maximum gas bubble radius, H the depth of the explosive below the free surface, W the weight of explosives and the constants K_1, K_2 were functions of the explosive type. Again these experimental results and relationships were derived for idealised conditions of an infinite body of energy transfer media without interaction from any solid boundary or free surface. It has been shown that the gas bubble behaviour was influenced by the presence of any solid boundary or proximity to the free surface of the medium because these boundaries would affect the after-flow of the medium. The bubble has been observed[2.70] to translate to a rigid boundary in close proximity to the charge.

Bebb[2.71], on the basis of experimental measurements and analytical work by Savic, derived an approximate ratio of the after flow energy flux to primary shock wave energy flux using the empirical equations.

$$E_f' : E_f = K_3 (R_1/R_e)^{-1} \qquad 2.13$$

where E_f' = After flow energy flux

E_f = Primary shock energy flux
K_3 = Constant
R_1 = Distance from the charge
R_e = Explosive charge radius

Hence the total energy in the transfer medium following an explosion at distance R_1 from the explosive was given by

$(4\pi R_1^2$ x primary energy flux density) +

$(4\pi R_1^2$ x (R_1/a_r) x after flow energy flux density)

where a_r was the radius of the gas bubble at the limit of the time integration.

Calculations based upon these relationships for a spherical charge and for R_1/R_e ratios of 50 to 1 gave primary energy results from 0.20 to 0.27, and after-flow energy results from 0.21 to 0.24, where the resultant energy was represented as a function of the total available chemical energy in the charge.

2.3.4 ENERGY TRANSFER IN EXPLOSIVE FORMING

Having briefly examined the information available in the literature which empirically and qualitatively represented the main phenomena associated with underwater explosions, it was considered that the application of this information to a study of energy transfer in the explosive forming processes applicable to New Zealand engineering and manufacturing conditions warranted consideration.

The experience of Baguley[1.7] at Physics and Engineering Laboratories D.S.I.R. suggested that a charge radius to stand-off ratio of less than ten was applicable, assuming that all the P.E.T.N. available within the Cordtex fuse was present as a spherical charge of density 1.60 gm/cc. Cordtex detonating fuse has been used in the majority[1.7,1.8,1.9] of experimental research in New Zealand into explosive forming, because of its ready availability and freedom from legal restrictions that apply to other explosive types.

With the low stand-off to charge size ratio, the presence and deformation of the blank was going to have a significant influence upon the incident pressure distribution and gas bubble behaviour. Since the theoretical studies available[2.72,2.73,2.74] on underwater explosions were usually developed for large charges at distance to charge size ratios of greater than ten, and often

assuming infinite bodies of water without boundaries or free surface, the resultant theories were not valid in the study of the explosive forming process.

Finally, a knowledge of the blank deformation could not be separated from a study of the energy transfer because of the interaction and the interdependence of these two processes on each other.

2.4 DEFORMATION OF PLATE SUBJECTED TO IMPULSIVE LOADING

The theoretical research into the response of plates subjected to impulsive loading such as occurs in explosive forming originated from studying the Underwater Explosive Research Laboratory (U.E.R.L.) diaphragm gauge, Fig 2.11 page 50 to improve its resolution and application.

The gauges consisted of a diaphragm of either copper or steel clamped to a gauge body giving it an air backing. The gauge was placed a fixed distance from the explosive charge and the subsequent depth of the centre of the approximately semi-spherical deformed diaphragm was used as a measure of the explosive effectiveness, as well as its potential for structural damage.

With the development of numerical techniques and the use of high speed large computers in the late sixties, there was considerable interest in the reponse of structures to dynamic overloads such as occur in earthquakes or from shock or blast waves associated with explosions. While there existed general review papers by Jones et al[2.75], Jones[2.76] and Rawlings[2.77] on the plastic response of plates or structures to dynamic loads, a review of these analytical and numerical techniques was carried out where it was applicable to explosive forming. The review was restricted to consideration of the response of circular plates because the basis of this study was the stand-off explosive free forming of

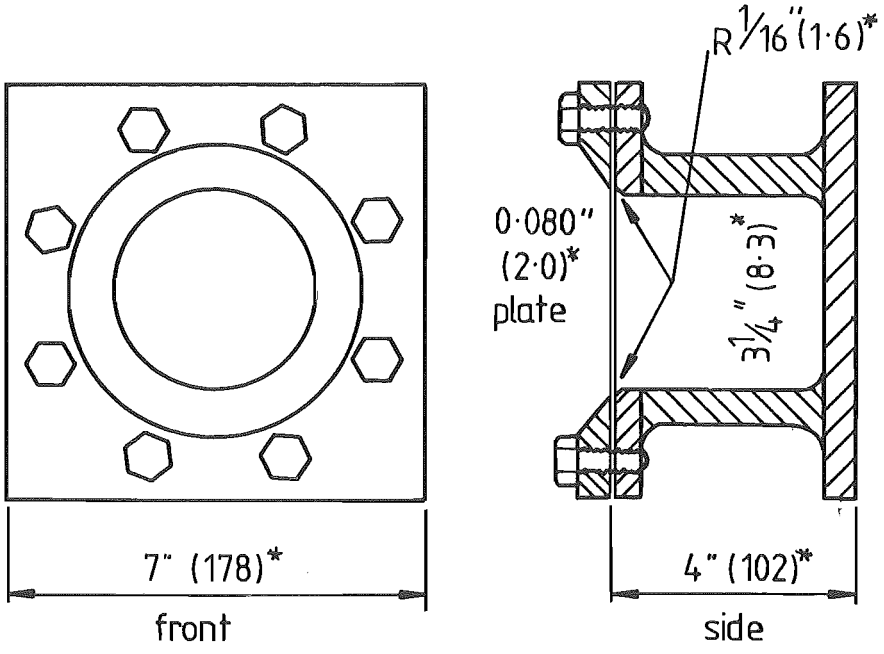

FIG 2·11 CONSTRUCTION OF UERL DIAPHRAGM GAUGE AFTER COLE [2·70]

*millimetres

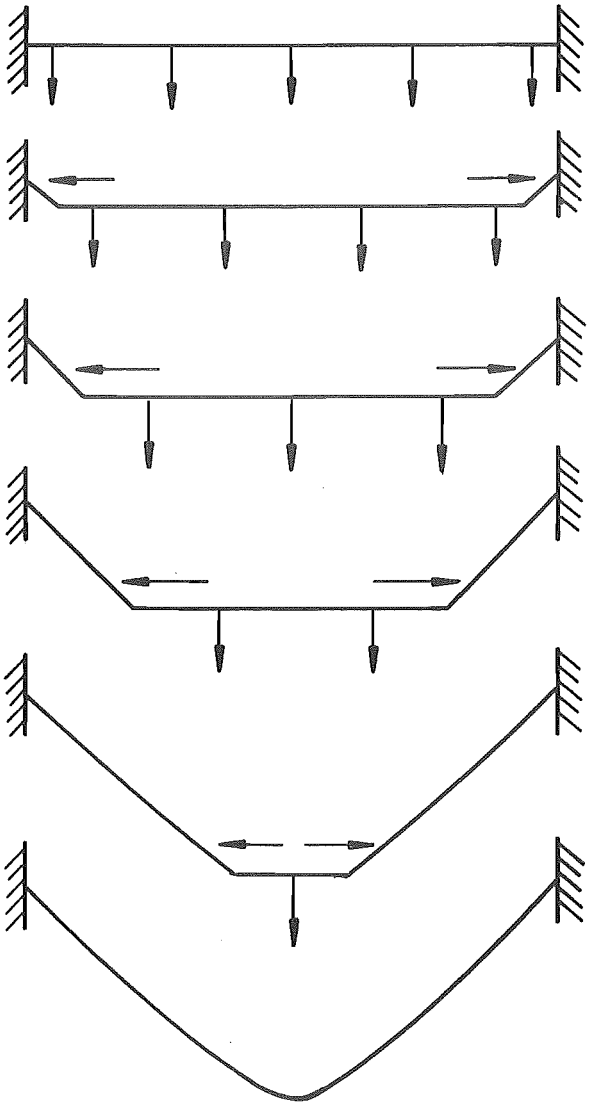

FIG 2·12 MODE OF DEFORMATION OF DAMPED CIRCULAR DISC DURING EXPLOSIVE FREE FORMING. (2·7)

circular blanks. The selection of the free forming operation of circular blanks was to reduce the number of parameters when considering the energy transfer and simplify the experimental procedures in the measurement of the blank velocity during deformation.

These studies could be considered in three general classifications.

2.4.1 MEMBRANE DEFORMATION THEORIES

These theories were derived on the assumption that the stress generated in response to the applied loading was predominantly a membrane stress system, and therefore the effect of bending on the subsequent deformation could be ignored. The other major assumption made in the membrane analysis was that the material behaviour was rigid-plastic and the elastic strain energy effects were also ignored.

Richardson et al[2.23] derived a model for a diaphragm mounted on an infinite baffle subjected to shock loading with allowance being made for the diffraction and rarefaction of the pressure pulse due to the diaphragm and baffle deformation. Following the assumption that the diaphragm deformed with a geometrically similar parabolic profile at all times, the pressure profile became;

$$P(t) = 2P_1(t) - m_o c_o \left(\frac{dz}{dt} + \left(\frac{2}{\theta_d}\right) z_c(t - \theta_d) - \left(\frac{2}{\theta_d^2}\right)\right) \int_{t-\theta_d}^{t} z_c(\tau_1)\, d\tau_c \qquad 2.14$$

where

$P(t)$ = Applied pressure pulse to the diaphragm surface
$P_1(t)$ = Initial incident pressure pulse without interfence
ρ_b = Transfer medium density
c_o = Velocity of sound in transfer medium
z_c = The central displacement of the diaphragm
T_1 = Lapsed time after diffraction wave arrived at the surface of the blank.
θ_d = Diffraction time
= a/c_o

Finally the following assumptions were made about the diaphragm deflection;

(1) Plastic deformation approximated by membrane tension.
(2) Negligible restraint by the medium behind the diaphragm.
(3) Thickness strain was negligible.

From the first assumption the stress was given by

$$\sigma_n \simeq \left(\frac{4\,\sigma_o\,h}{a^2}\right) z_c \qquad 2.15$$

and although this strictly applied for small spherical deformations the error introduced by this divergence from the parabolic deflection assumption was small.

Therefore the equation of motion was obtained for the diaphragm.

$$m\frac{d^2 z_c}{dt^2} = P(t) - \sigma_n(t) \qquad 2.16$$

The final form of the equation solved by Richardson et al was derived by the combination of equations 2.14,2.15 and 2.16. The solution so obtained only applied up to the time when the derivative of the central deflection with respect to time reached zero and the resultant deflection was the final deformation of the diaphragm.

Also if the plate was sufficiently thin the inertial effects could be ignored and for times of less than θ_d the diffraction terms in the equation 2.11 were ignored. This gave the following solution;

$$z_c = \frac{2P_m\theta}{m_o c_o} \frac{\theta_p}{\theta - \theta_p} (\exp(-t/\theta) - \exp(-t/\theta_p)) \qquad 2.17$$

where

$$\theta_p = \frac{m_o c_o a^2}{4\sigma_o h}$$

= the characteristic time i.e. 0.63 of the final deflection.

This gave the following final deflection of

$$\frac{2P_m\theta}{m_o c_o} \exp(-t_m/\theta_p)$$

for the initial pressure pulse given by the equation 2.1 where

$$t_m = \frac{\theta.\theta_p}{\theta-\theta_p} \ln(\theta/\theta_p)$$

The interesting conclusion reached from this result was that the maximum deflection was proportional to the incident impulse on blank $P_m\theta$ which was verified by the work of Boes[2.44]

Cavitation was shown to occur adjacent to the deforming blank and Richardson et al proposed the following criteria for the formation of such cavitation; that the diffraction time must exceed the cavitation time at the blank centre. The approximation to cavitation time was obtained by considering the central motion to be similar to that of an infinitely free plate of equal mass per unit area and given by

$$\theta_c = \frac{\theta}{\beta_1 - 1} \ln(\beta_1) \qquad 2.18$$

where $\beta_1 = \dfrac{m_o c_o \theta}{m}$

The energy transfer to the blank once cavitation occurred, was reduced to zero and any subsequent deformation was due to the kinetic energy the diaphragm possessed immediately prior to cavitation. Also the collapse of cavitation following its termination resulted in a water hammer effect supplying additional energy to 'round-out' to the final deformed profile.

This mathematical model of the deformation was limited in its application because of the assumptions made, particularly those concerned with the thickness strain and the parabolic deflection.

Hudson[1.4] developed a theory of diaphragm plastic deformation due to shock loading in which the energy was assumed to be imparted as a discrete impulsive loading, which resulted in the diaphragm having an initial normal velocity relative to its mountings. The deformation mechanism was assumed to be in the form of radial stretching and thinning of the flat portion of the blank, Fig 2.12 page 50 . The bending wave propagating from the clamped periphery towards the blank centre, did not absorb energy but supplied a discontinuity bringing the blank to rest in both the vertical and horizontal range following its passage.

Since the situation was extremely complex the following major simplifying assumptions were made by Hudson,

(1) Deformation was due to the passage of a plastic bending wave completely converting the kinetic energy of the plate into plastic deformation.

(2) The stresses associated with the wave were radial and circumferential principal stresses just ahead of the wave and the normal stress component along the generator of the tilted surface, a shear stress component and a circumferential normal stress component.

(3) The flat undeformed region retained its normal velocity throughout the deformation and was subject to uniform thinning, with a radial flow of material.

(4) The radial displacement of a particle was given by

$$U_1 = U_o\left(1 + \frac{q_1(t)}{a}\right)$$

where $q_1(t)$ = the normal coordinate of the superimposed constraint motion to ensure the uniform thinning of undeformed material.

(5) Elastic effects were negligible.

(6) Kinetic Energy of thinning was negligible.

(7) No work was done in the propagation of the plastic wave and there was no impulsive thinning associated with the wave.

(8) The material obeyed the Mises-Hencky yield criteria and followed the Prandtl-Reuss flow rule or stress-strain relationship.

From assumption (3) some form of constraint forces were necessarily superimposed upon the system which satisfied the conditions given but which did not result in additional work being done during the deformation.

Therefore by considering the conditions of equilibrium and continuity associated with the bending wave, a solution was obtained. For the case of non-work hardening yield the solution was

$$w = \frac{v_o}{c_m}(a - r) \qquad 2.19$$

$$h_f = h\left(\frac{r}{a}\right)^{(v_o/c_m)^2} \qquad 2.20$$

where v_o = the normal velocity
h_f = the final thickness
σ_y = the material yield stress
$c_m = \frac{\sigma_y}{m}$

For the case of work hardening

$$\sigma\left(\log\left(\frac{h_f}{h}\right)\right) = \sigma_y + w_o \log\left(\frac{h_f}{h}\right) \qquad 2.21$$

with suitable manipulation and approximations the solution was

$$h_f = h \exp\left(-\frac{c_m^2}{d_1^2}\left((1 - \kappa)^{\frac{1}{2}} - 1\right)\right) \qquad 2.22$$

$$w = -\frac{v_o}{c_m}\int_a^r (1 - \kappa)^{-\frac{1}{4}}\, dr \qquad 2.23$$

where $d_1^2 = \frac{w_o}{m}$

$$\kappa = 2\left(\frac{v_o^2 d_1^2}{c_m^4}\right)\log\left(\frac{r}{a}\right)$$

The assumption that the energy for plastic deformation was based upon the incident impulse on the blank again satisfied Boes's observations.

S.E. Corbett[2.37] modified the analysis with the assumption that the deformed blank approximated a cone in shape and the angle of tilt α_t was given by

$$\alpha_t = \mathrm{Tan}^{-1}\left(\frac{w_o}{a}\right)$$

This major simplification in connection with Hudson's technique of bending wave analysis resulted in the thickness distribution given by

$$h_i = h\left(\frac{r}{a}\right)^{4\sin^2\left(\frac{\alpha_t}{2}\right)} \qquad 2.24$$

where h_i = the instantaneous thickness
w_o = the central deflection of the diaphragm.

The experimental work conducted showed that, as with the Hudson analysis, the thickness strain distribution predictions were suitable for regions away from the blank centre, but approaching the centre the theory failed, as would be anticipated from the equations derived.

With both these theories no allowance was made for the pull-in of material at the edge of the die and in practice an error would arise because of this phenomenon's considerable influence on the strain distribution about the draw radius.

Boswell[1.8] extended the Hudson analysis to allow for strain rate as well as strain hardening and obtained the following expression;

$$h_i = h \exp\left\{\frac{m\left(\frac{r}{a}\right) - 0.06\,\frac{\chi_s}{mv_o^2}}{\frac{c_m^2}{v_o^2} + \frac{\chi_s}{mv_o^2}\ln(\dot{\varepsilon})}\right\} \qquad 2.25$$

where $\dot{\varepsilon}_i$ = the strain rate

χ_s = the strain rate coefficient from the following dynamic stress-strain relationship.

$$\sigma = \sigma_y + w_o \log\left(\frac{h_i}{h}\right) + \chi_s \log\left(\frac{d}{dt}\left(\log\left(\frac{h_i}{h}\right)\right)\right)$$

G.A. Thurston[2.5] solved the equations governing plastic membrane deformation of a diaphragm with respect to explosive forming

$$\sigma_t - \frac{\partial(\sigma_r)}{\sigma_r} = 0 \qquad 2.26$$

$$\frac{\partial}{\partial r}\left(r\,\sigma_r \frac{\partial w}{\partial r}\right) + pr\left(1 + \frac{u}{r}\right)\left(1 + \frac{\partial u}{\partial r}\right) = mrh\frac{\partial^2 w}{\partial t^2} \qquad 2.27$$

which were derived by Boyd[2.78] from the assumptions;

(1) Small finite-deflection theory applied.
(2) Bending strains neglected to give a membrane theory.
(3) Elastic strains neglected with comparison to plastic strains and a deformation theory of plasticity used with a power-law stress-strain relationship.
(4) Radial inertia terms neglected in the equation of motion.

The power-law was expressed

$$\bar{\sigma} = K\,\bar{\varepsilon}^{\,n}$$

for the material used.

By substitution, two equations of motion in terms of the radial and vertical deflection were obtained. These were solved numerically using an explicit finite-difference technique to determine the value of vertical deflection and therefore obtain the value of radial deflection by a Picard iterative procedure. G.A. Thurston improved the convergence to the correct solution by the use of Newton's method of correction.

For the case of die forming this method of solution was still used but the equation 2.27 was replaced by a constraint equation, giving the die shape as a function of the radius and radial displacement.

Considering the plate as a viscoplastic membrane Wojno et al[2.79] presented a perturbation solution based upon the linear eigenvalue problem. The results were compared with existing experimental data for contact explosive loading of steel and titanium plate and showed a strong correspondance.

2.4.2 BENDING DEFORMATION THEORIES

These analytical methods were based upon the assumption that the plastic deformation was due to the propagation of plastic bending hinges across the blank, any membrane stress being ignored. The analysis also was considered for either the clamped circular plate or the simply supported circular plate.

2.4.2.1 SIMPLY SUPPORTED CIRCULAR PLATES The majority of these bending analyses were based upon a rigid-plastic assumption, the elastic effects being effectively ignored. It should be realised that while this could adequately describe final deflections it would not describe the dynamic deflection.

H.G. Hopkins and W. Prager[2.80] extended the static limit analysis of a thin, circular, simply supported plate to determine the dynamic behaviour of such a plate subjected to a uniformly distributed load, which was instantaneously applied and released. The plate material was assumed to obey the Tresca yield condition, Fig 2.13 page 60 , and the associated flow rule.

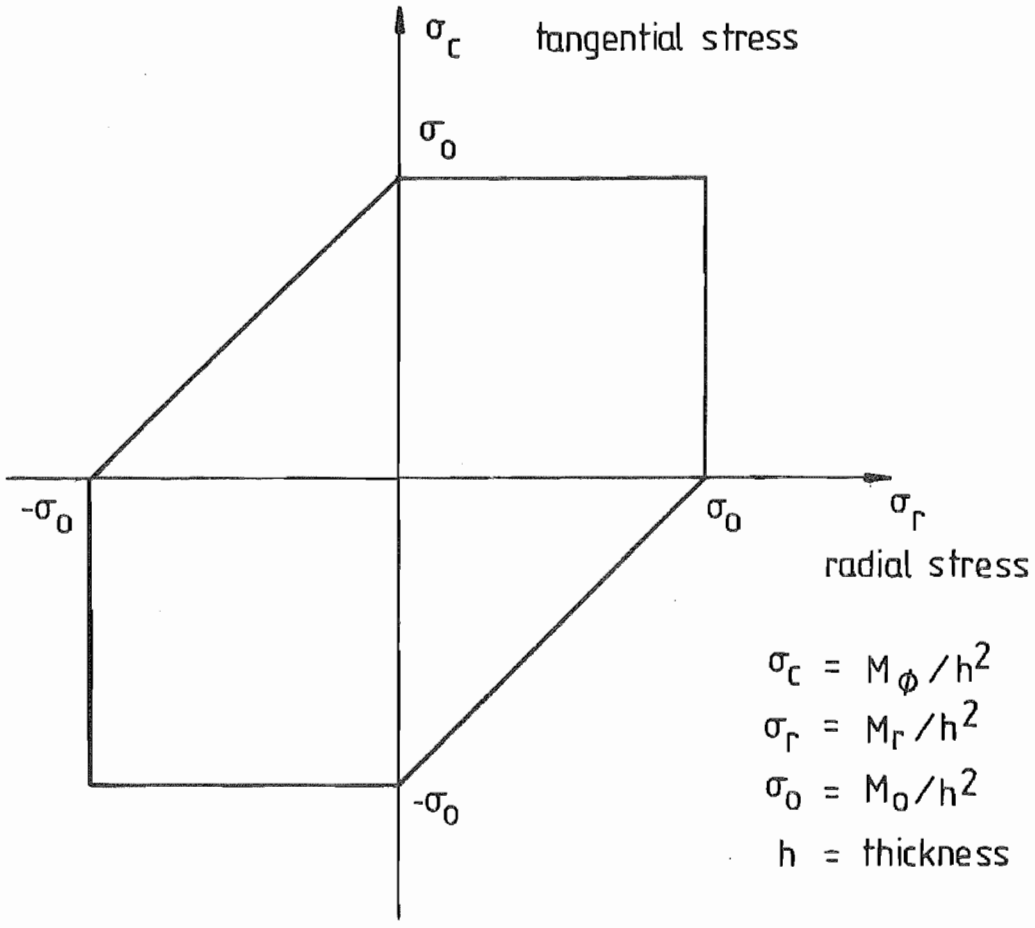

FIG 2·13 TRESCA YIELD CONDITION APPLIED TO HOPKINS ET AL (2·80)

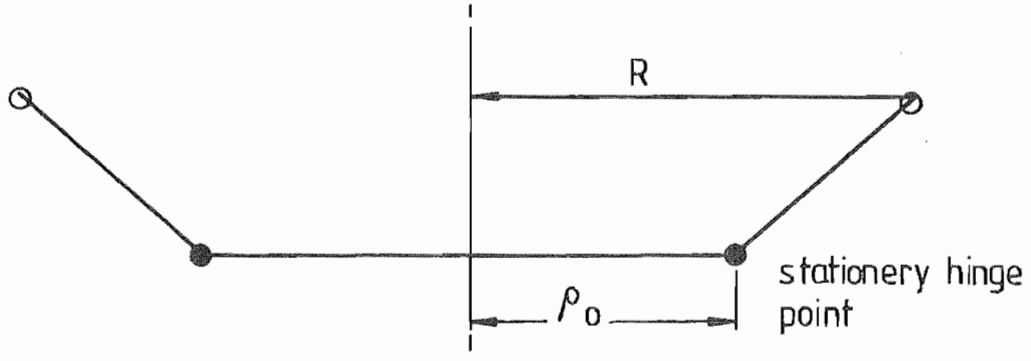

FIG. 2·14 FIRST PHASE DEFLECTION HOPKINS ET AL [2·80]

The aspect of the analysis of significance to explosive forming was the high load case, where the applied pressure was greater than twice the static pressure which gives rise to yield. The analysis was based upon these distinct phases; the first being the load application, during which period there existed a stationary plastic hinge circle, the radius of the hinge circle being a function of the applied pressure only. This phase resulted in the initial deformation in the form of a cone and the development of kinetic energy in the plate. The stationary hinge circle of the preceding phase then contracted until at the termination of the second phase, the hinge circle approached the centre of the plate. The final phase was the conversion of the kinetic energy existing at the completion of the second phase into plastic work.

The solution of the equation

$$\frac{\partial}{\partial r}(rM_r) - M_t = -\int_o^r (p - m\frac{\partial^2 w}{\partial t^2})r\,dr \qquad 2.29$$

under a rectangular load pulse for the necessary conditions of continuity and piecewise discontinuity across the hingle circle gave the following resultant deflection for the simply supported plate.

The first phase deflection Fig 2.14 p 60 $0 < t < T_1$ was given by

$$w(r,t) = \begin{cases} W(t) & 0 < r < \beta_o \\ W(t)\,\dfrac{R - r}{R - \beta_o} & \beta_o < r < R \end{cases} \qquad 2.30$$

where $W(t) = \dfrac{Pt^2}{2m}$

$$\frac{P}{2P_o} = \frac{R^3}{(R - \beta_o)^2(R + \beta_o)}$$

$$P_o = \frac{6M_o}{R^2}$$

= Static Yield Pressure

While the second phase deflection $T_1 < t < T_2$, as the plastic hinge circle propagated from β_o at time T_1 when unloading occurred to the centre at time T_2, was given by considering the velocity of the plate.

$$\frac{\partial w(r,t)}{\partial t} = \begin{cases} \frac{PT_1}{m} & 0 < r < \beta(t) \\ \frac{PT_1}{m}\frac{R - r}{R-\beta_o(t)} & \beta(t) < r < R \end{cases} \qquad 2.31$$

and

$$\left(\frac{\beta_o(t)}{R}\right)^3 - \left(\frac{\beta_o(t)}{R}\right)^2 - \left(\frac{\beta_o(t)}{R}\right) = \frac{2P_o t}{PT} - 1 \qquad 2.32$$

From the equation for the hinge circle propagation it was shown that at $\beta_o(T_2) = 0$

$$T_2 = \frac{PT_1}{2P_o}$$

and hence by consideration of continuity conditions across the propagating plastic hinge circle, it was shown by Hopkins et al[2.80] that the deflection was

$$w(r,T_2) = \frac{PT_1^2}{2m}\left[\frac{P}{2P_o}\left(2 - \frac{r^2}{R^2} - \frac{r^3}{R^3}\right) - 1\right], \quad 0 \leq r \leq \beta_o \qquad 2.33$$

The final deflection at the end of the third phase $T_2 < t < T_3$ was given by

$$w(r,T_3) = \begin{cases} \frac{PT_1^2}{2m}\left[\frac{P}{2P_o}\left(3 - \frac{r}{R} - \frac{r^2}{R^2} - \frac{r^3}{R^3}\right) - 1\right], & 0 \leq r \leq \beta_o \\ \frac{PT_1^2}{2m}\left[\frac{P}{2P_o}\left(3 - \frac{\beta_o}{R} - \frac{\beta_o^2}{R^2} - \frac{\beta_o^3}{R^3}\right) - 1\right]\left(1 - \frac{r}{a}\right), & \beta_o \leq r \leq R \end{cases} \qquad 2.34$$

Also of interest was the result for deflection at the plate centre

$$W(o,T_3) = \frac{I^2(\frac{3}{2} - \frac{P_o}{P})}{2mP_o}$$

where I = total impulse acting on plate

$= pT_1$

A.J. Wang[2.81] also developed an expression for the permanent deformation of a simply supported plastic plate subjected to impulsive loading. Again the analysis was based upon a rigid plastic material which obeyed the Tresca yield criteria and associated flow rule. Also it was assumed that the energy was impulsively transferred to the plate, which developed an instantaneous, transverse velocity. This kinetic energy was converted into plate deformation bringing the plate to rest in its permanently deformed shape.

The deformation mechanism was in two distinct phases, corresponding to the final two phases in the previously mentioned analysis. The first phase involved the propagation of a bending hinge from the outer boundary towards the plate centre and the second occurred when the plate moved as a whole following the approach of the hinge to the centre.

This gave the following equation for the deflected shape;

$$w(r,T) = \frac{m v_o^2 R^2}{24 M_o} (3 - \frac{r}{R} - (\frac{r}{R})^2 - (\frac{r}{R})^3) \qquad 2.34$$

where

v_o = the initial transverse velocity of the blank.

M_o = the limit moment by Tresca analysis.

Also the analysis assumed that the velocity distribution in the first mode of deformation was expressed as

$$\frac{\partial w}{\partial t}(r,t) = v_o \frac{R - r}{R - \beta_o(t)} \quad , \quad \beta_o(t) < r < R$$

$$= v_o \quad , \quad \beta_o(t) > r > 0 \qquad 2.35$$

where $\beta_o(t)$ gave the radius of the hinge circle at the time t.

Comparison of the results for the final central deflection obtained by Wang's[2.81] analysis with that from Hopkins[2.80] for the condition

$$mv_o = PT_1$$

was as is shown in Fig 2.15 page 65 .

As was anticipated, with increasing P the ratio of Hopkin's solution to Wang's approached unity asymtopically, because the applied impulse of Hopkin's solution made an increasingly closer approximation to the instantaneous velocity conditions associated with Wang's analysis.

R.G. Thomson[2.82] developed expressions to describe the 'Plastic Behaviour of Circular Plates under Impulsive Loadings of Gaussian Distribution'. Again an impulsive energy transfer was considered to impart to the plate an initial transverse velocity distribution; the plastic work being due to the absorption of the kinetic energy available to the plate. The plate material was assumed to follow the Tresca yield criteria and associated flow rule, as well as complying with thin shell assumptions. The two stage deformation proposed by A.J. Wang[2.81] applied, but the variation in momentum distribution resulted in the analysis being divided into three regions of momentum distribution.

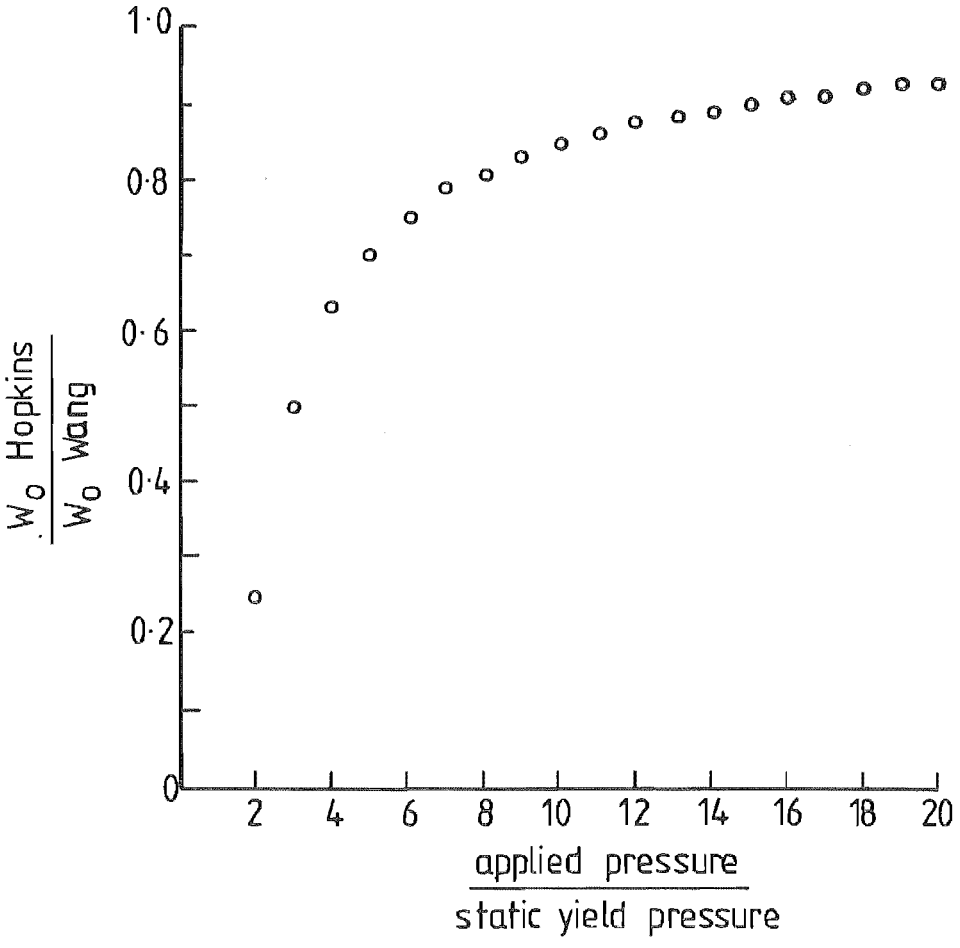

FIG 2·15 COMPARISON OF ANALYSIS BY HOPKINS AND WANG AS A FUNCTION OF PRESSURE RATIO APPLIED PRESSURE : STATIC YIELD PRESSURE

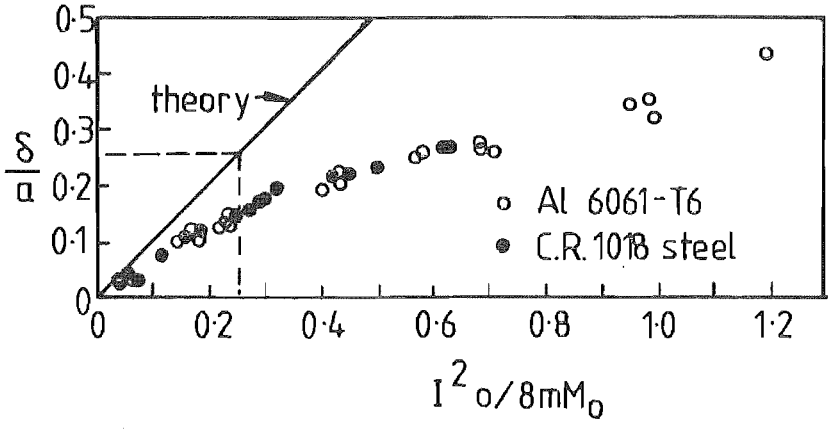

FIG 2·16 DEFLECTION IMPULSE RELATION FOR SIMPLY SUPPORTED PLATES [2·85]

Solution of the equation 2.29 for the necessary conditions resulted in an expression for the final deflection as well as the deflection history, strain rates and velocities in terms of the radius under consideration, the plate radius, elastic limit and the initial momentum distribution.

The final deflection was given by

$$w(r,t_2) = w(r,t_1) + (1 - \frac{r}{R})(\frac{mR^2v_o^2}{12M_o} \quad \frac{v_o}{2}) \qquad 2.36$$

where for the first term $w(r,t_1)$ the following case of $0 < t < t$

$$w(r,t) = v_o t(r)\exp(-b^2 r^2) + v_o \frac{mv_o R^2}{12M_o}(1 - \frac{r}{R})((\frac{3}{2}(\frac{\rho}{R})^2 + \frac{3}{2(bR)^2}$$

$$- \tfrac{1}{2} - \frac{\beta}{R})\exp(-2b^2\beta^2) - (\frac{3}{2}(\frac{r}{R})^2 - \frac{3}{2(bR)^2} - \tfrac{1}{2} - \frac{r}{R}))\exp(-2b^2r^2))$$

$$(\beta < r < \beta(o))$$

$$= v_o \frac{mv_o R^2}{12M_o}(1 - \frac{r}{R})((\frac{3}{2}(\frac{\beta_o}{R})^2 + \frac{3}{2(bR)^2} - \tfrac{1}{2} - \frac{\beta}{R})\exp(-2b^2\beta^2)$$

$$- (\frac{3}{2}(\frac{\beta(o)}{R})^2 + \frac{3}{2(bR)^2} - \tfrac{1}{2} - \frac{\beta(o)}{R})\exp(-2b^2r^2))$$

$$(\beta(o) < r < a)$$

2.37

where

t_1 = time taken for the plastic hinge circle to reach the plate centre.

t_2 = time at which all movement ceases and gives the permanent deformation of the plate.

$\beta(t)$ = β

= the radius of the hinge circle at time t.

$\beta(0)$ = the initial radius of the hinge circle.

$t(r)$ = the time at which the hinge circle passes through the radius r.

b = constant from the Gaussian momentum distribution $= \frac{1}{\sqrt{2}\, s}$

where the momentum distribution was a function of the form $e^{(-\frac{1}{2}(\frac{r}{s})^2)}$.

Hopkin's and Prager's work[2.80] was extended by Conroy[2.83] using similar assumptions and analysis methods to the case of a simply supported plate under a rectangular load pulse uniformly distributed over a central circular area while Mazalov et al's[2.84] extension of the original analysis considered the response of a circular piecewise nonhomogenous plate to a uniformly distributed pressure pulse.

The only major experimental work on the analysis of simply supported circular blanks was the work of Florence[2.85] in which the deformation, following impulsive loading by sheet explosives on simply supported blanks was compared with Wang's analysis for two materials. The results, Fig 2.16 page 65 , suggested that the resultant deformation was accurately described by Wang[2.81] for only a limited final deflection of less than one tenth the blank radius for steel and even less for aluminium alloys. The result suggested that Hopkin's et al[2.80] analysis would also be inadequate because of the similarity to the Wang analysis. Florence proposed that the error could be attributed to the exclusion of membrane stresses from the analysis and theories involving combined membrane and bending are discussed in the next section.

Wierzbicki[2.86] considered that the strain rates of the order of 100 - 500 sec would influence the resultant plate response and therefore analysed the dynamics of a rigid circular plate of viscoplastic material. The material yield condition was assumed to be described by the Huber-Mises relationship while the viscoplastic constitutive equation was

$$\dot{\varepsilon}_{ij} = \gamma_o \phi(F) \frac{\partial F}{\partial \sigma_{ij}} \qquad 2.38$$

where $\dot{\varepsilon}_y$ = strain rate

ϕ = $F^{\delta'}$

= a power function of F

F = $\sqrt{J_2'}/k_s - 1$

= excess of dynamic stress over the static yield

γ_o = viscosity constant

k_s = yield stress in simple shear

J_2' = second stress deviatoric

= $(\sigma_r^2 - \sigma_r \sigma_t + \sigma_t^2)/3$

σ_r = radial stress

σ_t = tangential stress.

The equations governing the plate deformation were obtained by consideration of the rates of curvature.

The resultant parabolic - type partial differential equations were not amenable to an analytical solution, and therefore a numerical technique was used. The equations were solved for the simply supported circular plate with a uniform pressure pulse of finite duration τ_o, using a finite difference representation of the equations in the spatial domain. Iteration to satisfy these conditions at each time pivotal point was carried out before integrating to the next pivotal point in the time domain by use of the Runge-Kutta technique. Using a viscosity γ_o of 200 sec and a power series (δ') of unity, the graphs Fig 2.17 page 69 show the results from this analysis compared with those obtained from Hopkins et al[2.80] analysis for similar conditions.

While Wierzbicki's analysis was more conservative than that derived by Hopkins et al, it was pointed out by the author that ignoring the membrane stress effectively restricted the application of the results obtained and a combined bending membrane analysis was justified.

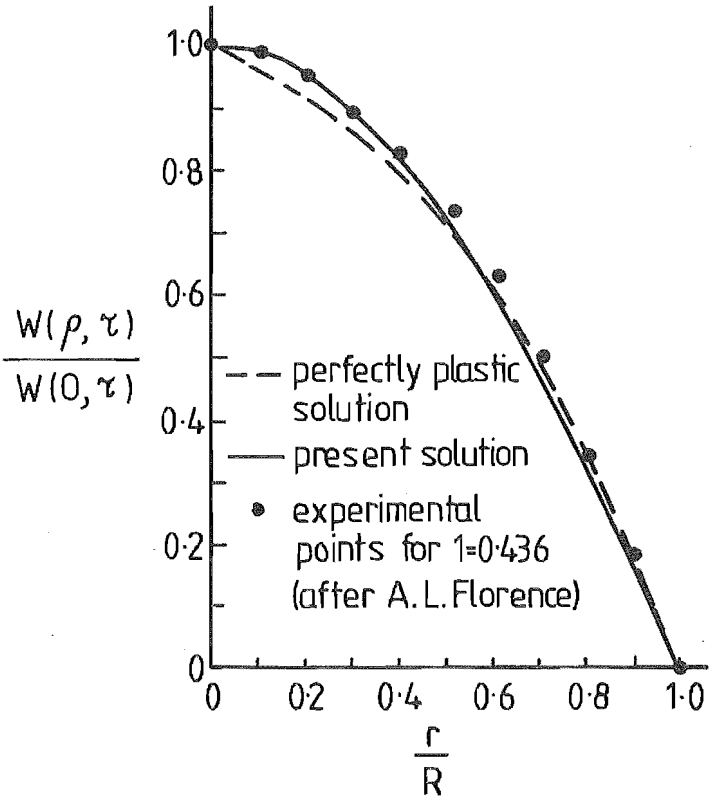

FIG 2·17 a. FINAL DEFORMATION PROFILE PREDICTED BY VISCO PLASTIC AND PERFECTLY PLASTIC SOLUTION COMPARED WITH EXPERIMENTAL DATA.
AFTER WIERZBICKI (2·86)

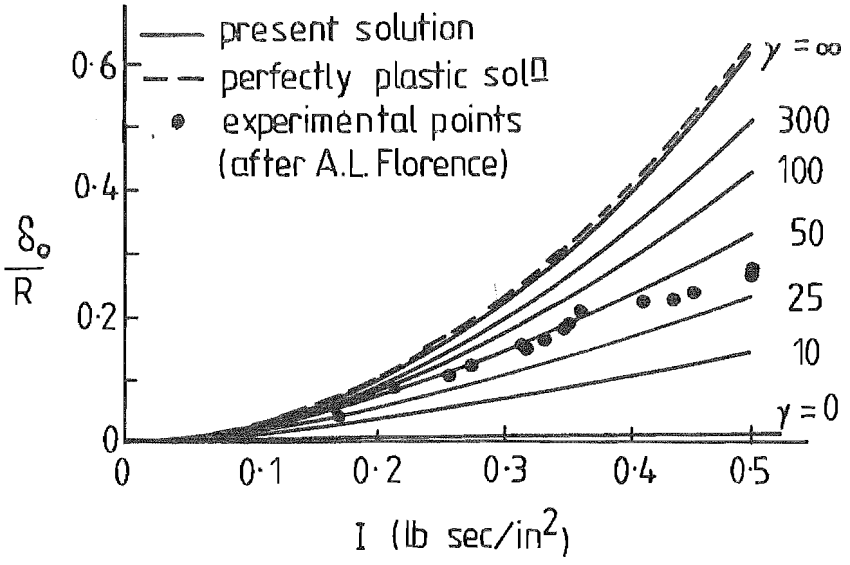

FIG 2.17b PERMANENT CENTRAL PLATE DEFLECTION δ_0/R vs APPLIED IMPULSE I. CURVES FOR SEVERAL VALUES OF VISCOSITY CONSTANT COMPARED WITH EXPERIMENTAL RESULTS (2·85) AND SOLUTION FOR PERFECTLY PLASTIC PLATES, AFTER WEIRZBICKI (2·86)

Youngdahl[2.87] modified the Hopkin's et al analysis to consider a uniformly distributed pulse of arbitrary time history with finite rise time. Of interest in the analysis of plastic deformation was the case for maximum pressure amplitude $P > 2P_o$ where P_o was the static yield for the plate. Because the arbitrary time history restricts the generality of any solution, coefficients were used by Youngdahl to describe the loading and graph Fig 2.18 page 71 ,shows the resultant central deflection δ_o/R.

2.4.2.2 CLAMPED CIRCULAR PLATES A.J. Wang and H.G. Hopkins[2.88] extended the analysis method of H.G. Hopkins and W. Prager[2.80] and developed a model for the mode of plastic deformation of built-in circular plate subjected to an impulsive loading; the plate being of a perfectly rigid-plastic material and following the assumptions associated with the previous hinge analysis techniques. The first of the two phases postulated for this deformation theory resulted from the motion of two plastic hinge circles and terminated when the faster propagating hinge circle approached the plate centre. The kinetic energy remaining after the completion of phase one was subsequently converted to plastic work by the motion of the final hinge circle.

Again the solution involved the equation 2.29 and conditions associated with the boundaries and hinge circles, but unfortunately because of the numerical complexity of the analysis, the only results calculated were the duration of each phase and the resultant polar deflection.

These results where

$$\text{Time of phase one} = 0.57 \frac{m v_o R^2}{12 M_o}$$

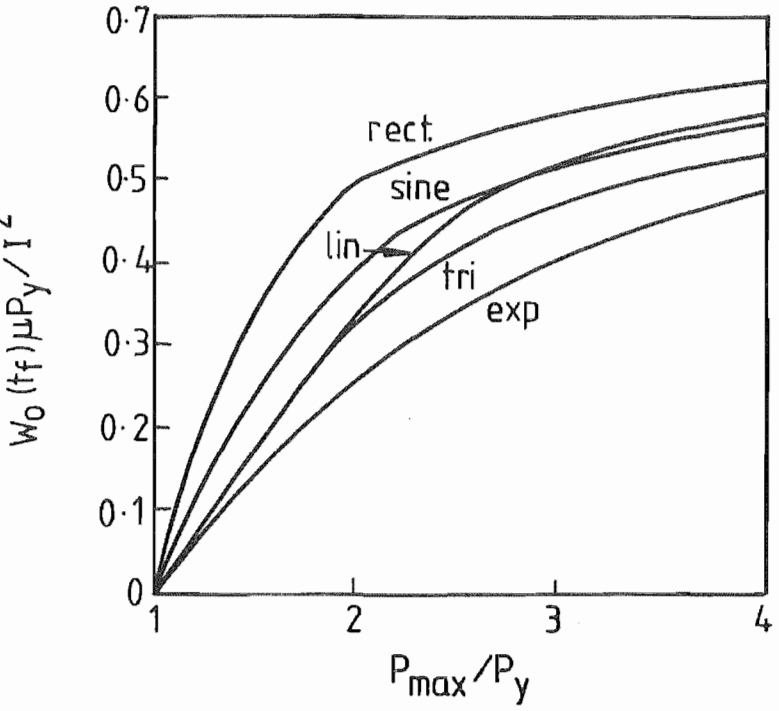

FIG 2·18a MAXIMUM DEFORMATION AS A FUNCTION OF THE MAXIMUM PRESSURE FOR VARIOUS PULSE SHAPES. AFTER YOUNGDAHL [2·87]

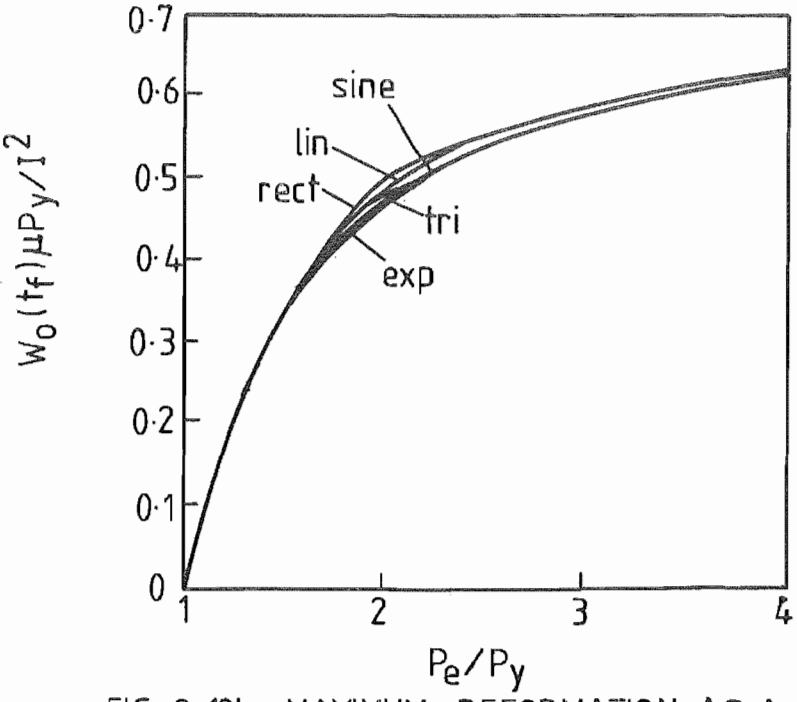

FIG 2·18b MAXIMUM DEFORMATION AS A FUNCTION OF THE EFFECTIVE PRESSURE FOR VARIOUS PULSE SHAPES AFTER YOUNGDAHL [2·87]

Time of phase two $= 0.51 \frac{m v_o R^2}{12 M_o}$

Polar deflection during phase one $= 0.57 \frac{m v_o^2 R^2}{12 M_o}$

Polar deflection during phase two $= 0.27 \frac{m v_o^2 R^2}{12 M_o}$

Florence[2.89] extended the analysis of Wang et al[2.88] by assuming that during the pressure pulse the hinge circles have a fixed stationary location, rather than originating from the rigid boundary and propagating inwards as in the work of Wang et al. On removal of the pressure, the hinge circles propagate inwards and when the inner hinge circle approaches the plate centre, propagation of the outer hinge circle ceases, the remaining kinetic energy being converted directly to plastic deformation without plastic hinge propagation.

Again the complexity of the equation governing the hinge circle behaviour precluded analytical solution and required a numerical solution. The results for the central deflection were given in Fig 2.19 page 73 for a rectangular pressure pulse of amplitude P_m and impulse I for a plate of radius R, density m, bending yield limit M_o and static yield pressure P_s.

A paper by Krajcinovic[2.90] applies the Florence analysis to the case of uniformly distributed pressure pulse with an arbitrary time history, and to generalise the resultant numerical solution, correlation factors based upon Youngdahl's work[2.87] were used. These were

P_e = Effective Pressure.

$= \frac{I}{2t_{me}}$

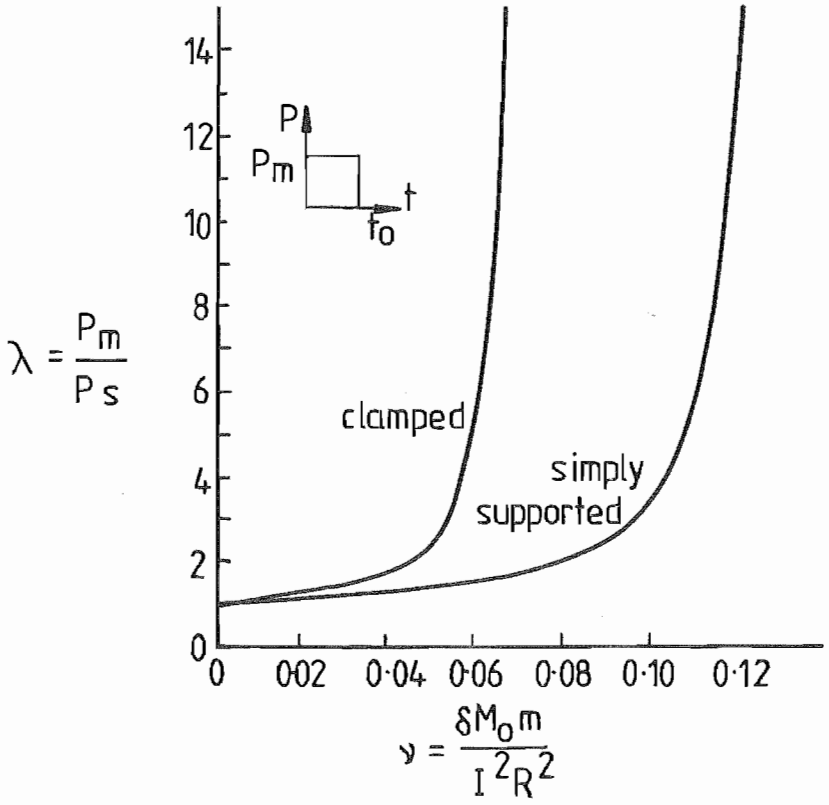

FIG 2·19 RELATIONSHIP BETWEEN δ, λ AND I [2·89]

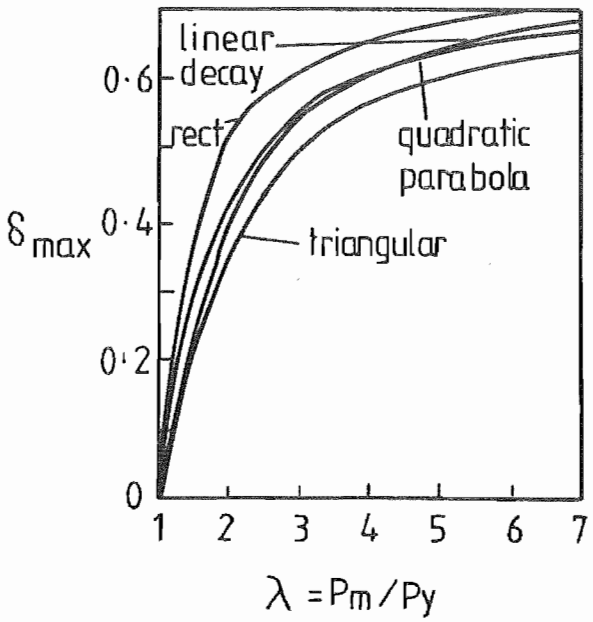

FIG 2·20a FINAL DEFLECTION AS A FUNCTION OF PULSE SHAPE.

AFTER KRAJCINOVIC [2·90]

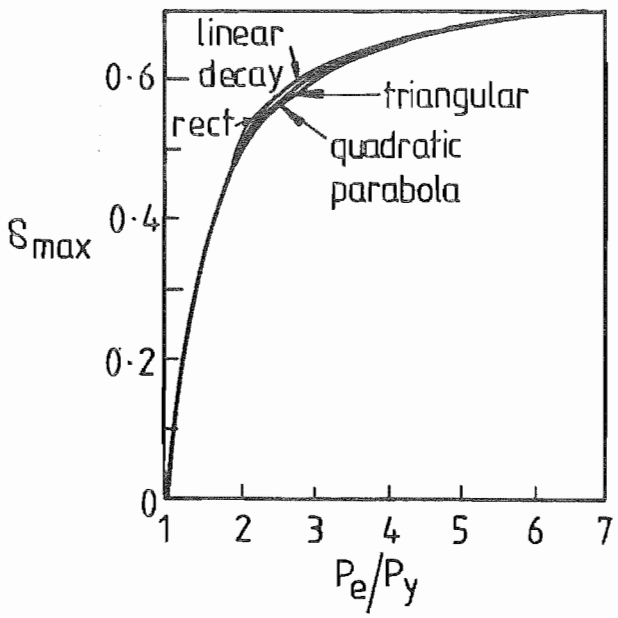

FIG 2·20b FINAL DEFLECTION AS A FUNCTION OF EFFECTIVE PRESSURE Pe FOR VARIOUS PULSE SHAPES

AFTER [2·90]

$$I = \text{Impulse}$$

$$= \int_{t_y}^{t_f} (t - t_y)p(t)dt$$

$$t_{me} = \text{Centroid of pulse}$$

$$= \frac{1}{I} \int_{t_y}^{t_f} (t - t_y)p(t)dt$$

where

t_y = time at onset of plastic deformation

t_f = time at completion of plastic deformation.

The result of this work was given in the graph, Fig 2.20 page 73 where the central deflection was given by δ_{max}.

The assumption of a bending mode of deformation was limited in its application to either the clamped or simply supported circular plate as was shown by the experimental results of Florence[2.85] and Wierzbicki et al[2.91]. Hence the combined bending and membrane stress situation had to be considered to achieve an accurate model of the dynamic final plastic deformation by the techniques discussed above.

2.4.3 COMBINED BENDING AND MEMBRANE STRESS PLASTIC DEFORMATION ANALYSIS

While Jones[2.76] considered both bending and membrane stresses his analysis involved an initial predominantly bending deformation mode which was solved by the method after Wang[2.81] for the first phase. A second stage membrane deformation stage was solved by the use of Bessel functions. The initial conditions considered for the second stage of the solution ensured continuity

of deflection and velocity but accepted a discontinuity in bending moments. A comparison with the experimental work of Florence Fig 2.21 page , suggested that the analysis gave a reasonable approximation to the plastic deformation of a simply supported plate subjected to an impulsive loading. However it should be pointed out that neither strain-rate nor work hardening effects were considered.

Wierzbicki[2.92] presented solutions for both the bending mode for small deflections and bending-membrane mode for large deflections for an impulsively loaded simply supported plate of strain rate sensitive material.

Using a constitutive equation

$$\dot{\varepsilon}_{ij} = \gamma_o \left(\frac{(\tfrac{1}{2} s_{ij} s_{ij})^{\frac{1}{2}}}{k_s} - 1 \right) \frac{s_{ij}}{(\tfrac{1}{2} s_{ij} s_{ij})^{\frac{1}{2}}} \quad \text{for } \tfrac{1}{2} s_{ij} s_{ij} > k_s$$

where

$\dot{\varepsilon}_{ij}$ = strain rate
s_{ij} = deviatoric stress
k_s = yield stress in simple shear
γ_o = viscosity constant

the problem was initially solved for a small deflection case for the bending stress alone and then the velocity distribution, and hence the deflection was obtained. Using the governing equation obtained by the principle of virtual work, and subsequently linearising the constitutive equation by the use of a "state of compression stress tensor", Wierzbicki used the small deflection result on the shape functions in a Galerkin procedure, and hence obtained a solution for the combined bending-membrane large deflection case.

The comparison of the results obtained by Wierzbicki with experimental work by Florence[2.85] was shown in Fig 2.22,page 76 , while a comparison with Jones[2.76] analysis for a five term expansion of the series of Bessel functions was given for the

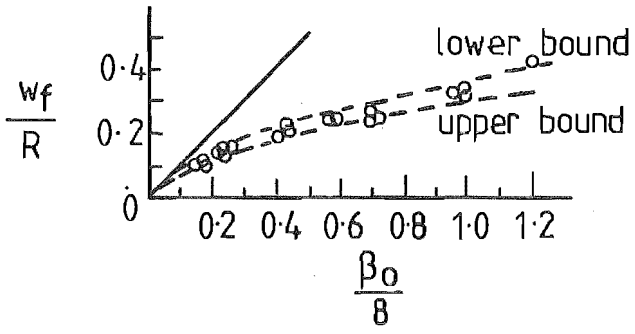

FIG·2·21a COMPARISON OF THEORY WITH EXPERIMENTAL RESULTS FOR AN IMPULSIVELY LOADED SIMPLY SUPPORTED PLATE.

o experimental results [2·85]
—— bending only [2·81]
- - - membrane-bending theory

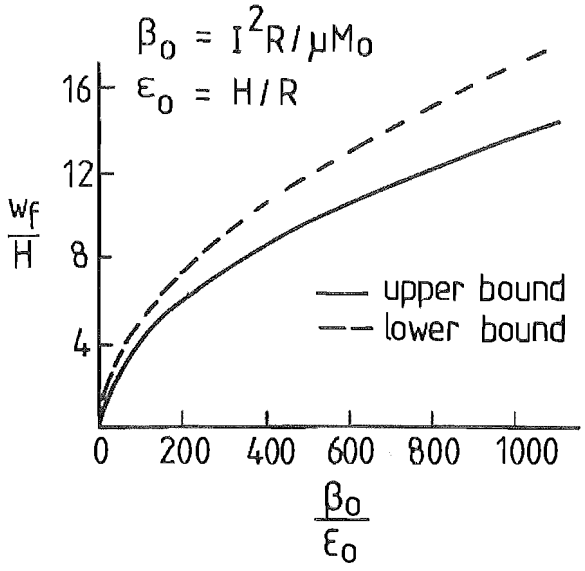

FIG 2·21b. DEFLECTION-IMPULSE RELATION FOR SIMPLY SUPPORTED CIRCULAR-RIGID PLASTIC PLATES AFTER JONES (2·76)

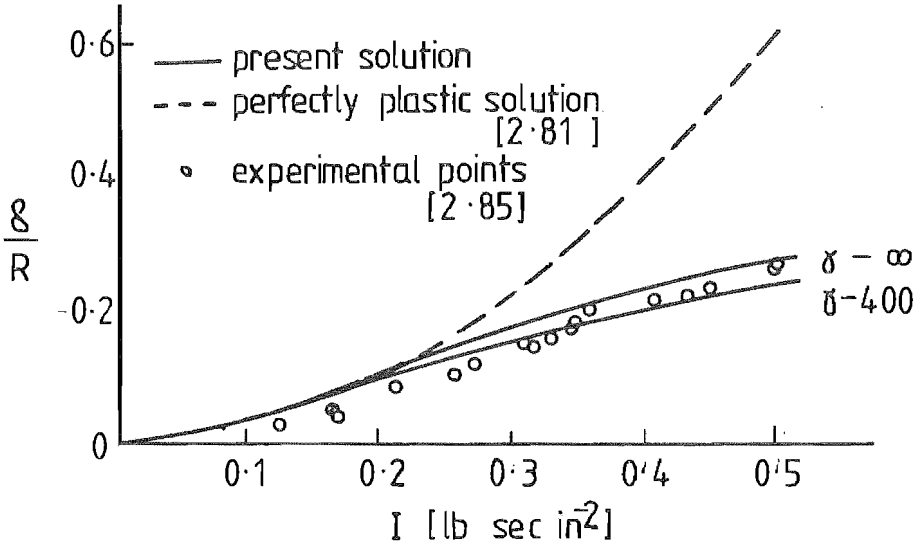

FIG 2·22 PERMANENT CENTRAL PLATE DEFLECTION vs APPLIED IMPULSE. PRESENT SOLUTION (LARGE DEFLECTION) AND PERFECTLY PLASTIC SOLUTION (SMALL DEFLECTION) AS COMPARED WITH EXPERIMENTAL RESULTS.

thickness to radius ratios in Fig 2.23,page 78 .

Wierzbicki et al[2.91] extended the analysis technique above to consider a clamped plate impulsively loaded to obtain solutions for the following cases;

(a) Viscoplastic bending action for small deflection.
(b) Viscoplastic bending-membrane action for small deflections (central deflection < 2h)
(c) Rigid-plastic bending-membrane action for large deflections
(d) Rigid-plastic bending-membrane action for all deflections.

and obtained a reasonable correlation, Fig 2.24 page 78 , with the experimental work they carried out. Again the range of application of the technique was limited to the viscoplastic case and it was considered by the author that the discrepancy between theoretical and experimental results would be due, in large deflections, to the assumption of small strains in the derivation of the equations governing motion, as well as having ignored strain sensitivity and strain hardening in this case.

Batra et al[2.93] derived a generalised incremental analysis for impulsively loaded circular plates to study their dynamic behaviour in the elastic- plastic range. The study enabled the deflection to be determined for a known initial velocity distribution in the deflection range where the combined bending moment and membrane forces were significant.

The numerical solution involved a finite element model and comparisons were made with experimental results in the literature. Finite element procedures have been used to describe the dynamic nonlinear elastic-plastic deformation of plates subjected to transient or shock loading and examples of these techniques have been presented by Wu et al[2.94], Mondkar et al[2.95] and Bathe et al[2.96].Current research mainly concentrates in the application of finite element techniques to this problem.

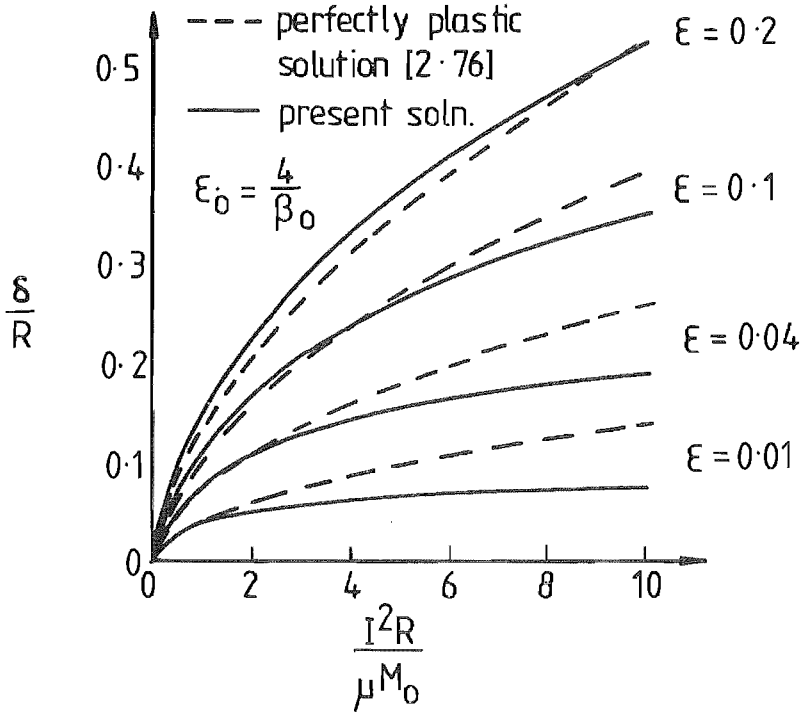

FIG 2·23 COMPARISON BETWEEN THE PRESENT THEORY (VISCOPLASTIC MATERIAL) AND THE THEORY OF JONES (PERFECTLY PLASTIC MATERIAL)

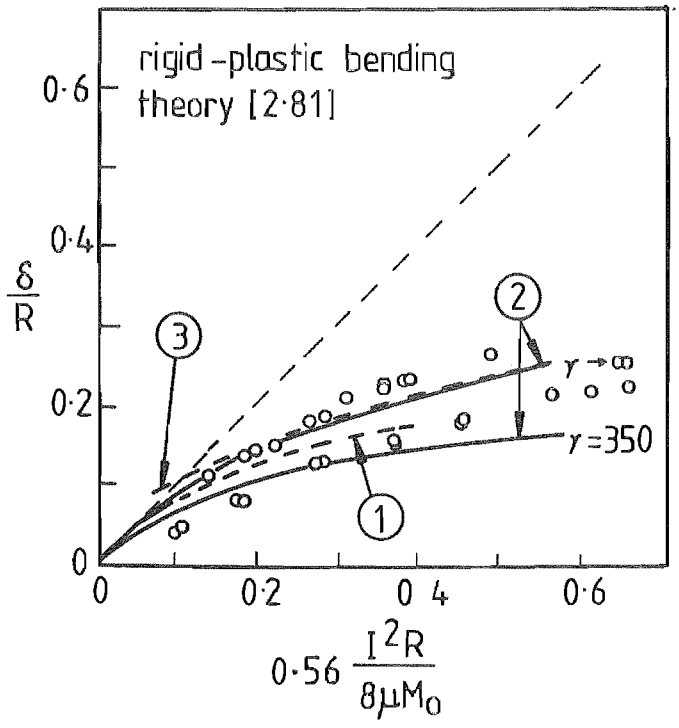

FIG 2·24 EXPERIMENTAL AND THEORETICAL CENTRAL DEFLECTIONS FOR CLAMPED PLATES

1. VISCOPLASTIC BENDING MEMBRANE ACTION FOR SMALL DEFLECTIONS
2. RIGID PLASTIC BENDING MEMBRANE ACTION FOR LARGE DEFLECTIONS
3. RIGID PLASTIC BENDING MEMBRANE ACTION FOR ALL DEFLECTIONS

2.4.4 GENERAL TECHNIQUES OF ANALYSIS

Wierzbicki[2.97] developed an interesting alternative method of representing the constitutive equation as a pseudo strain rate sensitive condition, and hence allowed a modal eigenfunction expansion technique to be applied. This superposition does not apply for plastic deformation and therefore it was accepted that the yield condition would be locally violated. The modification to the constitutive equation insured that the yield conditions were satisfied globally over the structure under consideration.

In considering the case of a simply supported circular plate the method of solution was applied, and a deformation profile derived from a given initial velocity distribution and a range of shape functions. An important advantage claimed for the analysis method was that it could be inverted, and from the desired deformation profile it was possible to calculate the required initial velocity or impulse radial distribution to free form the required shape.

The development of programs to determine the large dynamic deformation of bearers, rings, plates and shells has been reported by Witmer et al[2.98] ,Leech et al[2.99] and Marino et al[2.100], while comparison of the numerical results with the experimental studies has been carried out by Marino et al[2.101] and Duffey et al[2.102]. The program involved the use of an integral technique to describe the strain increments over each time step, while the spatial representation involved a lumped mass finite difference scheme. The lumped mass scheme in the thickness was such that the applied bending moments were considered to be resisted by separate discrete layers of material. For each time step, the stress-distribution at each spatial point was considered and hence the progression applied for the following material cases; 1) elastic material, 2)elastic, perfectly plastic material, 3) elastic, plastic strain hardening and strain rate sensitive material.

2.5 ENERGY TRANSFER

The energy transfer to the explosively formed blank has been of interest [2.69,2.103] because it determined the efficiency of the forming operation and the mechanisms involved influence the plastic deformation mechanisms, final strain distribution and hence the resultant material properties and in the case of free forming, the final product shape.

2.5.1 DEFORMATION/ENERGY TRANSFER CORRELATION

Noble and Oxley[2.104] developed a simple method of determining the amount of explosive necessary in the production of simple symmetrical shapes. The work done in plastically deforming the metals was given by;

$$\text{Work done} = h.Y.\Delta A$$

where h = thickness of the metal blank.
Y = yield stress of the metal.
ΔA = imposed change in area, to the first order of accuracy, due to biaxial loading.

The energy available at the blank surface due to the explosive was given by

$$\text{Energy} = \eta_t.A_o I.W$$

where A_b = the initial area of the blank normal to the incident explosive energy flux.

I = the energy flux available at the blank surface

η_t = transfer coefficient which allows for energy losses in the transfer medium due to friction, friction, turbulance and viscosity.

W = the weight of explosive.

To determine the weight of explosive necessary for a particular product, the work required to be done was equated with the energy available, and the charge weight expressed in terms of the stand-off, transfer coefficient, yield stress of the material and the geometry of the required shape.

This method implied the explosive was effectively a point charge and released its energy without any directionality, while the expression for work done in the blank assumed a biaxial stretch deformation and hence restricted its application to symmetrical shapes. The analysis was based upon a perfectly plastic material which further limited its accuracy.

Floral[2.103] carried out a more rigorous investigation into the forming of domes using an energy minimization technique which allowed consideration of large strains, edge pull-in effects and non-linear material behaviour. The deformed shape was assumed to take up either an ellipsoid or paraboloid shape in the vertical sense, while the radial displacement was described in a function which allowed for edge pull-in

A power law

$$\bar{\sigma} = K \bar{\varepsilon}^{n}$$

where $\bar{\sigma}$ = representative stress

$$= (\sigma_r^2 - \sigma_r \sigma_t + \sigma_t^2)^{\frac{1}{2}}$$

$\bar{\varepsilon}$ = representative strain

$$= (\frac{4}{3}(\varepsilon_r^2 + \varepsilon_r \varepsilon_t + \varepsilon_t^2))^{\frac{1}{2}}$$

gave the material properties and hence the strain energy was given by

$$U_s = \frac{K}{n+1} \int_v \bar{\varepsilon}^{n+1} dv$$
$$\int \varepsilon dv$$

Floral minimised the strain energy with respect to the arbitrary constants in the vertical and radial displacement functions using a computer based method, and thus allowed the total potential energy to be minimised. By equating the resultant potential energy to the energy delivered to the blank, the blank profile was obtained. The delivered energy was obtained by using the following relationship derived by Ezra to account for the proximity of the charge to the blank.

$$I = \frac{A_1 W^{\frac{f+1}{3}}}{S^f}$$

where A_1 and f were explosive dependent constants, W was the explosive charge weight and S was the explosive stand-off from the blank.

Hence Floral obtained the expression

$$\text{Energy} = \frac{A_1^2 W^{\frac{2(f+1)}{3}}}{mh} \frac{\pi}{2} \frac{D_o^2}{(\frac{D_o}{12})^{2f}} \frac{L^4}{D_o^4} \frac{1}{f+1} \left(\frac{1}{(\frac{L}{D_o})^{2(f+1)}} - \frac{1}{(\frac{L^2}{D_o^2} + \frac{1}{4})^{f+1}}\right)$$

where h was the initial thickness, m was the mass density L the axial distance from the charge to blank and D_o die diameter.

Experimental work reported in Floral's paper suggested that the effect of the edge pull-in required further study.

While these analyses gave results which correlated deflection to the estimated or empirically determined incident energy or impulse, they did not adequately describe the energy transfer mechanisms involved or enable the resultant strain rates within the deforming blank to be determined.

2.5.2 ENERGY ABSORBED BY BLANK

Johnson[2.105] in a summary of work carried out at the Manchester Institute of Science and Technology on High Energy Rate forming reported a simple technique of calculating the work done on a blank, relating it to the final thickness strain distribution and the stress-strain curve for the blank material. The derivation relied upon the assumption that the hoop and radial strain were approximately equal and hence, due to incompressibility, the thickness strain was of the opposite sign and twice the value of the hoop and radial strain. Therefore the representative strain based on the Hencky-Mises distortion energy theory became equivalent to the magnitude of the thickness strain, which gave an easy method of direct measurement of the representative strain.

It was also assumed that the material stress-strain curve could be represented by either the Swift equation

$$\bar{\sigma} = A^* (B^* + \bar{\varepsilon})^n$$

where A*, B* and n were material constants and in the case of annealed materials B* was taken as zero, or alternatively

$$\bar{\sigma} = Y + P^* \bar{\varepsilon}$$

where Y was the primary yield stress and P* was the plastic modulus for a rigid linear strain hardening material.

Hence the relationship applied to an annealed material gave

$$\text{Work Done} = \int_o^V A^* \frac{\bar{\varepsilon}^{n+1}}{n+1}\, dv$$

$$= \int_o^R 2\pi h\, A^* \frac{\bar{\varepsilon}^{n+1}}{n+1}\, r\, dr$$

while for linear strain hardening material

$$\text{Work Done} = \int_o^V (Y\,\bar{\varepsilon} + \frac{P^*\,\bar{\varepsilon}^2}{2})\, dv$$

$$= \int_o^R 2\pi h (Y\,\bar{\varepsilon} + \frac{P^*\,\bar{\varepsilon}^2}{2}) r\, dr$$

Finally it was assumed that the variation of hoop strain with respect to the initial radial position was given by

$$\varepsilon_t = \varepsilon_m (1 - \frac{r}{R})$$

where ε_m = strain constant.

r = initial reference radius

R = outer radius

Hence for the first case with B equal to unity gave

$$\text{Work Done} = \frac{2^{n+2}\ \pi\ R^2\ h\ A^*\ \varepsilon_m^{n+1}}{(n+1)\ (n+2)\ (n+3)}$$

while for the second case

$$\text{Work Done} = \pi\ R^2\ h\ {}_m(2Y + P^*\ \varepsilon_m)/3$$

The initial velocity of the blank was obtained by assuming that the kinetic energy was acquired in the passage of the shock wave over the blank and was entirely dissipated as plastic work, hence

$$v_o = \frac{2^{n+3}\ A^*\ \varepsilon_m^{n+1}}{m(n+1)\ (n+2)\ (n+3)}$$

where v_o = initial speed of the blank.
m = mass density

while for the strain hardening case

$$v_o = \frac{2}{3}\ \varepsilon_m \left(\frac{2Y + P^*\ \varepsilon_m}{m}\right)$$

Finally in method similar to that developed by Noble and Oxley, the plastic work done was related to the energy available at the blank surface, due to the explosive giving the following equation 2.26 .

$$\frac{R^2}{4S^2}\ \frac{c}{4} = \frac{2^{n+2}\ \pi\ R^2\ h\ A^*\ \varepsilon_m^{n+1}}{(n+1)\ (n+2)\ (n+3)}$$

where R = the blank radius.

S = the stand-off

c = the charge energy available

Also the assumption was made following Bebb[2.71], that approximately one quarter of the total energy available was associated with the shock wave as a reversible primary energy.

The second material property representation gave

$$\frac{R^2}{4S^2}\frac{c}{4} = \pi R^2 h \varepsilon_m \frac{(2Y + P^* \varepsilon_m)}{3}$$

It was obvious that the use of static stress-strain characteristics in the prediction of dynamic behaviour introduced a large element of uncertainity in the accuracy of the final result. However it did act as a guide and reduced the amount of experimental work necessary in setting up an installation to explosively form a product.

Sag[2.21] determined the spatial distribution of strain energy within a dish end manufactured by explosive forming by placing a grid on the blank and measuring the thickness and hoop strain. The incompressibility condition was then applied to obtain the equivalent strain from the Hencky-Mises distortion energy theory to be used in the power law representation of the material stress-strain characteristics.

Also, using a computer-based numerical summation the total strain energy for the blank was obtained and compared with the initial explosive energy available.

Sag derived the following relationships

$$\frac{DE}{W} = 0.01499\ W^{0.529} \quad \text{for Aluminium}$$

$$= 0.01709\ W^{0.301} \quad \text{for Stainless Steel}$$

$$= 0.02397\ W^{0.169} \quad \text{for Mild Steel}$$

where DE = Deformation Energy
W = Explosive Charge Weight

based upon a Cordtex charge wound in 200mm diameter circles and located one and one half the die diameter above the blank. The equivalent hydrostatic pressures were calculated to achieve the same deformation energies as were obtained by explosive forming.

2.5.3 DEFLECTION/ENERGY TRANSFER INTERACTIONS

Considerable effort was expended[2.20] in studying the interaction of deflection on energy transfer with particular emphasis upon the damage caused upon structures such as ships, by underwater explosions. As previously mentioned these analyses assume large explosive quantities at a significant distance from the deforming material and hence there was no interaction between the deforming surface and the mechanisms of energy release from the explosive. The analytical techniques described have been applied to diaphragm gauges[2.22,2.23] and while these methods give a basis for preliminary investigations into explosive forming, they do not adequately allow for the close proximity of the explosive charge to the deforming blank.

H.M. Shauer[2.69] reported on an analysis in which a reloading phase due to a combination of afterflow with gas bubble expansion and the collapse of cavitation immediately adjacent to the blank was considered. Initial deflection was considered to be caused by the idealised shock wave represented by

$$P_t = P_m \exp(-t/\theta)$$

for which acoustic approximations applied, and hence the total loading on the plate due to the incident and secondary radiated plane shock waves was given by

$$P' = 2P_t - mc \frac{\partial x}{\partial t}$$

where m = plate mass density

c = velocity of sound in energy transfer medium

$\frac{\partial x}{\partial t}$ = plate velocity.

At the onset of cavitation the loading on the plate ceased and the subsequent deformation was a function of the absorption of the kinetic energy in the blank immediately preceding cavitation.

On collapse of cavitation the plate was reloaded and, using linear hydrodynamic relationships and an idealised spherical gas bubble behaviour, the deflection was obtained.

Ezra et al[2.2] studied the interaction of the underwater shock wave with a deforming circular plate until cavitation occurred. It was assumed that since the time to cavitation was so small, the resultant deflection was satisfactorily described by a small deflection elastic bending analysis. Again as in the work of Schauer, a plane primary shock wave and acoustic theory was assumed.

Hence the governing equation was

$$D \bar{\nabla}^4 w = q(r,t) - mh \frac{\partial^2 w}{\partial t^2}$$

where $q(r,t) = 2P_m e^{-t/\theta} - \dot{m}_o c_o \frac{\partial w}{\partial t}$

and hence by separation of variables in a technique similar to that given in Chapter Five an expression was obtained for the deflection.

It was apparent that while some qualitative methods were available to describe the energy transfer in the explosive forming operation, the complexity and interaction of the energy transfer from the explosive to the transfer medium with blank deformation prevented a realistic quantitative analysis until more relevant experimental information was available, particularly associated with the pressure history in the region adjacent to the deforming blank.

2.5.4 EXPERIMENTAL STUDIES OF ENERGY TRANSFER

Some fundamental studies into the explosive forming have examined the deformation history of the blank by either the pin contactor method [2.24,2.27-2.29,2.106,2.107], high speed photography [2.108,2.109], streak photography [2.28,2.110] or high speed stereophotogrammetry [2.111,2.112].

Typical results for a pin contactor experimental program are given in Figs 2.25-2.28 pages 90, 91 the location for the first three Figures being at a radial distance from the blank centre of 3/16 of the blank radius. The results shown were for a charge size of 250mm of Cordtex with a No.6 electric detonator, wound into a spherical shape with an 89 mm stand-off for a free forming operation.

This result was verified by the alternative methods of measuring deformation history [2.28,2.113], the significant feature was the apparent reloading of the blank at a time of 0.3 - 0.45 milliseconds following the initial movement of the blank.

As can be seen from Fig 2.26, initially the impinging shock wave imparted an impulsive load to the blank and as suggested by most analytical models, the resultant kinetic energy was absorbed as plastic deformation until approximately 0.3 milliseconds had elapsed, following the initial deformation. Subsequently the blank was reloaded and the deformation velocity achieved a maximum at an

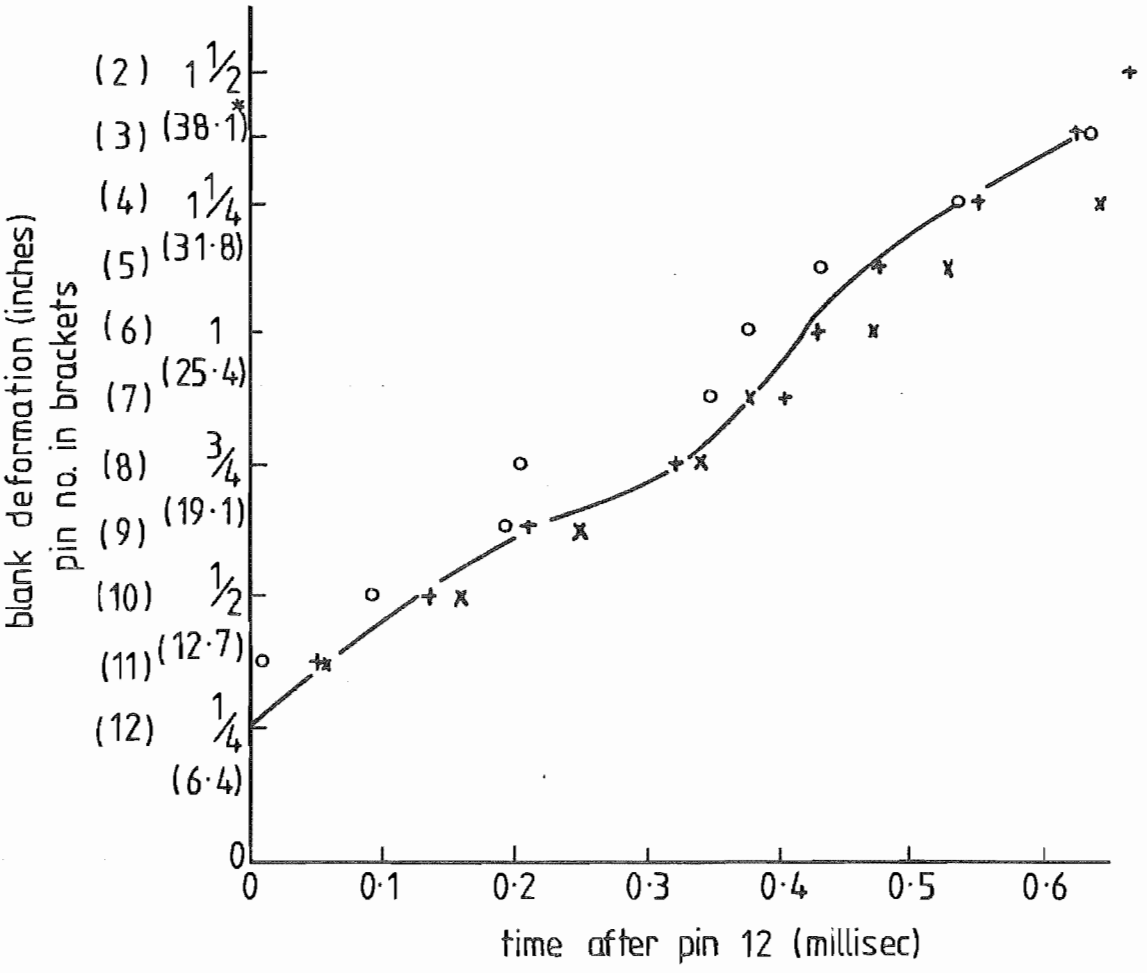

FIG 2·25 DEFORMATION vs TIME AT 3/16 OF BLANK RADIUS [2·107]

* in mm

** see Chapter 3

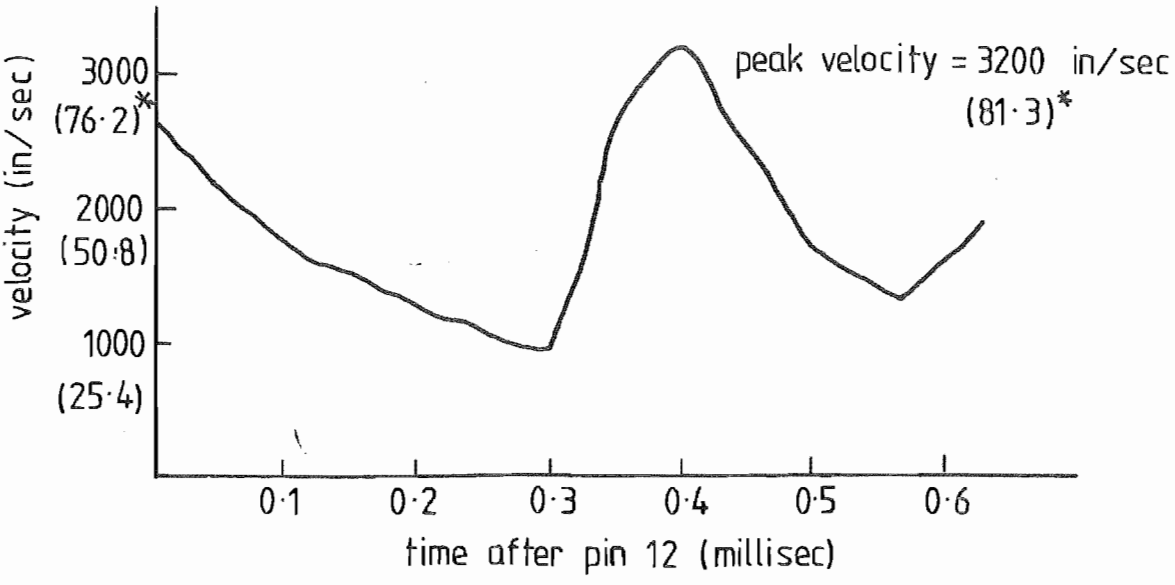

FIG 2·26 VELOCITY vs TIME AT 3/16 OF BLANK RADIUS [2·107]

* velocity in m/sec

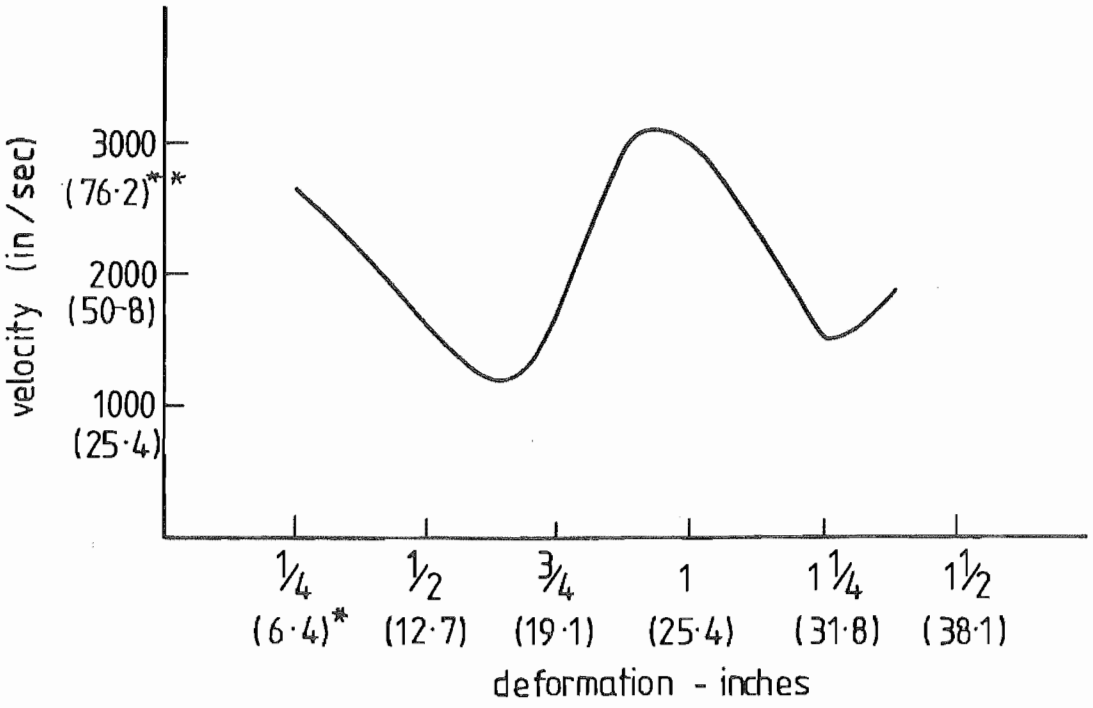

FIG 2·27 VELOCITY vs DEFORMATION AT 3/16 OF BLANK RADIUS (2·107)

* deformation in mm

** velocity in m/sec

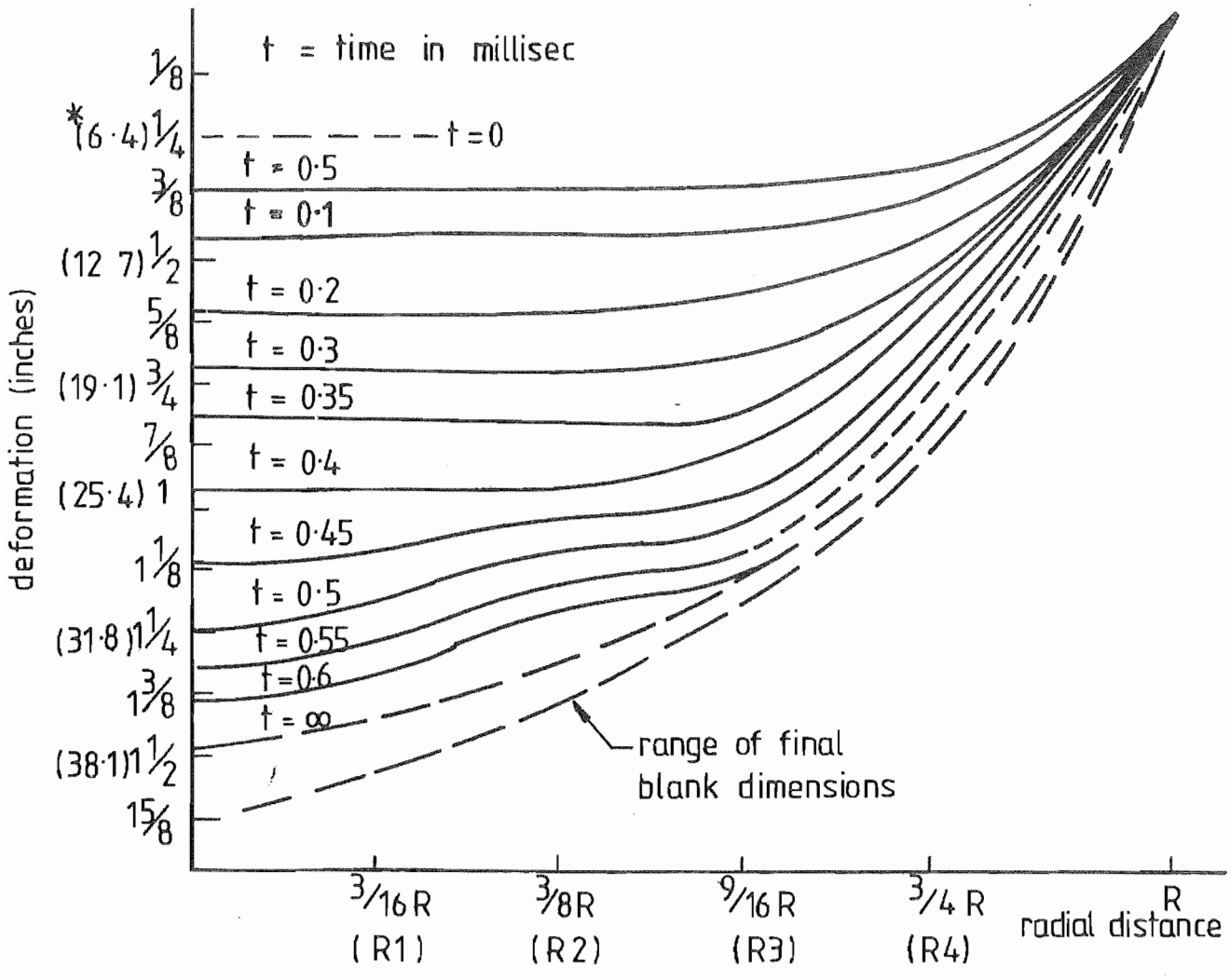

FIG 2·28 DEFORMATION PROFILE [2·107] *deformation in mm

elapsed time of approximately 0.4 milliseconds.

The reloading phase was attributed to either the gas bubble pulsation and migration[2.28] or to the collapse of a cavitation region in the energy transfer medium immediately adjacent to the deforming blank[2.69]. The suggested gas bubble mechanism was discarded because it was shown [2.113] that the time for gas bubble pulsation to achieve a size to give significant pressure pulses was considerably greater than that for the reloading phase.

The alternative mechanism involved the formation of a cavitation region immediately adjacent to the workpiece due to the velocity and reflection of the incident shock wave. Such cavitation has been observed[2.69,2.70]. The expansion of the gas bubble contributes to the subsequent collapse of the cavitation region as the blank velocity deceases, and the afterflow of the energy transfer medium as well as the water-hammer effect of this collapse was considered to give rise to the reloading phase.

The correlation between experimental work and analytical work by Schauer[2.69] suggested that this proposed mechanism of reloading was valid.

There was no experimental work reported, to the knowledge of the author, which measured the pressure history in the region immediately adjacent to the deforming blank. G.E. Hobson et al[2.28,2.33], during the development of an explosive forming machine carried out some pressure history measurements with transducers mounted in the walls of the pressure reflector and also mounted a transducer in a 5/8 inch (15.8mm) plate which was put in place of the blank. These results were restricted in their application because of the presence of the pressure reflector and the distance from the workpiece of the reflector-mounted transducers. In the case of the plate mounted transducer no blank deformation occurred and hence this result was of limited use in understanding the energy transfer mechanisms associated with the explosive forming process.

U. Nishiyama et al[2.114] photographically recorded the detonation and obtained some pressure history measurements using the collapsible air cell suggested by Johnson et al[2.29] to obtain water-hammer effects.

The pressure measurement was made within the air cell and hence was not in the region of immediate interest, Fig. 2.29, p 94.

It was apparent that there was a need for a method of measuring the pressure history in the region of the blank/energy transfer medium and to be able to correlate that to the resultant blank deformation for the following reasons;

(1) To obtain a better understanding of the energy transfer mechanism and the deformation/energy transfer interaction.

(2) To enable the development of an improved analytical model of blank deformation because the existing analytical models[1.4,2.37,2.76,2.81-2.93] relied upon idealised loading conditions.

(3) To develop some form of economic pressure instrumentation which would improve the repeatability of the explosive forming process by giving a basis of comparison between the forming operations.

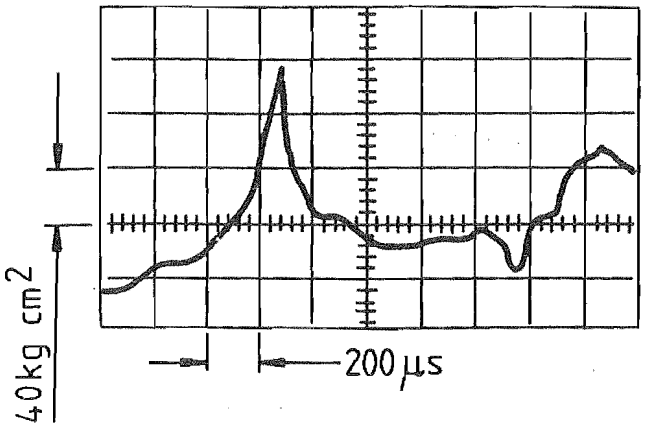

FIG 2·29 PRESSURE-TIME CURVE WHEN USING AN AIR-BAG WHOSE HEIGHT IS 1cm IN EXPLOSIVE FORMING WITH A Nº 6 ELECTRIC DETONATOR AT A STAND OFF DISTANCE OF 22cm AND A CHARGE DEPTH OF 33cm. [2·114]

CHAPTER THREE

INSTRUMENTATION

3.1 INTRODUCTION

Since in explosive forming finite discrete events occurred in the order of microseconds and the total duration of the operation was four to six milliseconds, any effective instrumentation required response times of the order of 1 MHz.

Instrumentation described in the literature was divided into two main regions; the first being measurement of deformation and hence deformation velocities and dynamic strain, while the second was the limited information on attempts to obtain the pressure history in the energy transfer medium. This chapter contains a review of methods of deformation measurement in explosive forming as well as pressure transducers available for the measurement of transient and high pressures.

Methods of calibration of dynamic pressure measurement systems are presented and the selection of an appropriate pressure transducer design discussed.

3.2 DEFORMATION MEASUREMENT

As was previously mentioned in Chapter 2.5.4 deformation history was used in an attempt to obtain an understanding of the loading history of the blank and the methods used to extract this information were the pin contractor method, high speed streak photography and high speed stereophotogrammetry.

3.2.1 PIN CONTACTOR METHOD

The pin contactor method, following Fyfe et al[2.24], involved a series of pins which were connected to charged R-C circuits. As the blank deformed it contacted these pins, which were placed at a known position and distance with respect to the blank and earthed the associated circuits. A typical layout was that of Hobson et al [2.28], the schematic of which is shown in Fig 3.1 page 97 .

As the flexible pins were struck, earthing the circuits, the signals of the decay of the associated discharged R-C circuits were recorded on an oscilloscope against an appropriate time base. Hence the time at which a particular radial location on the blank reached a known vertical position from rest was known, and therefore the deformation profile and deformation velocities calculated. It should be noted that the pin rigidity was important. It had to be sufficiently rigid to ensure that it could be accurately placed with respect to radial and vertical locations at the contact point but it should not be so rigid that it interfered with the vertical movement of the workpiece, following contact. A typical output trace was of the form shown in Fig 3.2 page 97, and it can be seen that pin polarity and height was organised so that a positive and negative pulse appeared alternatively on the trace. Typical results are shown in Chapter Two page 90 .

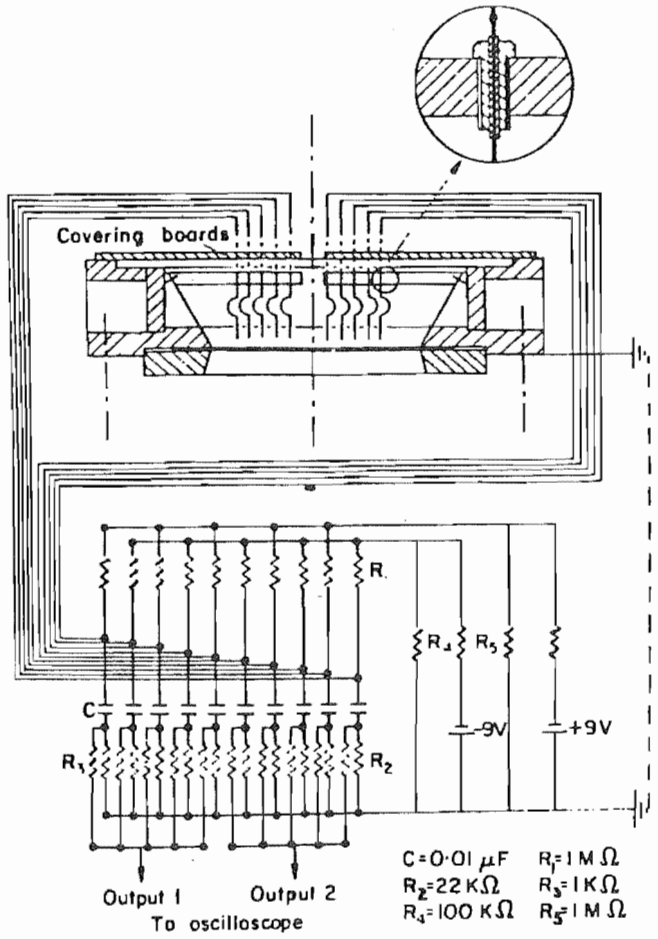

FIG 3·1 PIN CONTACTOR METHOD OF DEFLECTION AND VELOCITY MEASUREMENT AFTER HOBSON ET AL [2·28]

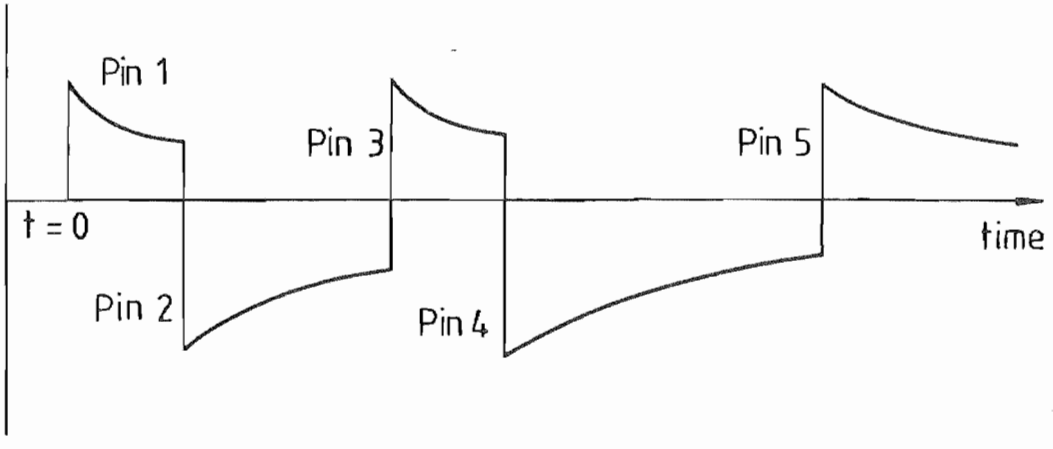

FIG 3·2 IDEALISED TRACE FROM PIN CONTACTOR METHOD

3.2.2 HIGH SPEED STREAK PHOTOGRAPHY

This technique used by Hudson et al[2.110] and Hobson et al[2.28] to determine the blank deformation history, involved placing a line of reflecting spots, symmetrical with respect to the centre, on the blank. Reflecting spots also were placed on the retaining ring in line with those on the blank to give a measurement reference. A high speed camera used in the streak or oscillographic mode, i.e. without framing, was arranged at an inclination to the blank, as shown in Fig 3.3 page 99 and so that the film moved at right angles to the line of spots. Lighting was arranged as shown in Fig 3.3.

As the blank deformed the locations of the reflecting spots were continuously recorded as a streak image on the film. Assuming axisymmetric blank deformation and considering the image spots symmetrically about the blank centre, the deformation history was calculated. The results obtained by Hobson et al using this method were used to confirm those derived from the pin contactor technique for the initial blank velocity.

The advantage of this system was that a continuous record of blank deformation was achieved and as opposed to silhouette high speed photography [2.108,2.109] convex phenomenon could be observed.

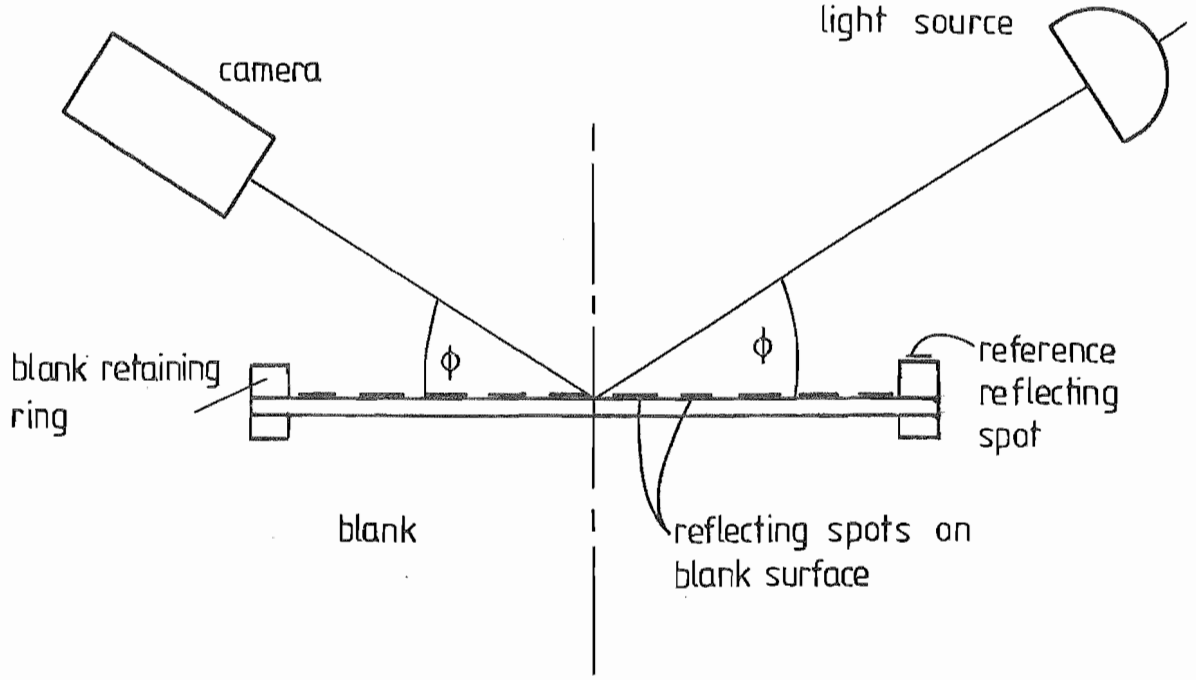

FIG 3·3 HIGH SPEED STREAK PHOTOGRAPHY
AFTER HOBSON ET AL (2·28)

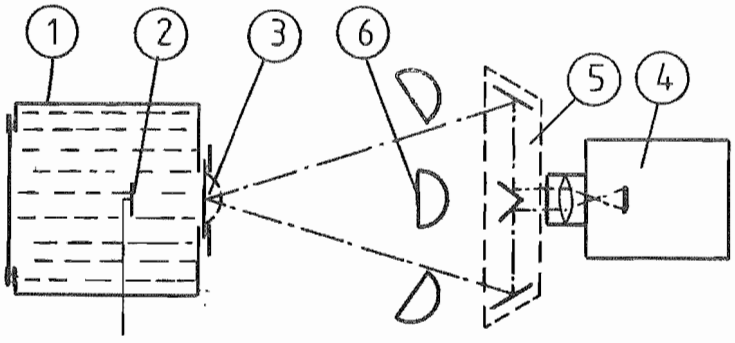

1. tank
2. explosives
3. specimen
4. film camera
5. stereoscopic attachment
6. reflectors

FIG 3·4 HIGH SPEED STEREOPHOTOGRAMMETRY
AFTER BEDNARSKI (2·111)

3.2.3 HIGH SPEED STEREOPHOTOGRAMMETRY

Following work reported by Rinehart et al[2.6] research on deformation measurement was carried out by T. Bednarski [2.111,2.112] based upon generating stereo image pairs within a single frame using the equipment shown in Fig 3.4 page 99.

The resultant contours were plotted for each frame with a stereo comparator, and hence the deformation history was obtained.

3.3 PRESSURE MEASUREMENT TECHNIQUES

As mentioned in the previous chapter it was apparent that a better understanding was required of the pressure history at the workpiece/energy transfer medium interface. An initial survey of pressure transducers available when this project began showed a lack of any appropriate commercially available pressure transducer which would be sufficiently robust to withstand the loading conditions and yet small enough to be able to be placed adjacent to the blank without modifying the behaviour of the process so that it negated the validity of the resultant information.

The anticipated operating conditions for the transducer were based upon a maximum charge of 0.5 metres of Cordtex of 10.5 gms per metre of PETN and a distance of 50 mm from the charge. The resultant maximum pressure P was 230 MPa while θ the decay constant was 12.9×10^{-6} sec . Therefore the following requirements for the pressure transducer were considered a minimum for explosive forming;

(i) Maximum recording range of 200 Mpa
(ii) Sensitivity of 0.1 of a Full Scale Reading.
(iii) Rise time of 10 microseconds
(iv) Maximum overload of greater than 100%
(v) Maximum height of recording surface above blank surface of 5 mm.

Although these specifications were less rigorous than would be anticipated from the description of the shock waves it was hoped that following the development of a prototype, the accuracy and dynamic performance of the transducer could be improved.

The construction of a pressure transducer was considered and a review of the techniques of dynamic pressure measurement was carried out.

3.3.1 STRAIN GAUGE PRESSURE MEASUREMENT TECHNIQUES

The diaphragm pressure transducer Fig 3.5 page 102, developed by Redshaw[3.1] and subsequently modified by Bert et al[3.2] used a specially developed diaphragm strain gauge to measure the surface strain in a circular diaphragm or plate subjected to a normal pressure. The recorded strain could be related to the applied presssure and hence the pressure loading was obtained.

The dynamic characteristics and sensitivity of the sensory element were the major limitation of this pressure transducer system.

Hence the diameter was determined by the following considerations:

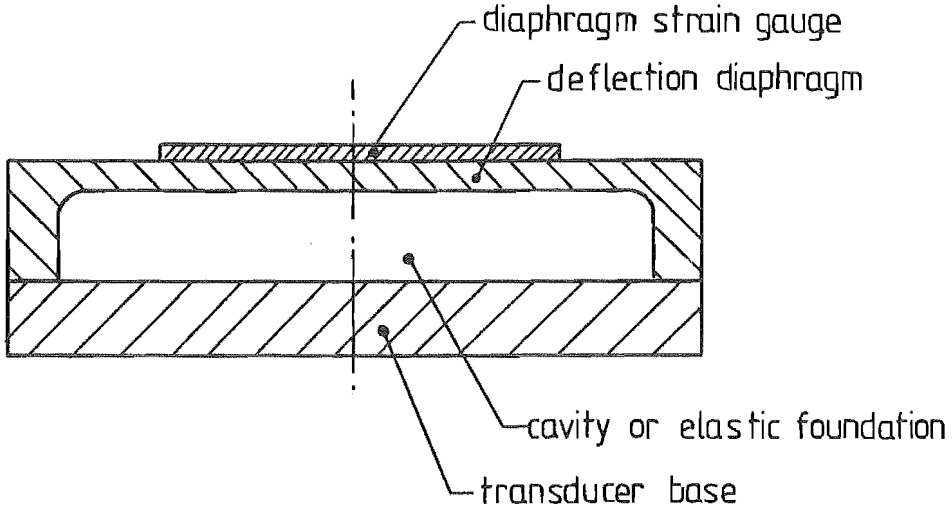

FIG 3·5 DIAPHRAGM STRAIN GAUGE TRANSDUCER

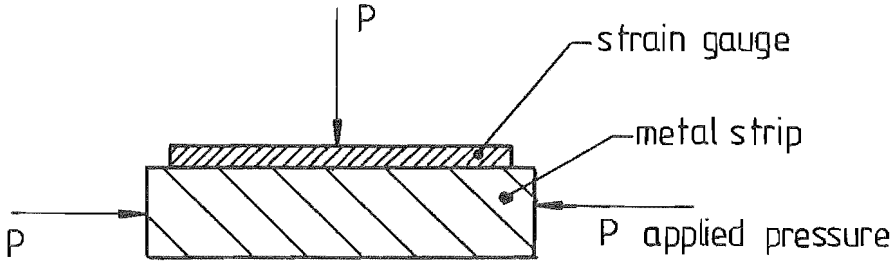

FIG 3·6 STRAIN GAUGE TRANSDUCER

(a) Availability of suitable commercial diaphragm strain gauges.
(b) Ability to meet the rise-time requirements.
(c) Suitable size to give a natural frequency which would meet the prototype specification.

Ideally the thickness of the diaphragm was based upon the following considerations;

(d) It should be adequate to keep the stress level at overload pressure below the proportional limit of the material selected.
(e) It should prevent the deflection over the full operating pressure range from exceeding approximately one-half of the thickness, since deflections larger than this would develop in-plane membrane stresses which would result in non-linearity in the response to pressure.
(f) It should result in a natural frequency which is as high as is feasible, consistent with the required sensitivity.

From Fig 3.5 page 102, it could be seen that the transducer was relatively simple and strong but the size range of the commericially available diaphragm strain gauges precluded development of a pressure transducer of this type. While alternative use could have been made of standard semiconductor strain gauges of small size(2.032x0.127x0.013 mm) which have been used for diaphragm pressure transducers in aerospace applications[3.3], the need to place a four gauge bridge on the transducer would have increased the diaphragm size to give unacceptably low dynamic characteristics.

Following the work of R.V. Milligan [3.4,3.5], the alternative use of a strain gauge mounted upon a metal strip as in Fig 3.6 page 102, was considered. Assuming a nondirectional pressure loading the measured strain could be related to the applied pressure by the relationship

$$e_x = \frac{P(1 - 2\nu)}{E}$$

and hence a linear pressure-strain relationship was obtained as a function of the mounting material and this was verified by experimental work [3.4,3.5]. At higher pressures of the order of 100 Kpsi (689 Mpa.) the piezoresistance effect for the strain gauge and leads was known to be significant[3.6].

An alternative use of strain gauges in a pressure transducer was that shown in Fig 3.7 page 105, and reported in the literature associated with shock loadings [3.7,3.8,3.9]. A resultant uniaxial strain was recorded in the rod or tube, one end of which was exposed to the pressure pulse and hence a pressure recording obtained. The major difficulty envisaged in the anticipated mode of operation was the required length of the transducer and therefore the ability for it to be located in the region of interest.

3.3.2 CAPACITANCE PRESSURE MEASUREMENT TECHNIQUES

The operation of the capacitance transducer, Fig 3.8 page 105, recorded the change in capacitance of the transducer due to pressure induced deflection of the sensory element. By calibration a relationship between the applied pressure and the recorded change of capacitance could be obtained.

By placing a dielectric elastic foundation between the sensory element and transducer base such as CaF_2 [3.10] rather than evacuating the cavity the applied voltage could be increased. This increased voltage reduced the influence of the spurious noise signals that were induced during the necessary amplification of the signal and from the cable connecting the transducer to the recording equipment.

Bagnoff[3.11] and Hanson et al [3.12] described a form of capacitance transducer developed for shock tunnel work, shown in Fig 3.9 page 106. The deformation of the transducer material following the initiation of the stress wave due to the impinging shock wave modified the capacitance between the surface and internal electrode.

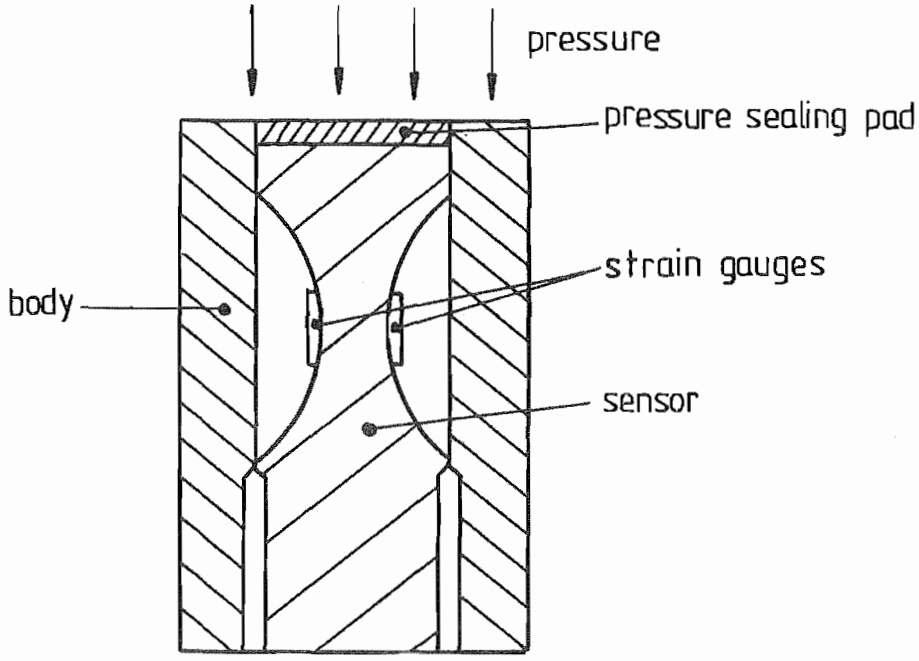

FIG 3·7 STRAIN GAUGE PRESSURE TRANSDUCER

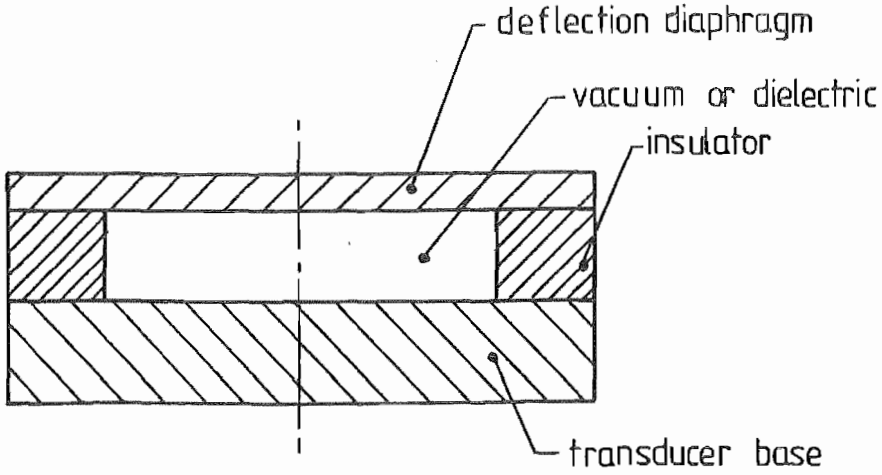

FIG 3·8 CAPACITANCE PRESSURE TRANSDUCER

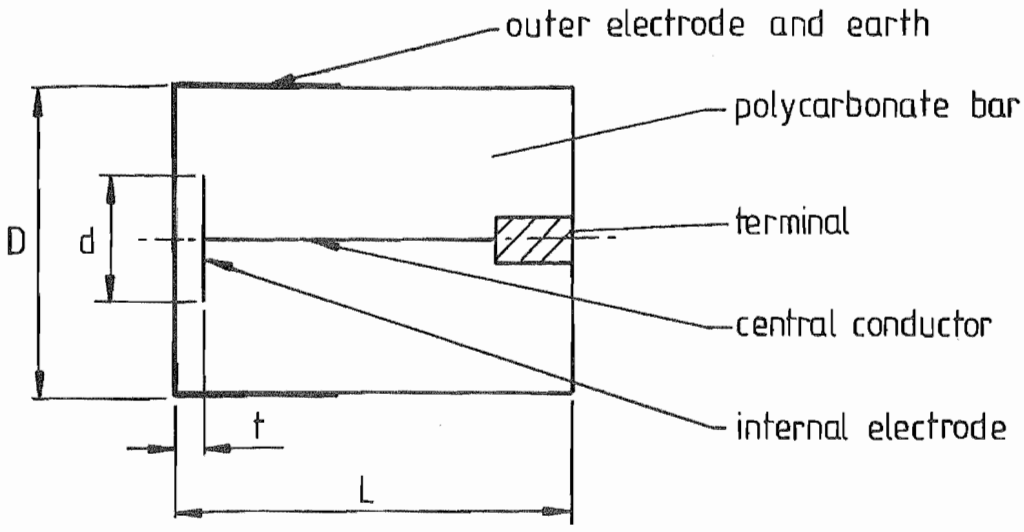

FIG 3·9 BAGANOFF PRESSURE TRANSDUCER [3·11]

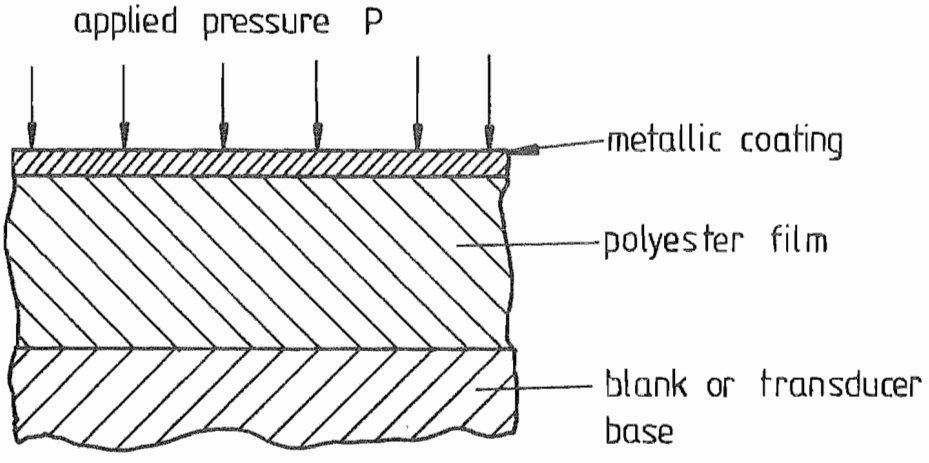

FIG 3·10 MYLAR FILM PRESSURE TRANSDUCER

By suitable adjustment of the capacitance thickness a rise time of 0.1 microseconds was reported in the literature [3.11,3.12]. However because the behaviour of the stress wave was far from an ideal plane stress wave,due to the surface and lateral stress disturbances, the ratio of outer electrode diameter to inner electrode diameter had to be greater than a fixed predetermined value. The ratio of capacitance plate diameters was determined from the disturbance and stress wave velocities and the dimension t. These disturbances were responsible for the limited accurate sequential recording time of the order of 5-10 micro-seconds for the system.

The major operational difficulty with this form of transducer was the short recording duration and the length of transducer required to eliminate the possibility of interference from the stress wave reflection off the free surface at the non-impingement end of the transducer.

An initial experimental investigation was carried out on a film transducer, Fig 3.10 page 106, to determine its sensitivity. The transducer was based upon a commercially available material, Mylar film, which consisted of a synthetic polyester dielectric film with a metallic coating on one surface. On application of pressure, the thickness of the dielectric, and therefore the capacitance of the system changed giving a method of determining the pressure acting.

The major difficulty with this sensory unit was the probability of destruction due to the loading conditions associated with explosive forming. While the gauge had the advantage of being cheap and easily constructed, the calibration would have been difficult and involved considerable time, and therefore the possibility of having to use a new gauge for each shot made it impractical.

3.3.3 PIEZOELECTRIC PRESSURE TRANSDUCER

In certain crystal structures with asymmetric charge distribution, orientated lattice deformation due to applied loads resulted in relative displacement of the positive and negative charges within the lattice. This produced equal external charges of opposite polarity on the crystal faces, in the orientation of the lattice deformation, and hence a potential difference between the relevant crystal surfaces. This phenomenon, called the Piezoelectric effect, has been considered an effective method of pressure history measurement and has been used extensively particularly for large transient pressures because the piezoelectric crystal's high transient response permits accurate detection and delineation of events of micro-second duration [2.70,2.71, 3.13-3.26].

A major advantage of the piezoelectric transducer was that the signal response followed the stress-strain curve of the material in the orientation of the applied load and provided the curve was linear for the operational range, the transducer response was linear with respect to the applied pressure. Also the high frequency limit was imposed by the mechanical resonance of the piezoelectric crystal and mountings, and crystals of 10 Megacycles natural frequency were commercially available.

Typically transducers involving piezoelectric crystals in shock tubes[3.18,3.21,3.22] were of a construction shown in Fig 3.11 page 109. Initially the transducer design [3.18]* was based upon a backing rod of material with a closely matched acoustic impedance to that of the piezoelectric crystal. This was considered to effectively decouple the piezoelectric element by eliminating stress wave reflections from the crystal surfaces,the stress waves instead

*NOTE: Basically an Impact bar transducer -see 3.3.6 page 112.

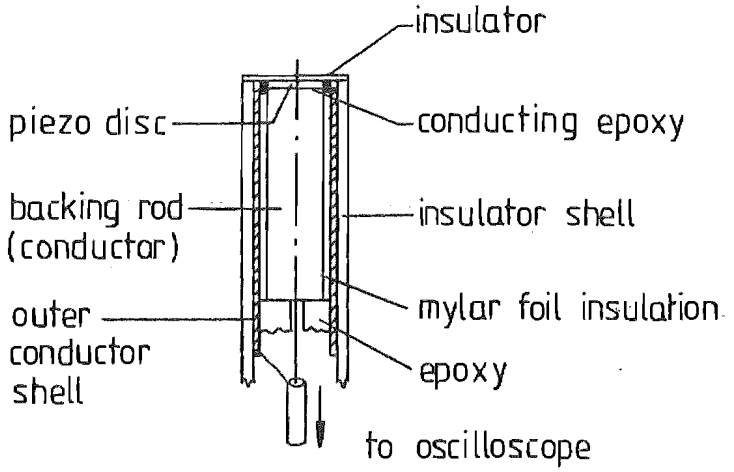

FIG 3·11 PIEZOELECTRIC PRESSURE TRANSDUCER AFTER YORK [3·21]

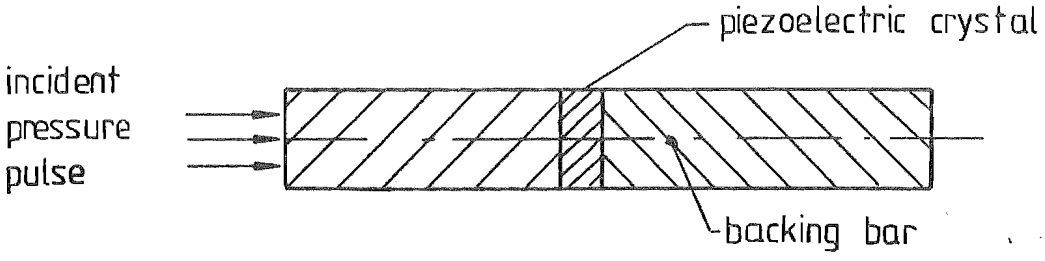

FIG 3·12 MINIATURISED IMPACT BAR TRANSDUCER

being propagated into the backing rod.

Later experimental analysis[3.21] suggested that acoustic impediance matching between the backing rod material and the crystal was not as critical as the ability of the backing rod to dampen out the sympathetic radial oscillations occurring in the piezoelectric crystal due to the passage of the stress wave. Obviously the length of the backing rod was significant in that the length of accurate continuous recording of the incident pressure was determined by the time taken for the stress wave reflected from the free end of the backing rod to impinge on the crystal.

Because of this length problem it was decided that this type of transducer was not satisfactory for use in explosive forming studies. Unfortunately piezoelectric crystals were also sensitive to temperature, vibration and electrical or magnetic noise.

While a piezoelectric crystal could be placed in the energy transfer medium without support or backing the possibility of damage was considerable due to the nature of the loading, given the crystals have high compressive strengths >600 Mn/m but low tensile strengths 80 Mn/m . Attaching the crystal to the blank would cause failure because of the plastic deformation experienced by the workpiece.

3.3.4 MAGNETOSTRICTIVE OR RELUCTANCE PRESSURE MEASUREMENT TECHNIQUES

The operation of the magnetostrictive transducers [3.27] was based upon a pressure induced change in reluctance. The resultant change in inductance of the circuit was then measured and gave a record of the dynamically applied pressure. These transducers usually consisted of a ferromagnetic material subjected to a polarizing magnetic field. The necessity to polarize the transducer

resulted in a bulky arrangement, while the frequency response of such transducers limited the operation to a narrow band width. Also since the measurement was based upon inductance of the circuit, static calibration was impossible.

3.3.5 PIEZORESISTANCE PRESSURE MEASUREMENT TECHNIQUES

Bridgman [3.28,3.29] used the piezoresistance effect of certain metals as a method of measuring high pressures and found that for many metals the resistance change with pressure was effectively linear and could be represented by

$$R = R_o(1 + b\Delta P)$$

where

R = instantaneous resistance
R_o = resistance at one atmosphere
b = pressure coefficient of resistance change
ΔP = incremental pressure change.

Modifications to this technique were carried out [3.30,3.31] to enhance sensitivity and accuracy. However the low sensitivity of the wire-type piezoresistance gauges precluded their use in explosive forming.

With the development of monolithic chip manufacture in the electronics industry, pressure transducers in which a sensory element such as an etched silicon n-type diaphragm, has an arrangement of p-doped regions diffused into the chip were developed [3.32 - 3.34]. Pressure change was monitored by measuring the piezoresistance change in the p-type material.

The change in resistance was not due to the distortion of the gauge geometry as in the previously discussed strain gauge cases, but to the change in the p-type material as a function of the applied strain to th e material. The p-type areas were usually arranged in a four arm Wheatstone bridge circuit and in some commercial transducers [3.33] the signal discrimination, conditioning and temperature compensation circuitry was built into the edge of the sensory element using monolithic thick film methods. Unfortunately the available transdcuers of this type were limited in pressure range and where hence not suitable for explosive forming.

3.3.6 MINATURISED IMPACT BAR PRESSURE MEASUREMENT TECHNIQUES

This pressure measurement system was based upon the Hopkinson Pressure Bar method[3.35].

Ideally a uniform pressure pulse impinging upon one end of a rod created a plane longitudinal stress wave governed by the one-dimensional waves equation [3.36,3.37]*

$$\frac{\partial^2 \sigma_{xx}}{\partial t^2} = C_w^2 \frac{\partial^2 \sigma_{xz}}{\partial x^2}$$

where

$$C_w^2 = \frac{1 - \nu}{(1 + \nu)(1 - 2\nu)} \left(\frac{E}{m}\right)$$

Note: This relationship assumed no dispersion of the longitudinal stress wave. However it has been shown [3.36] that dispersion occurred and hence transverse strain behaviour must be considered in an analytical study. Therefore, for only relatively slow applications of the load does the strain pulse approximate a plane wave.

The amplitude of the resultant stress pulse was directly related, by equilibrium conditions, to the magnitude of the incident pressure.

There were many methods of determining the stress wave in the bar but the most common one was the use of a piezoelectric crystal. This was done by sandwiching the piezoelectric disk in the impact bar; as the stress pulse traversed the crystal a charge was generated at the respective disk faces and the pressure determined. Care was taken at the crystal-impact bar faces to ensure no spurious stress wave reflections occurred, by matching the acoustic impediance of the bar to that of the piezoelectric crystal.

The rise-time and frequency range of the gauge were limited by the dimensions and material, which determined the dynamic characteristics of the impact bar. The disadvantages of this type of transducer were the deviation of the stress pulse from the ideal plane wave due to the surface and lateral stress wave disturbances and the length of time of sequential recording. The time of sequential recording of the pressure wave was determined by the time taken for reflected stress disturbances off the free end surface of the bar to reach the piezoelectric sensory element. Thus the required length of the bar was determined as a function of the velocity of wave propagation and the total time of the event to be recorded.

A typical transducer is shown in Fig 3.12 page 109.

Much work has been done to overcome these difficulties [3.36,3.38 - 3.40] either by variations in bar material, bar dimensions and/or sensory elements. The problem of length and reflected tension waves has been reduced by use of a tapered bar to transmit the incident compressive pulse into absorbent medium[3.41].

It was obvious that because of the required length of the transducer and the resulting mounting problem, this method of gauging was not suitable for energy transfer study in explosive forming.

3.3.7 MISCELLANEOUS PRESSURE MEASUREMENT TECHNIQUES

These processes involved the use of techniques which took advantage of the pressure sensitivity of a range of components and materials not normally considered to lie within the general grouping of pressure measurement techniques discussed so far.

3.3.7.1 DIODE TRANSDUCER Sikorski et al[3.42] showed that a tunnel diode in the ampification mode, with a suitable stabilising shunt resitance could be satisfactorily used as a pressure transducer.

The idealised characteristics of a tunnel diode in the amplifier mode is shown if Fig 3.13 page 115,and with the associated resultant effect of the pressure on the idealised characteristics. It can be seen that by selecting the value of bias current and shunt resistance, the operating point could be adjusted to give either maximum sensitivity for either a small range about a given pressure point or for a wide pressure range.

Sikorski et al claimed that 'the advantages of the tunnel diode transducers were (1) small size, (2) sensitivity, and (3) versatility.' The significant advantage of the high sensitivity was the low to moderate amplification required, with the resultant advantages of reduction in spurious noise signals, as well as a higher frequency band width. As has been explained[2.70] the small size meant satisfactory rise-times ,minor interference by the transducer on the shock wave form and the probability of being able to locate the sensory element in the region of interest immediately adjacent to the blank surface.

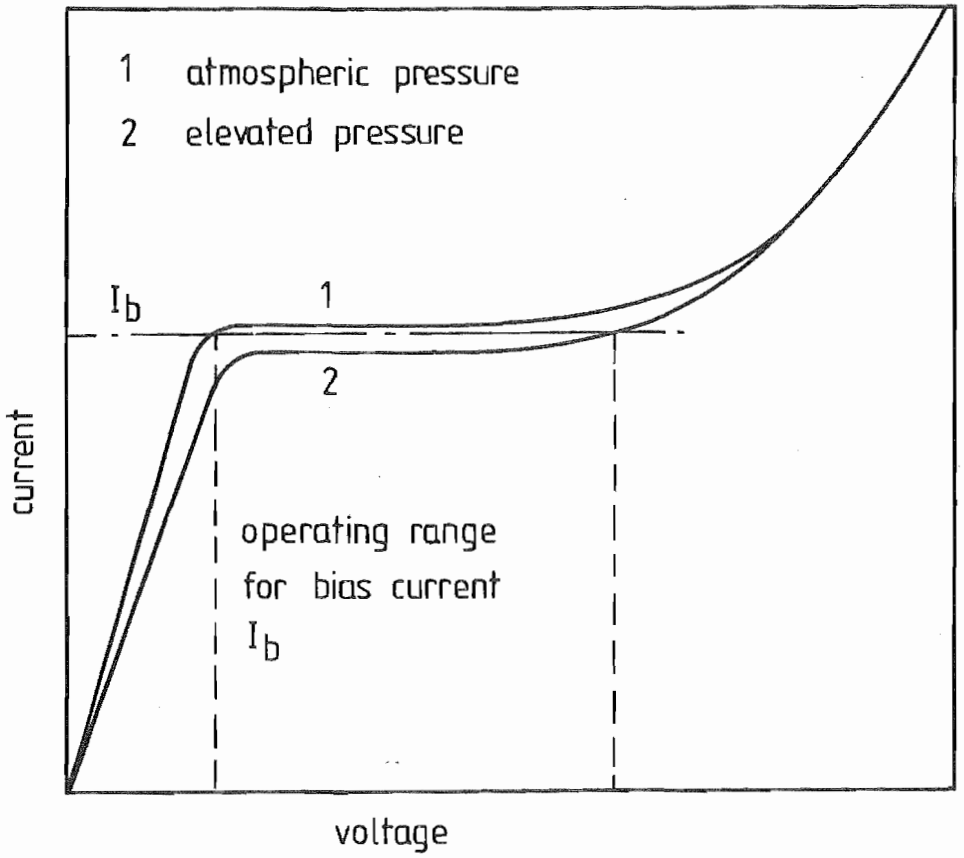

FIG 3·13 TUNNEL DIODE TRANSDUCER SHOWING IDEALISED CURRENT VOLTAGE CURVES FOR TUNNEL DIODE AND RESISTOR IN PARALLEL AFTER SIKOSKI [3·42]

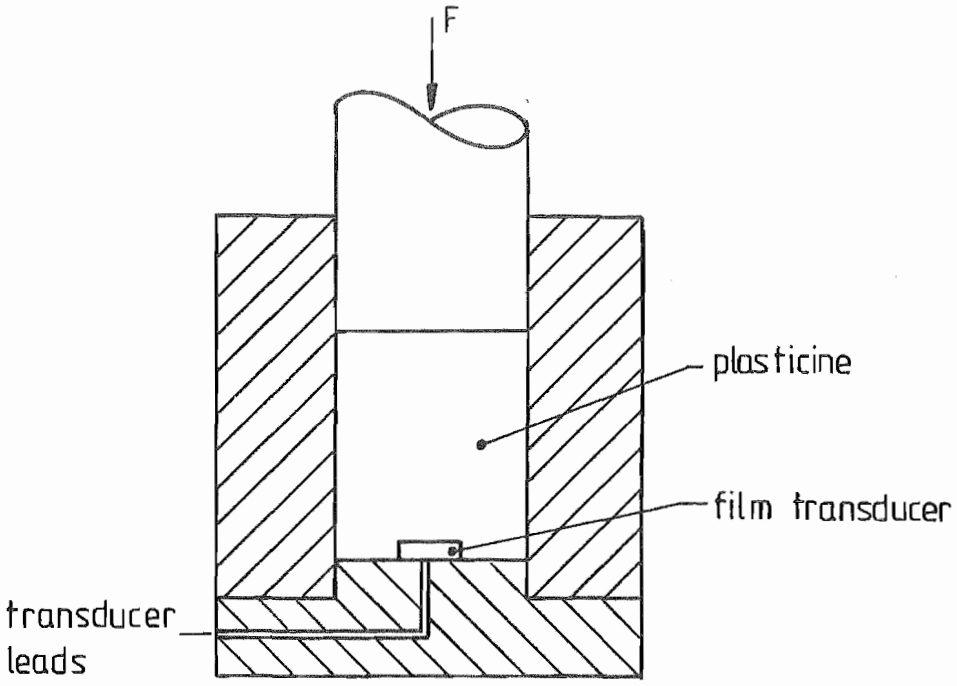

FIG 3·14 STATIC PRESSURE TEST RIG

The problem, which has been discussed by Cohen et al[3.43] was that of temperature sensitivity of the tunnel diode which they suggested could be minimised by the selection of a suitable operating point.

Wlodarski et al[3.44] reported on a study into the use of diode semiconductor devices to monitor rapidly varying pressures. The operating point was selected to minimise the temperature effects and two semiconductor types, silicon and gallium arsenide, were studied. Testing was carried out for both static and dynamic pressure loading and in the case of dynamic pressure loading a comparison of pressure measurement was obtained with a commercially available quartz crystal piezoelectric transducer. A satisfactory sensitivity was obtained in the static testing while good agreement between the diodes and the quartz transducer was obtained for the dynamic testing with differences of less than 1.5% for silicon and less than 5% for gallium arsenide.

3.3.7.2 TRANSISTOR TRANSDUCER Transistors as a pressure sensitive element were used by Sikorski et al[3.45] as the basis of a microphone. This would have given a cheap small and sensitive pressure transducer similar to the tunnel diode, by use of a suitable operating point on the characteristic.

3.3.7.3 CARBON RESISTOR TRANSDUCER The piezo-resistance behaviour of carbon resistors was sufficient to enable them to be mounted in a polyethylene rod and used by Watson [3.46] to determine the pressures associated with shock, blast and detonation waves. Further study into the piezo-resistance characteristics of five commercially available resistors of 1000ohms, in the range of 0-500psi.(3.4 MPa.) by Miller et al[3.47] gave a repeatability of better than 1%. On less accurate tests of up to 2,000 psi. (13.8 MPa.) these resistors still exhibited linear pressure response.

Some dynamic testing of up to 1 Kc. was carried out to compare the recordings with that of a commmercial pressure transducer and agreement was obtained.

This suggested that the linearity, a sensitivity of 1.5 - 0.55×10^{-5} $(\Delta R/R)(1/\Delta P)$,availability and the low cost could make the commercial carbon composition resistor a pressure transducer for both static and dynamic pressure measurement. The only apparent disadvantage was the temperature sensitivity of the carbon resistor.

Stankiewicz et al[3.48] described experiments carried out on commercially available carbon resistors for a range of pressures up to 11 Kilobars (1111.4 MPa.) and for temperatures of 295,77 and 4.2 K and found that while the pressure dependent variation of the resistance was non-linear the results were repeatable. It was noted that the resistors showed hysteresis effects on the removal of the pressure.

3.3.7.4 INTERMETALLIC RESIN TRANSDUCER Clark [3.49] showed that use could be made of resins processed with Zirconium Tetra-Chloride as pressure transducers because of the large change in electrical resistance exhibited when subjected to pressure. Because the resins could be applied as paints on to conducting surfaces it was obviously a versatile material for pressure measurement.

The advantages claimed for these resins were high sensitivity, simple construction of transducers and possible measurement of a wide range of pressure. The apparent disadvantages were those of hysteresis of up to 2% and poor dynamic response although by preloading the hysteresis was reduced. Another disadvantage was that of a non-linear pressure response.

3.3.7.5 RUBBER RESISTIVE TRANSDUCER As for the intermetallic resins, Massey et al[3.50] used a conductive rubber which underwent a change of resistance under compression. Unfortunately while the type of transducer described was sensitive, cheap and small it had a limited pressure range.

3.4 CALIBRATION

The pressure measurement system calibration was considered in two stages ;(1) static calibration and (2) dynamic calibration.

While it was recognised that the mode of operation of the system was critically dependent upon the dynamic characteristics of the proposed pressure transducer, it was considered that static calibration was significant in the preliminary work with the transducer, particularly with respect to sensitivity. This was because of the difficulty in achieving a repeatable, accurately defined, pressure pulse of the magnitude and rise times associated with explosive forming.

3.4.1 STATIC CALIBRATION The static calibration was necessary to determine the pressure response of the transducer throughout the operating range as well as determining the deviation from linearity within this range. Dead weight testing was the most appropriate equipment to do the static pressure calibration, but for the proposed range this was not feasible on the existing equipment in the Department. The initial investigation into the film capacitance transducer was conducted on the Amsler Compression machine Serial No 79/119 using a rig shown in Fig. 3.14 page 115.

The frictional error which was inherent in such a loading rig, when the pressure was measured as force per unit area was overcome by the method developed by King[3.51] with repeated cycling of the applied load about the theoretical value required, with a diminishing amplitude of piston displacement. In King's experiments the total frictional error was reduced to 1.4% of the applied pressure which was acceptable accuracy. Hence as an initial method of static calibration it was considered that this would be a satisfactory method during the development stage of the pressure transducer.

3.4.2 DYNAMIC CALIBRATION As can be seen from the authoritative review of dynamic pressure calibration[3.52], there was considerable difficulty in achieving an aperiodic dynamic calibration system with a risetime of the order of microseconds and the required pressure amplitude of 200 Mpa. While gas shock tubes give the required risetime, to obtain the required pressure amplitude, with this risetime, would have involved the development of an appropriate shock tube facility in the department which was not feasible. The alternative use of a periodic pressure generator[3.52] would not have achieved the necessary risetime.

It was considered that a technique of dynamic calibration of the pressure measurement system based upon the existing[2.70] theories of energy propagation from explosives detonated underwater would have been feasible. Since many theoretical and experimental investigations[2.20] have been conducted upon this phenomenon, it was considered that the use of an explosive charge underwater with the transducer located in the region, for which information was available would approach the requirement of a repeatable pressure pulse, similar to that anticipated during the explosive forming, to the accuracy specified.

3.5 PRESSURE TRANSDUCER

The requirements of high frequency and low risetimes limited the range of pressure transducers suitable for explosive forming research to the capacitance and piezoelectric types.

Initial investigations were carried out into the development of a film capacitance transducer, section 3.3.2, page 104, based upon Mylar's film. Lack of sensitivity and the delicate nature of the sensory element made this impractical for use in explosive forming. Other possible designs of the transducers considered were those in Fig. 3.15 page 121, for a capacitance transducer or Fig. 3.16 page 121, for a plate/foundation capacitance or piezo electric transducer. A capacitance transducer was chosen in preference to a piezoelectric transducer because it would be less sensitive to noise and spurious signals due to the stress waves generated in the sensory element, particularly those in the radial direction.

To ensure that the sensitivity of the transducer was adequate to delineate the reloading phase, it was decided to assume the initial pressure pulse would take the plate or plate/foundation combination into the geometrically non-linear deflection regime. Because of the difficulty associated with dynamic calibration and the assumption that operating in the non-linear deflection region would enhance the sensitivity in the reloading phase, numerical modelling of the proposed transducer behaviour was carried out, Chapter Four to Chapter Seven, for both the plate and plate/foundation systems.

An advantage of the plate transducer was that the major transverse stress waves which would be associated with the sensory element would have a frequency of $f_p = c_o/h$ where c_o was the velocity of sound in the plate and if h was sufficiently small the resultant effects of the stress waves could be filtered out. The disadvantage was that the natural frequency of the plate [3.53] was given by

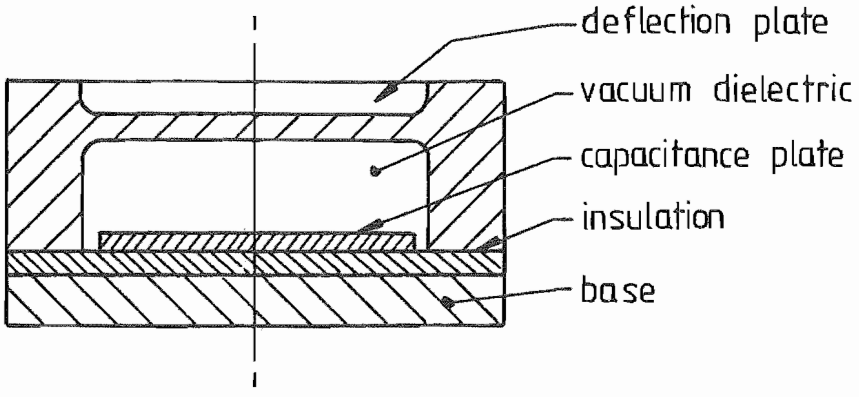

FIG 3·15 CAPACITANCE PRESSURE TRANSDUCER

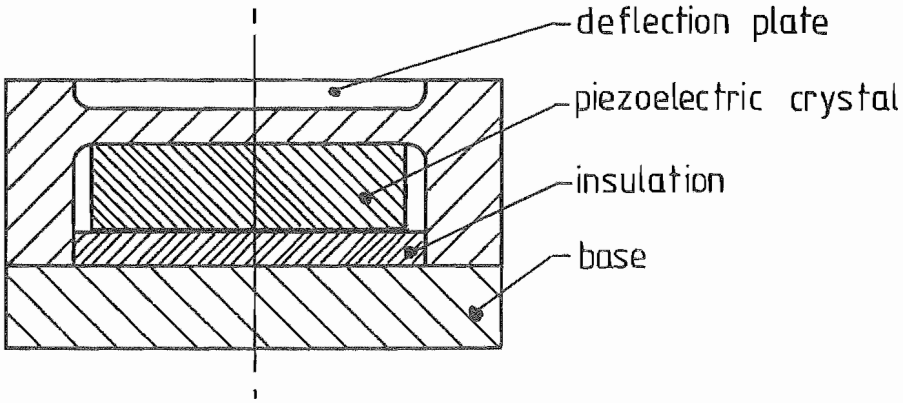

FIG 3·16 PIEZOELECTRIC PRESSURE TRANSDUCER

$$f_p = \frac{(3.196)^2 \sqrt{E}}{4\pi \sqrt{3m(1 - \nu^2)}} \left(\frac{h}{a^2}\right)$$

where a = plate radius
m = plate density
E = modulus of elasticity
ν = poisson's ratio

Therefore the plate thickness to radius ratio was a compromise between sensitivity, natural frequency and stress wave effects.

While the plate/foundation system would introduce stress waves which would be a function of the plate, foundation and base thickness and material density, the resultant natural frequency would be given by [3.53].

$$\frac{f_f}{f_p} = \left(1 + \frac{k}{D} \left(\frac{a}{3.196}\right)^4\right)^{\frac{1}{2}}$$

where k = Winkler foundation modulus
f_p = Plate frequency
f_f = Plate/foundation frequency
D = Plate flexural rigidity

$$= \frac{Eh^3}{12(1 - \nu^2)}$$

and hence increased as a function of the foundation modulus.

The design of the plate/foundation transducer was such that either a capacitance or piezoelectric transducer could be produced depending on the foundation used. Therefore the major factor influencing the initial dimensions was the commercial availability of PZT - 5A style F piezoelectric crystals with a 4.8 mm diameter and 0.3 mm thickness. These crystal dimensions gave the maximum possible parallel resonant frequency of the order of 6 MHz.

Following York [3.21] the transducer material was stainless steel with the following properties:

Density	= 7769 Kgm/m
Elastic modulus	= 196 GN/m
Poisson's ratio	= 0.3
Elastic limit	= 240 Mn/m

while the physical properties of the piezo electric materials were

Density	= 7600 Kgm/m^3
Elastic modulus (E_c^{33})*	= 52.9 GN/m^2
Poisson's ratio	= 0.3
Compressive strength	> 600 MN/m^2
Tensile strength	≈ 80 MN/m^2

Given that the transducer height was 5 mm and the speed of sound c in the stainless steel was 5020 m/sec ie $(E/m)^{\frac{1}{2}}$ the period for a stress wave to propogate to the blank/transducer interface was 1 μsec. Therefore high frequency contributions from the stress wave would limit the frequency range of the resultant transducer and filtering would be required. Although the speed of sound in the PZT - 5A was 2620 m/sec the multiple interfaces would give stress wave periods of 0.11 μsec as well as rapid attenuation due to the interface friction.

Since the transducer had to be able to include a piezoelectric crystal of radius 2.4 mm the minimum plate radius considered was 2.75 mm. Therefore a non-dimensional geometrical non-linear dynamic analysis was carried out to determine the transducer performance.

*Note: Because of the directionality of the properties of a piezoelectric crystal the superscript 33 represents the property normal to the plane of the disc.

3.5.1 TRANSDUCER OUTPUT

The potential difference between two parallel plates in a capacitor was given by [3.54]

$$v = \int_{o}^{t_c} \varepsilon_c \, dx = \varepsilon_c \, t_c$$

where t_c = plate separation

ε_c = field strength between plates

$= \sigma^*/\varepsilon_o \, \varepsilon_r$

ε_o = permittivity of free space

ε_r = relative permittivity of air/dielectric

and therefore

$$q_c = \sigma^* A_t$$

where A_t = area of plate giving

$$C = q_c/v$$

$$= \varepsilon_o \varepsilon_r \, A/t$$

for q_c = charge in coulombs.

Consideration of the plate deflection under a constant change condition resulted in a change in voltage as a function of the change in capacitance. The average separation of the plates would determine the voltage and was given by

$$t_{av} = \frac{1}{A_t} \int_{o}^{A_t} (t_c - a\alpha(\rho)) dA$$

$$= t_c - \frac{a}{A_t} \int_{o}^{A_t} \alpha(\rho) dA$$

where $\alpha(\rho)$ = deflection of plate.

Therefore the voltage change was

$$\Delta v = \varepsilon_c t_c - \varepsilon_c (t_c - \frac{a}{A_t} \int^{A_t} \alpha(\rho) dA)$$

$$= \frac{\varepsilon_c}{A_t} a \int^{A_t} \alpha(\rho) dA$$

Similarly by ignoring radial deflection after York, to the first order of accuracy ,the output from the piezoelectric crystal was proportional to the integral

$$\Delta v \ \alpha \ \int^{A_t} \alpha(\rho) dA$$

Hence the required information to describe the transducer performance was the integral $\int^{A_t} \alpha(\rho) dA$

For capacitance transducers, to ensure a uniform electrostatic field, an external ring can be used and would be maintained at a constant charge, Fig. 7.17, page 126 . Therefore calculations were also carried out to derive the integral $\int^{A_g} \alpha(\rho) dA$ where $A_g = 0.64\ A_t$.

For the reasons given above, a theoretical study was conducted into the response of proposed pressure transducers, Figs. 5.15 - 5.17.

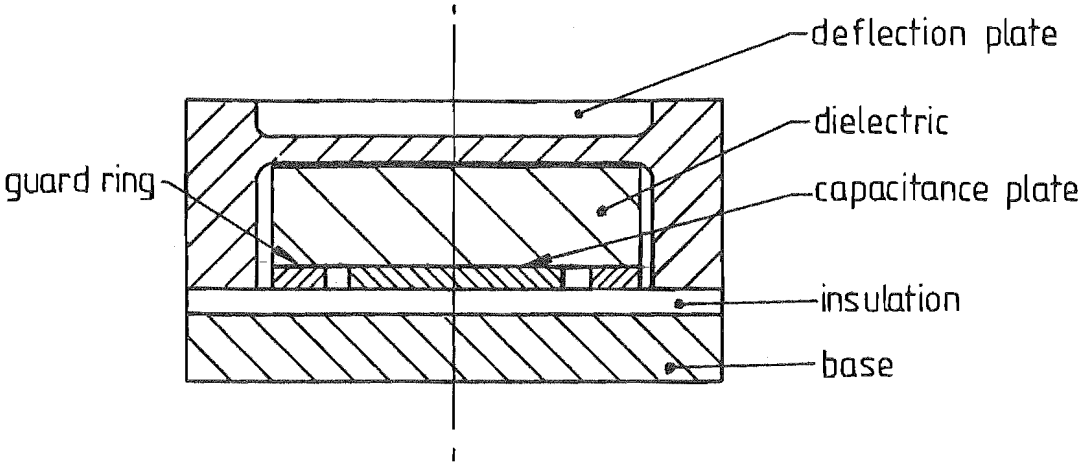

FIG 3·17 CAPACITANCE PRESSURE TRANSDUCER WITH GUARD RING

CHAPTER FOUR

ANALYSIS OF PRESSURE TRANSDUCER.

4.1 INTRODUCTION

Since the proposed pressure transducer would operate in a non-linear regime it was considered necessary to model its behaviour. This analysis was carried out in three stages. The first stage involved the static non-linear analysis of a plate on an elastic foundation. A comparision was made between the methods of representing the dielectric crystal behaviour,either as a linear Winkler[4.1] foundation characteristic,or as a Pasternak foundation characteristic[4.1] in the static analysis. Next, the non-linear dynamic transient response of the plate and the plate on an elastic foundation was considered. This gave a model of the response of the proposed pressure transducer to pressure pulse typical of a shock wave.

4.2 ASSUMPTIONS

The assumptions used in deriving the equations governing the non-linear behaviour of the pressure transducer were as follows:

(1) The plate material was perfectly elastic and obeyed Hooke's law.
(2) The plate material was isotropic and homogenous.
(3) The normals to the middle surface or plate meridan remained straight and normal to that surface after deformation.
(4) The plate was initially flat and of uniform

thickness.

(5) The load and deformation of the plate was axisymmetric.

(6) The normal stresses in the transverse direction were negligible.

(7) The slopes produced by flexure were moderately large but small in comparison with unity, and hence could be neglected and represented by $\frac{\partial w}{\partial r} = \psi$.

(8) The curvature of the plate meridian or bending axis could be represented by $\frac{\partial^2 w}{\partial r^2}$.

(9) The external forces acting on the plate were normal to the plate surface.

(10) The structural damping within the foundation and the plate/foundation interface could be represented by viscous damping.

(11) The foundation material was perfectly elastic, isotropic and homogenous.

(12) The foundation reactions were transmitted normal to the plate/foundation interface.

(13) Shear stresses could not be transmitted across the plate/foundation interface as the coefficient of friction was taken as zero.

(14) The density of the foundation material was significantly less than that of the plate material, and therefore in the dynamic analysis, the inertia term for the foundation was ignored.

(15) The foundation had a finite thickness and was supported by a rigid base

4.3 EQUATIONS GOVERNING PRESSURE TRANSDUCER BEHAVIOUR.

The derivation of the equations governing the non-linear behaviour of a plate supported by an elastic foundation was based on the above assumptions and consideration of the element Fig 4.1 page 130.

Taking moments in the r-z plane about the centre gave

$$(M_r + \frac{\partial M_r}{\partial r}\delta r)(r + \delta r)\delta\phi - M_r\, r\,\delta\phi - M_t\delta r\delta\phi + (Q + \frac{\partial Q}{\partial r}\delta r)(r + \delta r)\delta\phi\,\frac{\delta r}{2}$$
$$+ Qr\delta\phi\frac{\delta r}{2} + \frac{\partial w}{\partial r}(N_r + \frac{\partial N_r}{\partial r}\delta r)(r + \delta r)\delta\phi - N_r r\delta\phi \quad = \quad 0 \qquad 4.1$$

where M_r = Radial bending moment/unit length of circumference

$$= -D(\frac{\partial^2 w}{\partial r^2} + \frac{\nu}{r}\frac{\partial w}{\partial r})$$

M_t = Tangential bending moment/unit length of radius

$$= -D(\frac{1}{r}\frac{\partial w}{\partial r} + \nu\frac{\partial^2 w}{\partial r^2})$$

Q = Shear stress/unit length of circumference

N_r = Radial membrane force/unit length of circumference

$$= \frac{Eh^2}{1-\nu^2}(\frac{\partial u}{\partial r} + \frac{1}{2}(\frac{\partial w}{\partial r})^2 + \nu\frac{u}{r})$$

D = Flexural rigidity or plate stiffness

$$= \frac{Eh^3}{12(1-\nu^2)}$$

ν = Poisson's ratio for plate material

E = Modulus of elasticity for plate material

h = Plate thickness

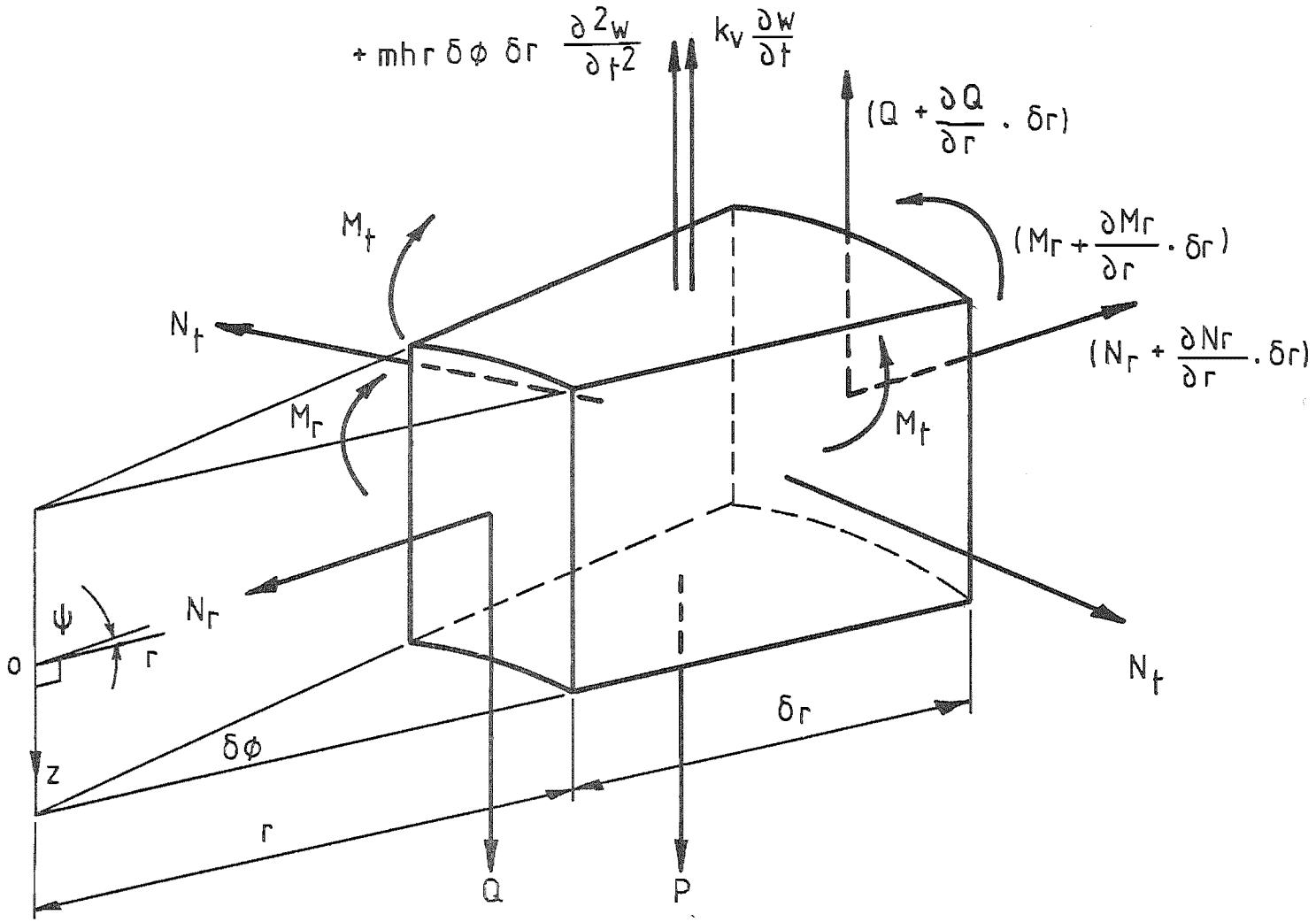

FIG 4·1 BENDING AND MEMBRANE STRESSES ACTING ON A PLATE ELEMENT SUBJECT TO DYNAMIC LOADING AND VISCOUS DAMPING

w = Vertical deflection

u = Radial deflection

r = Radius

$\frac{\partial w}{\partial r}$ = Slope.

Hence ignoring second order moments over the length of the element δr , the equation is reduced to

$$M_r + r\frac{\partial M_r}{\partial r} - M_t + N_r \frac{\partial w}{\partial r} r + Qr = 0 \qquad 4.2$$

Considering the transverse equilibrium and allowing for inertia after D'Alembert and viscous damping of the plate under the dynamic transient loading, the following equation is obtained for the shear stress.

$$Q = \frac{1}{r} \int_o^r (q(r,t) - mh \frac{\partial^2 w}{\partial t^2} - k_v \frac{\partial w}{\partial t} - F(w)) r.dr \qquad 4.3$$

where $q(r,t)$ = Load intensity

$F(w)$ = Foundation reaction

m = Density of the plate

k = Viscous damping coefficient of the plate as a function of vertical deflection.

t = Time

Therefore substituting for Q, M_r and M_t the equation 4.3 became

$$\frac{\partial^3 w}{\partial r^3} + \frac{1}{r}\frac{\partial^2 w}{\partial r^2} - \frac{1}{r^2}\frac{\partial w}{\partial r} - \frac{N_r}{D}\frac{\partial w}{\partial r} + \frac{1}{rD}\int_o^r (q(r,t) - mh \frac{\partial^2 w}{\partial t^2}$$

$$- k_v \frac{\partial w}{\partial t} - F(w)) r \, dr = 0 \qquad 4.4$$

Also considering the radial equilibrium for the element, Fig 4.1 page 130, and ignoring the radial inertia and damping, the

following relationship can be obtained.

$$(N_r + \frac{\partial N_r}{\partial r}\delta r)(r + \delta r)\delta\phi - N_r\, r\delta\phi - 2N_t\delta\phi\,\frac{\delta r}{2} = 0 \qquad 4.5$$

where N_t = Tangential membrane force/unit length of radius.

$$= \frac{Eh}{1-\nu^2}\left(\frac{u}{r} + \nu\frac{\partial u}{\partial r} + \frac{\nu}{2}\left(\frac{\partial w}{\partial r}\right)^2\right)$$

Again ignoring the second order terms the relationship gave

$$r\frac{\partial N_r}{\partial r} + N_r - N_t = 0 \qquad 4.6$$

which substituting for N_r and N_t became

$$\frac{\partial^2 u}{\partial r^2} + \frac{1}{r}\frac{\partial u}{\partial r} - \frac{u}{r^2} + \frac{\partial w}{\partial r}\cdot\frac{\partial^2 w}{\partial r^2} + \frac{(1-\nu)}{2r}\left(\frac{\partial w}{\partial r}\right)^2 = 0 \qquad 4.7$$

The integral term was removed from equation 4.4 by differentiation and resubstitution to give,

$$\frac{\partial^4 w}{\partial r^4} + \frac{2}{r}\frac{\partial^3 w}{\partial r^3} - \frac{1}{r^2}\frac{\partial^2 w}{\partial r^2} + \frac{1}{r^3}\frac{\partial w}{\partial r}$$

$$= \frac{1}{D}\left(\frac{\partial^2 w}{\partial r^2}N_r + \frac{\partial w}{\partial r}\frac{\partial N_r}{\partial r} + \frac{1}{r}\frac{\partial w}{\partial r}N_r + q(r,t) - mh\frac{\partial^2 w}{\partial t^2} - k_v\frac{\partial w}{\partial t} - F(w)\right) \qquad 4.8$$

Hence equations 4.4 and 4.8 govern the dynamic behaviour of a plate under conditions satisfying the given assumptions. The resultant relationships are a dynamic analogue to the von Karman equations governing the non-linear behaviour of a circular plate, as have been used by Nowinski[4.2] and Huang[4.3] in vibration analysis.

Substitution with equation 4.6 gave an alternative form

$$\nabla^4 w = \frac{1}{D}\left(\frac{\partial^2 w}{\partial r^2}N_r + \frac{1}{r}\frac{\partial w}{\partial r}N_t + q(r,t) - mh\frac{\partial^2 w}{\partial t^2}\right.$$

$$\left. - k_v\frac{\partial w}{\partial t} - F(w)\right) \qquad 4.9$$

where ∇^4 was the biharmonic operator and was equivalent to

$$\left(\frac{\partial^4}{\partial r^4} + \frac{2}{r}\frac{\partial^3}{\partial r^3} - \frac{1}{r^2}\frac{\partial^2}{\partial r^2} + \frac{1}{r^3}\frac{\partial}{\partial r}\right)$$

By eliminating the radial displacement from the relationship for the membrane forces and applying Hooke's law, the compatibility equation

$$\frac{\partial(N_t + N_r)}{\partial r} = -\frac{Eh}{2r}\left(\frac{\partial w}{\partial r}\right)^2 \qquad 4.10$$

can be obtained.

Hence the equations governing the dynamic non-linear deflections of a plate were

$$\nabla^4 w = \frac{1}{D}\left(\left(\frac{\partial^2 w}{\partial r^2} + \frac{1}{r}\frac{\partial w}{\partial r}\right)\frac{Eh}{1-\nu^2}\left(\frac{\partial u}{\partial r} + \frac{1}{2}\left(\frac{\partial w}{\partial r}\right)^2 + \frac{\nu u}{r}\right)\right.$$

$$+ \frac{\partial w}{\partial r}\frac{Eh}{1-\nu^2}\left(\frac{\partial^2 u}{\partial r^2} + \frac{\nu}{r}\frac{\partial u}{\partial r} - \frac{\nu}{r^2}u + \frac{\partial w}{\partial r}\frac{\partial^2 w}{\partial r^2}\right)$$

$$\left. + q(r,t) - mh\frac{\partial^2 w}{\partial t^2} - k_v\frac{\partial w}{\partial t} - F(w)\right) \qquad 4.11$$

$$\frac{\partial^2 u}{\partial r^2} + \frac{1}{r}\frac{\partial u}{\partial r} - \frac{u}{r^2} + \frac{\partial w}{\partial r}\frac{\partial^2 w}{\partial r^2} + \frac{1-\nu}{2r}\left(\frac{\partial w}{\partial r}\right)^2 = 0 \qquad 4.12$$

4.3.1 DYNAMIC TRANSIENT RESPONSE FOR PLATE AND FOUNDATION

The relationships governing the non-linear dynamic transient response of the pressure transducer is given by equations 4.11 and 4.12

These equations describe the non-linear behaviour of a plate in contact with an elastic foundation. The reaction of the foundation was described by either the Winkler[4.1] relationship.

$$F(w) = k_f w \qquad 4.13$$

where k_f = Modulus of the foundation reaction if the foundation was considered to be linear, or following Pasternak [4.1] by

$$F(w) = k_f w - G\bar{\nabla}^2 w \qquad 4.14$$

where G = Pasternak Foundation Constant

$$\bar{\nabla}^2 = \left(\frac{\partial^2}{\partial r^2} + \frac{1}{r}\frac{\partial}{\partial r}\right)$$

The non-dimensional form of these relationships was obtained as follows

$$\nabla^4\alpha - G^*\nabla^2\alpha + k^*\alpha = \frac{\varepsilon(\rho,\tau)}{\delta} - \frac{\partial^2\alpha}{\partial\tau^2} - \chi\frac{\partial\alpha}{\partial\tau}$$

$$+ 12\delta^2\left(\frac{\partial\zeta}{\partial\rho} + \frac{1}{2}\left(\frac{\partial\alpha}{\partial\rho}\right)^2 + \nu\frac{\zeta}{\rho}\right)\nabla^2\alpha + 12\delta^2\frac{\partial\alpha}{\partial\rho}\cdot$$

$$\left(\frac{\partial^2\zeta}{\partial\rho^2} + \frac{\nu}{\rho}\frac{\partial\zeta}{\partial\rho} - \frac{\nu}{\rho^2}\zeta + \frac{\partial\alpha}{\partial\rho}\frac{\partial^2\alpha}{\partial\rho^2}\right) \qquad 4.15$$

$$\frac{\partial^2\zeta}{\partial\rho^2} + \frac{1}{\rho}\frac{\partial\zeta}{\partial\rho} - \frac{\zeta}{\rho^2} + \frac{\partial\alpha}{\partial\rho}\frac{\partial^2\alpha}{\partial\rho^2} + \frac{1}{2\rho}\left(\frac{\partial\alpha}{\partial\rho}\right)^2(1-\nu) = 0 \qquad 4.16$$

where $\alpha = w/a$ Vertical displacement parameter

$\rho = r/a$ Radial parameter

$\zeta = u/a$ Radial displacement parameter

$\delta = a/h$ Radius to thickness ratio

$\varepsilon(r,t) = \dfrac{q(r,t)\,a^4}{Eh^4}\,12(1-\nu^2)$

= Load parameter.

$\tau = t.\left(\dfrac{D}{mha^4}\right)^{\frac{1}{2}}$

= Time parameter

$\chi = k_v.\left(\dfrac{mha^4}{D}\right)^{\frac{1}{2}}$

= Vertical Damping parameter

$G^* = G.(\frac{a^2}{D})$

= Non-dimensional Pasternak foundation constant

$k^* = k_f.(\frac{a^4}{D})$

= Non-dimensional Winkler foundation constant

$\nabla^2 = (\frac{\partial^2}{\partial\rho^2} + \frac{1}{\rho}\frac{\partial}{\partial\rho})$, $\nabla^4 = \nabla^2\,\nabla^2$

It should be noted that the Winkler foundation is the limiting case when $G^* = 0$.

4.3.2 STATIC DEFLECTION FOR PLATE ON ELASTIC FOUNDATION.

Also of interest was the static form of the equations which was

$$\nabla^4\alpha - G^*\nabla^2\alpha + k^*\alpha = \frac{\varepsilon}{\delta} + 12\delta^2(\frac{d\zeta}{d\rho} + \frac{1}{2}(\frac{d\alpha}{d\rho})^2 + \frac{\zeta}{\rho})$$

$$+ 12\delta^2\,(\frac{d\alpha}{d\rho})(\frac{d^2\zeta}{d\rho^2} + \frac{\nu}{\rho}\frac{d\zeta}{d\rho} - \frac{\nu}{\rho^2}\zeta + \frac{d\alpha}{d\rho}\frac{d^2\alpha}{d\rho^2}) \qquad 4.17$$

$$\frac{d^2\zeta}{d\rho^2} + \frac{1}{\rho}\frac{d\zeta}{d\rho} - \frac{\zeta}{\rho^2} + \frac{d\alpha}{d\rho}\frac{d^2\alpha}{d\rho^2} + \frac{1}{2\rho}(\frac{d\alpha}{d\rho})^2(1-\nu) = 0 \qquad 4.18$$

4.4 BOUNDARY CONDITIONS

The solution was obtained for the fixed edge condition because this gave the idealised boundary condition which best approximated the proposed transducer.

4.4.1 OUTER SPACE BOUNDARY

At the outer boundary, $\rho=1$, the following conditions were associated with the fixed edge condition:

$$(\alpha)_{\rho=1} = 0 \qquad 4.19$$

$$\left(\frac{\partial\alpha}{\partial\rho}\right)_{\rho=1} = 0 \qquad 4.20$$

$$(\zeta)_{\rho=1} = 0 \qquad 4.21$$

4.4.2 INNER SPACE BOUNDARY

At the inner boundary, $\rho=0$, the following conditions apply;

$$\left(\frac{\partial\alpha}{\partial\rho}\right)_{\rho=0} = 0 \qquad \text{Symmetry} \qquad 4.22$$

$$\zeta(o,\tau) = 0 \qquad \text{Continuity} \qquad 4.23$$

At the centre, equation 4.5 became singular but the physical system implied that a relationship existed for the condition $\rho=0$

Applying L'Hopital's rule to a term $\left(\frac{1}{\rho}\frac{\partial\alpha}{\partial\rho}\right)$ gave the limit

$$\text{Limit}_{\rho \to 0} \left(\frac{1}{\rho}\frac{\partial\alpha}{\partial\rho}\right) = \left(\frac{\partial^2\alpha}{\partial\rho^2}\right)_{\rho=0} \qquad 4.24$$

and hence the term $(\frac{1}{\rho^3}\frac{\partial\alpha}{\partial\rho})$ became $(\frac{1}{\rho^2}\frac{\partial^2\alpha}{\partial\rho^2})_{\rho=0}$

Considering the boundary condition equation 4.22, the physical system, and the form of the "exact" solution by Way[4.4] for the static case, it was assumed that the solution for the vertical deflection could be represented by a symmetric function of the vertical deflection α with respect to the radius.

Therefore $$(\frac{\partial^3\alpha}{\partial\rho^3})_{\rho=0} = 0 \qquad 4.25$$

and by applying L'Hopital to the term $(\frac{1}{\rho} \cdot \frac{\partial^3\alpha}{\partial\rho^3})$ was

$$\text{Limit}_{\rho \to 0} (\frac{1}{\rho}\frac{\partial^3\alpha}{\partial\rho^3}) = (\frac{\partial^4\alpha}{\partial\rho^4})_{\rho=0} \qquad 4.26$$

Finally considering the term $(\frac{\zeta}{\rho})$,

application of L'Hopital rule gave,

$$\text{Limit}_{\rho \to 0} (\frac{\zeta}{\rho}) = (\frac{\partial\zeta}{\partial\rho})_{\rho=0} \qquad 4.27$$

Substitution of the equations 4.24, 4.25 and 4.26 into the equation 4.15 gave the equation

$$3\frac{\partial^4\alpha}{\partial\rho^4} - 2G^*\frac{\partial^2\alpha}{\partial\rho^2} + k^*\alpha = \frac{\varepsilon}{\delta} - \frac{\partial^2\alpha}{\partial\tau^2} - \chi\frac{\partial\alpha}{\partial\tau}$$

$$+ 24\delta^2(1+\nu)\frac{\partial^2\alpha}{\partial\rho^2} \cdot \frac{\partial\zeta}{\partial\rho} \qquad 4.28$$

which governs the behaviour of the centre, $\rho=0$, of the plate.

4.4.3 INITIAL TIME BOUNDARY

Since the pressure was due to a transient dynamic shock wave the resultant initial boundary conditions with respect to time were assumed to be as follows.

$$(\alpha)_{\tau=0} = 0 \qquad 4.30$$

$$(\zeta)_{\tau=0} = 0 \qquad 4.31$$

$$\left(\frac{\partial\alpha}{\partial\tau}\right)_{\tau=0} = 0 \qquad 4.32$$

4.5 DISCUSSION OF ANALYSIS

With plates of diameter to thickness ratios which generate bending the major limitation of the application of the analysis was that as the deflection increased and approached twice the thickness of the plate, the curvature of the meridian axis could no longer be represented by $\frac{\partial^2\alpha}{\partial\rho^2}$, while the value of the slope would become significant with respect to unity, and hence could no longer be represented by $\frac{\partial\alpha}{\partial\rho}$. Therefore, the derivation of the equations 4.1 and 4.2 would not be valid, and an alternative analysis based on that proposed by Reissner[4.5] would have had to be developed for the plate/foundation case.

This would have resulted in a relationship less tractable by finite difference techniques.

In the case of static deflection of the plate, the equations derived by Reissner[4.5] were

$$r\frac{dN_r}{dr} + N_r - N_t\cos\psi - r\frac{d\psi}{dr}Q + rp = 0$$

$$r\frac{dQ}{dr} + Q + r\left(\frac{d\psi}{dr}N_r + N_t\frac{\sin\psi}{r}\right) + rq = 0$$

$$r\frac{dM_r}{dr} + M_r - M_t\cos\psi - rQ = 0$$

where

$$M_r = -D\left(\frac{\partial \psi}{\partial r} + \nu \frac{\sin \psi}{r}\right)$$

= Radial bending moment/unit length of circumference

$$M_t = -D\left(\frac{\sin \psi}{r} + \nu \frac{\partial \psi}{\partial r}\right)$$

= Tangential bending moment/unit length of radius

$$N_r = \frac{Eh}{1 - \nu^2}\left(\frac{\partial u}{\partial r} + \frac{1}{2}\frac{\partial^2 u}{\partial r^2} + \frac{1}{2}\frac{\partial^2 w}{\partial r^2} + \frac{\nu u}{r}\right)$$

= Radial membrane force/unit length of circumference

$$N_t = \frac{Eh}{1 - \nu^2}\left(\nu\frac{\partial u}{\partial r} + \frac{\nu}{2}\frac{\partial^2 u}{\partial r^2} + \frac{\nu}{2}\frac{\partial^2 w}{\partial r^2} + \frac{u}{r}\right)$$

= Tangential membrane force/unit length of radius

ψ = Angle between the radial direction and the radial tangent to the deformed middle surface of the plate.

Q = Stress resultant normal to the deformed surface.

q = Force normal to the plate surface.

p = Force parallel to the plate surface.

Since very large deflections would decrease the response time and increase the degree of non-linearity of the transducer, it was decided to limit the analysis to the range $0 < \delta\alpha(0,\tau) < 2$. Therefore the initial assumptions on plate behaviour were considered to be sufficiently accurate to obtain the results on which to finalise the transducer design.

The assumptions associated with the plate/foundation interface and foundation behaviour initially appeared to limit the

application of the solution. However the current range of analysis of the static and dynamic non-linear deflection of beams on elastic foundations as well as plates [4.6,4.7,4.8] were all based on similar simplifying assumptions,either stated or implied. This did not adversely affect the application of these results and therefore to avoid the inherent complexities and numerical difficulties associated with the plate/foundation friction and foundation inertia,the initial assumptions were considered realistic and the equations 4.15 and 4.16 governing the transducer behaviour were solved.

The analysis was initially carried out using finite difference numerical technique for the spatial domain and a recurrence relationship in the time domain as is shown in Chapter Six. To give a basis of comparison, and to allow the determination of the frequency of the system, a modal analysis was also carried out as can be seen in Chapter Five.

CHAPTER FIVE

MODAL ANALYSIS OF PLATE/FOUNDATION COMBINATION

5.1 INTRODUCTION

To provide a known solution by which the numerical procedure could be verified, the eigenfunction expansion technique for the linear forced vibration solution, presented by T.M. Hrudey[5.1] to determine the response of a plate subject to a transient load, was expanded to the case of a clamped circular plate on a foundation and subject to viscous damping. Two foundation characteristics were considered;

(1) Pasternak[4.1] foundation with the reaction

$$q(\rho,\tau) = k^*\alpha(\rho,\tau) - G^* \nabla^2 \alpha(\rho,\tau)$$

(2) Linear Winkler[4.1] foundation with a reaction of the form

$$q(\rho,\tau) = k^* \alpha(\rho,\tau)$$

The resultant governing equations were studied using separation of variables for the case of a step function pressure pulse, and an exponentially decaying pressure pulse with respect to time.

5.2 LINEAR ANALYSIS

The non-dimensional equation governing the plate behaviour was for the Pasternak foundation ,section 4.3.1 page 133 .

$$\nabla^4\alpha(\rho,\tau) - G^*\nabla^2\alpha(\rho,\tau) + k^*(\rho,\tau) + \frac{\partial^2\alpha(\rho,\tau)}{\partial\tau^2} + \chi\frac{\partial\alpha(\rho,\tau)}{\partial\tau} = \varepsilon(\tau) \qquad 5.1$$

Substitution of $\alpha(\rho,\tau)=\alpha'(\rho)\Gamma(\tau)$ in to the homogenous portion of equation 5.1 gave

$$\Gamma(\tau)\nabla^4\alpha'(\rho) - \Gamma(\tau)G^*\nabla^2\alpha'(\rho) + \Gamma(\tau)k^*\alpha'(\rho) + \alpha'(\rho)\frac{\partial^2\Gamma(\tau)}{\partial\tau^2} + \chi\,\alpha'(\rho)\frac{\partial\Gamma(\tau)}{\partial\tau} = 0 \qquad 5.2$$

or

$$(\nabla^4 - (\lambda_2^2 - \lambda_1^2)\nabla^2 - \lambda_1^2\,\lambda_2^2)\alpha'(\rho)\Gamma(\tau) = 0 \qquad 5.3$$

where

$$\lambda_2^2 - \lambda_1^2 = G^*$$

$$\lambda_1^2\,\lambda_2^2 = -\frac{1}{\Gamma(\tau)}\frac{\partial^2\Gamma(\tau)}{\partial\tau^2} - \frac{\chi}{\Gamma(\tau)}\frac{\partial\Gamma(\tau)}{\partial\tau} - k^*$$

It should be noted that in the case of the Winkler foundation the value of G^*goes to zero and λ_1 equals λ_2.

$$(\nabla^4 - \lambda^4)\,\alpha'(\rho)\,\Gamma(\tau) = 0 \qquad 5.4$$

In the case of a damped system provided $\Gamma(\tau)$ was a function of the form $\Gamma_m(\tau') = A_m e^{\epsilon_m\tau}$ or for the undamped system $\Gamma_m(\tau)$ was a function of the form $\Gamma_m(\tau) = A_m\sin\omega_m\tau + B_m\cos\omega_m\tau$, then the term λ_1^2,λ_2^2 becomes independent of radial position giving the eigenvector equation for the Pasternak foundation

$$(\nabla^2 + \lambda_1^2)(\nabla^2 - \lambda_2^2)\alpha'(\rho) = 0 \qquad 5.5$$

Therefore the vertical deflection was

$$\alpha'(\rho) = C_1 J_o(\lambda_1\rho) + D_1 I_o(\lambda_2\rho) + E_1 Y_o(\lambda_1\rho) + F_1 K_o(\lambda_2\rho) \qquad 5.6$$

while for the Winkler foundation

$$\alpha'(\rho) = C_1 J_o(\lambda\rho) + D_1 J_o(\lambda\rho) + E_1 Y_o(\lambda\rho) + F_1 K_o(\lambda\rho) \qquad 5.7$$

where J ,Y ,I and K were Bessel functions of the first, second, modified first and modified second kind respectively. and since the deflection at $\rho=0$ was finite and λ_1, λ_2 were real, the coefficients E_1 and F_1 were equated to zero and the deflection given by

$$\alpha'(\rho) = C_1 J_o(\lambda_1\rho) + D_1 I_o(\lambda_2\rho) \qquad 5.8$$

for the Pasternak case with the Winkler foundation being

$$\alpha'(\rho) = C_1 J_o(\lambda\rho) + D_1 I_o(\lambda\rho) \qquad 5.9$$

But applying the boundary condition at $\rho=1$

$$\alpha'(\rho) = 0$$

$$\frac{\partial \alpha'(\rho)}{\partial \rho} = 0$$

gave

$$\begin{aligned} C_1 J_o(\lambda_1) + D_1 I_o(\lambda_2) &= 0 \\ -C_1 \lambda_1 J_1(\lambda_1) + D_1 \lambda_2 I_1(\lambda_2) &= 0 \end{aligned} \qquad 5.10$$

by application of Bessel function recurrence relationships [5.2]

Separation of the constants gave the frequency equation for $G^* \neq 0$

$$\frac{-\lambda_1 J_1(\lambda_1)}{J_o(\lambda_1)} = \frac{\lambda_2 I_1(\lambda_2)}{I_o(\lambda_2)} \qquad 5.11$$

or

$$\lambda_1 J_1(\lambda_1) I_o(\lambda_2) + \lambda_2 J_o(\lambda_1) I_1(\lambda_2) = 0$$

while for $G^* = 0$

$$-\frac{J_1(\lambda)}{J_o(\lambda)} = \frac{I_1(\lambda_2)}{I_o(\lambda_2)} \qquad 5.12$$

or

$$J_1(\lambda) I_o(\lambda) + J_o(\lambda) I_1(\lambda) = 0$$

Therefore the resultant orthonormal eigenfunction associated with λ_{1m}, λ_{2m} the m^{th} roots of the frequency equation was for $G^* \neq 0$

$$\bar{\alpha}_m(\rho) = G_m J_o(\lambda_{1m}\rho) I_o(\lambda_{2m}) - J_o(\lambda_{1m}) I_o(\lambda_{2m}\rho) \qquad 5.13$$

and for $G^* = 0$

$$\bar{\alpha}_m(\rho) = G_m J_o(\lambda_m) I_o(\lambda_m) - J_o(\lambda_m) I_o(\lambda_m \rho) \qquad 5.14$$

Application of orthogonality conditions with respect to the radius parameter ρ as a weight function resulted in the following relationship for the eigenfunction Appendix A

$$\int \rho \, \bar{\alpha}_m(\rho) \bar{\alpha}_n(\rho) d\rho = \begin{cases} 0 & m \neq n \\ 1 & m = n \end{cases} \qquad 5.15$$

Therefore

$$G_m = \sqrt{E_m}\, J_o(\lambda_{1m})\, I_o(\lambda_{2m}) \qquad 5.16$$

where

$$E_m = 1 + \tfrac{1}{2}\frac{J_1^2(\lambda_{1m})}{J_o^2(\lambda_{1m})} - \tfrac{1}{2}\frac{I_1^2(\lambda_{2m})}{I_o^2(\lambda_{2m})} \qquad 5.17$$

It should be noted that by squaring the frequency equation 5.11

$$\lambda_{1m}^2 \frac{J_1^2(\lambda_{1m})}{J_o^2(\lambda_{1m})} = \lambda_{2m}^2 \frac{I_1^2(\lambda_{2m})}{I_o^2(\lambda_{2m})} \qquad 5.18$$

for the condition $G^* = 0$ i.e. $\lambda_{1m} = \lambda_{2m}$ the solution reverts to the Winkler case with $E_m = 1$

The resultant orthonormal modal shape for the m^{th} roots of the frequency equation was given by

$$\bar{\alpha}_m(\rho) = \frac{1}{\sqrt{E_m}}\left(\frac{J_o(\lambda_{1m}\rho)}{J_o(\lambda_{1m})} - \frac{I_o(\lambda_{2m}\rho)}{I_o(\lambda_m)}\right) \qquad 5.19$$

for the Pasternak foundation, and for the Winkler case by

$$\bar{\alpha}_m(\rho) = \left(\frac{J_o(\lambda_m\rho)}{J_o(\lambda_m)} - \frac{I_o(\lambda_m\rho)}{I_o(\lambda_m)}\right) \qquad 5.20$$

Solution of the vertical deflection equation was now obtained by summation of the modes of free vibration according to

$$\alpha(\rho,\tau) = \sum_{m=0}^{\infty} A_m(\tau)\bar{\alpha}_m(\rho) \qquad 5.21$$

where $A_m(\tau)$ were unknown functions of time satisfying the requirements for the separation of variables.

Substitution in the governing equation 5.1, gave on separation of variables

$$\sum_{m=0}^{\infty} (A_m(\tau)\nabla^4\bar{\alpha}_m(\rho) - G^* A_m(\tau)\nabla^2\bar{\alpha}_m(\rho) + k^* A_m(\tau)\bar{\alpha}_m(\rho) + \chi \frac{dA_m(\tau)}{d\tau}\bar{\alpha}_m(\rho) + \frac{d^2A_m(\tau)}{d\tau^2}\bar{\alpha}_m(\rho)) = \varepsilon(\tau) \qquad 5.22$$

for $G^* \neq 0$ while for $G^* = 0$

$$\sum_{m=0}^{\infty} (A_m(\tau)\nabla^4\bar{\alpha}_m(\rho) + k^* A_m(\tau)\bar{\alpha}_m(\rho) + \chi \frac{dA_m(\tau)}{d\tau}\bar{\alpha}_m(\rho) + \frac{d^2A_m(\tau)}{d\tau^2}\bar{\alpha}_m(\rho)) = \varepsilon(\tau) \qquad 5.23$$

Expanding the applied pressure amplitude as a generalised Fourier series expansion of unity, based upon the natural frequencies of the plate, gave

$$\varepsilon(\tau) = \varepsilon(\tau) \sum_{m=0}^{\infty} A_m \bar{\alpha}_m(\rho) \qquad 5.24$$

where a_m were constants with respect to the orthogonal set of functions $\int_o^1 \rho\bar{\alpha}_n(\rho)\bar{\alpha}_m(\rho)d\rho$. Hence Fourier constants(5.3) were obtained ,Appendix B for $G^* \neq 0$

$$a_m = \int_o^1 \rho\,\bar{\alpha}_m(\rho)d\rho = \frac{1}{\sqrt{E_m}}\left(\frac{J_1(\lambda_{1m})}{J_o(\lambda_{1m})} - \frac{I_1(\lambda_{2m})}{I_o(\lambda_{2m})}\right) \qquad 5.25$$

In the case $\lambda_{1m} = \lambda_{2m}$ for $G^* = 0$, $E_m = 1$ and therefore

$$a_m = \left(\frac{J_1(\lambda_m)}{J_o(\lambda_m)} - \frac{I_1(\lambda_m)}{I_o(\lambda_m)}\right) \qquad 5.26$$

Substitution into equation 5.22

$$\sum_{m=0}^{\infty} \left(\frac{d^2A_m(\tau)}{d\tau^2}\bar{\alpha}_m(\rho) + \chi\frac{dA_m(\tau)}{d\tau}\bar{\alpha}_m(\rho) + (\lambda_{1m}^2\lambda_{2m}^2 + k^*)\right.$$

$$\left.A_m(\tau)\bar{\alpha}_m(\rho)\right) = \varepsilon(\tau)\sum_{m=0}^{\infty} a_m\bar{\alpha}_m(\rho) \qquad 5.27$$

The equations were reduced by multiplying through by $\rho\bar{\alpha}_m(\rho)$ and applying the orthogonality condition which gave

$$\frac{d^2A_m(\tau)}{d\tau^2} + \chi\frac{dA_m(\tau)}{d\tau} + (\lambda_{1m}^2\lambda_{2m}^2 + k^*)A_m(\tau) = \varepsilon(\tau)a_m \qquad 5.28$$

Hence for loading, in which the pressure varies as a known function of time, the resultant equation for the m^{th} root can be solved to give the required coefficient, and summation of the roots gives the required deflection.

5.2.1 RECTANGULAR PULSE LOADING CASE.

Consider the loading case

$$\varepsilon(\tau) = \varepsilon(H(\tau) - H(\tau - \tau d)) \qquad 5.29$$

where τd = time of load application and $H(\tau)$ was the Heaviside step function which gave the following equation of coefficients

$$\frac{d^2A_m(\tau)}{d\tau^2} + 2\chi_m\omega_m\frac{dA_m(\tau)}{d\tau} + \omega_m^2A_m(\tau) = \varepsilon(H(\tau) - H(\tau - \tau d)) \qquad 5.30$$

where for $G^* \neq 0$

$$\omega_m^2 = \lambda_{1m}^2\lambda_{2m}^2 + k^*$$

while for $G^* = 0$

$$\omega_m^2 = \lambda_m^4 + k^*$$

and

$$\chi_m = \frac{\chi}{2\omega_m}$$

The initial boundary conditions in the time domain gave

$$\frac{dA_m(o)}{d\tau} = 0$$

$$A_m(o) = 0$$

The solution form will be a function of the damping for the specific mode and therefore the underdamped $\chi_m < 1$, the critically damped $\chi_m = 1$ and the overdamped $\chi_m > 1$ as well as the undamped conditions $\chi_m = 0$ were considered. It should be noted that the result for the Winkler foundation can be obtained from that for the Pasternak foundation using the condition $\lambda_{1m} = \lambda_{2m} = \lambda_m$. Therefore only the relationships for the Pasternak foundation are quoted.

5.2.1.1 UNDERDAMPED CONDITION $\chi_m < 1$ Using the Laplace transformation with the initial boundary conditions, the coefficients $A_m(\tau)$ were obtained

$0 < \tau < \tau d$

$$A_m(\tau) = \frac{\varepsilon a_m}{\omega_m^2}\left(1 - e^{-\chi_m\omega_m\tau}\cos\Omega_m\tau - \frac{2\chi_m\omega_m}{\Omega_m}\, e^{-\chi_m\omega_m\tau}\sin\Omega_m\tau\right)$$

$\tau > \tau d$

$$A_m(\tau) = \frac{\varepsilon a_m}{\omega_m^2}\left(e^{-\chi_m\omega_m(\tau-\tau d)}\left(\cos\Omega_m(\tau-\tau d) + \frac{2\chi_m\omega_m}{\Omega_m}\sin\Omega_m(\tau-\tau d)\right)\right.$$
$$\left. - e^{-\chi_m\omega_m\tau}\left(\cos\Omega_m\tau + \frac{2\chi_m\omega_m}{\Omega_m}\sin\Omega_m\tau\right)\right)$$

where

$$\Omega_m = \omega_m(1 - \chi_m^2)^{\frac{1}{2}}$$

5.2.1.2 CRITICALLY DAMPED CONDITION $\chi_m = 1$ Again using the Laplace transformation with the initial boundary conditions, the coefficients were obtained

$0 < \tau < \tau d$

$$A_m(\tau) = \frac{\varepsilon a_m}{\omega_m^2}(1 - e^{-\omega_m\tau} - \omega_m\tau\, e^{-\omega_m\tau})$$

$\tau > \tau d$

$$A_m(\tau) = \frac{\varepsilon a_m}{\omega_m^2}(e^{-\omega_m(\tau-\tau d)}(1 + \omega_m(\tau-\tau d) - e^{-\omega_m\tau}(1 + \omega_m\tau))$$

5.2.1.3 OVERDAMPED CONDITION $\chi_m > 1$ Applying the initial boundary conditions and Laplace transformation the coefficients $A_m(\tau)$ were obtained

$o < \tau < \tau d$

$$A_m(\tau) = \frac{\varepsilon a_m}{\omega_m^2}(1 - e^{-\chi_m\omega_m\tau}\cosh\Omega_m'\tau - \frac{2\chi_m\omega_m}{\Omega_m} e^{-\chi_m\omega_m\tau}\sinh\Omega_m'\tau)$$

$\tau > \tau d$

$$A_m(\tau) = \frac{\varepsilon a_m}{\omega_m^2}(e^{-\chi_m\omega_m(\tau-\tau d)}(\cosh\Omega_m'(\tau-\tau d) + \frac{2\chi_m\omega_m}{\Omega_m'}\sinh\Omega_m'(\tau-\tau d))$$
$$- e^{-\chi_m\omega_m\tau}(\cosh\Omega_m'\tau + \frac{2\chi_m\omega_m}{\Omega_m'}\sinh\Omega_m'\tau))$$

where

$$\Omega_m' = \omega_m(\chi_m^2 - 1)^{\frac{1}{2}}$$

5.2.1.4 UNDAMPED CONDITION $\chi_m = 0$ The coefficients were derived from the underdamped case with $\chi = 0$ giving

$0 < \tau < \tau d$

$$\alpha(\rho,\tau) = \sum_{m=0}^{\infty} \frac{\varepsilon a_m}{\omega_m^2} (1 - \cos \omega_m \tau)$$

$\tau > \tau d$

$$\alpha(\rho,\tau) = \sum_{m=0}^{\infty} \frac{\varepsilon a_m}{\omega_m^2} (\sin \omega_m \tau \sin \omega_m \tau d + \cos \omega_m \tau (\cos \omega_m \tau d - 1))$$

5.2.2 EXPONENTIAL DECAY LOADING CASE

Consider the loading case

$$\varepsilon(\tau) = \varepsilon_m e^{-\tau/\theta}$$

for the underdamped, critically damped, overdamped and undamped cases; again applying the Laplace transformation and obtaining the required coefficients. As mentioned above the Pasternak foundation is the general case while the Winkler foundation is satisfied by $G^* = 0$ or $\lambda_{1m} = \lambda_{2m} = \lambda_m$ and hence only the Pasternak foundation solution is presented.

5.2.2.1 UNDERDAMPED CONDITION $\chi_m < 1$ The coefficients were

$$A_m(\tau) = \frac{\varepsilon_m a_m \theta^2}{1 - 2\chi_m \omega_m \theta + \omega_m^2 \theta^2} (e^{-\tau/\theta} - e^{-\chi_m \omega_m \tau} (\cos \Omega_m \tau - \frac{1}{\theta \Omega_m} \times$$

$$(1 - \chi_m \omega_m \theta) \sin \Omega_m \tau)$$

where

$$\Omega_m = \omega_m(1 - \chi_m^2)^{\frac{1}{2}}$$

5.2.2.2 CRITICALLY DAMPED CONDITION $\chi_m = 1$ From application of the Laplace transformations the coefficients were

$$A_m(\tau) = \frac{\varepsilon_m a_m \theta^2}{1 - 2\chi_m\omega_m\theta + \omega_m^2\theta^2} e^{-\tau/\theta} - e^{-\omega_m\tau}(1 - (\frac{1}{\theta} - \omega_m)\tau)$$

5.2.2.3 OVERDAMPED CONDITION $\chi_m > 1$ As previously the coefficients were

$$A_m(\tau) = \frac{\varepsilon_m a_m \theta^2}{1 - 2\chi_m\omega_m\theta + \omega_m^2\theta^2} (e^{-\tau/\theta} - e^{-\chi_m\omega}(\cosh\Omega_m'\tau - \frac{1}{\theta\Omega_m}(1 - \chi_m\omega_m A)\sinh\Omega_m'\tau))$$

where

$$\Omega_m' = \omega_m(\chi_m^2 - 1)^{\frac{1}{2}}$$

5.2.2.4 UNDAMPED CONDITION $\chi_m = 0$ From the underdamped case the coefficients for $\chi = 0$ were

$$A_m(\tau) = \frac{\varepsilon_m a_m \theta}{1 + \omega_m^2\theta^2} (e^{-\tau/\theta} - \cos\omega_m\tau + \frac{1}{\theta\omega_m}\sin\omega_m\tau)$$

5.2.3 DEFLECTION

The resultant deflection is given by

$$\alpha(\rho,\tau) = \sum_{m=0}^{\infty} A_m(\tau) \frac{1}{\sqrt{E_m}} \left(\frac{J_o(\lambda_{1m}\rho)}{J_o(\lambda_{1m})} - \frac{I_o(\lambda_{2m}\rho)}{I_o(\lambda_{2m})}\right)$$

for the Pasternak foundation while for the Winkler foundation or plate

$$\alpha(\rho,\tau) = \sum_{n=0}^{\infty} A_m(\tau) \left(\frac{J_o(\lambda_m\rho)}{J_o(\lambda_m)} - \frac{I_o(\lambda_m\rho)}{I_o(\lambda_m)}\right)$$

5.2.4 ROOTS OF FREQUENCY EQUATION

The roots of the equations for the plate, Fig 5.1 page 153, or the equation for the Pasternak foundation, Fig 5.2 page 153 $G^*= 50$, or Fig. 5.2 page 153 $G^*= 100$, for the range 0-10, were obtained by using a Newton-Raphson[5.4] iterative procedure

$$(\lambda_m)_{i+1} = (\lambda_m)_i - \frac{f(\lambda_m)_i}{\left(\frac{df(\lambda_m)}{d\lambda_m}\right)_i}$$

where i = iterative step number and which for the case $G \neq 0$ gave the relationship

$$f(\lambda_{1m}, \lambda_{2m}) = \lambda_{1m} J_1(\lambda_{1m}) I_o(\lambda_{2m}) + \lambda_{2m} J_o(\lambda_{1m}) I_1(\lambda_{2m})$$

where $\lambda_{2m} = (G + \lambda_{1m})^{\frac{1}{2}}$

$$\frac{df(\lambda_m)}{d\lambda_{1m}} = J_o(\lambda_{1m}) \left(\frac{\lambda_{1m}}{2} + \frac{\lambda_{2m}}{2}\right) I_o(\lambda_{2m}) + \frac{\lambda_{1m}}{\lambda_{2m}} I_1(\lambda_{2m}) + \frac{\lambda_{2m}}{2} I_2(\lambda_{2m})$$

$$+ J_1(\lambda_{1m}) I_o(\lambda_{2m}) + \frac{\lambda_{1m}^2 - \lambda_{2m}^2}{\lambda_{2m}} I_1(\lambda_{2m}) + J_2(\lambda_{1m}) - \frac{\lambda_{1m}}{2} I_o(\lambda_{2m})$$

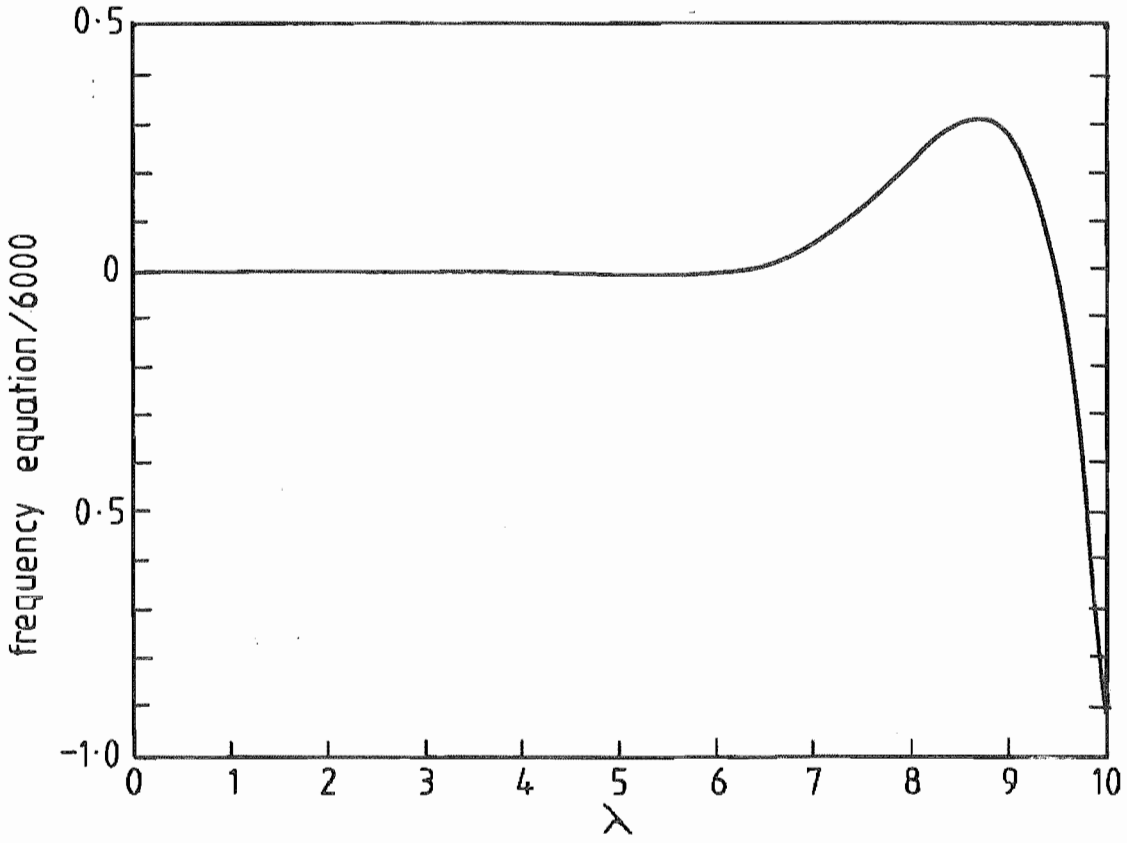

FIG 5·1 PLOT OF FREQUENCY EQUATION $J_1(\lambda)\, I_0(\lambda) + J_0(\lambda)\, I_1(\lambda)$

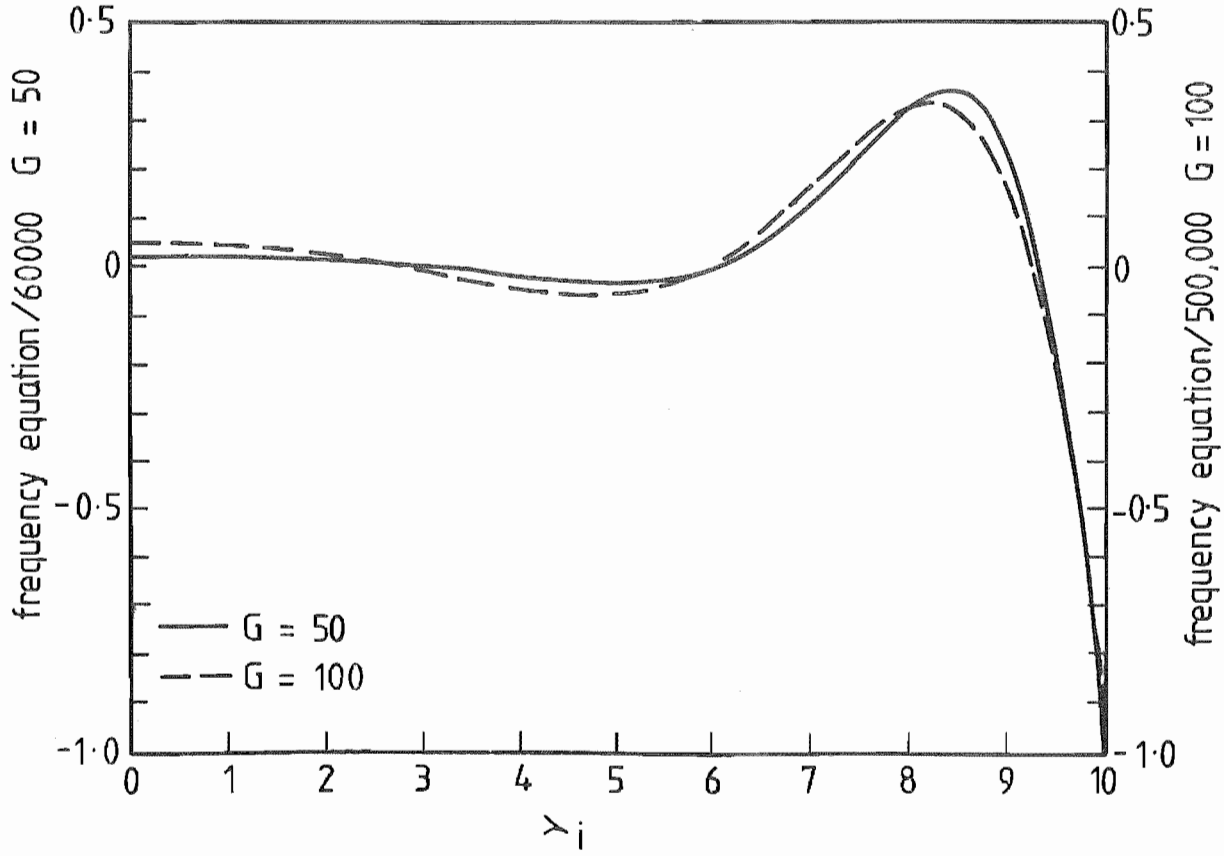

FIG 5·2 PLOT OF FREQUENCY EQUATION, $\lambda_1 J_1(\lambda_1)\, I_0(\lambda_2)$ & $\lambda_2\, J_0(\lambda_1)\, I_1(\lambda_2)$, vs λ_1 FOR A PASTERNAK FOUNDATION WHERE $\lambda_2 = (G + \lambda_1^2)^{1/2}$

while for the case $G^* = 0$ was

$$f(\lambda_m) = J_1(\lambda_m)\, I_o(\lambda_m) + J_o(\lambda_m)\, I_1(\lambda_m)$$

$$\frac{df(\lambda_m)}{d\lambda_m} = J_o(\lambda_m)\, I_o(\lambda_m) + \tfrac{1}{2}(J_o(\lambda_m)\, I_2(\lambda_m) - J_2(\lambda_m)\, I_o(\lambda_m))$$

The convergence of this procedure for roots of greater than 10 became unstable because of the relative magnitudes of the function and the first derivative. The rapidly increasing magnitude of the function can be seen from the limited number of roots shown in Figs 5.1 & 5.2 and hence the first derivative became large as the root was approached. The use of a modified Newton-Raphson procedure did not give adequate convergence, so an initial approximation based on an accepted convergence when the change in value of the roots, due to the iterative procedure was less than 1×10^{-6}, was obtained. Using this value a logarithmic search was carried out in an attempt to locate the roots more accurately. It was found that the logarithmic search did not change the roots' value within the first five decimal places, so subsequently for the Pasternak foundation the convergence criteria used was that associated with the initial approximation. Because the roots for the linear case only needed to be calculated once for each value of G^* and are presented for $G^*=0$ in Appendix C, for $G^*=50$ in Appendix D, and for $G^*=100$ in Appendix E, this time representation was acceptable in computer time.

5.2.5 FLOW DIAGRAM - LINEAR SOLUTION PROGRAM

The flow diagram for the program to determine the deflection and bending moment at the plate centre is given in Fig 5.3 page 155.

The first thirty roots were obtained and it was found that these gave an adequate description of the deflection and bending moment as can seen in Figs 5.4 page 156 & 5.5 page 156 where the results are compared following summation over 29 and 30 roots.

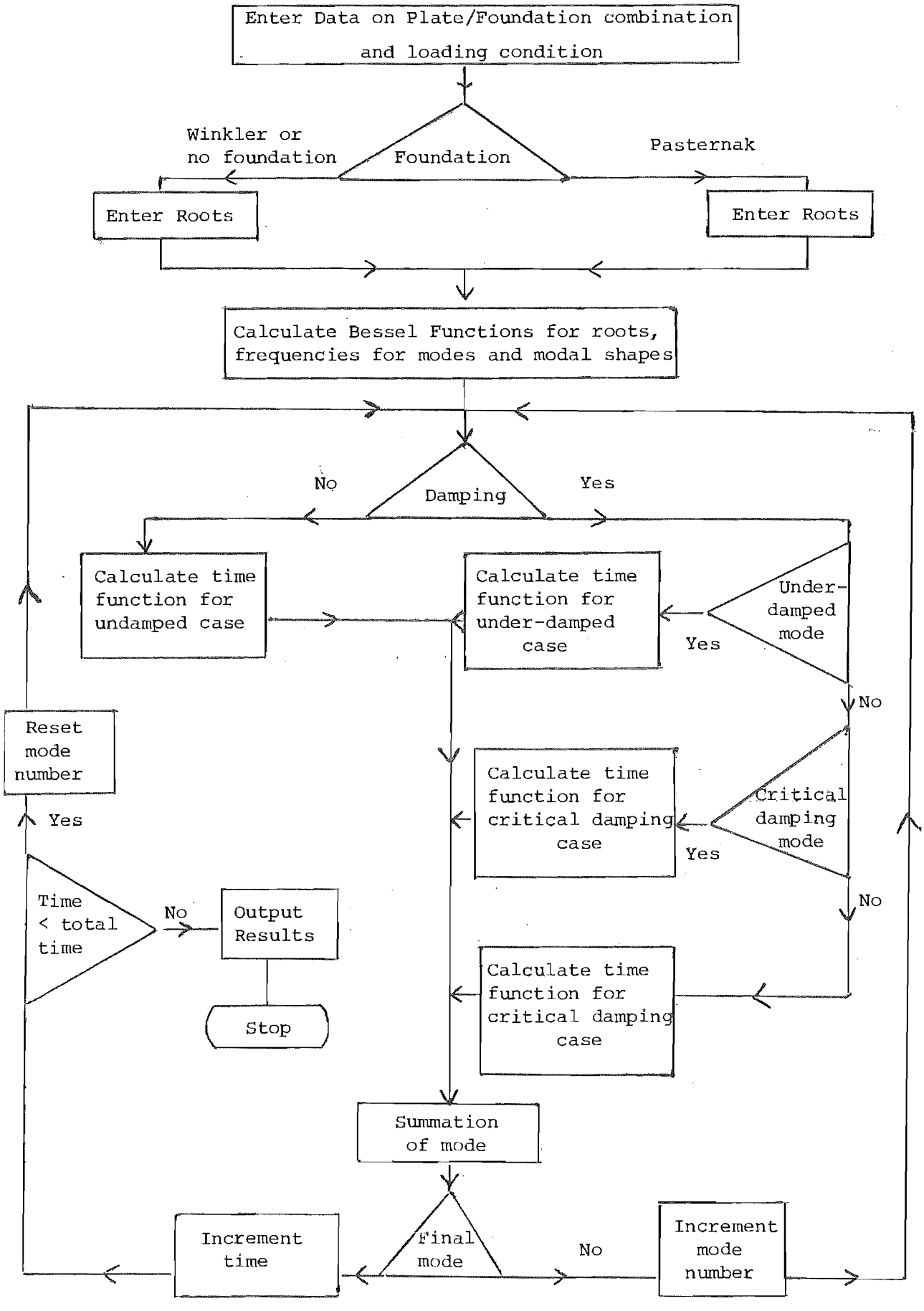

FIGURE 5.3 FLOW DIAGRAM LINEAR PROGRAM

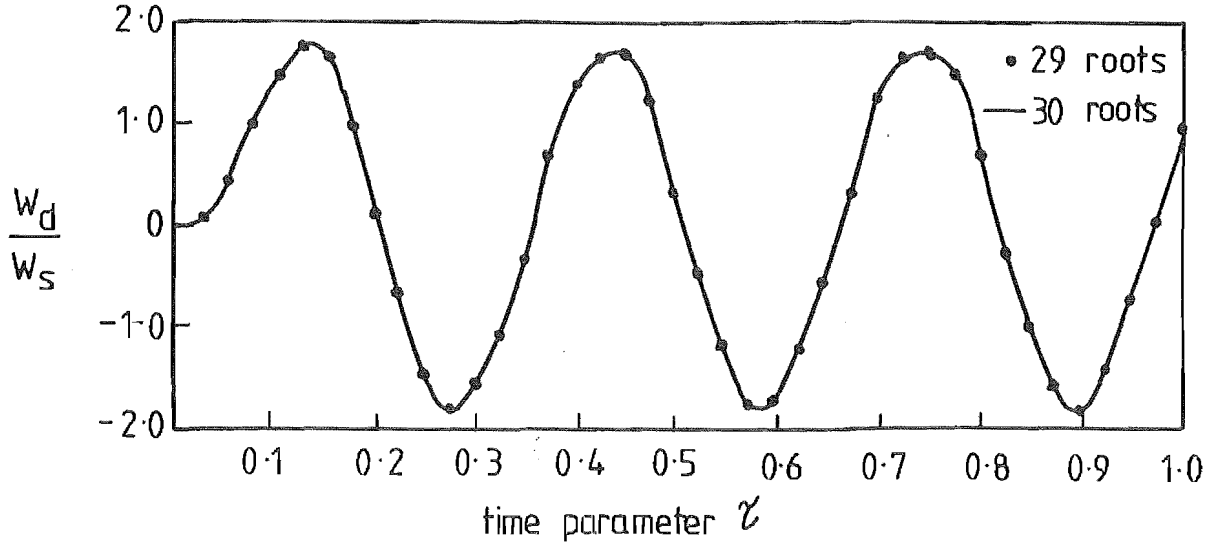

FIG 5·4 RATIO DYNAMIC DEFLECTION : STATIC DEFLECTION AT PLATE CENTRE vs TIME

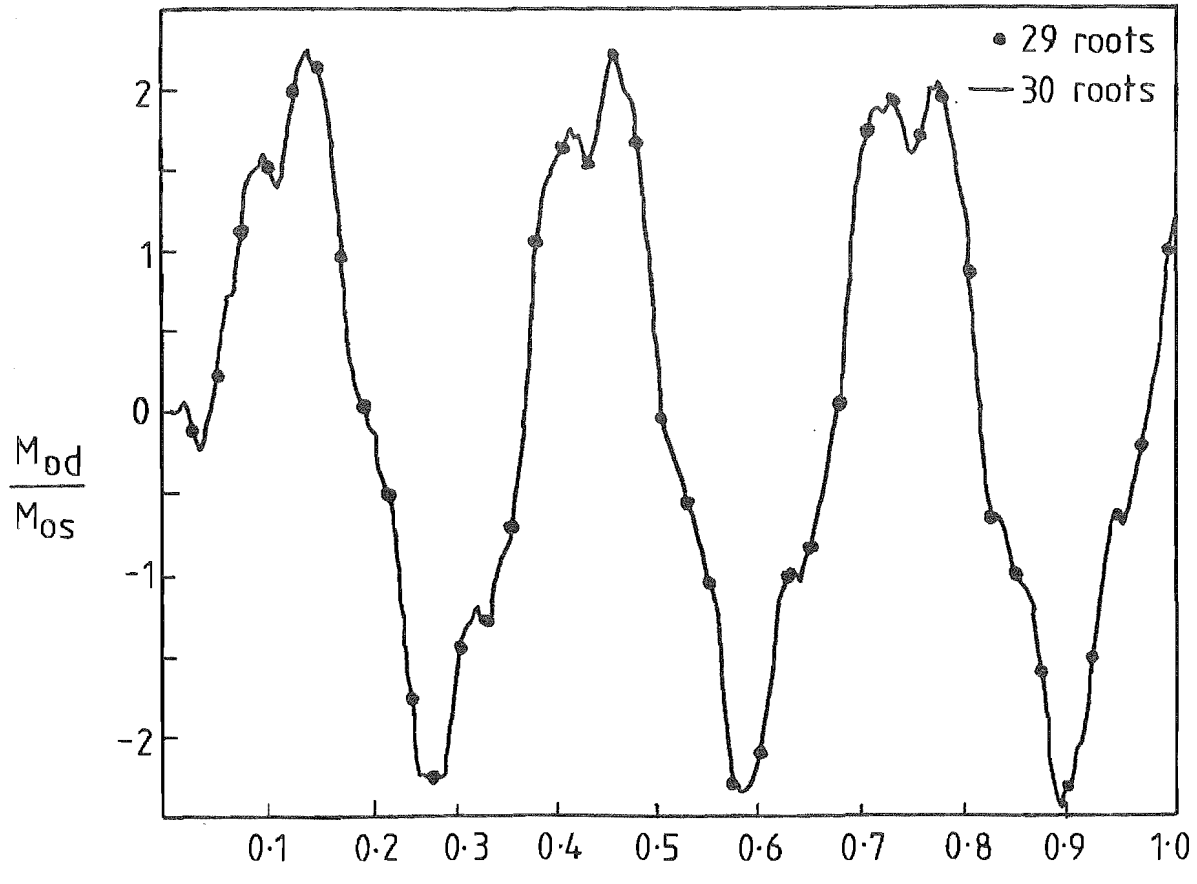

FIG 5·5 RATIO OF DYNAMIC BENDING MOMENT : STATIC BENDING MOMENT AT PLATE CENTRE vs TIME

5.3 NON - LINEAR ANALYSIS

The eigenfunction expansion technique used to determine the response of a plate subject to a transient load was expanded to the case of non-linear deflection of a clamped circular plate on a foundation with a linear Winkler characteristic, and subject to viscous damping with quasi-linearisation of the eigenroots over small time increments in the time domain.

The dynamic loading was considered to be a pressure pulse, uniformly distributed across the plate, with a time dependent amplitude. H.H. Berger's[5.5] assumption was used to allow effective decoupling of the governing equations. The known errors associated with this assumption[5.6,5.7] particularly with respect to the simply supported condition were appreciated. However it gave a basis of comparison for the numerical non-linear program as there was no known information in the literature to verify the program accuracy for a foundation. Radial inertia and radial damping were ignored.

The non-dimensional equations governing the plate behaviour were;

$$\nabla^4\alpha(\rho,\tau) - \gamma^2\,\nabla^2\alpha(\rho,\tau) + k^*\alpha(\rho,\tau) + \frac{\partial^2\alpha(\rho,\tau)}{\partial\tau^2} + \chi\,\frac{\partial\alpha(\rho,\tau)}{\partial\tau} = \varepsilon(\tau) \qquad 5.31$$

where from Berger's assumption

$$\left(\frac{\partial\zeta(\rho,\tau)}{\partial\rho} + \tfrac{1}{2}\left(\frac{\partial\alpha(\rho,\tau)}{\partial\rho}\right)^2 + \frac{\zeta(\rho,\tau)}{\rho}\right) = \frac{\gamma^2}{12\delta^2} \qquad 5.32$$

Since the equation 5.31 was of an identical form to the previous linear case with the Pasternak foundation equation 5.2, the solution for the modal shapes of the vertical deflection was of the form

$$-\alpha_m(\rho) = \frac{1}{\sqrt{E_m}} \left(\frac{J_o(\lambda_{1m}\rho)}{J_o(\lambda_{1m})} - \frac{I_o(\lambda_{2m}\rho)}{I_o(\lambda_{2m})} \right) \qquad 5.33$$

where

$$E_m = 1 + \tfrac{1}{2} \frac{J_1^2(\lambda_{1m})}{J_o^2(\lambda_{1m})} - \tfrac{1}{2} \frac{I_o^2(\lambda_{2m})}{I_o^2(\lambda_{2m})}$$

and λ_{1m} , λ_{2m} were the m^{th} roots of the equations

$$\lambda_1 J_1(\lambda_1) I_o(\lambda_2) + \lambda_2 J_o(\lambda_1) I_1(\lambda_2) = 0 \qquad 5.34$$

$$\lambda_2^2 - \lambda_1^2 = \gamma^2 \qquad 5.35$$

with γ^2 being a function of the deflection associated with the mode.

5.3.1 CONSTANT LOADING CASE

Therefore, for a constant load applied at time $\tau = 0$, the vertical deflection was defined as in section 5.2.1 in the region $0 < \tau < \tau d$. Again the solution form will be a function of the damping for the specific mode and therefore the underdamped $\chi_m < 1$, the critically damped $\chi_m = 1$, the overdamped $\chi_m > 1$ as well as the undamped condition $\chi_m = 0$, were considered. The form of the coefficients was as for the previous section 5.2.

5.3.1.1 UNDERDAMPED CONDITION $\chi_m < 1$ The coefficients were described by

$$A_m(\tau) = \frac{\varepsilon a_m}{\omega_m^2} \left(1 - e^{-\chi_m \omega_m \tau^*} \left(\cos \Omega_m \tau^* - \frac{2\chi_m \omega_m}{\Omega_m} \sin \Omega_m \tau^*\right)\right)$$

where

$$\omega_m^2 = (\lambda_{1m}^2 \lambda_{2m}^2 + k^*)$$

$$\Omega_m = \omega_m (1 - \chi_m^2)^{\frac{1}{2}}$$

$$\chi_m = \frac{\chi}{2\omega_m}$$

τ^* = Effective elapsed time.

Since the vertical deflection was non-linear λ_{1m}, λ_{2m} were functions of the deflection for the mode at a given point in real time and as a result ω_m varied with deflection. The effective elapsed time τ^* was the equivalent time that the specific mode of the plate/foundation combination could be considered to be loaded if the current value of ω_m was constant throughout the loading. Therefore τ^* varied as a function of the previous deflection history for the given mode and its derivation is discussed in section 5.3.4.

5.3.1.2 CRITICALLY DAMPED CONDITION $\chi_m = 1$ As previously the coefficients were described by

$$A_m(\tau) = \frac{\epsilon a_m}{\omega_m^2}\left(1 - e^{-\omega_m \tau^*}(1 + \omega_m \tau^*)\right)$$

5.3.1.3 OVERDAMPED CONDITION $\chi_m > 1$ Again as previously described the coefficients

$$A_m(\tau) = \frac{\epsilon a_m}{\omega_m^2}\left(1 - e^{-\chi_m \omega_m \tau^*}\left(\cosh\Omega_m' \tau^* + \frac{2\chi_m \omega_m}{\Omega_m'} \sinh\Omega_m' \tau^*\right)\right)$$

where

$$\Omega_m' = \omega_m(\chi_m^2 - 1)^{\frac{1}{2}}$$

5.3.1.4 UNDAMPED CONDITION $\chi_m = 0$ As for the section 5.2.1.4 the coefficients were

$$A_m(\tau) = \frac{\epsilon a_m}{\omega_m^2}\left(1 - \cos\omega_m \tau^*\right)$$

5.3.2 DEFLECTION

As previously, the resultant deformation is given by

$$\alpha(\rho,\tau) = \sum_{m=0}^{\infty} A_m(\tau)\,\frac{1}{\sqrt{E_m}}\left(\frac{J_o(\lambda_{1m}\rho)}{J_o(\lambda_{1m})} - \frac{I_o(\lambda_{2m}\rho)}{I_o(\lambda_{2m})}\right)$$

5.3.3 RADIAL DEFLECTION

Based upon Berger's assumption the modal shape of the radial deflection corresponding to the m^{th} root at a given point in time was obtained by assuming that since the radial inertia and damping were ignored, then the radial deflection was given by

$$\left(\frac{\partial \zeta_m(\rho)}{\partial \rho} + \tfrac{1}{2}\left(\frac{\partial \alpha_m(\rho)}{\partial \rho}\right)^2 + \frac{\zeta_m(\rho)}{\rho}\right)_{\tau} = \frac{\lambda_{2m}^2 - \lambda_{1m}^2}{12\delta^2} \qquad 5.36$$

But for the constant load case the vertical deflection for the m^{th} mode at the time τ was

$$\alpha_m(\rho,\tau) = A_m(\tau)\cdot\frac{1}{\sqrt{E_m}}\left(\frac{J_o(\lambda_{1m}\rho)}{J_o(\lambda_{1m})} - \frac{I_o(\lambda_{2m}\rho)}{I_o(\lambda_{2m})}\right)$$

Therefore since $\zeta(\rho)$ was finite at $\rho=0$ the corresponding radial deflection for the m^{th} mode was, from the Appendix F

$$\zeta_m(\rho) = \rho\frac{(\lambda_{2m}^2 - \lambda_{1m}^2)}{24\delta^2} - \frac{\rho}{4}\frac{(A_m(\tau))^2}{E_m}\left\{\frac{\lambda_{1m}^2}{J_o^2(\lambda_{1m})}\left[(J_1^2(\lambda_{1m}\rho)\right.\right.$$

$$- J_o(\lambda_{1m}\rho)J_2(\lambda_{1m}\rho))] + \frac{\lambda_{2m}^2}{I_o(\lambda_{2m})}[(I_1^2(\lambda_{2m}\rho) - I_o(\lambda_{2m}\rho)I_2(\lambda_{2m}\rho))]$$

$$+ \frac{4\lambda_{1m}\lambda_{2m}}{\lambda_{1m}^2+\lambda_{2m}^2}\,\frac{1}{J_o(\lambda_{1m})I_o(\lambda_{2m})}[(\lambda_{1m}J_2(\lambda_{1m})I_1(\lambda_{2m}) + \lambda_{2m}J_1(\lambda_{1m})]$$

$$\left.\left.I_2(\lambda_{2m}\rho))\right\}\right. \qquad 5.37$$

At the boundary $\rho=1$, $\zeta(\rho)=0$ because the edge was fixed and therefore

$$0 = \frac{\lambda_{2m}^2 - \lambda_{1m}^2}{24\delta^2} - \frac{1}{4E_m}\frac{\lambda_{1m}^2}{J_o^2(\lambda_{1m})}(J_1^2(\lambda_{1m}) - J_o(\lambda_{1m})J_2(\lambda_{1m}))$$

$$+ \frac{\lambda_{2m}}{J_o^2(\lambda_{2m})}(I_1^2(\lambda_{2m}) - I_o(\lambda_{2m})I_2(\lambda_{2m})) + \frac{4\lambda_{1m}\lambda_{2m}}{\lambda_{1m}^2+\lambda_{2m}^2} \cdot J_o(\lambda_{1m})I_o(\lambda_{2m})$$

$$(\lambda_{1m}J_2(\lambda_{1m})I_1(\lambda_{2m}) + \lambda_{2m}J_1(\lambda_{1m})I_2(\lambda_{2m})) \qquad 5.38$$

Therefore the roots of the m^{th} mode must satisfy both the equation 5.34 and equation 5.38 under the free vibration condition.

5.3.4 SOLUTION OF ROOTS FOR MODE

The roots for the m^{th} mode were obtained at the time τ by the simultaneous solution of the frequency equation 5.34 and the radial boundary condition equation 5.38, that is the location of the roots for the following equations;

$$F_1 = \lambda_1 J_1(\lambda_{1m})I_o(\lambda_{2m}) + \lambda_{2m}J_o(\lambda_{1m})I_1(\lambda_{2m})$$

$$F_2 = \frac{\lambda_{2m}^2 - \lambda_{1m}^2}{24\delta^2} - \tfrac{1}{4}\frac{(A_m(\tau))^2}{E_m}\left\{\frac{\lambda_{1m}^2}{J_o^2(\lambda_{1m})}(J_1^2(\lambda_{1m}) - J_o(\lambda_{1m})J_2(\lambda_{1m}))\right.$$
$$+ \frac{\lambda_{2m}^2}{J_o^2(\lambda_{2m})}(I_1^2(\lambda_{2m}) - I_o(\lambda_{2m})I_2(\lambda_{2m}))\frac{4\lambda_{1m}\lambda_{2m}}{\lambda_{1m}^2+\lambda_{2m}^2}$$

$$\left.(\lambda_{1m}J_2(\lambda_{1m})I_1(\lambda_{2m}) + \lambda_{2m}J_1(\lambda_{1m})I_2(\lambda_{2m}))\right\} \qquad 5.39$$

where $F_1 = 0$ and $F_2 = 0$

The roots which satisfied both functions F_1 and F_2 were obtained using an iterative technique based upon the Newton- Raphson method. At a point on the surfaces F_1 and F_2 corresponding to the point $(\lambda_{1m})_i$, $(\lambda_{2m})_i$ the previous i^{th} iteration, the tangent planes to the surfaces were found and the intersection of the traces of these planes in the surface z=0 was taken as the next value of the roots $(\lambda_{1m})_{i+1}$, $(\lambda_{2m})_{i+1}$.

The tangent plane to the funcion $F(\lambda_{1m}, \lambda_{2m})$ at the i^{th} iteration i.e. point (λ_{1m}) , (λ_{2m}) was given by

$$z - F_1(\lambda_{1m},\lambda_{2m})_i - \left(\frac{\partial F_1}{\partial \lambda_{1m}}\right)_i ((\lambda_{1m})_{i+1} - (\lambda_{1m})_i)$$

$$+ \left(\frac{\partial F_1}{\partial \lambda_{2m}}\right)_i ((\lambda_{2m})_{i+1} - (\lambda_{2m})_i) \qquad 5.40$$

where Z defines the tangent plane to the function and assuming continuous partial derivatives of the first order over the region of interest. Therefore the trace of the tangent plane in the surface z=0 would contain a closer approximation to the required roots at $(\lambda_{1m})_{i+1}$, $(\lambda_{2m})_{i+1}$ where the trace intersects with that for the tangent plane to $F_2(\lambda_{1m},\lambda_{2m})_i$ at point $(\lambda_{1m})_i$, $(\lambda_{2m})_i$ and the surface z=0. Therefore the trace for the tangent plane to F_1 was obtained

$$-F_1(\lambda_{1m}, \lambda_{2m})_i = \left(\frac{\partial F_1}{\partial \lambda_{1m}}\right)((\lambda_{1m})_{i+1} - (\lambda_{1m})_i) + \left(\frac{\partial F_1}{\partial \lambda_{2n}}\right)_i$$

$$((\lambda_{2m})_{i+1} - (\lambda_{2m})_i)$$

and hence

$$\left(\frac{\partial F_1}{\partial \lambda_{1m}}\right)_i (\lambda_{1m})_{i+1} + \left(\frac{\partial F_1}{\partial \lambda_{2m}}\right)_i (\lambda_{2m})_{i+1} = \left(\frac{\partial F_1}{\partial \lambda_{1m}}\right)_i (\lambda_{1m})_i$$

$$+ \left(\frac{\partial F_1}{\partial \lambda_{2m}}\right)_i (\lambda_{2m})_i - F_1(\lambda_{1m}, \lambda_{2m})_i$$

$$= H_1$$

Similarly for the second function the trace of the tangent plane at point $(\lambda_{1m})_i$, (λ_{2m}) in the surface z=0 was described by

$$(\frac{\partial F_2}{\lambda_{1m\,i}})(\lambda_{1m})_{i+1} + (\frac{F_2}{\lambda_{2m}})(\lambda_{2m})_{i+1}$$

$$= (\frac{\partial F_2}{\partial \lambda_{1m\,i}})(\lambda_{1m})_i + (\frac{\partial F_2}{\partial \lambda_{2m}})(\lambda_{2m})_i - F_2(\lambda_{1m}, \lambda_{2m})_i$$

$$= H_2$$

The intersection of the traces gave the next approximation to the required roots

$$(\lambda_{1m})_{i+1} = (H_1(\frac{\partial F_2}{\partial \lambda_{2m\,i}}) - H_2(\frac{\partial F_1}{\partial \lambda_{2m\,i}})/H_3 \qquad 5.41$$

$$(\lambda_{2m})_{i+1} = (H_1(\frac{\partial F_2}{\partial \lambda_{1m\,i}}) - H_2(\frac{\partial F_1}{\partial \lambda_{1m}}))/H_3$$

where

$$H_3 = (\frac{\partial F_1}{\partial \lambda_{1m\,i}})(\frac{\partial F_2}{\partial \lambda_{2m\,i}}) - (\frac{\partial F_2}{\partial \lambda_{1m\,i}})(\frac{\partial F_1}{\partial \lambda_{2m\,i}})$$

The iterations were initiated using the linear root λ_m for the m^{th} mode such that $\lambda_{1m} = \lambda_{2m} = \lambda_n$ and then iterations were continued until the value of F_1 and F_2 were less than $1x10^{-6}$.

The derivatives for the constant load case are given in Appendix G and H.

5.3.5 DETERMINATION OF ELAPSED TIME

The method of determining the effective elapsed time was based upon the assumption of continuity of the solution at the mid-point between the discrete pivotal points in the time domain for each mode, therefore for the m^{th} mode

$$\alpha_m(\rho,\tau^*_{m,i} + \frac{\Delta\tau}{2}) = \alpha_m(\rho,\tau^*_{m,i+1} - \frac{\Delta\tau}{2}) \qquad 5.42$$

where $\tau^*_{m,i}$ = effective elapsed time at the i^{th} time step

$\tau^*_{m,i+1}$ = effective elasped time at the $i+1^{th}$ time step

$\Delta\tau$ = time increment.

For each modal shape iteration to a solution for the roots λ_{1m} , λ_{2m} and τ^*_m was carried out based upon the equations for the roots 5.34, 5.38 and the mid-point requirement.

$$\bar{\alpha}_m(\rho)\ A_m(\tau^*_{n,i} + \frac{\Delta\tau}{2}) = \bar{\alpha}_m(\rho)\ A_m(\tau^*_{n,i+1} - \frac{\Delta\tau}{2})$$

It was initiated by taking the effective elapsed time for the specific mode at the previous pivotal point in the time domain and the real time increment was added to give the first approximation to the effective elapsed time at the current time. Initially the roots λ_{1m} , λ_{2m} for the value of τ^*_m were calculated and subsequently a new value of τ^*_m obtained for the given time step and a further iteration carried out to determine new roots λ_{1m}, λ_{2m}. The iteration was terminated when the change in the elapsed time was less than 0.01% between successive iteration steps.

Each mode has an individual effective elapsed time τ^*_m .

5.3.6 FLOW DIAGRAM NON - LINEAR SOLUTION PROGRAM

The flow diagram for the program to determine the deflection for the non-linear case is given in Fig 5.6 page 166.

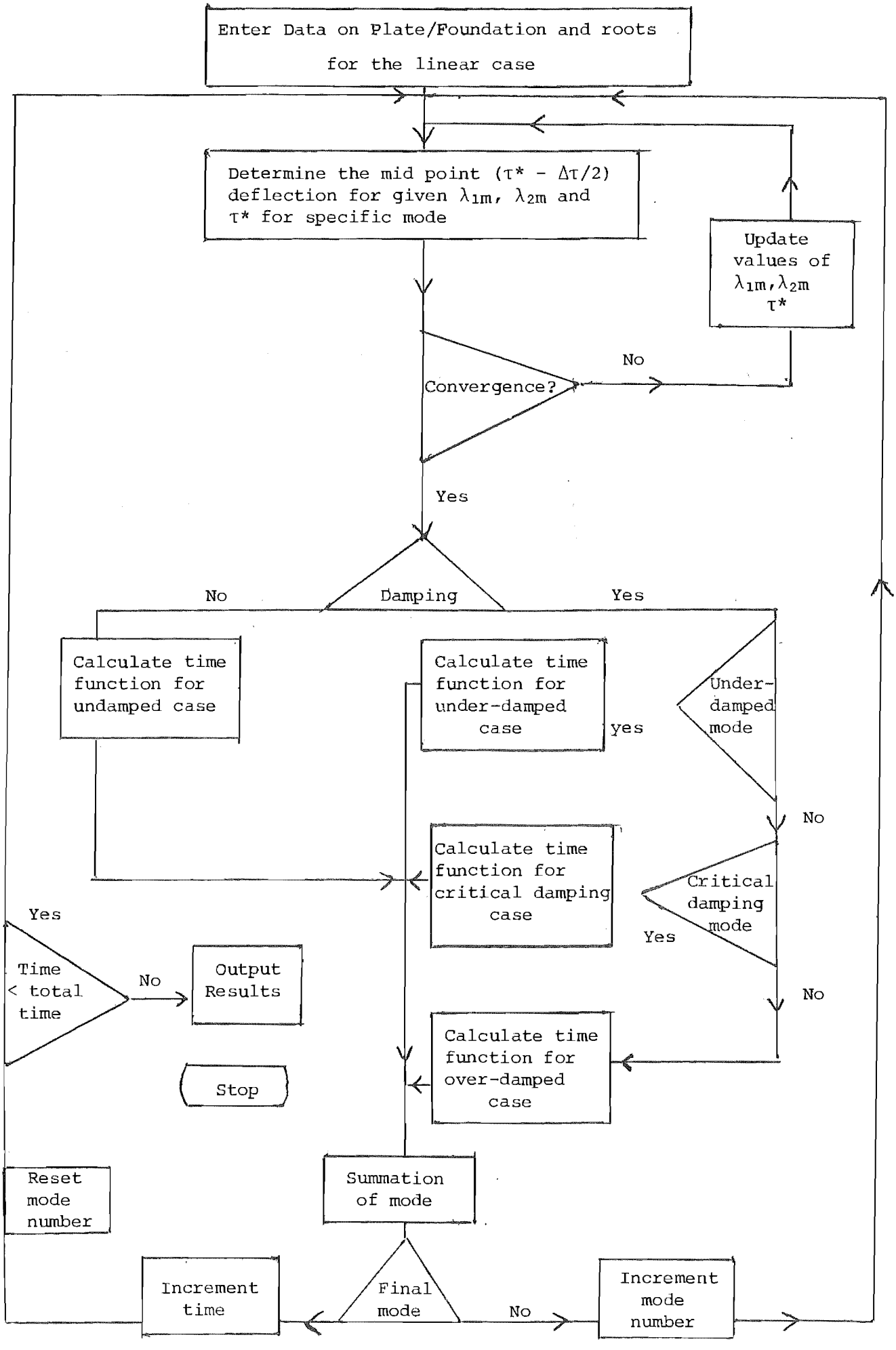

FIGURE 5.6 FLOW DIAGRAM NON-LINEAR PROGRAM

CHAPTER SIX

NUMERICAL SOLUTION OF GOVERNING EQUATIONS

6.1 INTRODUCTION

The first approximate solutions to the coupled Von Karman equations 4.11 ,4.12 governing the static non-linear deflection of plates were derived by assuming a shape function for the plate. Constants associated with the shape function were obtained by considering the minimum of either the variation of applied load as calculated from the shape function and governing equations in the work of Nadai[6.1], or the total strain energy in the case of Timoshenko[6.2].

An exact series solution of static non-linear deflection was obtained by Way[4.4]. The first derivative of vertical deflection with respect to radius was described by an odd series function of radius while the radial membrane stress was given by an expansion of an even series function of radius. The coefficient relationships were derived by substituting the series in the governing equations. The solution was obtained by initially estimating values for the constant and first coefficient of the even and odd series respectively, and the deflection and stresses were then calculated. This process was repeated for a range of constant and first coefficient values and the radius at which the outer boundary conditions,were met was determined. While this did not satisfy the inner boundary condition, if sufficient numerical cases were considered then interpolation enabled the appropriate starting values to be obtained, and hence the non-linear static deformation to be determined so that it satisfied the boundary conditions as well as the governing equations.

The assumption that the second invariant of the membrane strains in the strain energy expression was negligible was made by Berger[5.5]. While this assumption has no physical interpretation, because it effectively reduced the coupling of the Von Karman equations and therefore simplified the solution technique, it has been the basis of subsequent static[6.3] and dynamic [6.4,6.5,6.6,6.7] analysis of non-linear deflections in thin shells and plates. This lack of interpretation has given rise to some controversy[5.6,5.7,6.8], particularly with respect to the simply supported edge condition.

For the static analysis the modified equations were

$$\nabla^4 - 12\delta^2\left(\frac{d\zeta}{d\rho} + \tfrac{1}{2}\left(\frac{d\alpha}{d\rho}\right)^2 + \frac{\zeta}{\rho}\right)\nabla^2\alpha = \frac{\varepsilon}{\delta} \qquad 6.1$$

$$\frac{d\zeta}{d\rho} + \tfrac{1}{2}\left(\frac{d\alpha}{d\rho}\right)^2 + \frac{\zeta}{\rho} = \frac{\gamma^{*2}}{12\delta^2} \qquad 6.2$$

where $\nabla^2 = \left(\frac{d^2}{d\rho^2} + \frac{1}{\rho}\frac{d}{d\rho}\right)$

$\frac{\gamma^{*2}}{12\delta^2}$ = Constant of integration

$= \varepsilon_{rm} + \varepsilon_{r\theta}$

ε_{rm} = Radial Membrane stress Strain

$\varepsilon_{r\theta}$ = Circumferential Membrane Strain.

and the parameters were those defined in Chapter 4, page 134.

The general solution of these equations for a fixed edge circular plate with a uniform loading was

$$\alpha(\rho) = \frac{\varepsilon}{4\delta\gamma^{*2}} \frac{2(I_o(\gamma^*) - I_o(\gamma^*\rho))}{\gamma^* I_1(\gamma^*)} - \rho^2 + 1$$

$$\zeta(\rho) = \frac{\gamma^{*2}}{24\delta^2} - \frac{\rho}{16}\frac{\varepsilon^2}{\delta^2\gamma^4}\frac{I_1^2(\gamma\rho) - I_o(\gamma\rho)I_2(\gamma\rho)}{I_1^2(\gamma)}$$

$$- 4\frac{I_2(\gamma\rho)}{\gamma I_1(\gamma)} + \tfrac{1}{2}\rho^2 \qquad 6.3$$

where the value of γ^* satisfying the loading condition was determined from the following non-linear relationship

$$\varepsilon^2 = \frac{\frac{1}{3}\gamma^{*6}}{\frac{3}{4} - \frac{1}{2}\left(\frac{I_o(\gamma^*)}{I_1(\gamma^*)}\right)^2 - \frac{I_o(\gamma^*)}{\gamma^* I_1(\gamma^*)} + \frac{4}{\gamma^{*2}}} \qquad 6.4$$

The equations were nondimensionalised for comparison with 4.18,4.19 given that I_o, I_1 and I_2 were modified Bessel functions of the zero, first and second order respectively.

Schmidt[6.9] noted that the solutions obtained for the non-linear deflections of circular plates were relatively insensitive to the values of Poisson's ratio and therefore rearranged the Von Karman's equations and developed a perturbation solution based upon a parameter μ where

$$\mu = 1 - \nu$$

By substituting

$$\frac{dw}{dr} = \sum_{n=1}^{\infty} \mu^n \frac{dw_n}{dr} \qquad 6.5$$

$$w = \sum_{n=1}^{\infty} \mu^n w_n \qquad 6.6$$

$$u = \sum_{n=1}^{\infty} \mu^n u_n \qquad 6.7$$

in the governing equations and equating coefficients of parameters a series of equations were obtained which could be successively integrated. It was of major interest that the first resultant equations were identical to those derived from the assumption of Berger. As was indiciated, if the Poisson's ratio was assumed to be equal to unity[6.9] then the second membrane strain invariant was

eliminated from the strain energy equation. This argument was further pursued to claim a physical justification for Berger's governing equations, although it should be noted that the Poisson's ratio can never be greater than 0.5. Further work was carried out by Schmidt et al[6.10] extending this perturbation technique to non-symmetric non-linear deflection of a circular plate.

All the techniques discussed above gave solutions to the Von Karman equations with varying degrees of accuracy and complexity of calculation. However they were not easily adapted for use on a computer.

Therefore the development of a numerical technique to represent and solve the equations governing the non-linear deflection of a circular plate was studied, with emphasis on obtaining a method of representation which was capable of being used to solve the static and dynamic case.

6.2 NON - LINEAR NUMERICAL TECHNIQUES

As pointed out by Haisler[6.11],in the last ten years considerable research effort has been involved in obtaining solutions to structural problems involving geometrical non-linearity. The resultant increase in papers on this topic has paralleled the availablity of the large high speed computer and the development of increasingly efficient numerical alogrithms has made studies of these problems either possible or economically feasible. A paper by Murthy et al[6.12], dealing specifically with non-linear bending of elastic plates of variable profile, references in the introduction the exponents of the various techniques of solution of the non-linear plate problem, and as such is of value.

Since no generalised theory for the numerical solution of non-linear equations exists, there has developed a large range of techniques capable of solving particular non-linear problems. The majority of these methods involve the modification of existing linear numerical techniques.

Finite element techniques have been used for non-linear transient analysis of plates[6.13,6.14,6.15]. However the initial decision on the numerical technique preceded these publications and hence a finite difference technique was considered.

6.2.1 STATIC CASE CIRCULAR PLATE.

The first case considered was the solution of the non-linear static deflection of a circular plate with a fixed edge condition and governed by the following equations,

$$\frac{d^4\alpha}{d\rho^4} + \frac{2}{\rho}\frac{d^3\alpha}{d\rho^3} - \frac{1}{\rho^2}\frac{d^2\alpha}{d\rho^2} + \frac{1}{\rho^3}\frac{d\alpha}{d\rho} = \frac{\varepsilon}{\delta} + 12\delta^2\left(\frac{d^2\alpha}{d\rho^2} + \frac{1}{\rho}\frac{d\alpha}{d\rho}\right)$$

$$\left(\frac{d\zeta}{d\rho} + \tfrac{1}{2}\left(\frac{d\alpha}{d\rho}\right)^2 + \frac{\nu\zeta}{\rho}\right) + 12\delta^2\left(\frac{d\alpha}{d\rho}\right)\left(\frac{d^2\zeta}{d\rho^2} + \frac{\nu}{\rho} - \frac{d\zeta}{d\rho} - \frac{\nu}{\rho^3}\zeta + \frac{d\alpha}{d\rho}\frac{d^2\alpha}{d\rho^2}\right)$$

$$\frac{d^2\zeta}{a\rho^2} + \frac{1}{\rho}\frac{d\zeta}{d\rho} - \frac{\zeta}{\rho^2} + \frac{d\alpha}{d\rho}\frac{d^2\alpha}{d\rho^2} + \frac{1}{2\rho}\left(\frac{d\alpha}{d\rho}\right)^2 = 0 \qquad 6.8$$

Keller et al[6.16] reported a numerical iterative computer procedure based upon a central finite difference representation of the Von Karman equations with respect to the first derivative of deflection $\frac{d\alpha}{d\rho}$. It was observed that the direct iteration procedure only converged for a limited range of load parameters and therefore an interpolation parameter was introduced to enhance the range for which the iteration converged.

A finite difference representation was applied by Mah[6.17] to the governing equations derived by a variational method for large non-linear deflection of a circular plate. To enable the iteration to converge for a reasonable range of deflections the following iteration scheme was used. The calculations were initially solved for a load in the linear deflection regime and the non-linear solution obtained. Subsequently the non-linear terms from the previous solution were used when the calculations were repeated, following the load being incrementally increased. As the deflection and non-linearity increased, the incremental load step was decreased to further extend the convergence range of the iteration scheme.

To numerically determine the deflection and stress levels, it was decided that the use of a central finite difference representation of the spatial relationship in the governing equation would best allow a method which could be used in the static and dynamic cases.

Initially the numerical solution was based on a modified form of the Von Karman equations.

$$\frac{d^2\phi}{dr^2} + \frac{1}{r}\frac{d\phi}{dr} - \frac{\phi}{r^2} = \frac{\phi N_r}{D} + \frac{1}{rD}\int_o^r (q(r)rdr \qquad 6.9$$

$$\frac{d^2u}{dr^2} + \frac{1}{r}\frac{du}{dr} - \frac{u}{r^3} = -(\phi\frac{d\phi}{dc} + \frac{1-\nu}{2r}(\phi)^2) \qquad 6.10$$

where

ϕ = $\frac{dw}{dr}$

w = Vertical deflection

u = Radial deflection

r = Radial position

q(r) = Applied load

D = Flexural rigidity

ν = Poisson's ratio

Advantage was taken of the identical form of the left hand sides of the equations of moment and radial equilibrium; the equation 6.9 being initially solved for slope or first derivative of the vertical deflection with respect to radius and the second equation 6.10 for radial deflection only. It was also noted that for the fixed edge circular plate, the boundary conditions for the slope and radial deflection were identical.

$$\phi_{r=0} = 0, \quad u_{r=0} = 0$$
$$\phi_{r=a} = 0, \quad u_{r=a} = 0 \qquad 6.11$$

Substituting central finite difference equations for the derivatives on the left hand side of the equation resulted in the following difference relationships for the ith pivotal point for the jth iteration where i= 2,3,4, . . . n-2,n-1 given that the plate was divided radially into n equidistant pivotal points excluding the boundaries:

$$\phi_{j,i+1}\left(1+\frac{1}{i}\right) - \phi_{j,i}\left(2+\frac{1}{i^2}\right) + \phi_{j,i-1}\left(1-\frac{1}{i}\right)$$
$$= \frac{\Delta r^2}{D}\left((\phi N_r)_{j-1,i} + \frac{1}{i\Delta r}\sum_{\ell=0}^{i} q(\ell\Delta r)\,\ell\,\Delta r\,\Delta r\right) \qquad 6.12$$

$$u_{j,i+1}\left(1+\frac{1}{i}\right) - u_{j,i}\left(2+\frac{1}{i^2}\right) + u_{j,i-1}\left(1-\frac{1}{i}\right)$$
$$= -\Delta r^2\left(\phi\frac{d\phi}{dr} + \frac{1-\nu}{i\Delta r}\phi^2\right)_{j-1,i} \qquad 6.13$$

where , $\Delta r = \frac{a}{n+1}$

Applying the boundary conditions at r=0 gave the following for the first pivotal point.

$$2\phi_{j,2} - 3\phi_{j,1} = \frac{\Delta r^2}{D}\left((\phi N_r)_{j-1,1} + \frac{1}{\Delta r}q(\Delta r)\Delta r^2\right) \qquad 6.14$$

$$2u_{j,2} - 3u_{j,1} = -\Delta r^2\left(\phi\frac{d\phi}{dr} + \frac{1-\nu}{\Delta r}\phi^2\right)_{j-1,1} \qquad 6.15$$

while the nth pivotal point gave

$$-\phi_{j,n}(2 + \frac{1}{n^2}) + \phi_{j,n-1}(1 - \frac{1}{n})$$

$$= \frac{\Delta r^2}{D}((\phi N_r)_{j-1,n} + \frac{1}{n\Delta r}\sum_{\ell=0}^{n} q(\ell\Delta r)\ell\Delta r\Delta r) \qquad 6.16$$

$$-u_{j,n}(2 + \frac{1}{n^2}) + u_{j,n-1}(1 - \frac{1}{n})$$

$$= -\Delta r^2((\phi\frac{d\phi}{dr}) + \frac{1 - \nu}{n\Delta r}(\phi)^2)_{j-1,n} \qquad 6.17$$

The grouping of the equations 6.12 - 6.17 gave the matrix relationships

$$\underline{K'}\,\underset{\sim}{\phi} = \underset{\sim}{L'} + \underset{\sim}{F'}_1 \qquad 6.18$$

$$\underline{K'}\,\underset{\sim}{u} = \underset{\sim}{F'}_2 \qquad 6.19$$

where $\underline{K'}$ = Matrix of Coefficients

$\underset{\sim}{L'}$ = Load Vector

$\underset{\sim}{F'}_1$ = Vector of equivalent pseudo-loads containing the non-linear terms

$\underset{\sim}{F'}_2$ = Vector of equivalent pseudo-loads containing the non-linear terms.

The solution involved a deferred-correction method, Appendix I , at each iteration step to determine both the slope and radial deflection with an iterative technique to correct the non-linear terms and allow convergence on the correct result as is shown by the flow diagram 6.1,page 175.

It was found that the program solved the problem and converged for the range of deflection under consideration in the transducer operation without requiring any form of interpolation technique. The advantage of the initial method for solving the static deflection was that it involved an identical co-efficient matrix for each of the governing equations which simplified the

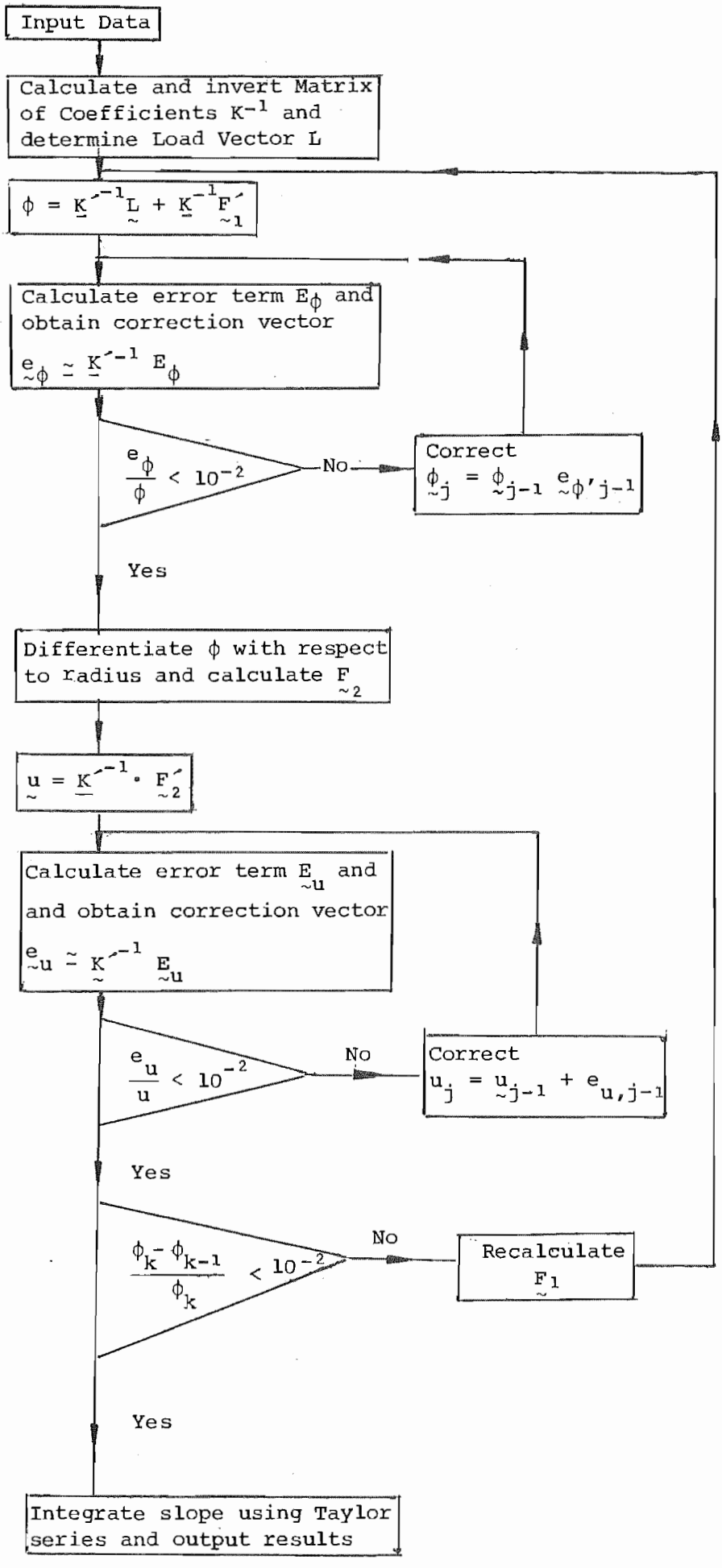

FIGURE 6.1 FLOW DIAGRAM OF STATIC CENTRAL DIFFERENCE PROGRAM FOR SLOPE

programming. This resulted in an efficient use of memory, a reduced program development time as well as optimising the computer execution time required for solution because only a single matrix inversion was required. With appropriate modification of the coefficient matrix, boundary conditions other than those associated with the clamped edge could be and were considered. However this resulted in different coefficient matrices for the vertical and radial governing equations. Hence two coefficient matrices were generated and inverted which eliminated the advantages discussed above.

The disadvantage of this technique was that the matrix operation gave the slope rather than the vertical deflection, and hence any subsequent adaption of the program to solve the dynamic deflection of the circular plate or circular plate/foundation combination became numerically difficult.

Therefore a second numerical technique was used to obtain the following representation of the nondimensional governing equation 6.8 by substitution of the finite difference equations given in Appendix J for the ith pivotal point and the jth iteration where i = 1,2,3,4.....n-3,n-2

$$(1 + \frac{1}{i} + \frac{1}{12i^2} - \frac{1}{12i^3})\alpha_{j,i+2} + (-4 - \frac{2}{i} - \frac{4}{3i^2} + \frac{2}{3i^3})\alpha_{j,i+1}$$

$$+ (6 + \frac{5}{2i^2})\alpha_{j,i} + (-4 + \frac{2}{i} - \frac{4}{3i^2} - \frac{2}{3i^2})\alpha_{j,i-1} + (1 - \frac{1}{i} + \frac{1}{12i^2}$$

$$+ \frac{1}{12i^3})\alpha_{j,i-2} = \Delta\rho^4(\frac{\varepsilon_i}{\delta}) + \Delta\rho^4 .12\delta^2((\frac{d^2\alpha}{d\rho^2} + \frac{1}{\rho}\frac{d\alpha}{d\rho})(\frac{d\zeta}{d\rho} + \tfrac{1}{2}(\frac{d\alpha}{d\rho})^2 + \frac{\nu}{\rho}\zeta)$$

$$+ \frac{d\alpha}{d\rho}(\frac{d^2\zeta}{d\rho^2} + \frac{\nu}{\rho}(\frac{d\zeta}{d\rho}) - \frac{\nu}{\rho^2}\zeta + \frac{d\alpha}{d\rho}\frac{d^2\alpha}{d\rho^2}))_{j-1,i} \qquad 6.20$$

$$(-\frac{1}{12} - \frac{1}{12i})\zeta_{j,i+2} + (\frac{4}{3} + \frac{2}{3i})\zeta_{j,i+1} + (\frac{5}{2} - \frac{1}{i^2})\zeta_{j,i} + (\frac{4}{3} - \frac{2}{3i})\zeta_{j,i-1}$$

$$+ (-\frac{1}{12} + \frac{1}{12i})\zeta_{j,i-2} = -\Delta\rho^2(\frac{d\alpha}{d\rho}\frac{d^2\alpha}{d\rho^2} + \frac{1-\nu}{2\rho}\frac{d\alpha}{d\rho})_{j-1,i} \qquad 6.21$$

where n was the number of equidistant pivotal points excluding the boundaries $\rho = 0$ and $\rho = 1$

$$\Delta\rho = \frac{1}{n}$$

$$\rho = i\Delta\rho$$

Now at the boundary $\rho = 0$, according to the analysis presented in Chapter Four page 137 the governing equation became,

$$3\frac{d^4\alpha}{d\rho^4} = \frac{\varepsilon}{\delta} + 24\delta^2(1+\nu)\frac{d^2\alpha}{d\rho^2}\cdot\frac{d\alpha}{d\rho} \qquad 6.22$$

which on substitution for the derivatives from Appendix J gave the relationship

$$18\alpha_{j,0} - 24\alpha_{j,1} + 6\alpha_{j,2} = \Delta\rho^2\left(\frac{\varepsilon_o}{\delta} + 24\delta^2(1-\nu)\left(\frac{d^2\alpha}{d\rho^2}\right)\left(\frac{d\zeta}{d\rho}\right)\right)_{j-1,0} \qquad 6.23$$

using the bounding condition $\left(\frac{d\alpha}{d\rho}\right)_{\rho=0} = 0$.

At the pivotal point i=1 the following equations were obtained for the initial vertical and radial deflections.

$$-4\alpha_{j,0} + 8\frac{2}{3}\alpha_{j,1} - 6\frac{2}{3}\alpha_{j,2} + 2\alpha_{j,3} = \Delta\rho^4\left(\frac{\varepsilon_1}{\delta}\right) + \Delta\rho^4\, 12\delta^2$$

$$\left(\left(\frac{d^2}{d^2} + \frac{1}{\Delta\rho}\frac{d\alpha}{d\rho}\right)\left(\frac{d\zeta}{d\rho} + \tfrac{1}{2}\left(\frac{d\alpha}{d\rho}\right)^2 + \frac{\nu}{\Delta\rho}\zeta\right) + \frac{d\alpha}{d\rho}\left(\frac{d^2\zeta}{d\rho^2} + \frac{\nu}{\rho}\left(\frac{d\zeta}{d\rho}\right) - \frac{\nu}{\rho^2}\zeta\right.\right.$$

$$\left.\left. + \frac{d\alpha}{d\rho}\frac{d^2\alpha}{d\rho^2}\right)\right)_{j-1,i} \qquad 6.24$$

$$-\frac{7}{2}\zeta_{j,1} + 2\zeta_{j,2} - \frac{1}{6}\zeta_{j,3} = -\Delta\rho^2\left(\frac{d\alpha}{d\rho}\frac{d^2\alpha}{d\rho^2} + \frac{1-\nu}{2\Delta\rho}\left(\frac{d\alpha}{d\rho}\right)^2\right)_{j-1,1} \qquad 6.25$$

while at the pivotal point i= 2 for the radial equation $\zeta_{j,0}=0$ and hence the equation was

$$(-\frac{1}{12}-\frac{1}{12_j})\ \zeta_{j,i+2}+(\frac{4}{3}+\frac{2}{3i})\ \zeta_{j,i+1}+(\frac{5}{2}-\frac{1}{i^2})\ \zeta_{j,i}$$

$$+(\frac{4}{3}-\frac{2}{3i})\ \zeta_{j,i-1}=-\Delta\rho^2(\frac{d\alpha}{d\rho}\frac{d^2\alpha}{d\rho^2}+\frac{1-\nu}{2\rho}(\frac{d\alpha}{d\rho})^2)_{j-1,i} \qquad 6.26$$

The equations for the pivotal point i=n-1 was

$$(-4-\frac{2}{i}-\frac{4}{3i^2}+\frac{2}{3i^3})\alpha_{j,i+1}+(6+\frac{5}{2i^2})\alpha_{j,i}+(-4+\frac{2}{i}-\frac{4}{3i^2}-\frac{2}{3i^3})\alpha_{j,i-1}$$

$$+(1-\frac{1}{i}+\frac{1}{12i^2}+\frac{1}{12i^3})\alpha_{j,i-2}=\Delta\rho^4\ (\frac{\varepsilon_i}{\delta})+\Delta\rho^4\ 12\delta^2$$

$$((\frac{d^2\alpha}{d\rho^2}+\frac{1}{\rho}\frac{d\alpha}{d\rho})(\frac{d\zeta}{d\rho}+\tfrac{1}{2}(\frac{d\alpha}{d\rho})^2+\frac{\nu}{\rho}\zeta)+\frac{d\alpha}{d\rho}(\frac{d^2\zeta}{d\rho^2}+\frac{\nu}{\rho}\frac{d\zeta}{d\rho}$$

$$-\frac{\nu}{\rho}\zeta+\frac{d\alpha}{d\rho}\ \frac{d^2\alpha}{d\rho^2}))_{j-1,i} \qquad 6.27$$

$$(\frac{4}{3}+\frac{2}{3i})\zeta_{j,i+1}+(-\frac{5}{2}-\frac{1}{i^2})\zeta_{j,i}+(\frac{4}{3}-\frac{2}{3i})\zeta_{j,i-1}+(-\frac{1}{12}+\frac{1}{12i})\zeta_{j,i-2}$$

$$=-\Delta\rho^2(\frac{d\alpha}{d\rho}\frac{d^2\alpha}{d\rho^2}+\frac{1-\nu}{2\rho}(\frac{d\alpha}{d\rho})^2)_{j-1,i} \qquad 6.28$$

while the equations for the pivotal point i=n were

$$(7+\frac{1}{i}+\frac{31}{12}\frac{1}{i^2}-\frac{1}{12i^3})\alpha_{j,i}+(-4+\frac{2}{i}-\frac{2}{3i^2}-\frac{2}{3}\frac{1}{i^3})\alpha_{j,i-1}$$

$$+(1-\frac{1}{i}+\frac{1}{12i^2}+\frac{1}{12i^3})\alpha_{j,i-2}=\Delta\rho^4(\frac{\varepsilon_i}{\delta})+\Delta\rho^4\ 12\delta^2$$

$$((\frac{d^2\alpha}{d\rho^2}+\frac{1}{\rho}\frac{d\alpha}{d\rho})(\frac{d\zeta}{d\rho}+\tfrac{1}{2}(\frac{d\alpha}{d\rho})^2+\frac{\nu}{\rho}\zeta)+\frac{d\alpha}{d\rho}(\frac{d^2\zeta}{d\rho^2}+\frac{\nu}{\rho}\frac{d\zeta}{d\rho}-$$

$$\frac{\nu}{\rho^2}\zeta+(\frac{d\alpha}{d\rho})(\frac{d^2\alpha}{d\rho^2}))_{j-1,i} \qquad 6.29$$

$$(-\frac{5}{2}-\frac{1}{i^2}+((1+\frac{1}{i})(-\frac{1}{2(i+1)}/12\ (1+\frac{1}{2(i+1)}))\zeta_{j,i}+(\frac{4}{3}-\frac{2}{3_i})\zeta_{j,i-1}$$

$$+(-\frac{1}{12}+\frac{1}{12i})\zeta_{j,i-2}=-\Delta\rho^2((\frac{d\alpha}{d\rho})(\frac{d\alpha}{d\rho}\frac{d^2\alpha}{d\rho^2}+\frac{1-\nu}{2\rho}(\frac{d\alpha}{d\rho})^2)_{j-1,i} \qquad 6.30$$

Hence the grouping of the equations 6.20 - 6.30 gave the matrix relationships

$$\underline{\underline{K}}_{\alpha}\,\underset{\sim}{\alpha} = \underset{\sim}{L} + \underset{\sim}{F}_1 \qquad 6.31$$
$$\underline{\underline{K}}_{\zeta}\,\underset{\sim}{\zeta} = \underset{\sim}{F}_2$$

Where $\underline{\underline{K}}_{\alpha}$ = Matrix of coefficients for vertical deflection.

$\underset{\sim}{L}$ = Load Vector

$\underset{\sim}{F}_1$ = Vector of equivalent pseudo-loads containing the non-linear terms in the moment equilibrium equation.

$\underline{\underline{K}}_{\zeta}$ = Matrix of coefficients for radial deflection.

$\underset{\sim}{F}_2$ = Vector of equivalent pseudo-loads containing the non-linear terms in the radial equilibrium equations.

$\underset{\sim}{\alpha}$ = Vector of vertical nondimensional deflections for the pivotal points.

$\underset{\sim}{\zeta}$ = Vector of radial nondimensional deflection for the pivotal points.

As for the previously described method of solution a deferred -correction scheme, Appendix I , was applied at each iteration step to the vertical and radial deflection within an iterative technique to account for the non-linearity. To obtain convergence over the required range of deflections $0 < \delta\alpha < 1.5$ a simple averaging interpolation technique was applied to each iteration step. The program logic is shown in the flow diagram Fig 6.2,page 180. On convergence being satisfied a further iteration was carried out to confirm the correct value had been obtained.

The advantage of this method of representing the governing equations at the pivotal points was the capability of the program to be modified to enable the solution of the non-linear deflection of a circular plate/foundation combination. This was due to the direct representation of vertical deflection rather than the slope as in the previous case. The method also could be used in the solution for the dynamic transient loading of both the circular plate and the circular plate/foundation combinations undergoing non-linear deflection. This was simplified by the direct representation of the

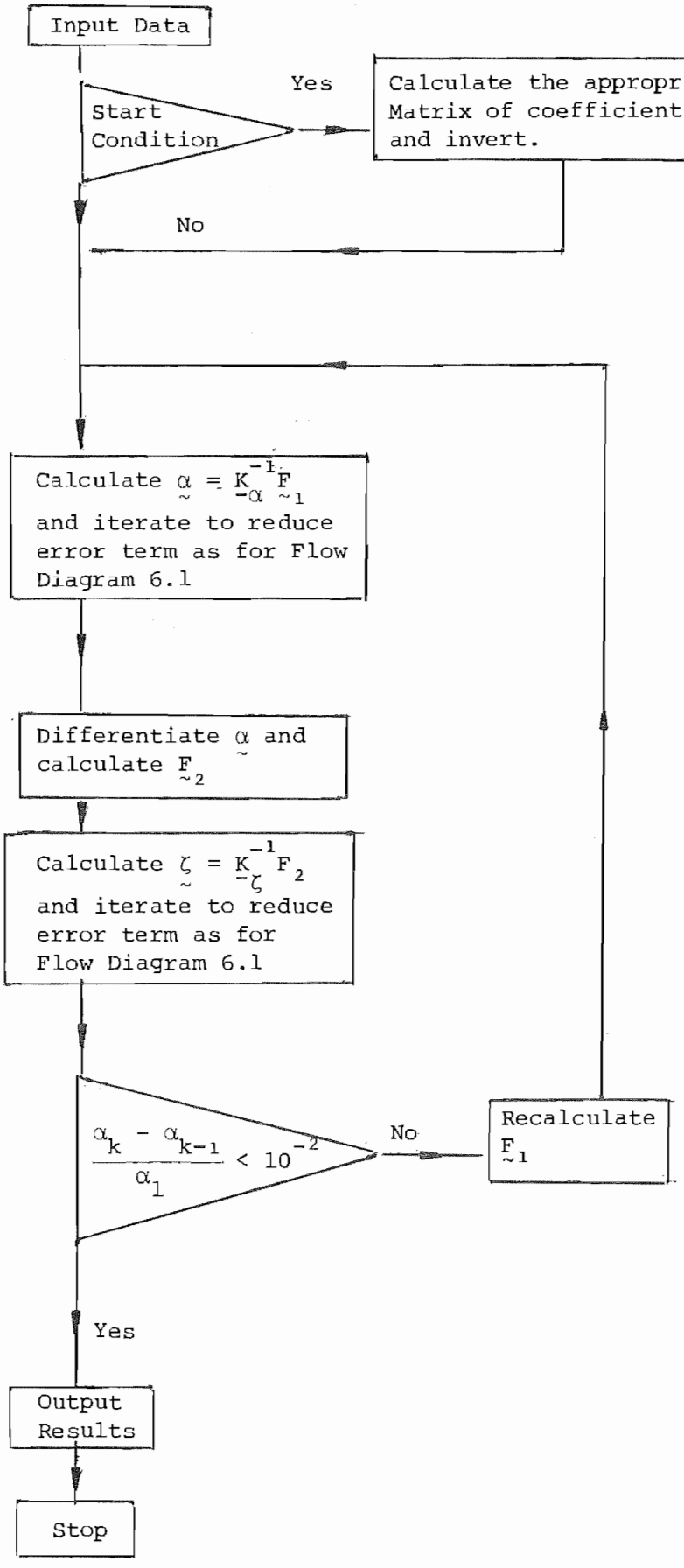

FIGURE 6.2 FLOW DIAGRAM OF NON-LINEAR STATIC CENTRAL DIFFERENCE PROGRAM

applied load and acceleration at a pivotal point, rather than the integral of the moment of these forces from the centre of the plate to the particular pivotal point as occurred in the previous technique.

To verify the accuracy of the spatial representation for the governing equation, solutions from the numerical program were compared with results from the well-known analytical model,

$$\alpha = \frac{\varepsilon}{64} \times 12(1 - \nu^2)(1 - \rho^2)^2 \qquad (6.32)$$

of static linear deflection for a fixed edge plate. The radial profiles for deflection, Fig 6.3 page 182, slope Fig 6.4 page 182 and second derivative $\frac{d^2\alpha}{d\rho^2}$, Fig 6.5 page 183 were obtained.

Since the non-linear term in the governing equation is a function of slope and second derivative, and numerical differentiation has inherent inaccuracies, the error profile is presented for 40 radial pivotal points, Fig 6.6 page 183. The load parameter value of 15 was used which gave a central deflection $\delta\alpha_o$ of 2.56, which was twice the anticipated deflection range for the subsequent use of the program. The large apparent percentage errors were a function of the values of the dependent variables approaching zero. The absolute magnitude of errors for slope and second derivative over the range of step size $\Delta\rho = 1/20$ to $\Delta\rho = 1/50$ was 0.004 to 0.002 with the relevant magnitudes of the dependent variables being that shown in Figs 6.2 - 6.5

While the selection of a large number of pivotal points in the radial direction reduced the error in the initial determination of the deflection, it increased the computational effort and therefore on the basis of the above results, a spatial step size of 1/30 was considered adequate.

Results of non-linear static deflection were compared with results from the literature[4.4] and using the Berger relationship equations 6.1 & 6.2. The central deflection was plotted against load parameter as can be seen in Fig 6.7 page 184, while Fig 6.8

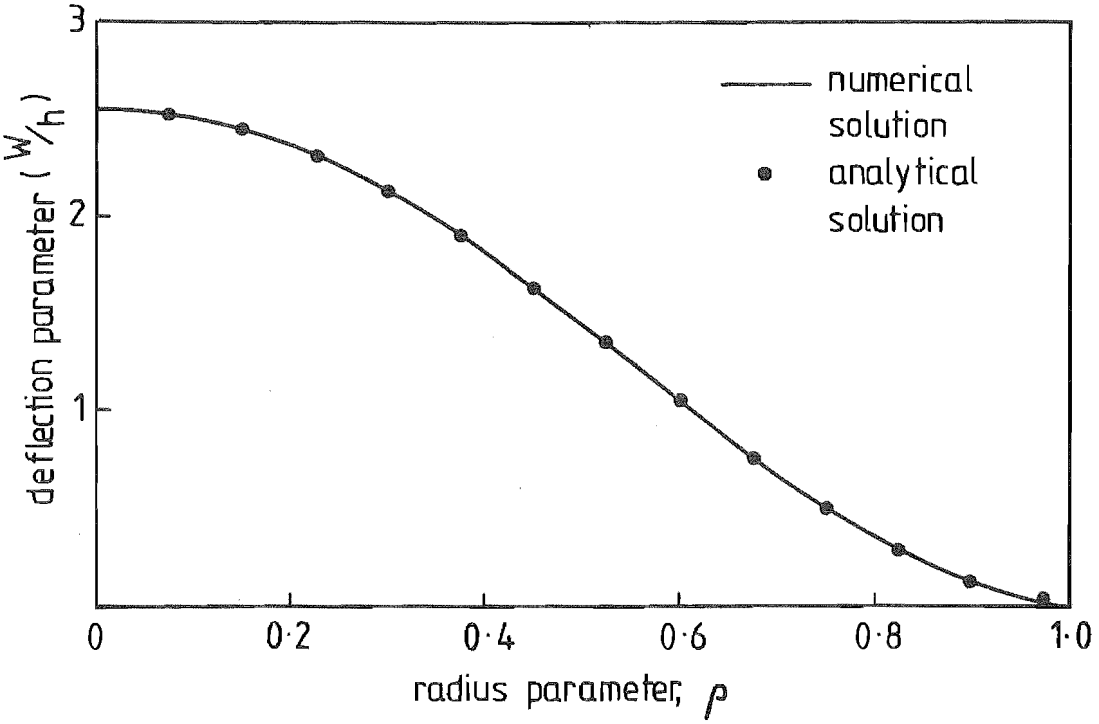

FIG. 6·3 LINEAR DEFLECTION PROFILE FOR $E = 15$, $\nu = 0{\cdot}3$ $\delta = 40$, $\Delta\rho = 1/40$

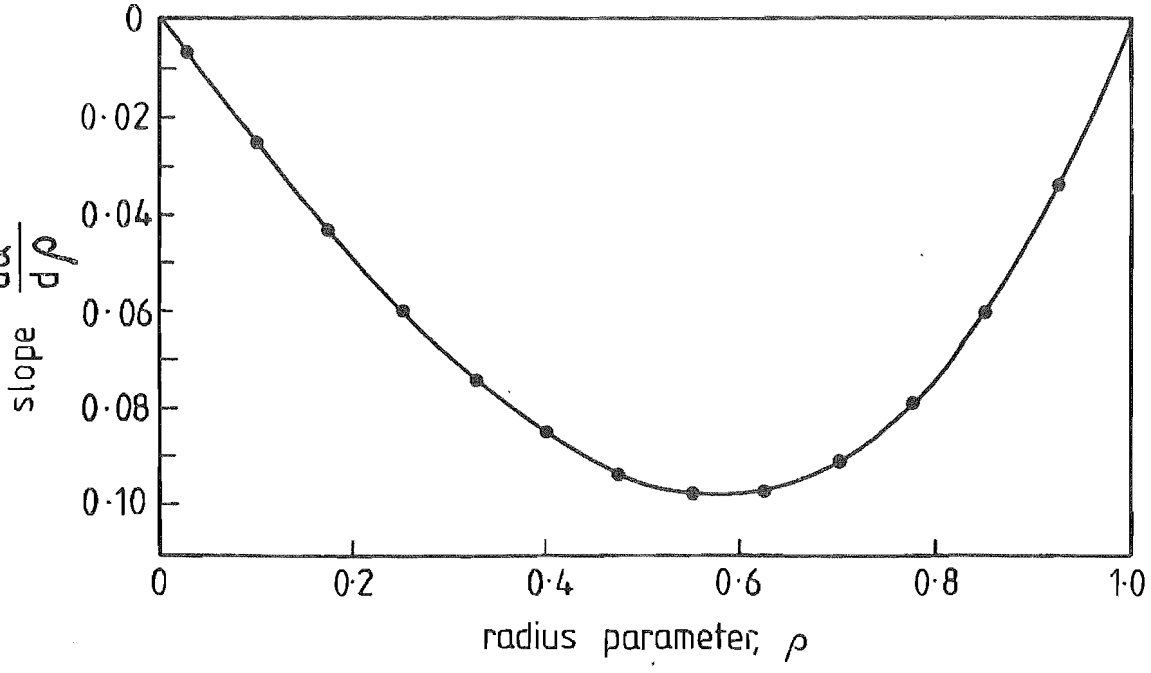

FIG. 6·4 PROFILE OF SLOPE FOR LINEAR CASE $E = 15$, $\nu = 0{\cdot}3$ $\delta = 40$, $\Delta\rho = 1/40$

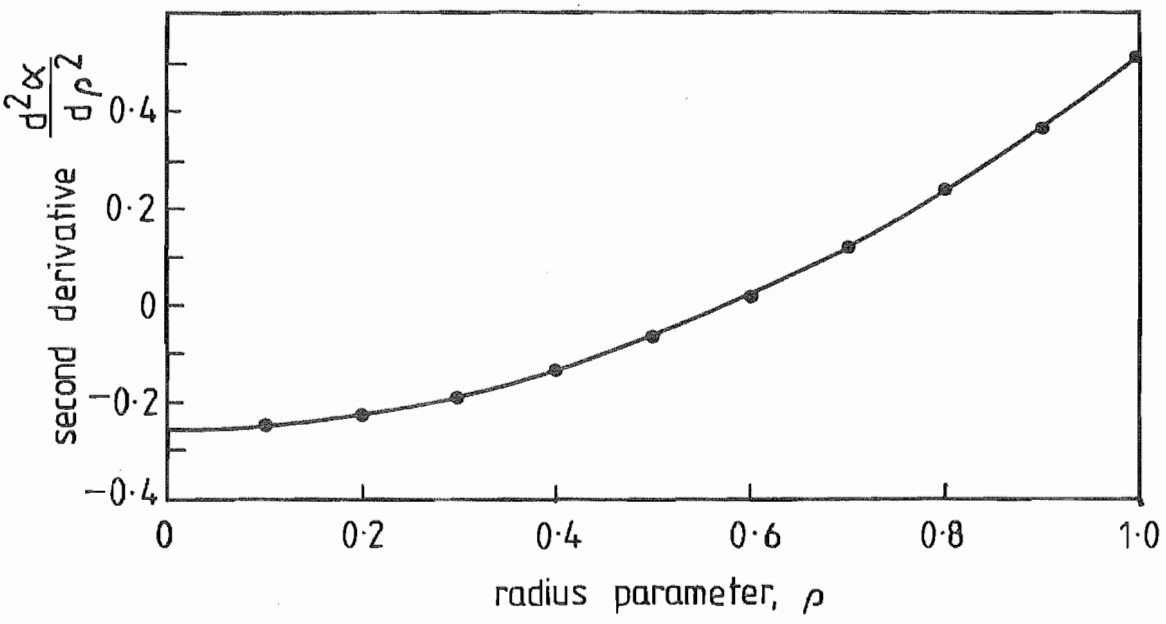

FIG. 6·5 PROFILE OF SECOND DERIVATIVE FOR LINEAR CASE

$\varepsilon = 15,\ \nu = 0{\cdot}3,\ \delta = 40,\ \Delta\rho = 1/40$

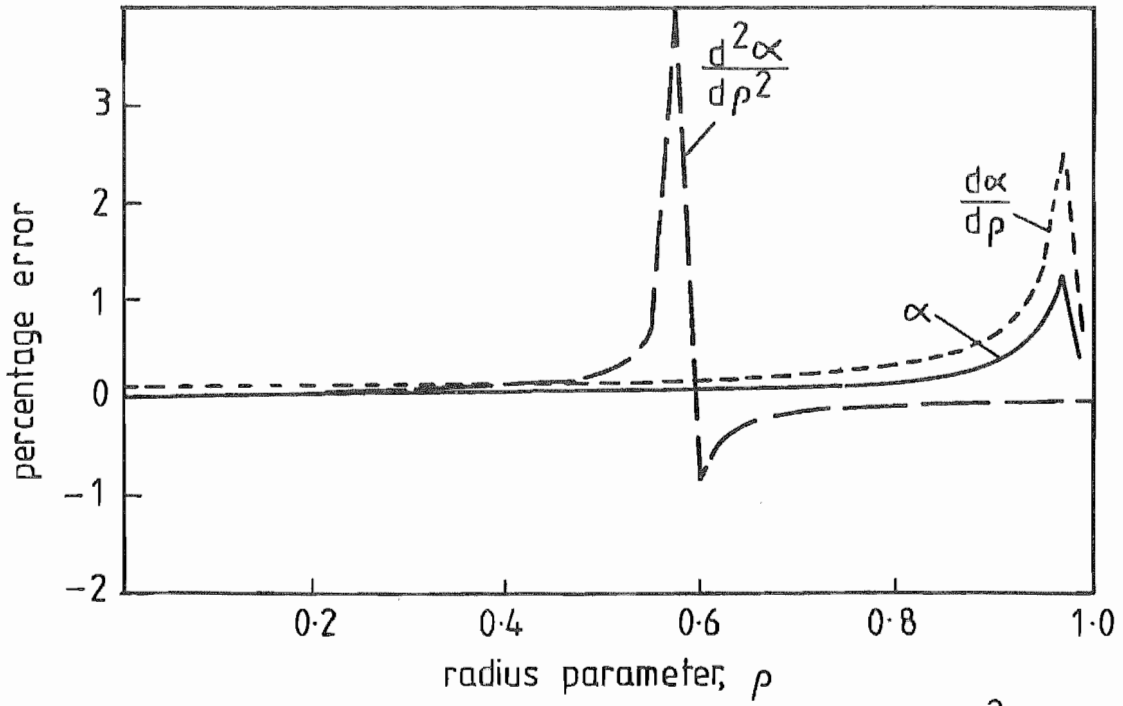

FIG 6·6 PERCENTAGE ERROR IN DEFLECTION, $\frac{d\alpha}{d\rho}$ AND $\frac{d^2\alpha}{d\rho}$ FOR LINEAR CASE $\varepsilon = 15,\ \nu = 0{\cdot}3,\ \delta = 40,\ \Delta\rho = 1/40$

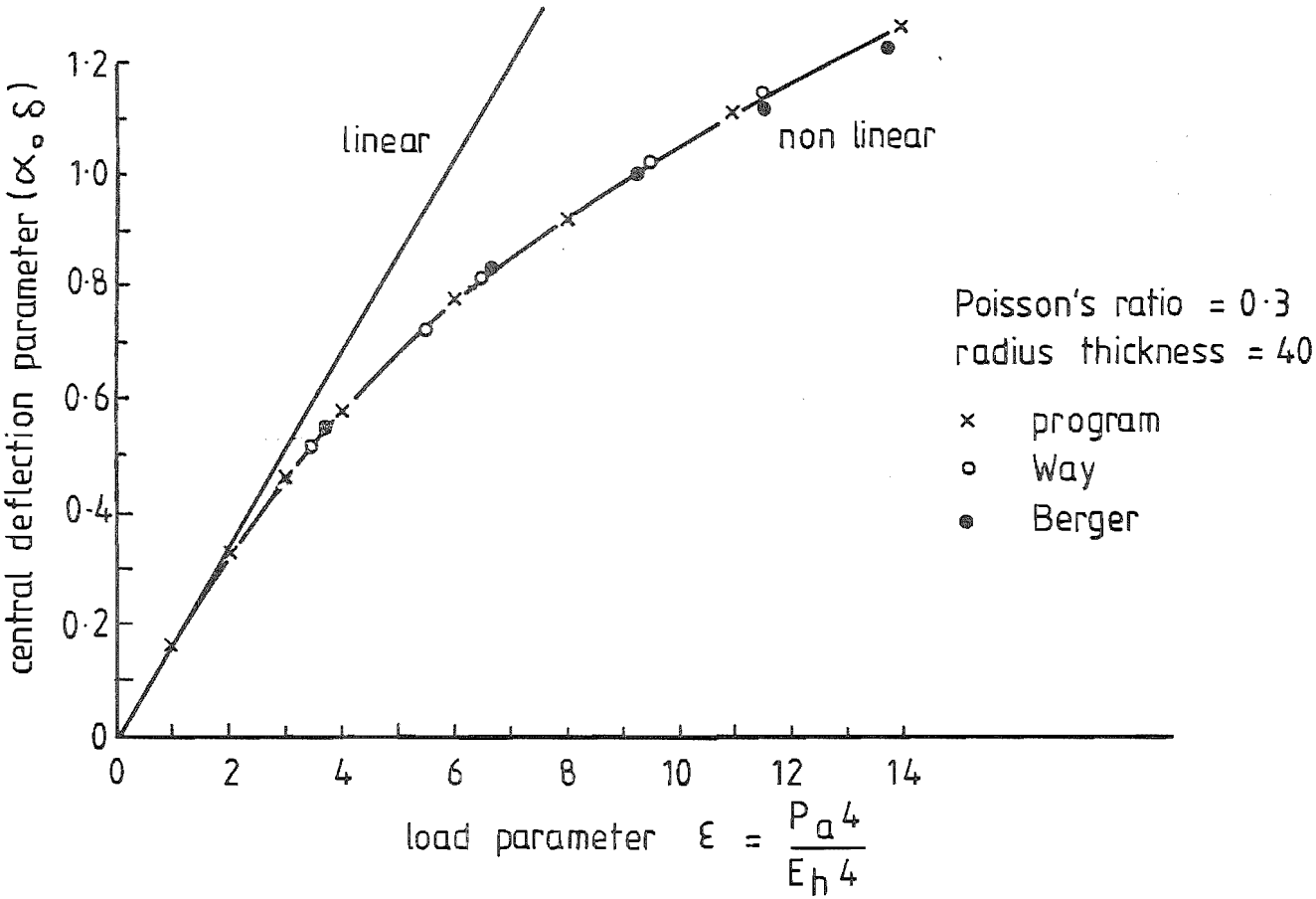

FIG 6·7 CENTRAL DEFLECTION vs LOAD PARAMETER $\nu = 0{\cdot}3$

page 186 gives the central and edge radial bending stress in relation to the central deflection. Finally, there is a plot of central membrane stress and radial edge membrane stress against central deflection, Fig 6.9 page 187 . The profile of the radial in-plane deflection is shown in Fig. 6.10 page 188 and the discrepancy between the finite difference technique applied to the Von Karman equations and the Berger assumption can be seen. The vertical deflection profile Fig. 6.11 page 189 shows good agreement.

As can be seen the progam results agree with those from the exact solution after Way[4.4] and with the exception of the central membrane stress, coincides with those obtained from the Berger's equations. Hence it was considered that the spatial finite difference scheme adequately described the non-linear behaviour of the plate.

6.2.2 STATIC CASE: CIRCULAR PLATE WITH FOUNDATION.

The equations governing the deflection of a circular plate on an elastic Pasternak foundation were

$$F(w) = k_f(w) - G_f \bar{\nabla}^2 (w) \qquad 6.33$$

where the foundation characteristic in terms of the nondimensional parameters was given by

$$F^*(\alpha) = k^*\alpha - G^*\nabla^2\alpha \qquad 6.34$$

where $F^*(\alpha)$ = Reactive Nondimensional force

G^* = Nondimensional Pasternak constant 6.35

k^* = Nondimensional Klinker constant

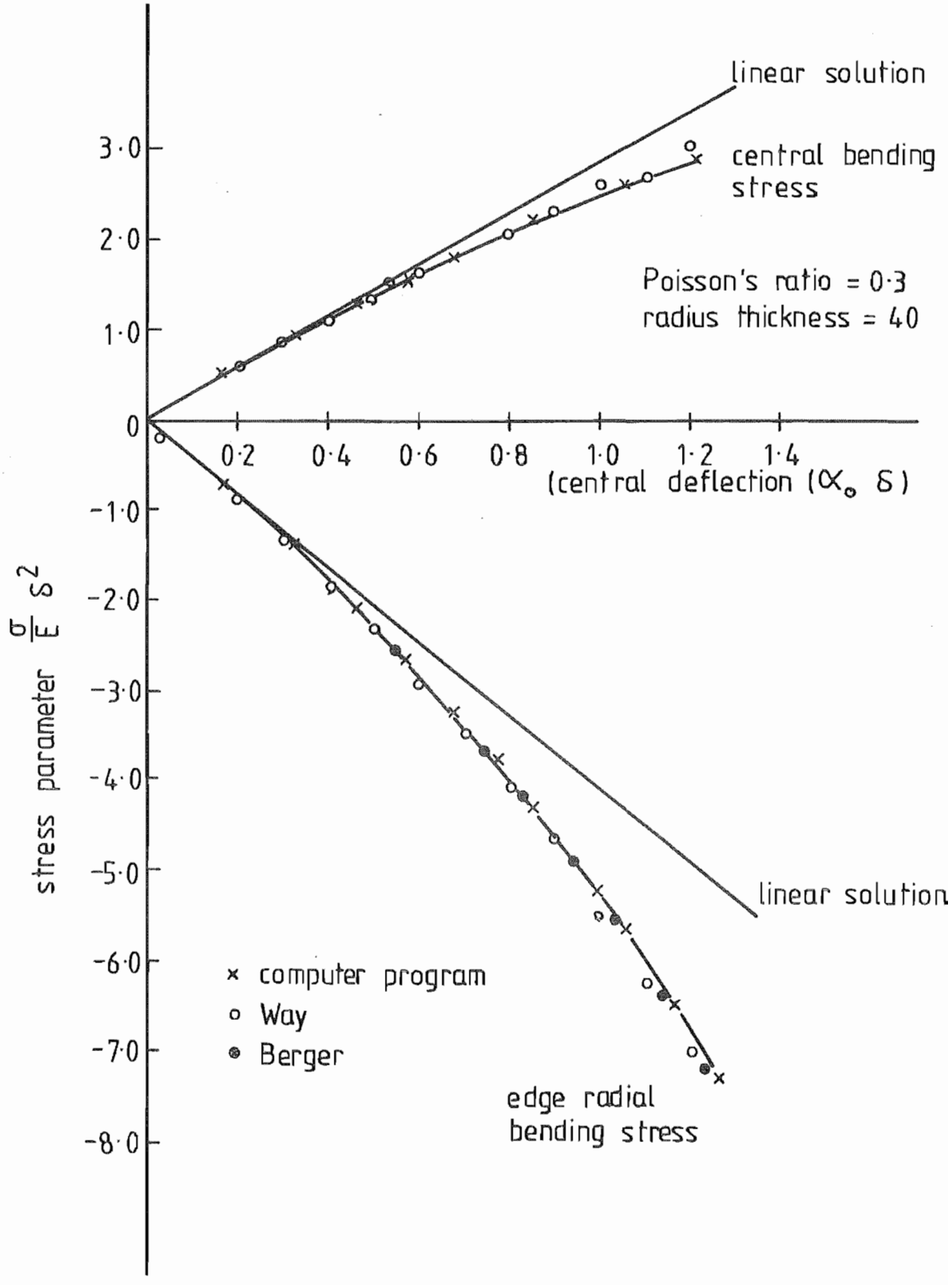

FIG 6·8 BENDING STRESS vs CENTRAL DEFLECTION

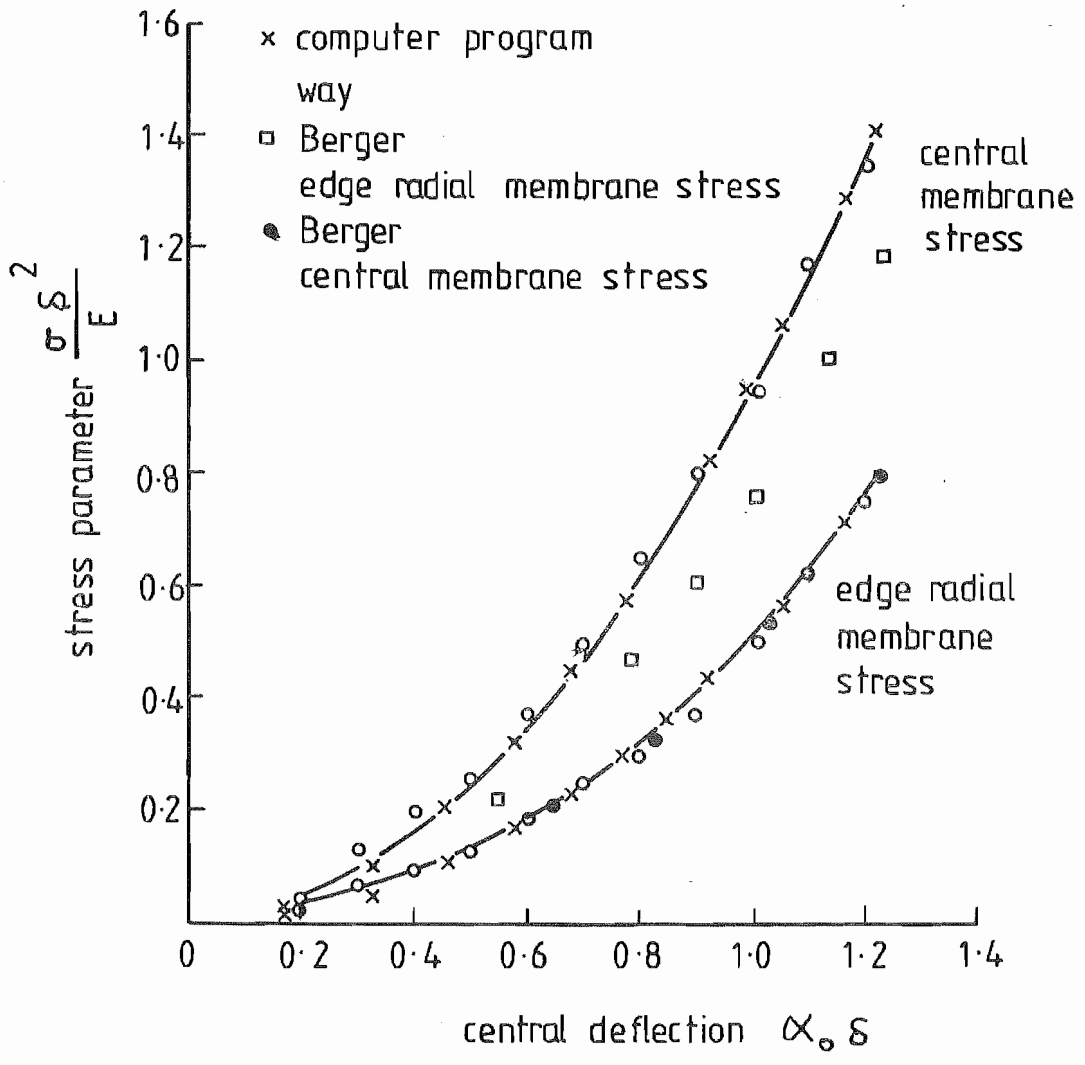

FIG 6·9 BENDING MEMBRANE STRESS vs CENTRAL DEFLECTION

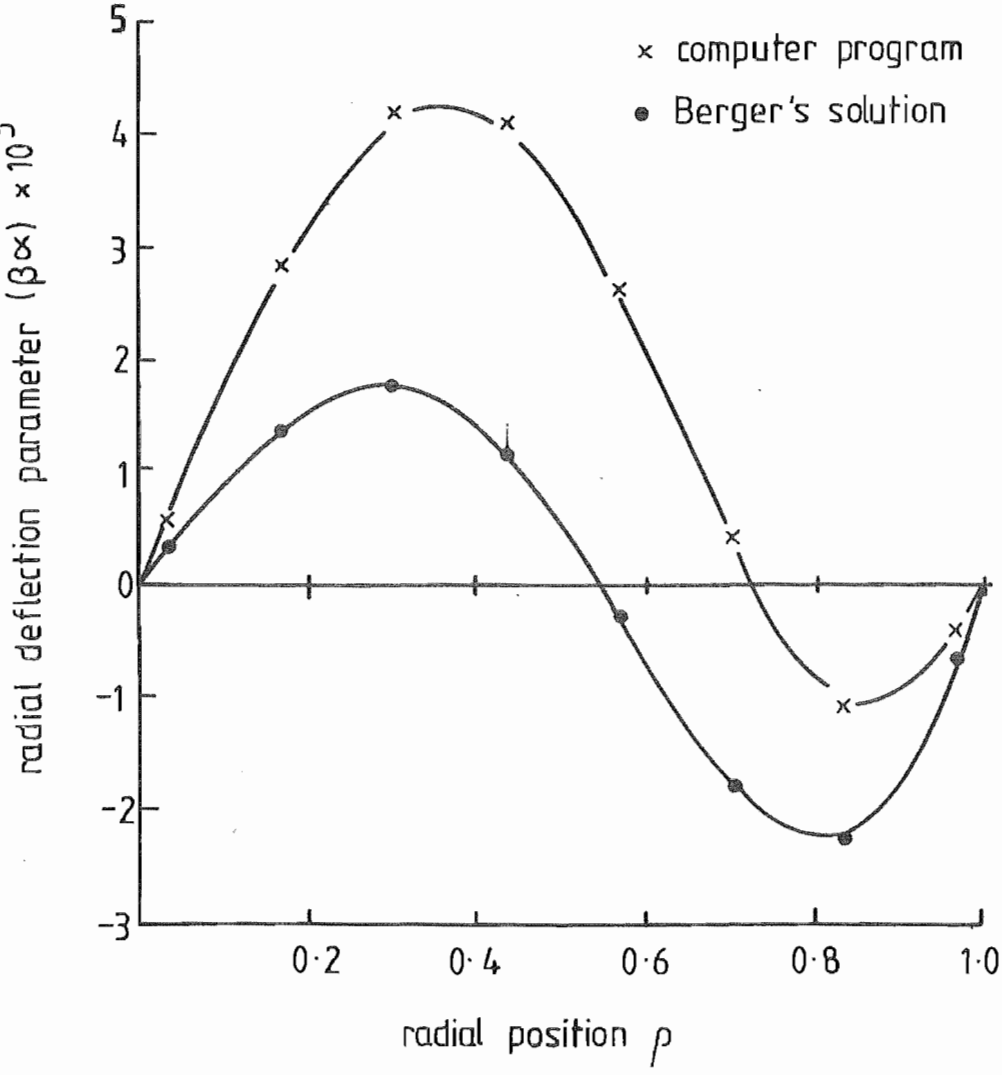

FIG 6·10 RADIAL IN-PLANE DEFLECTION vs RADIAL POSITION FOR $\varepsilon = 10$, $\lambda = 0{\cdot}3$, $\delta = 40{\cdot}0$

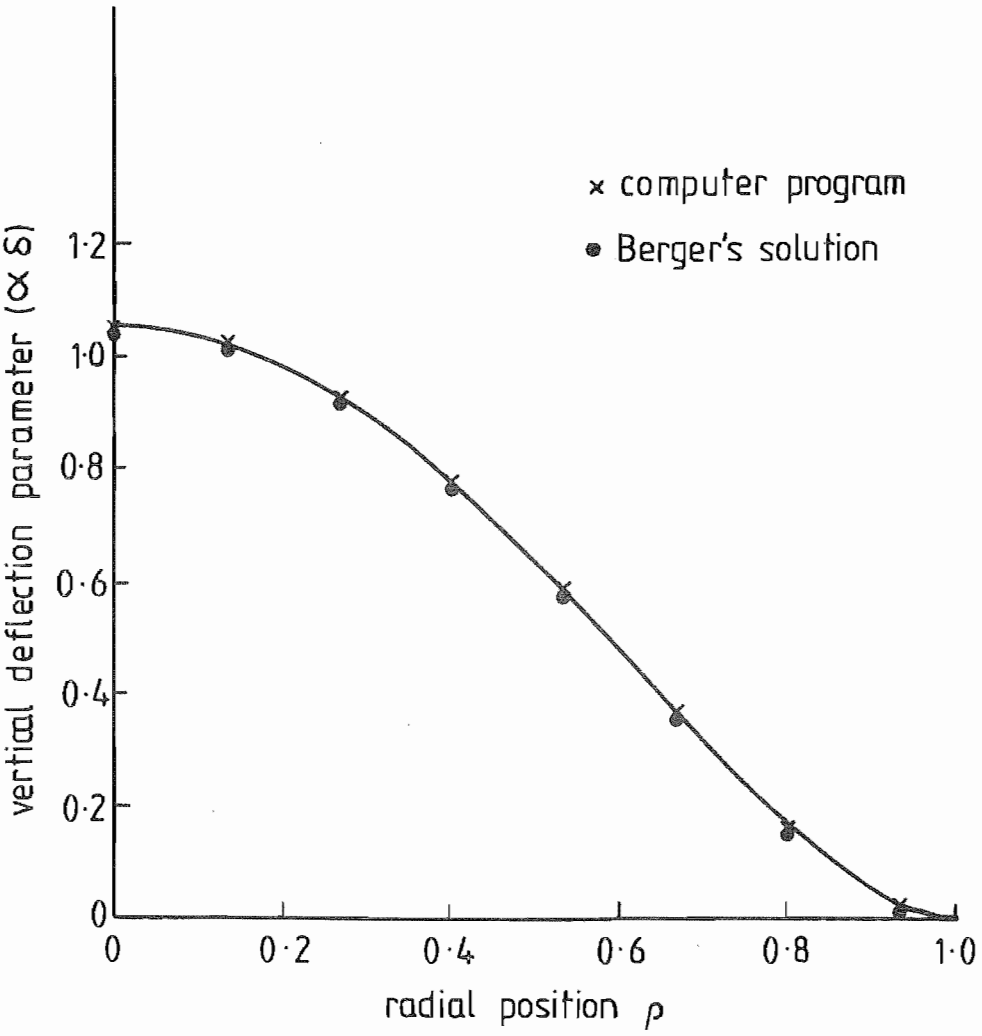

FIG 6·11 VERTICAL DEFLECTION vs RADIAL POSITION FOR $\varepsilon = 10, \lambda = 0{\cdot}3, \delta = 40$

Therefore applying the difference equations Appendix J, the reaction can be restated as follows

$$F^*(\alpha) = k^*\alpha_i - \frac{G^*}{\Delta\rho^2}\,\alpha_{i+2}\left(-\frac{1}{12} - \frac{1}{12_i}\right) + \alpha_{i+1}\left(\frac{4}{3} + \frac{1}{6_i}\right)$$

$$+ \alpha_i\left(-\frac{5}{6} - \frac{1}{2_i}\right) + \alpha_{i-1}\left(\frac{4}{3} - \frac{1}{6_i}\right) + \alpha_{i-2}\left(-\frac{1}{12} + \frac{1}{12_i}\right) \qquad 6.35$$

and applying the same boundary conditions as for the plate equation it being noted at the boundary $\rho = 0$ that the equation reduces to

$$F^*(\alpha)_{\rho=0} = k^*\alpha_o - \frac{2G^*}{\Delta\rho^2}\left(\alpha_2\left(-\frac{1}{12}\right) + d_1\left(\frac{4}{3}\right) + \alpha_o\left(-\frac{5}{6}\right) + \alpha_{-1}\left(\frac{4}{3}\right)\right.$$

$$\left. + \alpha_2\left(-\frac{1}{12}\right)\right) \qquad 6.36$$

The matrix of coefficient can be modified as follows,

$$\underline{K}'\,\underset{\sim}{\alpha} = \underline{K}_{\alpha}\,\underset{\sim}{\alpha} + \underline{R}\,\underset{\sim}{\alpha} \qquad 6.37$$

where the foundation reaction defined by

$$\underline{F}^*\,\underset{\sim}{\alpha} = \underline{R}\,\underset{\sim}{\alpha}$$

and $\underline{R}$ = Matrix ofcoefficients for foundation reaction

$\underline{K}'_{\alpha}$ = Matrix of coefficients for vertical deflection of plate/foundation combination

Hence the problem can be solved by using the same procedure as for the plate case with the alternative matrix of coefficients $\underline{K}'_{\alpha}$, Fig 6.2 page 180.

The Winkler foundation characteristic can be solved as a special case of the Pasternak foundation if G = 0.0. The results from S.N. Sinha's work [6.3] gave a basis of comparison with those obtained from the program, Fig 6.12 page 191 , and the plot of central deflection against load parameter for a range of foundation characters shows the agreement between the methods. The work of Sinha considered a Winkler foundation and by using Berger's assumption obtained a solution to equations governing the non-linear

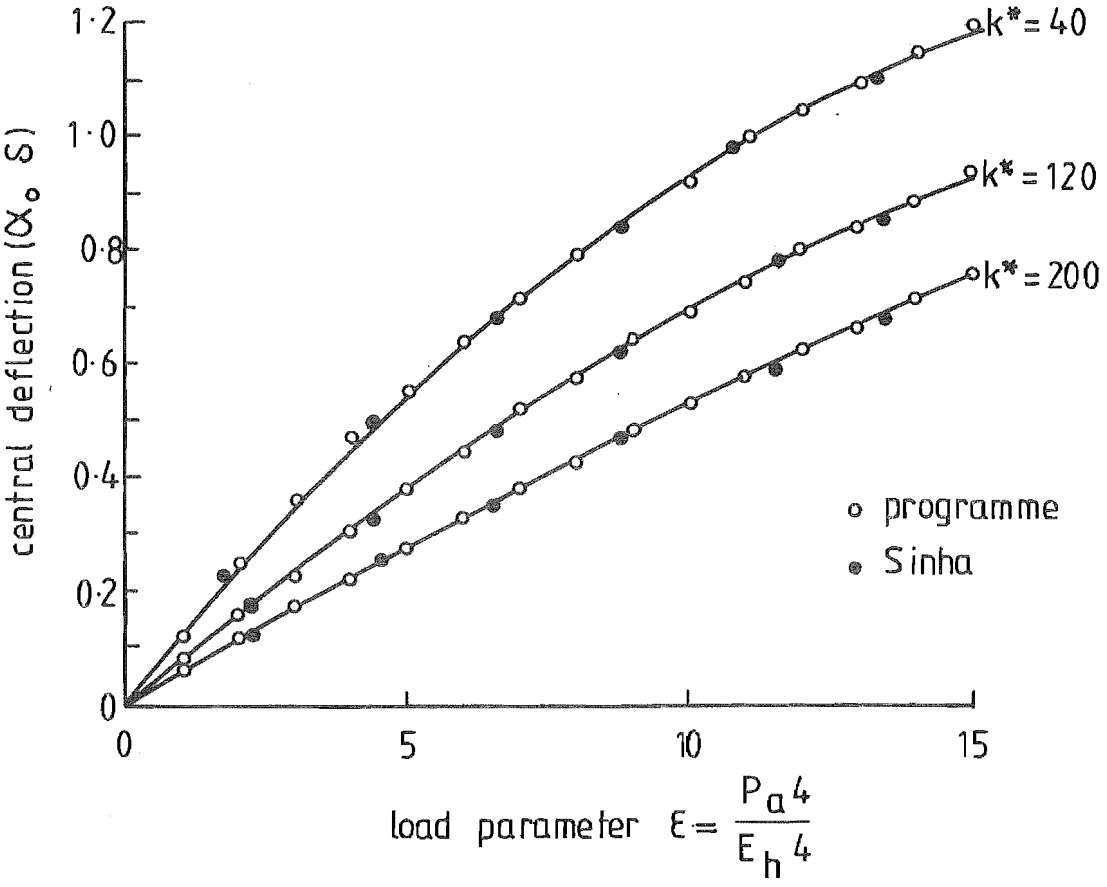

FIG 6·12 CENTRAL DEFLECTION vs LOAD PARAMETER FOR WINKLER FOUNDATION $\lambda = 0{\cdot}3$

deflection of a circular plate on an elastic foundation.

$$\nabla^4\alpha - 12\delta^2\left(\frac{d\zeta}{d\rho} + \tfrac{1}{2}\left(\frac{d\alpha}{d\rho}\right)^2 + \frac{\zeta}{\rho}\right)\nabla^2\alpha + k^*\alpha = \frac{\varepsilon}{\delta}$$

$$\frac{d\zeta}{d\rho} + \tfrac{1}{2}\left(\frac{d\alpha}{d\rho}\right)^2 + \frac{\zeta}{\rho} = \frac{\gamma^2}{12\delta^2} \qquad 6.38$$

6.2.3 DYNAMIC CASE CIRCULAR PLATE/FOUNDATION

The equations governing the dynamic transient non-linear deflection of a circular plate were the dynamic form of the Von Karman equations.

$$\frac{\partial^4\alpha}{\partial\rho^4} + \frac{2}{\rho}\frac{\partial^3\alpha}{\partial\rho^3} - \frac{1}{\rho^2}\frac{\partial^2\alpha}{\partial\rho^2} + \frac{1}{\rho^3}\frac{\partial\alpha}{\partial\rho} - \left(\frac{\partial^2\alpha}{\partial\rho^2} + \frac{1}{\rho}\frac{\partial\alpha}{\partial\rho}\right) + k^*\alpha$$

$$= \frac{\varepsilon(\rho,\tau)}{\delta} - \frac{\partial^2\alpha}{\partial\tau^2} - \chi\frac{\partial\alpha}{\partial\tau} + 12\delta^2\left(\frac{\partial^2\alpha}{\partial\rho^2} + \frac{1}{\rho}\frac{\partial\alpha}{\partial\rho}\right)\left(\frac{\partial\zeta}{\partial\rho} + \tfrac{1}{2}\left(\frac{\partial\alpha}{\partial\rho}\right)^2\right.$$

$$\left. + \frac{\nu}{\rho}\zeta + 12\delta^2\left(\frac{\partial^2\alpha}{\partial\rho}\right)\left(\frac{\partial^2\zeta}{\partial\rho^2} + \frac{\nu}{\rho}\frac{\partial\zeta}{\partial\rho} - \frac{\nu}{\rho^2}\zeta + \frac{\partial\alpha}{\delta\rho}\frac{\partial^2\alpha}{\partial\rho^2}\right) = 0\right.$$

$$\frac{\partial^2\zeta}{\partial\rho^2} + \frac{1}{\rho}\frac{\partial\zeta}{\partial\rho} - \frac{\zeta}{\rho^2} + \frac{\partial\alpha}{\partial\rho}\frac{\partial^2\alpha}{\partial\rho^2} + \frac{1-\nu}{2\rho}\left(\frac{d\alpha}{d\rho}\right)^2\Big) = 0 \qquad 6.39$$

The technique of representation for the spatial pivotal points was identical to that used in the solution of the static case, and the time domain could be represented by either a direct integration operator or a reccurence scheme.

6.2.3.1 TIME DOMAIN The second order equation governing the behaviour in the time domain for the plate/foundation combination was

$$\underline{\underline{M}}\,\ddot{\underset{\sim}{\alpha}} + \underline{\underline{C}}\,\dot{\underset{\sim}{\alpha}} + \underline{\underline{K}}\,\underset{\sim}{\alpha} + \underset{\sim}{F} = 0 \qquad 6.40$$

where $\underline{K}$ = Matrix of Coefficients

$\underline{C}$ = The nondimensional viscous damping coefficient

$\underline{M}$ = 1 following the form of the time nondimensional parameter used.

and the dot denotes partial differentiation with respect to nondimensional time.

As discussed by Argyris et al[6.18] when considering the first order dynamic equation, M = 0, in relation to diffusion analysis, the time domain could be represented by either modal analysis such as in Chapter 5, or recurrence relationship/direct integration operators in a discrete step by step procedure.

The modal analysis required the separation of the spatial and time variable and the subsequent superposition of the orthonormalised eigenmodes to achieve the solution. The computational effort could be reduced by consideration of only the few dominant fundamental modes in typical engineering problems. However the accuracy of the solution was a function of the number of modes for which the summation was carried out.

For linear elastic problems the spatial and time representation could be decoupled since C and K were constant while F was independent of α. Therefore the dominant orthonormal eigenfunctions had only to be determined at the initiation of the solution program and the summation of the modes' contribution applied at each time interval, (see section 5.2, page 142). The forcing function could be expanded as an infinite series of the orthonormal eigenfunctions. Therefore the resultant time representation for each mode was determined from the governing equation, the initial boundary conditions in the time domain and the forcing function. For the application of this technique to obtain an exact solution to the linear case see section 5.3.

For a non-linear dynamic system where K was a function of α while F was a function of previous deflection as well as time, the orthonormalised eigenmodes had to be determined at each time step as in section 5.3, or over a limited number of time steps with an assumption of quasilinearisation between pivotal time points to ensure decoupling. Also the assumption of superposition failed and therefore the resultant solution of the geometrical non-linear deflection of the plate was inexact. This is discussed in detail in section 7.4, page 261 .

Since the determination of orthonormalised eigenmodes was demanding in computer time, and superposition failed in the case of geometrical non-linearity, the alternative recurrence relationship in the time domain was initially considered.

This method, commonly used in dynamic structural analysis, represented time as a series of finite discrete time domains and subsequently uses a specific relationship between the nodal points in time which satisfied the governing equations. This resulted in a time-stepping or recurrence solution which progressed through the time domain.

6.2.3.2 RECURRENCE RELATIONSHIP/DIRECT INTEGRATION

OPERATOR The deflection, velocity and acceleration could be represented by direct integration operators of the form,

$$\dot{\underset{\sim}{\alpha}}_{t+1} = \dot{\underset{\sim}{\alpha}}_{t} + \gamma \ddot{\underset{\sim}{\alpha}}_{t} \Delta\tau + (1 - \gamma) \ddot{\underset{\sim}{\alpha}}_{t+1} \Delta\tau$$

$$\underset{\sim}{\alpha}_{t+1} = \underset{\sim}{\alpha}_{t} + \dot{\underset{\sim}{\alpha}}_{t} \Delta\tau + \beta \ddot{\underset{\sim}{\alpha}}_{t+1} \Delta\tau \qquad 6.41$$

for the nodal points t+1 and t where $\Delta\tau$ is the time step length and γ, β were constants associated with the specific integration operator.

Alternatively Zienkiewicz[6.19] derived a recurrence relationship, based upon a finite element approximation, of the form

$$[\underline{M} + \gamma\Delta\tau\underline{C} + \beta\Delta\tau^2\underline{K}]\underset{\sim}{\alpha}_{t+1} + [-2\underline{M} + (1 - 2\gamma)\Delta\tau\underline{C} + (\tfrac{1}{2} - 2\beta+\gamma)\Delta\tau^2\underline{K}]\underset{\sim}{\alpha}_{t}$$

$$[\underline{M} - (1 -\gamma)\Delta\tau\underline{C} + (\tfrac{1}{2} + \beta - \gamma)\Delta\tau^2\underline{K}]\underset{\sim}{\alpha}_{t-1} + \underset{\sim}{\overline{f}}\,\Delta\tau^2 = 0 \qquad 6.42$$

where

$$\underset{\sim}{\overline{f}} = \underset{\sim}{f}_{t+1}\,\beta + \underset{\sim}{f}_{t}\,(\tfrac{1}{2} - 2\beta + \gamma) + \underset{\sim}{f}_{t-1}\,(\tfrac{1}{2} + \beta - \gamma)$$

and the subscripts define the nodal points in time while γ,β are specific to the particular recurrence scheme.

When selecting a scheme for the time domain the suggested criteria after H.M. Hilber et al[6.20] is

'(1) Unconditional stability when applied to linear problems
(2) No more than one set of implicit equations should have to be solved at each time step
(3) Second order accuracy
(4) Controllable algorithmic dissipation in the higher modes
(5) Self-starting'

The basis of the first condition was to ensure that the relationship was convergent and stable for a time step which allowed an economical presentation of the forcing function and from Krieg[6.21] implied an implicit scheme.

The second condition was to minimise the computer requirements for large solution schemes. Previous experience had indicated the superiority of the second order accuracy. Because of the finite number of points used to define the shape of the plate/foundation combination, the higher frequency modes could not be accurately represented. Therefore algorithmic dissipation in the higher modes was desirable to damp out any spurious contribution by these modes. However numerical dissipation in the lower modes would give rise to relative period error in the solution.

To achieve the final condition of self-starting, the algorithm should contain the initial time boundary conditions. While this criteria would suggest the time domain should be defined by a direct integration operator, at the time of developing the dynamic program a Houbolt recurrence scheme[6.22] was used and subsequently modified following Zienkiewicz, to allow a range of schemes.

For the second order dynamic equation either a three-point or four-point recurrence scheme could be applied. Initially the stability of the three-point recurrence scheme was considered, after Zienkiewicz, for viscous damping.

6.2.3.2.1 THREE POINT RECURRENCE RELATIONSHIP As had been established by using a weighted residual approach[6.19], the general three-point recurrence relationship in the time domain, for linear conditions was given by

$$[\underline{M} + \gamma\Delta\tau\underline{C} + \beta\Delta\tau^2\underline{K}]\,\underset{\sim}{\alpha}_{n+1} + [-2\underline{M} + (1 - 2\gamma)\Delta\tau\underline{C} + (\tfrac{1}{2} - 2\beta + \gamma)\Delta\tau^2\underline{K}]\,\underset{\sim}{\alpha}_{n}$$

$$+ [\underline{M} - (1 - \gamma)\Delta\tau\underline{C} + (\tfrac{1}{2} + \beta - \gamma)\Delta\tau^2\underline{K}]\,\underset{\sim}{\alpha}_{n-1} + \overline{\underset{\sim}{f}}\Delta\tau^2 = 0 \qquad 6.43$$

where

$$\bar{\underset{\sim}{f}} = \bar{\underset{\sim}{f}}_{n+1} + \underset{\sim}{f}_{n}(\tfrac{1}{2} - 2\beta + \gamma) + \underset{n-1}{f}(\tfrac{1}{2} + \beta - \gamma)$$

$\Delta\tau$ = Time increments between nodal points

β, γ = Constants dependent upon the specific recurrence relationship and are given in the Table 6.1

γ	β	Scheme
1/2	0	Central Explicit
1/2	1	Backward
1/2	1/6	Linear Accleration *
1/2	1/10	
3/2	4/5	Galerkin
1/2	1/12	Fox Goodwin
1/2	1/4	Constant Average Accleration *

TABLE 6.1 Coefficients for Three-point Recurrence scheme (after Zienkewicz)

*Note: From the Newmark family of integration schemes

The stability criteria was obtained by considering the linear equation of the general form [6.23]

$$M_i \ddot{\alpha}_i + C_i \dot{\alpha}_i + k_i \alpha_i + f_i = 0 \qquad 6.44$$

it being noted that for this case $M_i = 1$ due to the nondimensional form of time in the governing equation. As for section 5.2 , using the real eigenvalues of the free vibration

$$\omega_i^2 = k_i$$

modal decomposition was applied.

Again the homogenous equation was considered with $f_i = 0$ and a solution of the form

$$(\alpha_i)_{n+1} = \lambda^*(\alpha_i)_n$$

$$(\alpha_i)_n = \lambda^*(\alpha_i)_{n-1}$$

was assumed. Therefore substitution into the general recurrence relationship for a single degree of freedom gave the characteristic equation

$$\lambda^{*2}\,[1 + \gamma\Delta\tau C_i + \beta\Delta\tau^2 k_i] + \lambda^*[-2 + (1 - 2\gamma)\Delta\tau C_i + (\tfrac{1}{2} - 2\beta+\gamma)\Delta\tau^2 k_i]$$

$$+[1 - (1 - \gamma)\Delta\tau C_i + (\tfrac{1}{2} + \beta - \gamma)\Delta\tau^2 k_i] = 0 \qquad 6.45$$

substituting

$$q_i = \Delta\tau C_i$$

$$= 2x_i\omega_i\Delta\tau$$

$$p_i = \Delta\tau^2 k_i$$

$$= \omega_i^2\,\Delta\tau^2$$

where $x_i = \dfrac{C_i}{2\omega_i}$ and represented a fraction of the critical damping, following the definition of the nondimensional time parameter gave

$$\lambda^{*2}[1 + \gamma q_i + \beta p_i] + \gamma^*[-2 + (1 - 2\gamma)q_i + (\tfrac{1}{2} - 2\beta + \gamma)p_i]$$

$$+ [1 - (1 - \gamma)q_i + (\tfrac{1}{2} + \beta - \gamma)p_i] = 0 \qquad 6.46$$

but substituting

$$g = \frac{q_i + (\frac{1}{2} + \gamma)p_i}{1 + \gamma q_i + \beta p_i} \qquad \ell = \frac{-q_i + (\frac{1}{2} - \gamma)p_i}{1 + \gamma q_i + \beta p_i}$$

gave the roots

$$\lambda^*_{1,2} = \frac{(2 - g) \pm \sqrt{(2-g)^2 - 4(1 + \ell)}}{2} \qquad 6.47$$

For the roots to be complex and hence the procedure to be stable

$$(2 - g)^2 < 4(1 + \ell)$$

From Appendix K this gave

$$\theta_i^{*2}(4\beta - (\gamma + \tfrac{1}{2})^2) + 2\theta^*\chi_i(2\gamma - 1) + 4(1 - \chi_i^2) > 0$$

where $\theta_i^* = \omega \Delta \tau_i$

which in the case of $\chi_i = 0$ reduced to the given condition[6.23] for the undamped case

$$\theta_i^{*2}(4\beta - (\gamma + \tfrac{1}{2})^2) > -4 \qquad 6.48$$

Considering the limit condition for the inequality

$$\theta_i^{*2}(4\beta - (\gamma + \tfrac{1}{2})^2) - 2\theta_i^* \chi_i(2\gamma - 1) + 4(1 - \chi_i^2) = 0 \qquad 6.49$$

then

$$\theta^* < \frac{-2\chi_i(2\gamma-1) \pm \sqrt{4\chi_i^2(2\gamma-1)^2 - 16(4\beta-(\gamma+\frac{1}{2})^2)(1-\chi_i^2)}}{2(4\beta - (\gamma + \frac{1}{2})^2)} \qquad 6.50$$

gave the limiting condition for θ_i^* and since $\theta_i^* = \Delta\tau\omega_i$ and $\omega_i = \frac{2\pi}{T_i}$ where T_i was the period of the frequency ω_i.

$$\frac{\Delta\tau.2\pi}{T_i} < \frac{-2\chi_i(2\gamma-1) \pm \sqrt{4\chi_i^2(2\gamma-1)^2 - 16(4\beta-(\gamma+\tfrac{1}{2})^2)(1-\chi_i^2)}}{2(4\beta - (\gamma+\tfrac{1}{2})^2)} \qquad 6.51$$

As pointed out by Sharpe[6.24] from the form of the equation, unconditional stability was dependent upon

$$4\beta - (\gamma + \tfrac{1}{2})^2 = 0$$

which was independent of damping as well as being consistent with the condition obtained by that author for the case $\gamma = 1/2$, $\beta = 1/6$, in that the equation reduced to

$$\frac{\Delta\tau}{T_i} < \frac{1}{\pi}\frac{\sqrt{1 - x_i^2}}{\sqrt{1 - 4\beta}}$$

$$< \frac{\sqrt{3}}{\pi}(1 - \chi_i^2)^{\frac{1}{2}} \qquad 6.52$$

taking the positive condition.

The modulus of λ^* was required to determine if artificial numerical damping occurred and for stability had to satisfy

$$|\lambda^*| = (1 + \ell)^{\frac{1}{2}} < 1$$

Therefore squaring the term

$$-1 < \ell < 0$$

and substituting for ℓ gave

$$-1 < \frac{-2\chi_i\theta^* + (\tfrac{1}{2} - \gamma)\theta^{*2}}{1 + 2\chi_i\,\gamma\theta^* + \beta\,\theta^{*2}} < 0 \qquad 6.53$$

which again for χ_i =0, the undamped case satisfied the known relationship[6.23]

$$\gamma = \tfrac{1}{2}$$

for no algorithmic dissipation.

Conditional stability will occur for real roots of provided that

$$|\lambda_1^*, \lambda_2^*| < 1$$

Therefore the stability criteria for damped single degree of freedom systems can be presented as Fig 6.13 page 202 for $\gamma = 1/2$. It can be seen from Fig 6.13 that for the Newmark scheme $\gamma = 1/2$, $\beta = 1/6$ the results confirm those presented by Sharpe.

Plots of the modulus of the roots λ_1^* ,λ_2^* or the 'spectral' radius Figs 6.14 - Fig 6.19 pages 203 - 205 show the limit on stability as well as the influence of the combination of viscous damping and algorithmic damping for the three-point recurrence schemes. The limiting case $\chi_i = 0$ gave the results presented in other works[6.20,6.23,6.25]. It can be seen that as reported [6.20] high order modes exhibit minimal damping.

In the literature[6.20,6.25] results have been presented for undamped systems on the relative period error as a function of the time step size, Fig 6.20 page 206 . Since numerical experimentation using the results from the linear case and a modal solution was to be carried out, further analysis on the relative period error for a damped system was not considered justified.

With the recurrence scheme, for transient loading conditions, a starting procedure was required to initiate the solution. Since the initial boundary conditions for the time domain were zero velocity and displacement, to the first order of accuracy it was assumed that

$$\alpha_{-1} = \alpha_1$$

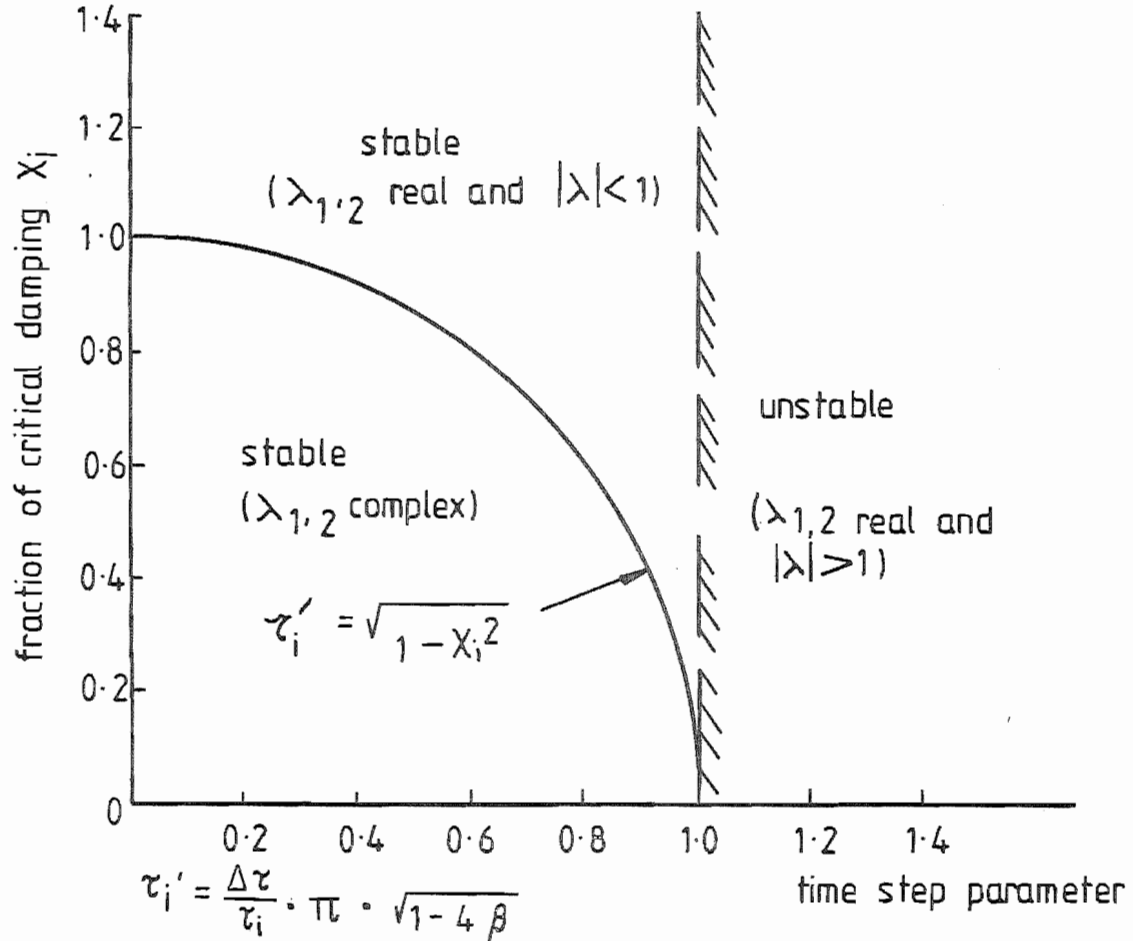

FIG 6·13 STABILITY CRITERIA FOR THREE POINT RECURRENCE SCHEME FOR SINGLE DEGREE OF FREEDOM WITH $\gamma = 1/2$

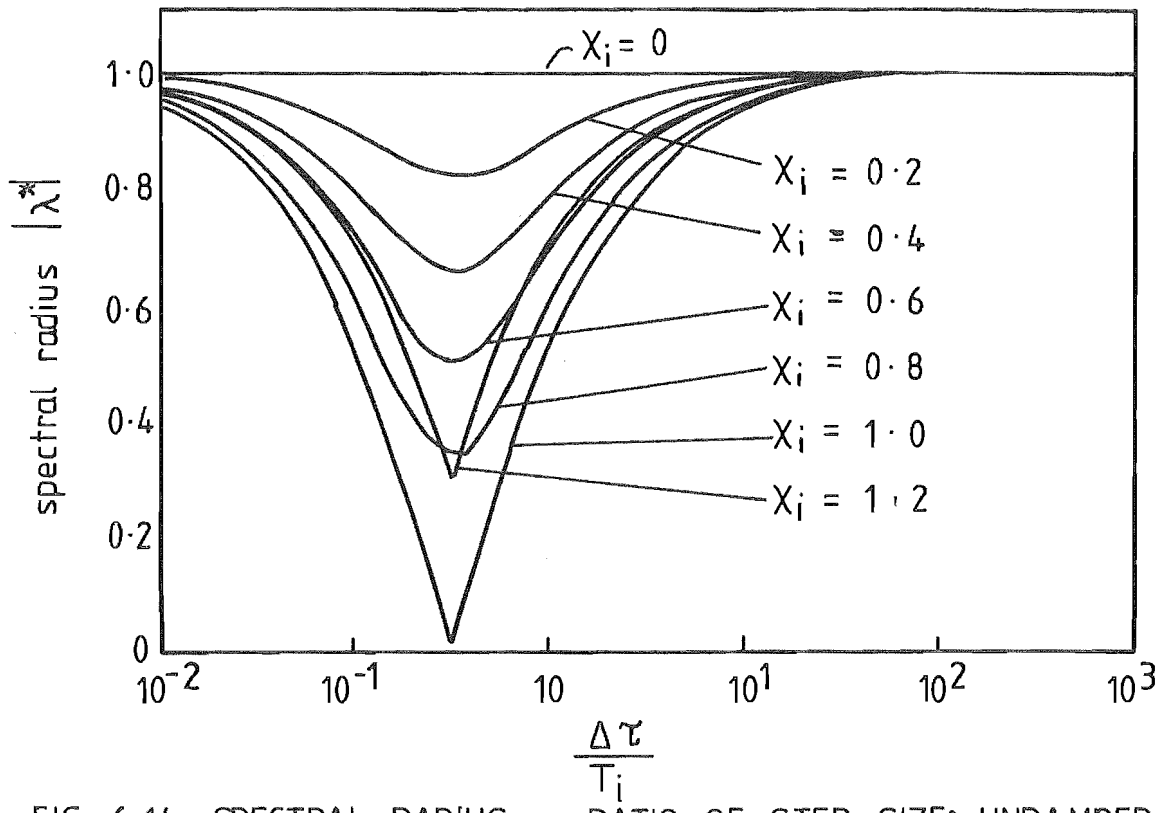

FIG 6·14 SPECTRAL RADIUS vs RATIO OF STEP SIZE: UNDAMPED PERIOD FOR VISCOUS DAMPING $\gamma = 1/2$, $\beta = 1/4$, AND X_i IS FRACTION OF CRITICAL DAMPING

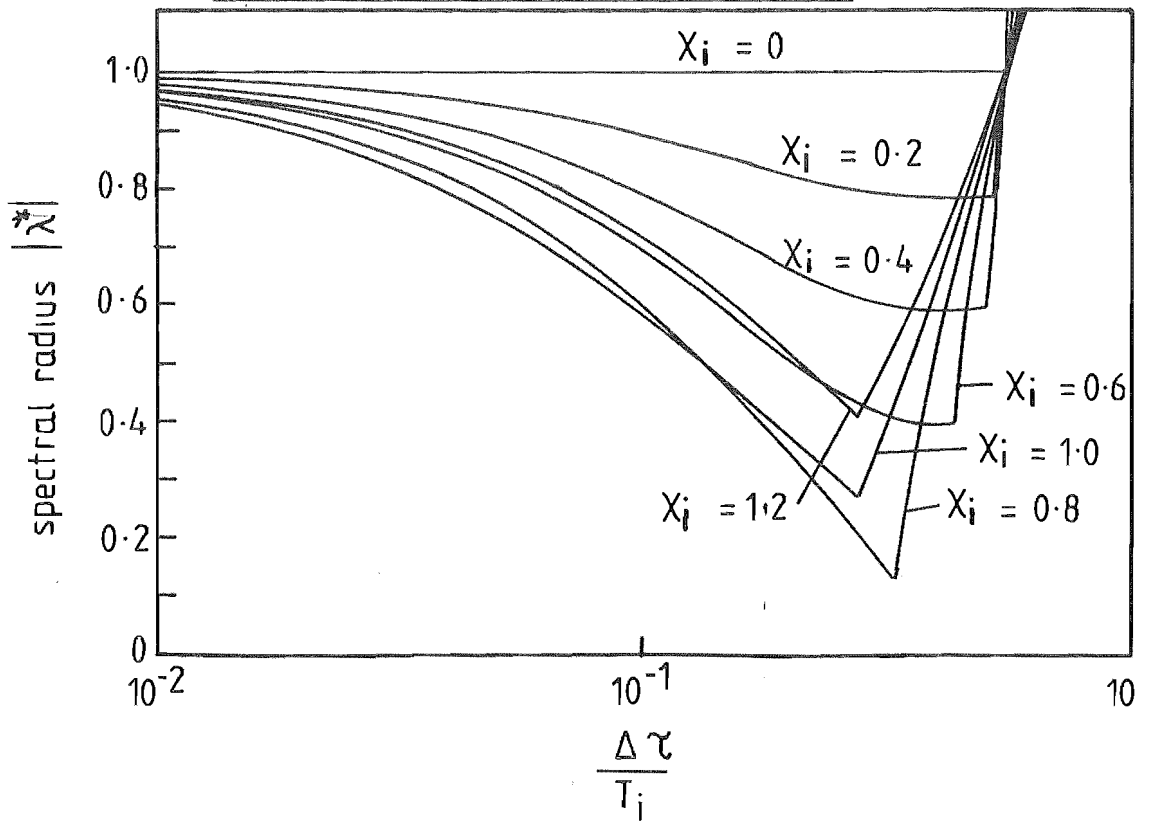

FIG 6·15 SPECTRAL RADIUS vs RATIO OF STEP SIZE: UNDAMPED PERIOD FOR VISCOUS DAMPING $\gamma = 1/2$, $\beta = 1/6$, AND X_i IS FRACTION OF CRITICAL DAMPING

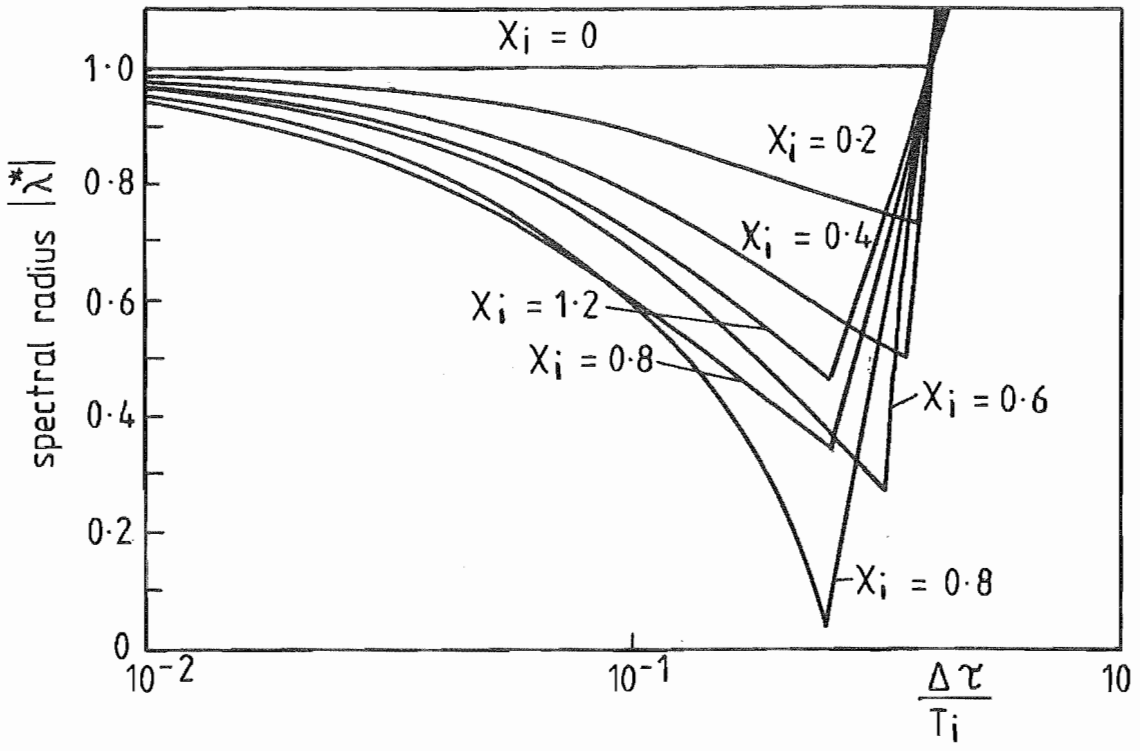

FIG 6·16 SPECTRAL RADIUS vs RATIO OF STEP SIZE: UNDAMPED PERIOD FOR VISCOUS DAMPING $\gamma = 1/2$ $\beta = 1/10$ X_i IS FRACTION OF CRITICAL DAMPING

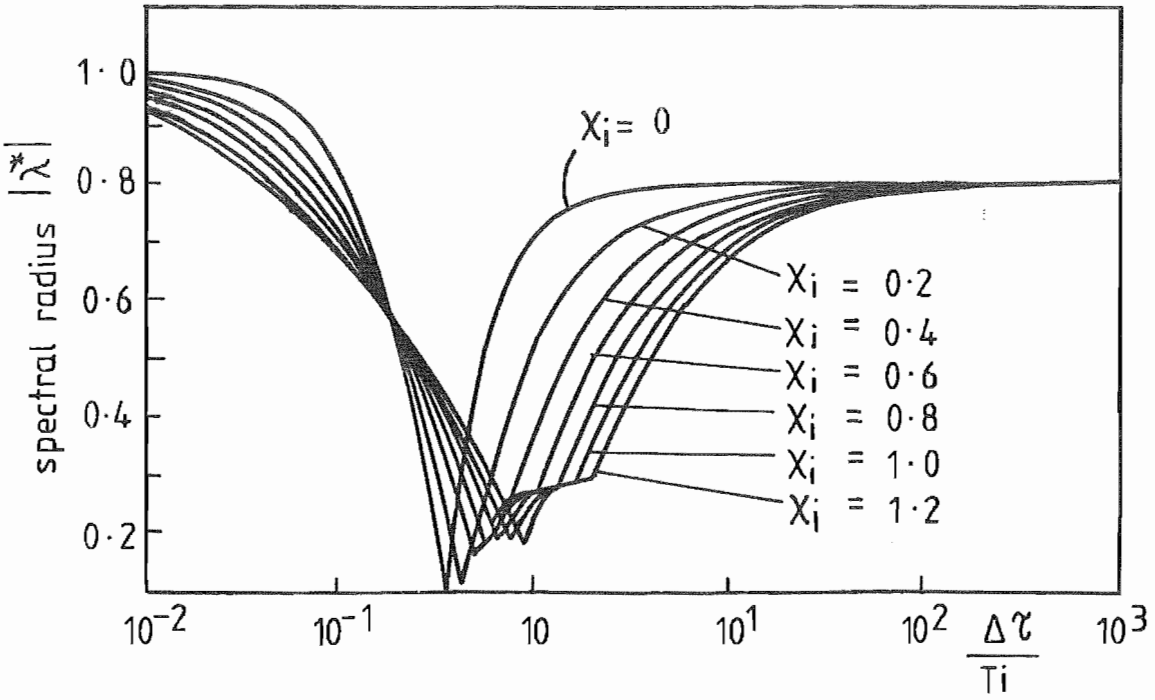

FIG 6·17 SPECTRAL RADIUS vs RATIO OF STEP SIZE: UNDAMPED PERIOD FOR VISCOUS DAMPING $\gamma = 3/2$, $\beta = 4/5$, X_i IS FRACTION OF CRITICAL DAMPING

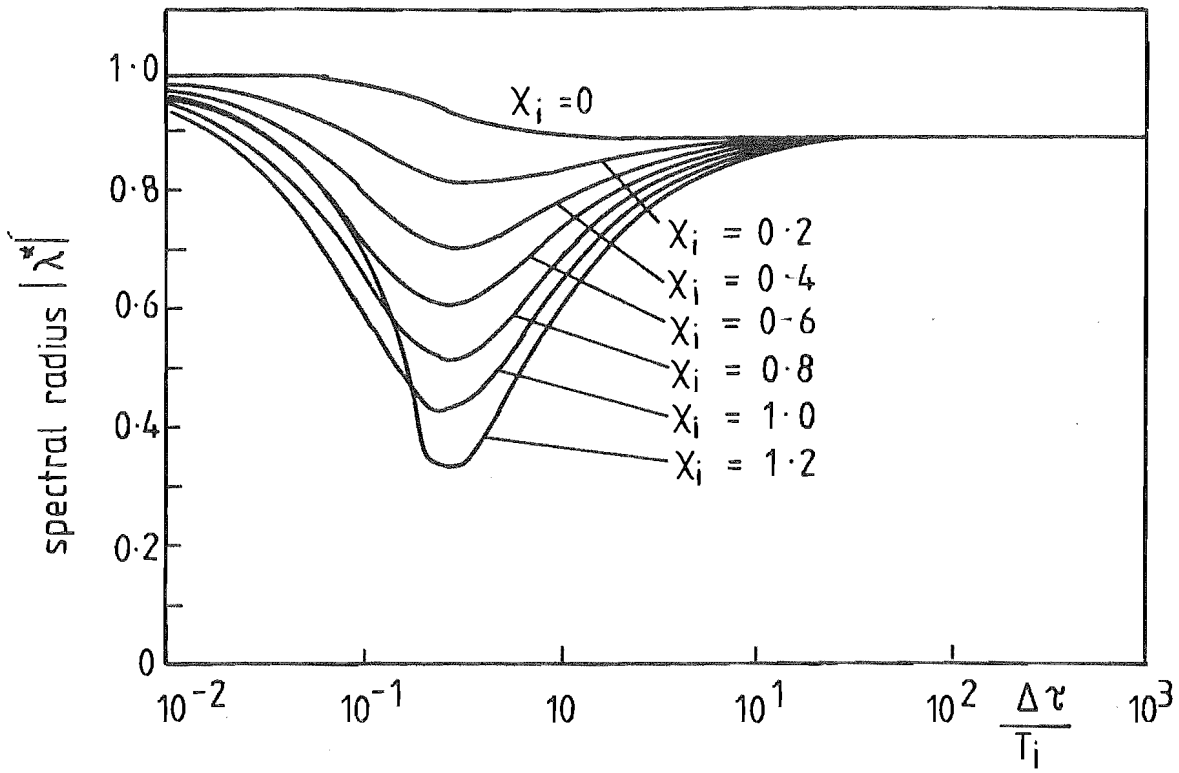

FIG 6·18 SPECTRAL RADIUS vs RATIO OF STEP SIZE: UNDAMPED PERIOD FOR VISCOUS DAMPING $\gamma = 0·6$, $\beta = 0·5$, X_i IS FRACTION OF CRITICAL DAMPING

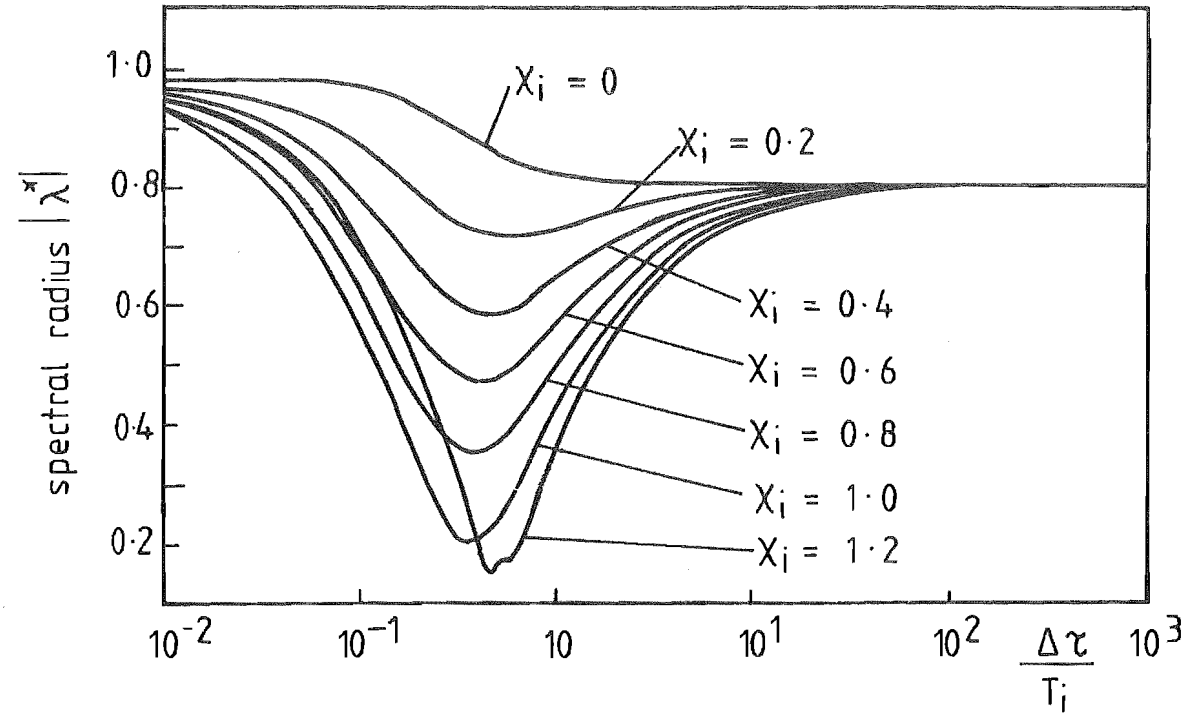

FIG 6·19 SPECTRAL RADIUS vs RATIO OF STEP SIZE: UNDAMPED PERIOD FOR VISCOUS DAMPING $\gamma = 0·6$, $\beta = 0·3025$, AND X_i IS FRACTION OF CRITICAL DAMPING

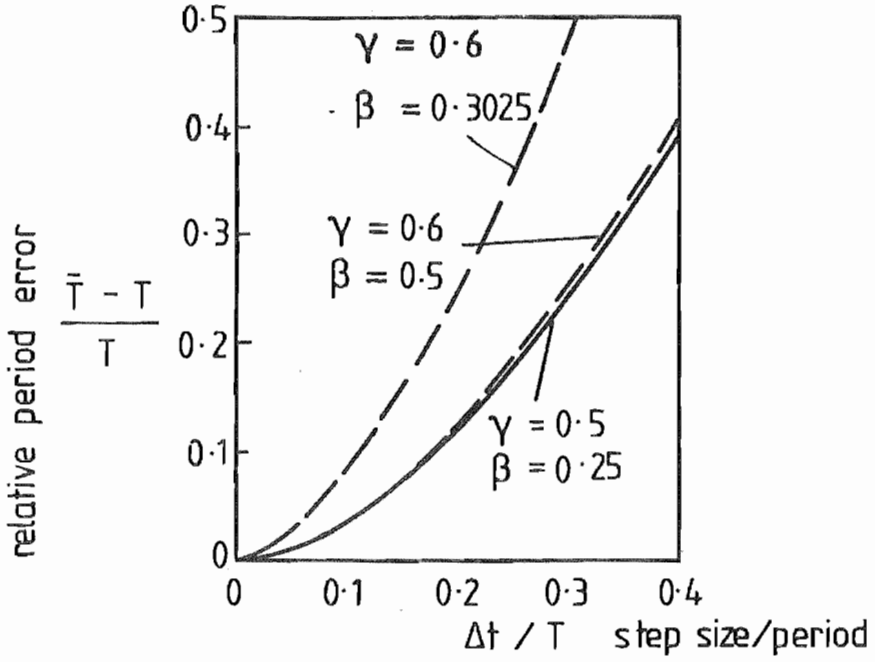

FIG 6·20 THREE LEVEL (NEWMARK) EXPRESSION RELATIVE PERIOD ERROR vs Δt/T

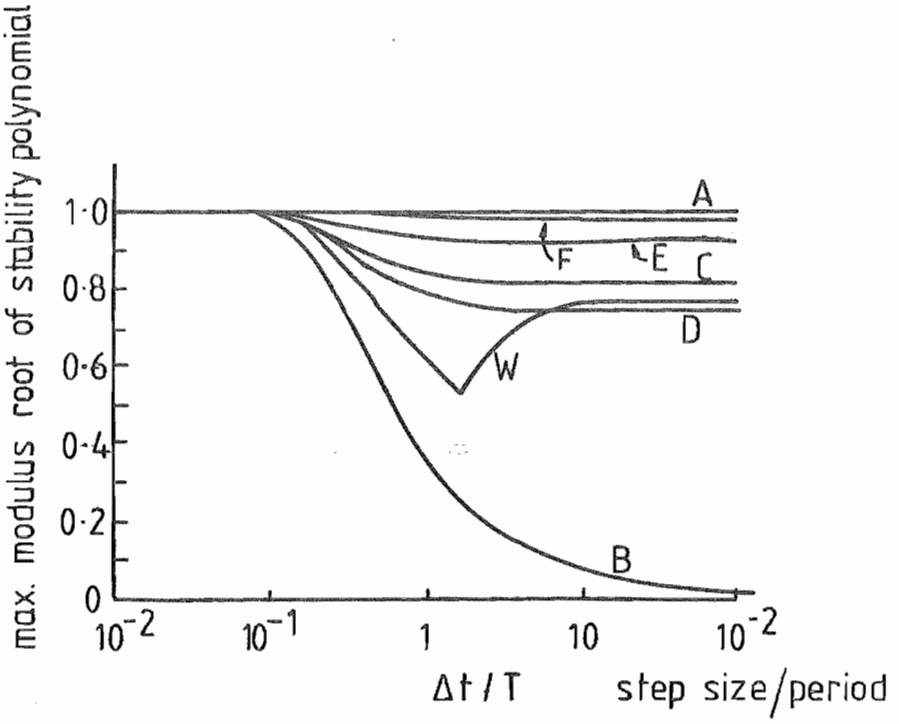

FIG 6·21 MAXIMUM MODULUS ROOT OF POLYNOMIAL AGAINST Δt/T

and that the pressure loading was applied from time $\tau = 0$. Hence the value of α_1 was calculated and thus the recurrence relationship applied for the solution of all subsequent displacements.

6.2.3.2.2 FOUR POINT RECURRENCE RELATIONSHIP An extension of the weighted residual method of Zienkiewicz[6.26] using cubic shape functions resulted in the Four-point Recurrence Scheme

$$\underline{M}(\gamma - 1) + (\tfrac{1}{2}\beta - \gamma + \tfrac{1}{3})\underline{C}\Delta\tau + (\tfrac{1}{6}\eta - \tfrac{1}{2}\beta + \tfrac{1}{3}\gamma)\underline{K}\Delta\tau^2 \; \underset{\sim}{\alpha}_{n+1}$$

$$+ (-3\gamma + 4)\underline{M} + (-\tfrac{2}{3}\beta + 4\gamma - \tfrac{3}{2})\underline{C}\Delta\tau + (-\tfrac{1}{2}\eta + 2\beta - \tfrac{3}{2}\gamma)\underline{K}\Delta\tau^2 \; \underset{\sim}{\alpha}_{n}$$

$$+ (3\gamma - 5)\underline{M} + (\tfrac{3}{2}\beta - 5\gamma + 3)\underline{C}\Delta\tau + (\tfrac{1}{2}\eta - \tfrac{5}{2}\beta + 3\gamma)\underline{K}\Delta\tau^2 \; \underset{\sim}{\alpha}_{n-1}$$

$$+ (-\gamma + 2)\underline{M} + (-\tfrac{1}{2}\beta + 2\gamma - \tfrac{11}{6})\underline{C}\Delta\tau + (-\tfrac{1}{6}\eta + \beta - \tfrac{11}{6}\gamma + 1)\underline{K}\Delta\tau^2 \; \underset{\sim}{\alpha}_{n-2}$$

$$+ (\tfrac{1}{6}\eta - \tfrac{1}{2}\beta + \tfrac{1}{3}\gamma)\underset{\sim}{f}_{n+1}\Delta\tau^2 + (-\tfrac{1}{2}\eta + 2\beta - \tfrac{3}{2}\gamma)\underset{\sim}{f}_{n}\Delta\tau^2$$

$$+ (\tfrac{1}{2}\eta - \tfrac{5}{2}\beta + 3\gamma)\underset{\sim}{f}_{n-1}\Delta\tau^2 + (-\tfrac{1}{6}\eta + \beta - \tfrac{11}{6}\gamma + 1)\underset{\sim}{f}_{n-2}\Delta\tau^2 = 0 \qquad 6.54$$

for the initial equation 6.40, where as previously

$\Delta\tau$ = time increment between nodal points

β, γ, η = constants dependent upon the specific recurrence relationship and are given in the Table 6.2

η	β	γ	Scheme
27	9	3	Houbolt
702/35	36/5	13/5	Galerkin
16.244	6.039	2.40	Wilson $\theta' = 1.4$
18.125	6.583	2.50	Wilson $\theta' = 1.5$
24	8	3	
22	8	3	

Table 6.2 Coefficients for the Four-point Recurrence Scheme (after Zienkiewicz)

Also the coefficients for the four-point scheme can be related to θ' schemes by the relationship,

$$\eta = 2 + 4\theta' + 3\theta'^2 + \theta'^3$$

$$\beta = \frac{4}{3} + 2\theta' + \theta'^2$$

$$\gamma = 1 + \theta'$$

The given general stability conditions for the undamped case were

$$\frac{3}{2} < \gamma < \frac{\beta}{3} + \frac{1}{2}$$

$$\frac{3}{4} + \frac{9}{2}\beta - 5\gamma < \eta < -9\gamma^2 + 3\beta\gamma + 13\gamma - 6 \qquad 6.55$$

and Figs 6.21 page206 & 6.22 page 210 show the 'spectral' radius and the relative period error for specific values of ζ,β,γ as a function of the ratio of the time step to the undamped period. Again graphical data is available only for the undamped case although Wood[6.27] has established stability criteria for a damped system of the form

$$\ddot{\alpha} + \chi_i \dot{\alpha} + \omega^2 \alpha = \rho e^{is\tau}$$

Therefore numerical experimentation was carried out using the linear analytical model and the numerical program, for the cases of viscous damping.

As with the three-point recurrence scheme a starting procedure was required, a typical example being that associated with the Houbolt recurrence where the initial conditions in time were

$$\alpha(\rho,0) = 0$$

$$\dot{\alpha}(\rho,0) = 0$$

and the acceleration and velocity for the nodal point $\Delta\tau = 0$ were given by

$$\frac{\partial^2 \alpha(\rho,0)}{\partial \tau^2} = \frac{1}{\Delta\tau^2}\left(\alpha(\rho,\Delta\tau) - 2\alpha(\rho,0) + \alpha(\rho,-\Delta\tau)\right)$$

$$\frac{\partial \alpha(\rho,0)}{\partial \gamma} = \frac{1}{6\Delta\tau}\left(2\alpha(\rho,\Delta\tau) + 3\alpha(\rho,0) - 6\alpha(\rho,-\Delta\tau) + \alpha(\rho,-2\Delta\tau)\right)$$

Substitution in the governing equation gave

$$\frac{\partial^2 \alpha(\rho,0)}{\partial \tau^2} = \frac{\varepsilon(o)}{\delta}$$

resulting in the initial starting conditions

$$\alpha(\rho,-\Delta\tau) = \frac{\varepsilon(o)}{\delta}\Delta\tau^2 - \alpha(\rho,\Delta\tau)$$

$$\alpha(\rho,-2\Delta\tau) = 6\frac{\varepsilon(o)}{\delta}\Delta\tau^2 - 8\alpha(\rho,\Delta\tau)$$

Curve Label	η	β	δ
A	15.25	6	2.5
B	27	9	3
C	53.85	19	6.5
D	22	8	3
E	20.275	7.65	3
F	430.5	154	51.5
W	16.224	6.093	2.4

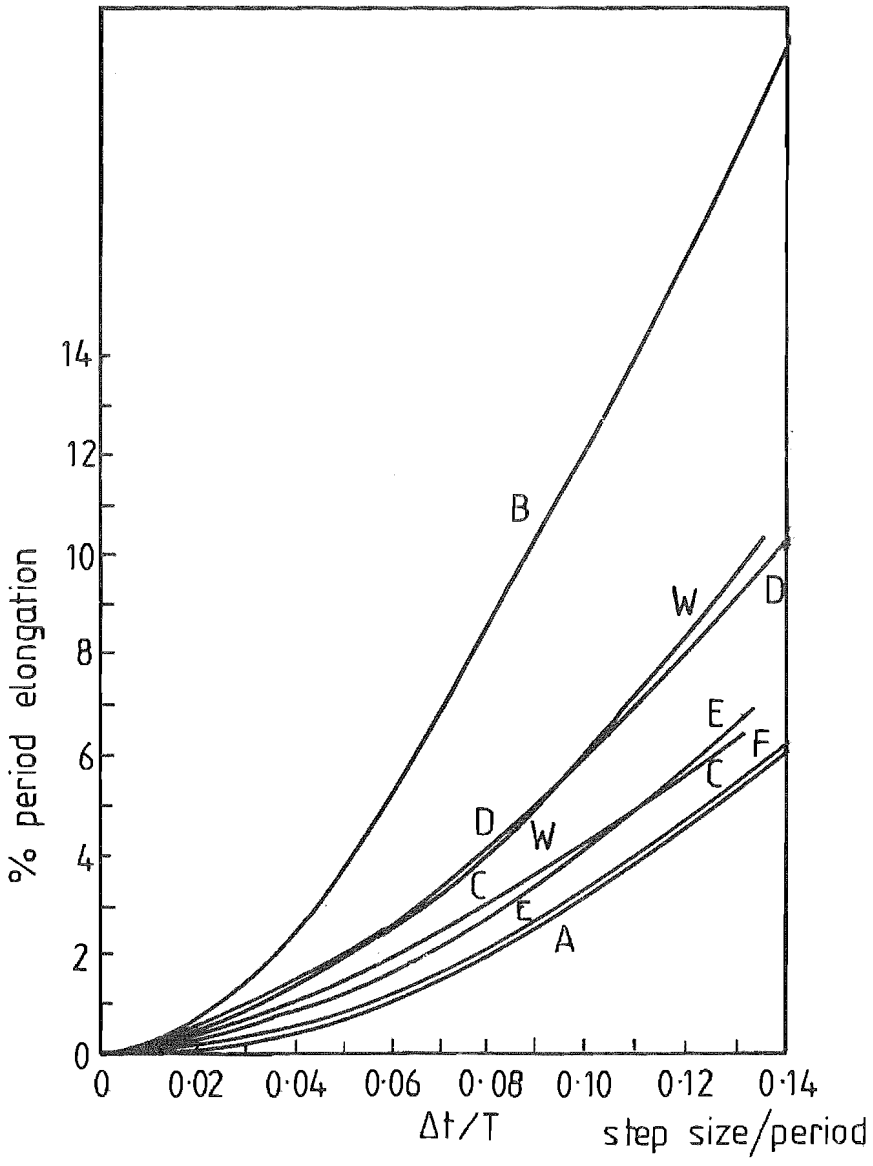

FIG 6·22 PERCENTAGE PERIOD ELONGATION AGAINST $\Delta t/T$

which were substituted into the appropriate recurrence relationship to give the required starting conditions for the first three nodal points in time. Therefore there were two inversions or partitions required of the coefficient matrix.

While the recurrence scheme did not satisfy all the suggested criteria[6.20] particularly items 4 & 5 page 195, it had been initially decided to use the Houbolt relationship. Subsequently this was expanded to the general three-point and four-point recurrence schemes to represent the time domain.

As for the three-point scheme, numerical experimentation was carried out for the linear case with the exact solution from the modal analysis.

6.2.3.2.3 DIRECT INTEGRATION OPERATOR Finally, because of the stability and self-starting characteristics, a Newmark scheme[6.27] for

$$\begin{aligned} \underset{\sim i+1}{\alpha} &= \underset{\sim i}{\alpha} + \Delta\tau\underset{\sim i}{\dot{\alpha}} + \Delta\tau^2(\tfrac{1}{2}-\beta)\underset{\sim i}{\ddot{\alpha}} + \Delta\tau^2\beta\underset{\sim i+1}{\ddot{\alpha}} \\ \underset{\sim i+1}{\dot{\alpha}} &= \underset{\sim i}{\dot{\alpha}} + \tfrac{1}{2}\Delta\tau(\underset{\sim i}{\ddot{\alpha}} + \underset{\sim i+1}{\ddot{\alpha}}) \end{aligned} \qquad 6.56$$

was reformulated to give

$$\underset{\sim i+1}{\ddot{\alpha}} = \frac{1}{\Delta\tau^2\beta}(\underset{\sim i+1}{\alpha} - \underset{\sim i}{\alpha} - \Delta\tau\underset{\sim i}{\dot{\alpha}} - \Delta\tau^2(\tfrac{1}{2}-\beta)\underset{i}{\ddot{\alpha}})$$

$$\underset{\sim i+1}{\dot{\alpha}} = \underset{\sim i}{\dot{\alpha}} + \tfrac{1}{2}\Delta\tau(\underset{\sim i}{\ddot{\alpha}} + \underset{\sim i+1}{\ddot{\alpha}})$$

Substitution into the original equation 6.40 gave

$$\begin{aligned} &(\underline{M}\frac{1}{\Delta\tau^2\beta} + \underline{C}\tfrac{1}{2}\frac{1}{\Delta\tau\beta} + \underline{K})\underset{\sim i+1}{\alpha} \\ &= \underset{\sim i+1}{f} + \underline{M}\frac{1}{\Delta\tau^2\beta}(\underset{\sim i}{\alpha} + \Delta\tau\underset{\sim i}{\dot{\alpha}} + \Delta\tau^2(\tfrac{1}{2}-\beta)\underset{\sim i}{\ddot{\alpha}}) \\ &- \underline{C}(\underset{\sim i}{\dot{\alpha}}(1 - \frac{1}{2\beta}) - \frac{1}{2\Delta\tau\beta}\underset{\sim i}{\alpha} + (\tfrac{1}{2}\Delta\tau - \frac{\Delta\tau(\tfrac{1}{2}-\beta)}{2\beta}) \end{aligned} \qquad 6.57$$

This scheme was implemented by modifying the coefficient matrix and gave a basis for comparison with the recurrence schemes.

The starting condition was, for the time $\Delta\tau$,

$$\underset{\sim}{\alpha}_i = 0$$

$$\dot{\underset{\sim}{\alpha}}_i = 0$$

$$\ddot{\underset{\sim}{\alpha}}_i = 0$$

The response of this technique of representing the time domain has been analysed by Sharpe[6.24] and shown to be satisfactory although the relative period error can become significant at large time steps.

6.2.4 DYNAMIC CENTRAL DIFFERENCE PROGRAM

The technique of solution described above was grouped into a single program, with the logic shown in flow diagram,Fig 6.23 page 213. This program was capable of solving the impact loading case giving either a linear or non-linear dynamic deflection of a plate or plate/foundation combination such as occurred in the proposed transducer.

The linear dynamic results were used to verify the program performance against known results as well as results determined by alternative programming techniques.

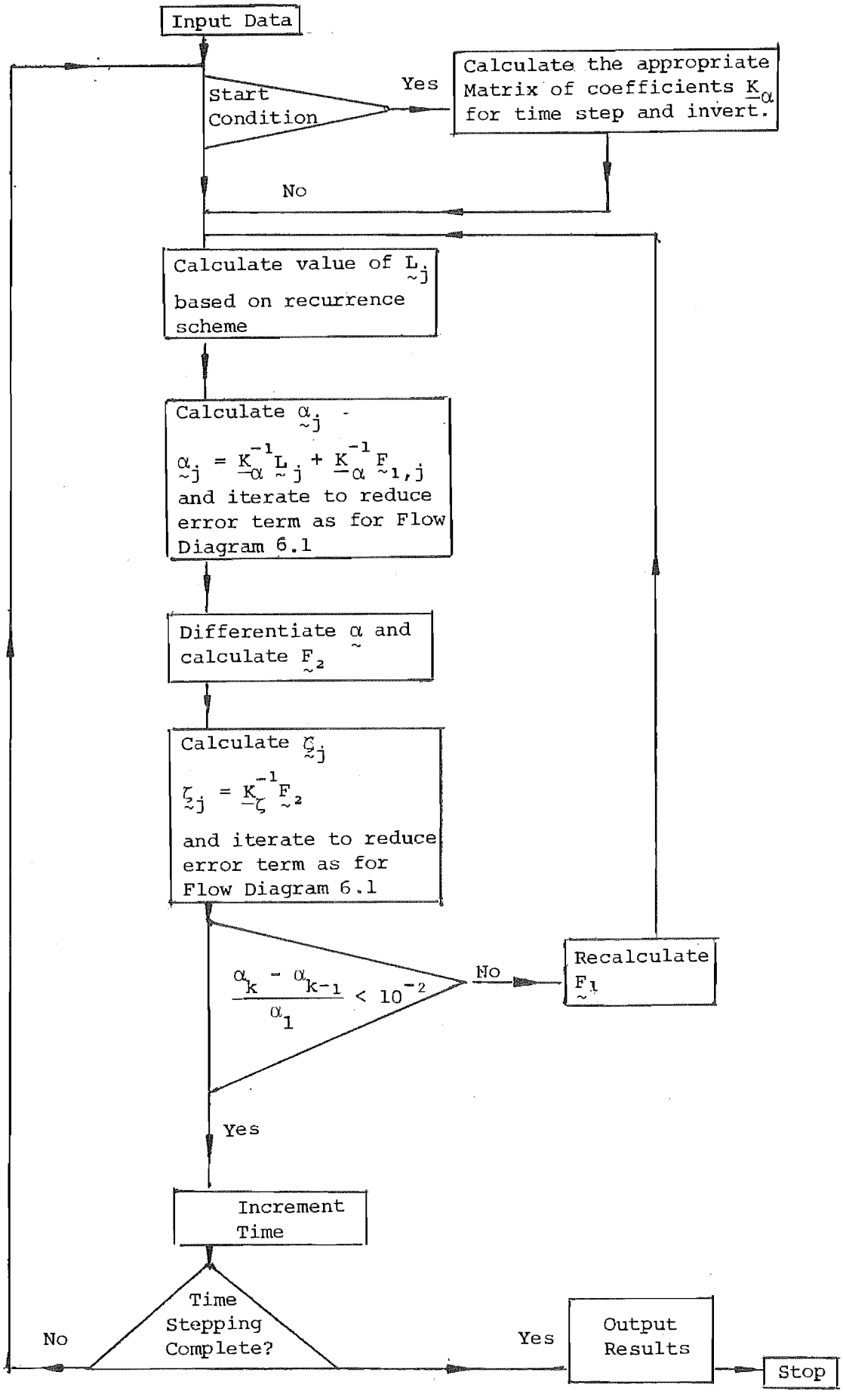

FIGURE 6.23 FLOW DIAGRAM OF NON-LINEAR DYNAMIC CENTRAL DIFFERENCE PROGRAM

CHAPTER SEVEN

RESULTS AND DISCUSSION

7.1 INTRODUCTION

The results from the linear modal analysis were used to determine the appropriate recurrence scheme to represent the time domain. The comparison was based upon a rectangular pulse load of $\varepsilon = 10$, $\tau_d = 0.2$, $\nu = 0.3$ because this was a stringent test of the stability and accuracy of the time response by ensuring that the maximum deflection was approached prior to the removal of the load. The influence of viscous damping was also considered for the linear deflection and the accuracy of the selected time domain alogarithm confirmed.

In addition, the linear modal analysis was used to verify the alogarithm describing the vertical deflection for the plate and plate/foundation combination, particularly that associated with the Pasternak foundation. This was because of the inaccuracy in the only published results for the non-linear dynamic response of a fixed edge circular plate/Pasternak foundation combination when subjected to a step load condition of $\varepsilon = 10$. The load cases used in this comparison where the step load, the rectangular pulse load, and the exponentially decaying load. The rectangular pulse load $\varepsilon = 10, \tau_d = 0.2$ was used for the reasons discussed previously while the step load $\varepsilon = 10$ has been used for the results presented in the literature on non-linear plate behaviour. The exponentially decaying load described the anticipated initial pressure pulse acting in the explosive forming, section 2.3, page 35 .

The non-linear dynamic results for the plate obtained from the central difference were compared with those of Alwar et al[7.1] and Coleby et al[7.5] and the quasi-linearisation technique applied by Alwar et al discussed. The boundary conditions considered were

extended and solutions for the clamped edge and the simply supported immovable edge outer boundary determined for the non-linear dynamic response.

The plate/foundation non-linear transient deflection was calculated using the numerical program for both the Winkler and Pasternak foundation characteristic and the results discussed in relation to those of Nath[7.7]. The differences between Nath's results for the Winkler foundation and the numerical solution are discussed for the plate with a fixed edge boundary condition. A closer agreement was obtained for the simply supported plate boundary. For the Pasternak foundation with a fixed edge plate,the discussion centres on the erroneous results presented by Nath and a comparison is made with those obtained from the program. The form of the response for the simply supported plate boundary was similar for the program and Nath's research,while there was a variation in maximum deflection amplitude.

The results of the non-linear modal analysis were compared with those from the numerical program and the discrepancy discussed.

Finally the design performance of the pressure transducer is presented as well as typical deflection and stress profiles for a plate subject to an exponentially decaying load.

7.2 LINEAR RESPONSE

An 'exact' solution for the linear dynamic response of the plate and the plate/foundation combination using the modal analysis section 5.1- 5.2.5 was obtained for the step load, rectangular pulse load and an exponentially decaying load. The step load case for the plate was used to examine the three and four point recurrence schemes discussed in section 6.2.3.1-6.2.3.2.3.

Undamped and viscously damped dynamic deflection of the plate was calculated for the load cases and the results compared with those derived from the numerical programs. Similarly the 'exact' solution for the Winkler and Pasternak foundations were determined for a range of values k^* and G^* and showed aggreement with the numerically derived results.

7.2.1. LINEAR MODAL ANALYSIS

The central deflection of a plate subject to a rectangular pulse load of $\varepsilon = 10$ for $\tau = 0.0$ to $\tau = 0.2$ is given in Fig. 7.1, page 217. It can be seen that the amplitude of the resultant sinusoidal deflection was not constant but varied by 4.7%. Fig. 7.2 page 217 contains the deflection associated with the first root as well as the summation of deflection for the higher order roots 2-30 which did not sum to zero but to an alternating deflection of variable frequency with a mean value of the order of 3.8 times that of the first root. Therefore the higher order roots of the modal analysis beat against the first order root giving the observed variation in the deflection amplitude. The resultant central deflection time graph was used to determine the accuracy, algorithmic damping and relative period error associated with specific three-point and four-point recurrence schemes used in the time domain, sections 6.2.3.1-6.2.3.2.3, for a range of time step sizes.

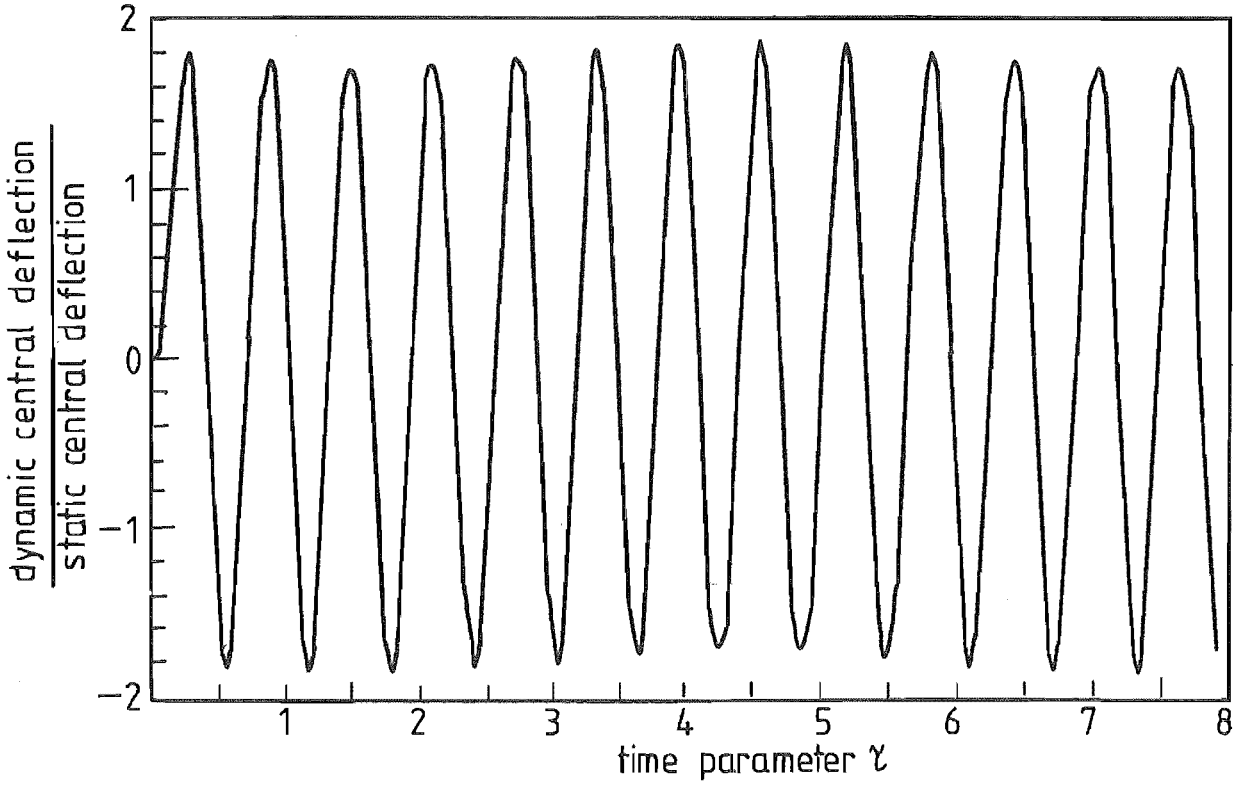

FIG 7·1 CENTRAL DEFLECTION vs TIME FOR LINEAR MODAL ANALYSIS OVER 30 ROOTS, RECTANGULAR PULSE LOAD $\mathcal{E} = 10, \tau_d = 0{\cdot}2, \lambda = 0{\cdot}3$
NOTE: STATIC DEFLECTION FOR $\mathcal{E} = 10, \lambda = 0{\cdot}3$

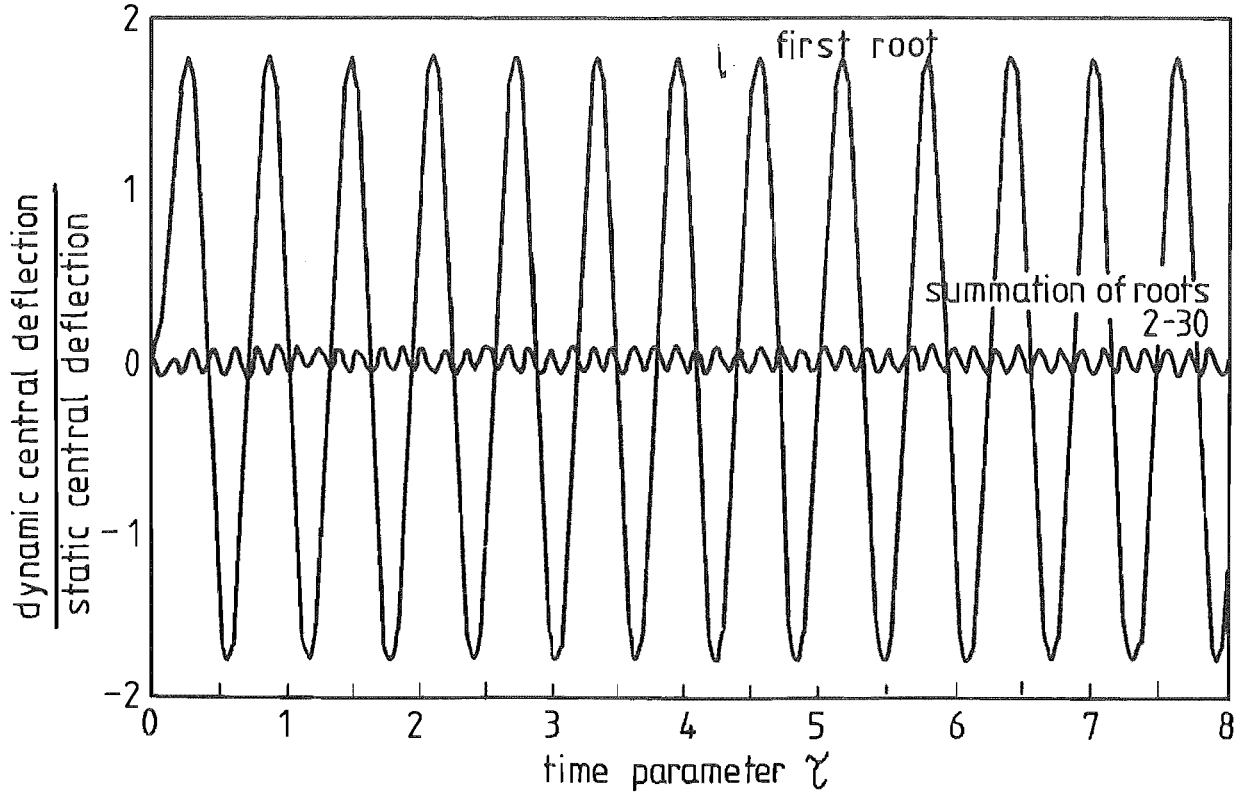

FIG 7·2 CENTRAL DEFLECTION vs TIME FOR FIRST ROOT AND ROOTS TWO - THIRTY, $\mathcal{E} = 10, \tau_d = 0{\cdot}2, \lambda = 0{\cdot}3$

7.2.2. TIME DOMAIN - NUMERICAL EXPERIMENTATION

A comparison between the dynamic deflection results from the modal analysis and the finite difference program, using a Newmark direct integration operator $\beta = \frac{1}{4}$, $\gamma = \frac{1}{2}$, $\Delta\tau = 0.0075$ is shown in Fig. 7.3 page 219 while Fig. 7.4 page 219 gives the results for the corresponding central bending moments. As would be anticipated the accuracy of the central radial bending moment from the numerical program was less than that for deflection because of the inherent inaccuracies associated with central difference differentiation techniques, particularly at boundaries.

The absolute differences between the deflection results are presented in Fig. 7.5 page 220 and the increasing amplitude with time showed the influence of errors in waveform and period. The apparent disparity between the error graph and the deflection is due to the plotted resolution being less i.e. $\Delta\tau = 0.01$ than the time step $\Delta\tau = 0.0075$ used in the calculation. Error conditions defined as

$$\text{Error} = \left(\frac{\alpha_o \text{ dynamic}}{\alpha_o \text{ static}}\right)_{\text{program}} - \left(\frac{\alpha_o \text{dynamic}}{\alpha_o \text{ static}}\right)_{\text{modal}}$$

for specific three point recurrence schemes are presented in Fig. 7.5 - 7.9 p 220-2 for the rectangular pulse loads, of $\varepsilon = 10$ for $\tau = 0.0 - 0.2$, with time step size of $\Delta\tau = 0.005$ and $\Delta\tau = 0.010$ while Fig. 7.10 shows the deflection for $\beta = 0.8$, $\gamma = 1.5$ and time step size of $\Delta\tau = 0.005$, 0.0075 and 0.010.

Alogarithmic damping is apparent in Fig. 7.7 - 7.10 as was expected from the spectral radius, Fig. 6.17 - 6.19 pages 204-5 , with no relative period error being in evidence while Fig. 7.5 - 7.6 exhibit the effects of relative period error with limited amplitude change, which was anticipated, section 6.2.3.2.1. Therefore the Newmark, $\beta = 0$, $\gamma = 0.25$, gave the best representation of the time domain for the three point recurrence scheme and was adopted for the nonlinear analysis. The results for the comparison of the four-point recurrence schemes with respect to the linear modal analysis are given in the Figs.. 7.11 - 7.15 pages 223.5. The Houbolt recurrence relationship, Fig. 7.11, exhibited alogrithmic damping characteristics of the scheme [6.23], as the time step size

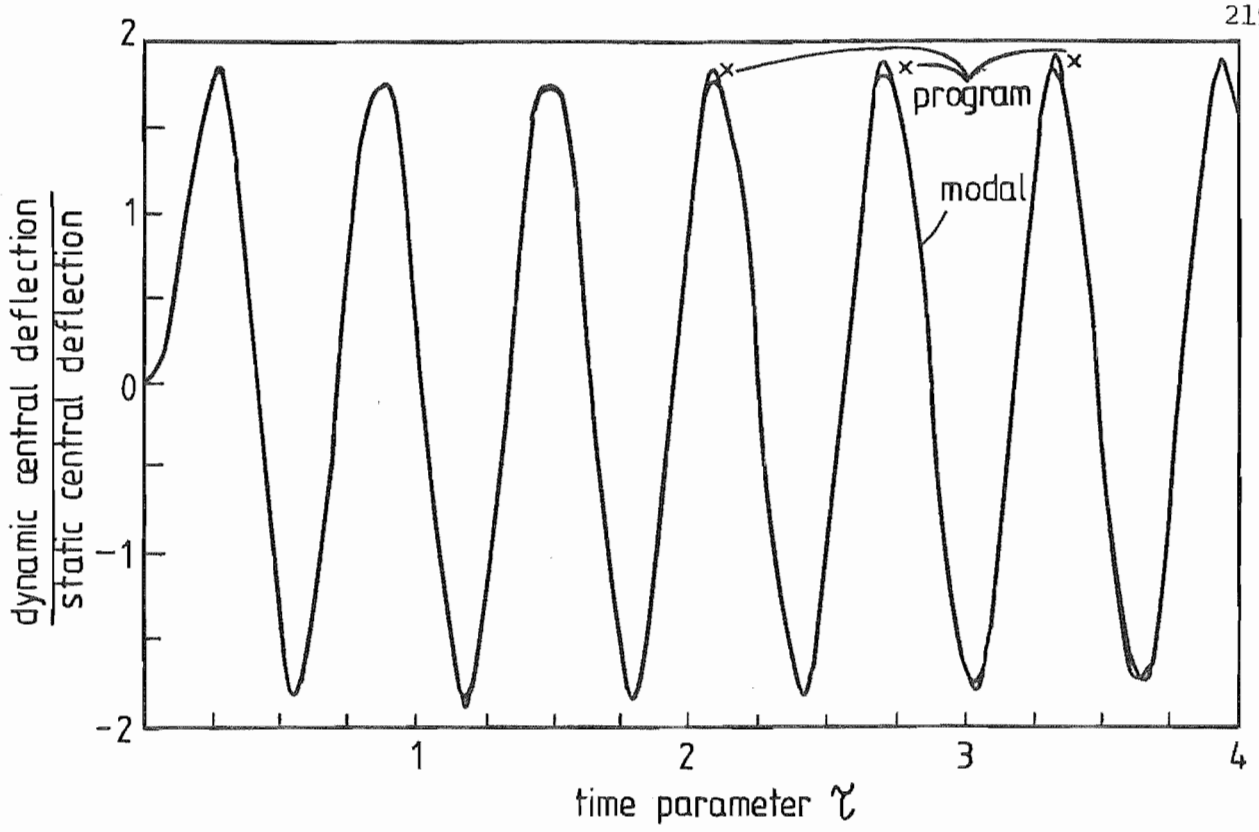

FIG 7·3 CENTRAL DEFLECTION vs TIME FOR $\varepsilon = 10$, $\tau_d = 0{\cdot}2$, $\nu = 0{\cdot}3$

NOTE: STATIC DEFLECTION FOR $\varepsilon = 10$, $\nu = 0{\cdot}3$

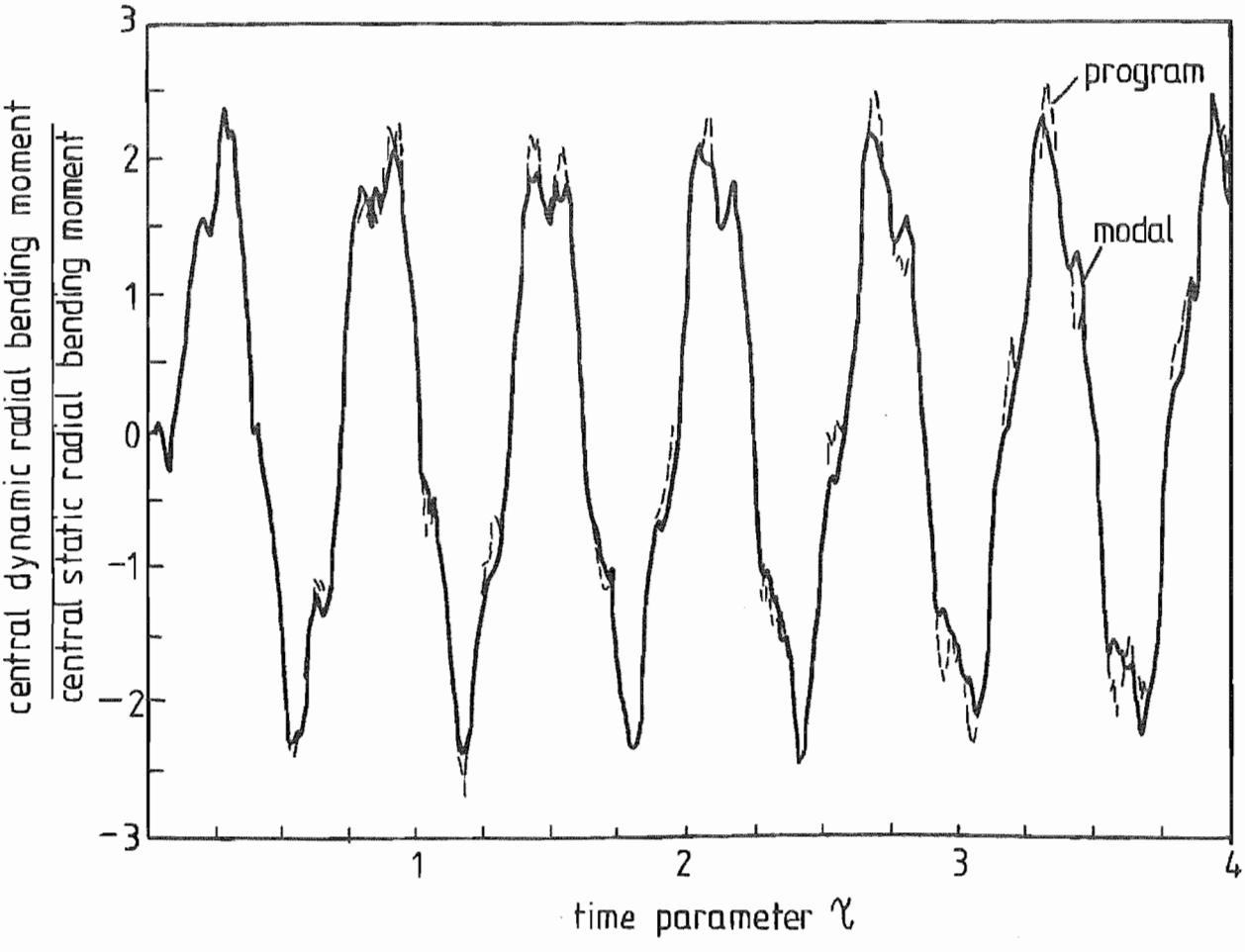

FIG 7·4 CENTRAL RADIAL BENDING MOMENT vs TIME FOR $\varepsilon = 10$, $\nu = 0{\cdot}3$

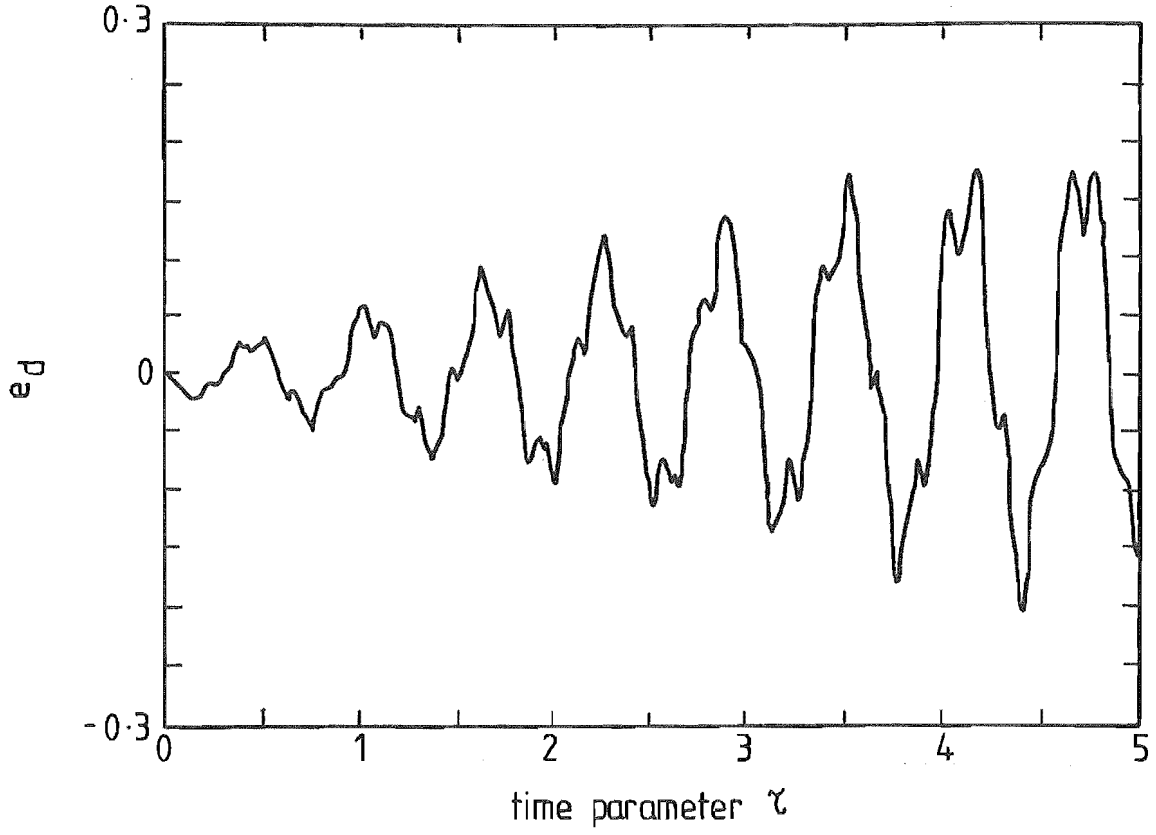

FIG 7·5 DIFFERENCE BETWEEN CENTRAL DEFLECTION FROM NUMERICAL METHOD AND MODAL ANALYSIS FOR LINEAR CASE
$\varepsilon = 10, \tau_d = 0{\cdot}2, \nu = 0{\cdot}3.$

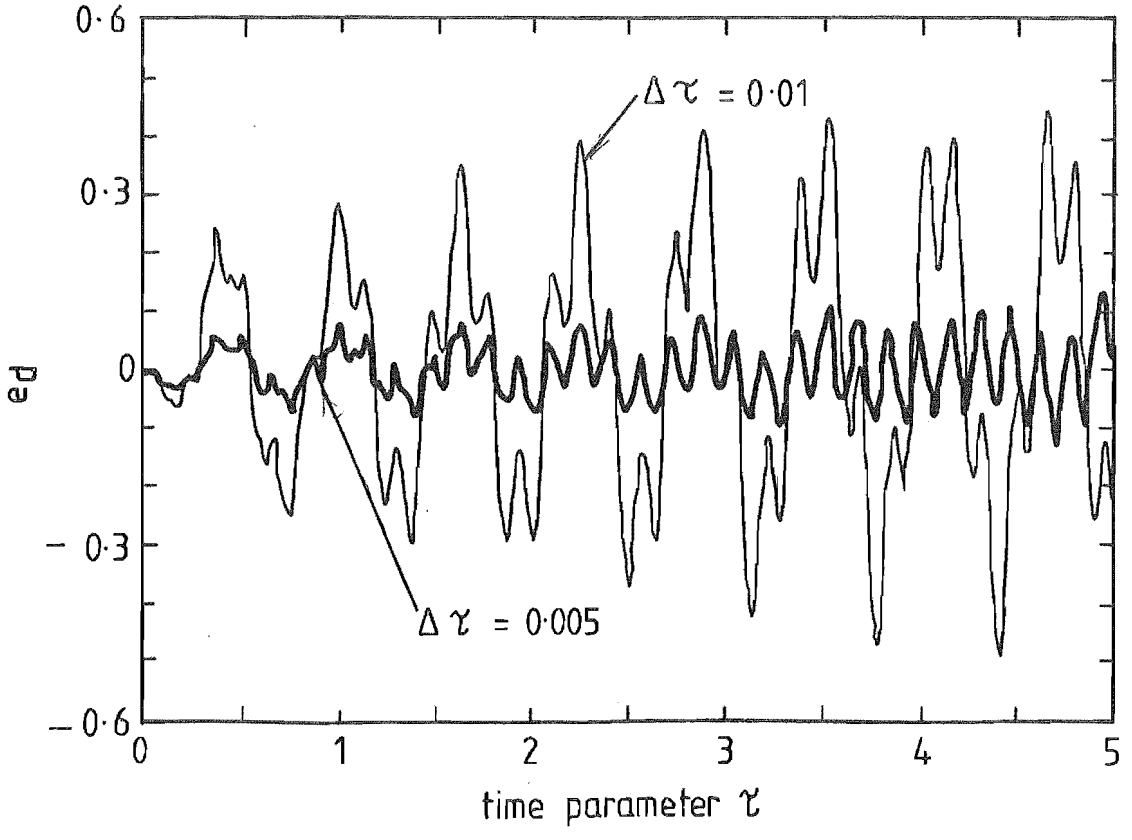

FIG 7·6 ABSOLUTE ERROR vs TIME NEWMARK RECURRENCE SCHEME
$\gamma = 0{\cdot}5, \beta = 0{\cdot}25, \varepsilon = 10, \tau_d = 0{\cdot}2, \nu = 0{\cdot}3$

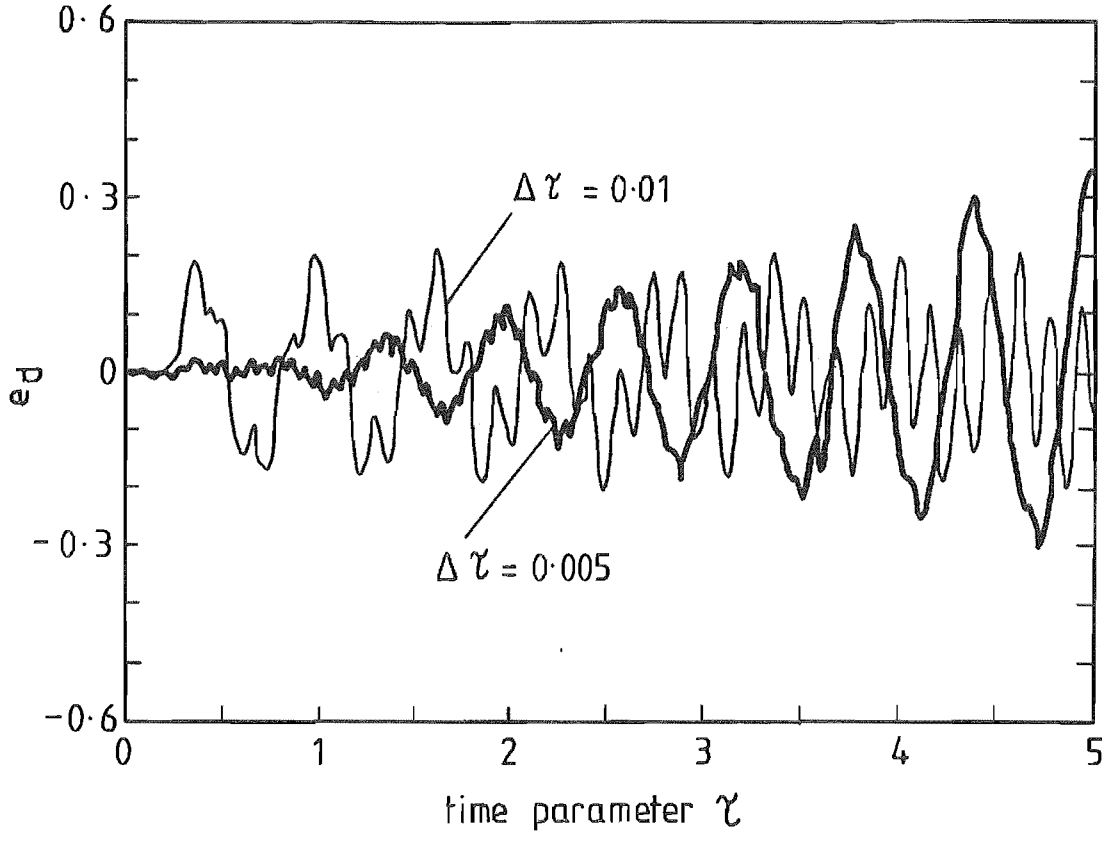

FIG 7·7 ABSOLUTE ERROR vs TIME NEWMARK DIRECT INTEGRATION OPERATOR $\gamma = 0{\cdot}5$, $\beta = 0{\cdot}25$, $\varepsilon = 10$, $\tau_d = 0{\cdot}0 - 0{\cdot}2$, $\vartheta = 0{\cdot}3$

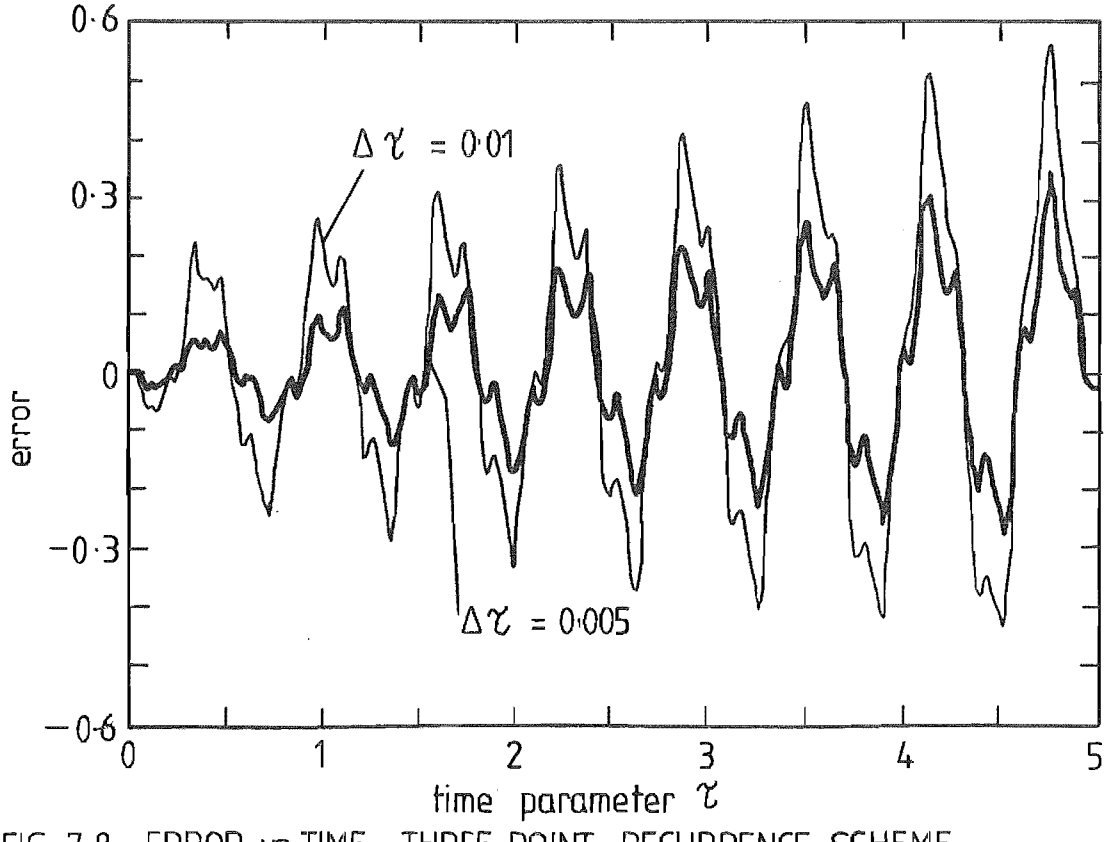

FIG 7·8 ERROR vs TIME THREE POINT RECURRENCE SCHEME $\gamma = 0{\cdot}6$, $\beta = 0{\cdot}3025$, $\varepsilon = 10$, $\tau_d = 0{\cdot}2$, $\vartheta = 0{\cdot}3$

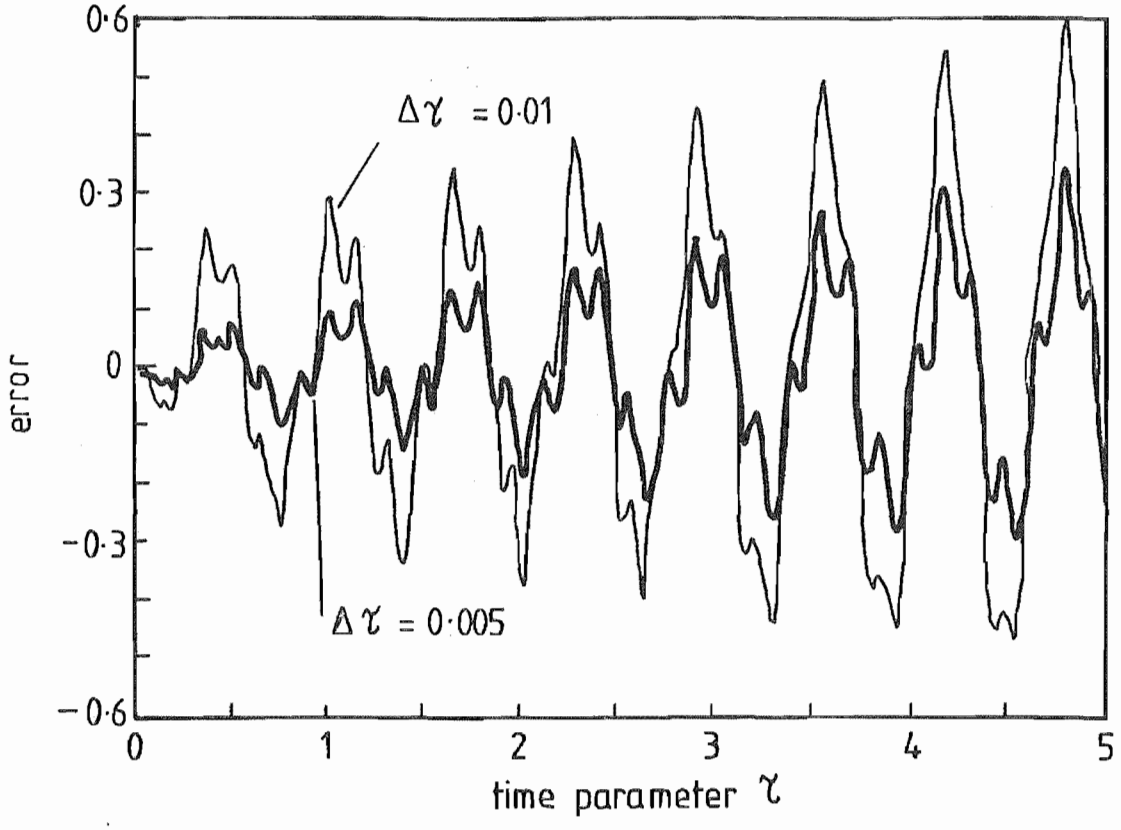

FIG 7·9 ERROR vs TIME THREE POINT RECURRENCE SCHEME
$\gamma = 0{\cdot}6$, $\beta = 0{\cdot}5$, $\varepsilon = 10$, $\tau_d = 0{\cdot}0 - 0{\cdot}2$, $\lambda = 0{\cdot}3$

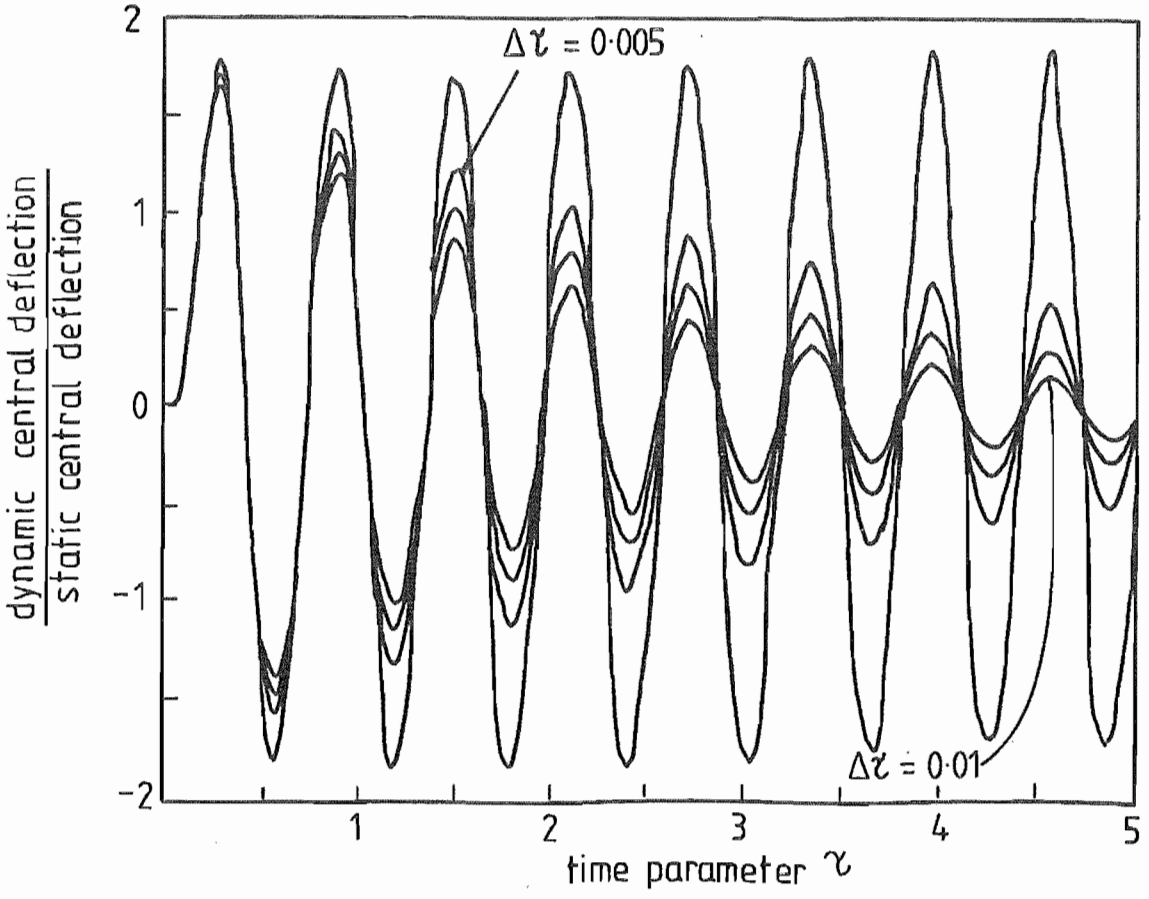

FIG 7·10 DEFLECTION vs TIME GALERKIN THREE POINT RECURRENCE SCHEME $\gamma = 1{\cdot}5$, $\beta = 0{\cdot}8$, $\varepsilon = 10$, $\tau_d = 0{\cdot}2$, $\lambda = 0{\cdot}3$ $\Delta\tau = 0{\cdot}005$, $0{\cdot}0075$, $0{\cdot}0$

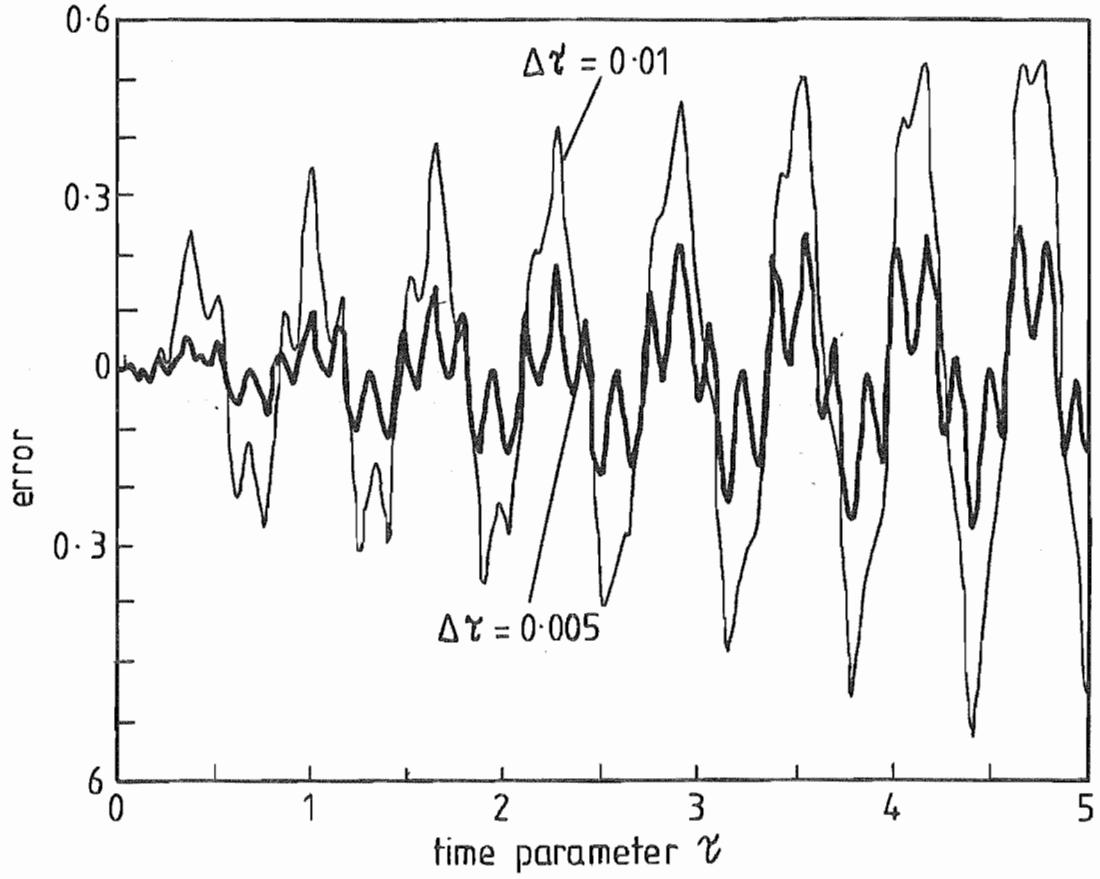

FIG 7·11 ERROR vs TIME HOUBOLT FOUR POINT RECURRENCE SCHEME
$\eta = 27, \beta = 9, \gamma = 3$

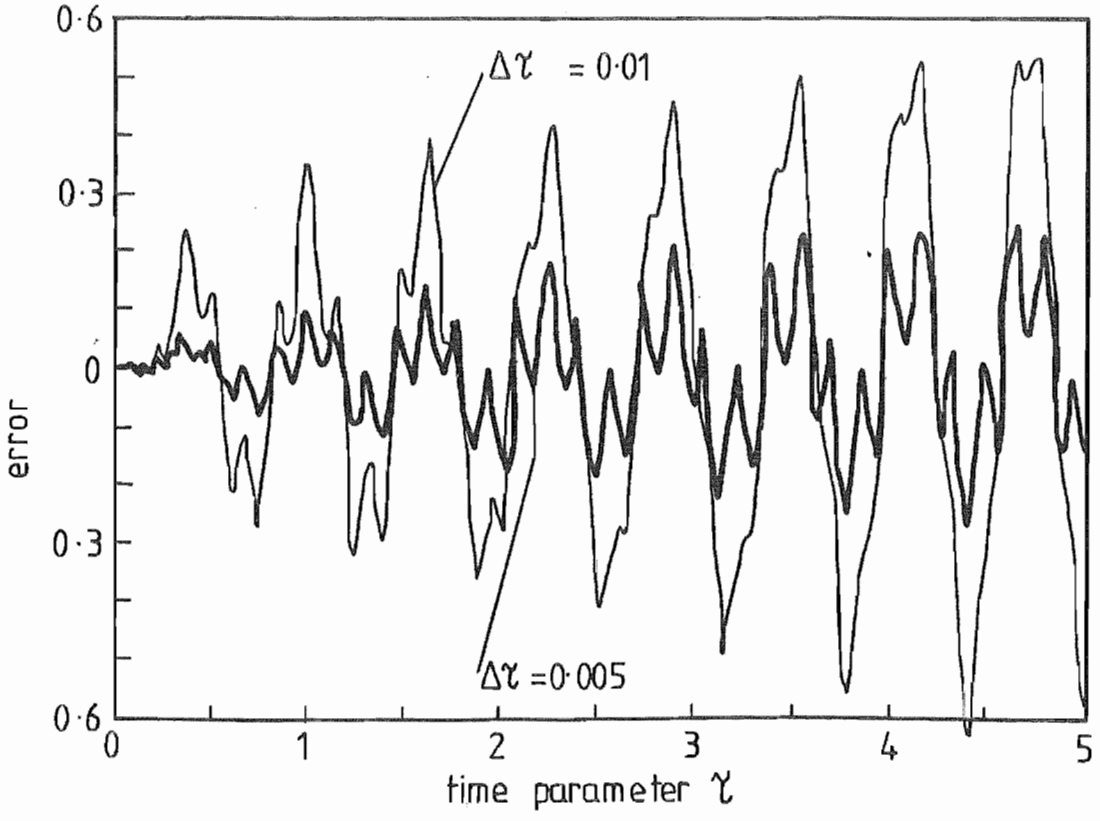

FIG 7·12 ERROR vs TIME FOUR POINT RECURRENCE SCHEME
$\eta = 24 \beta = 8 \gamma = 3$

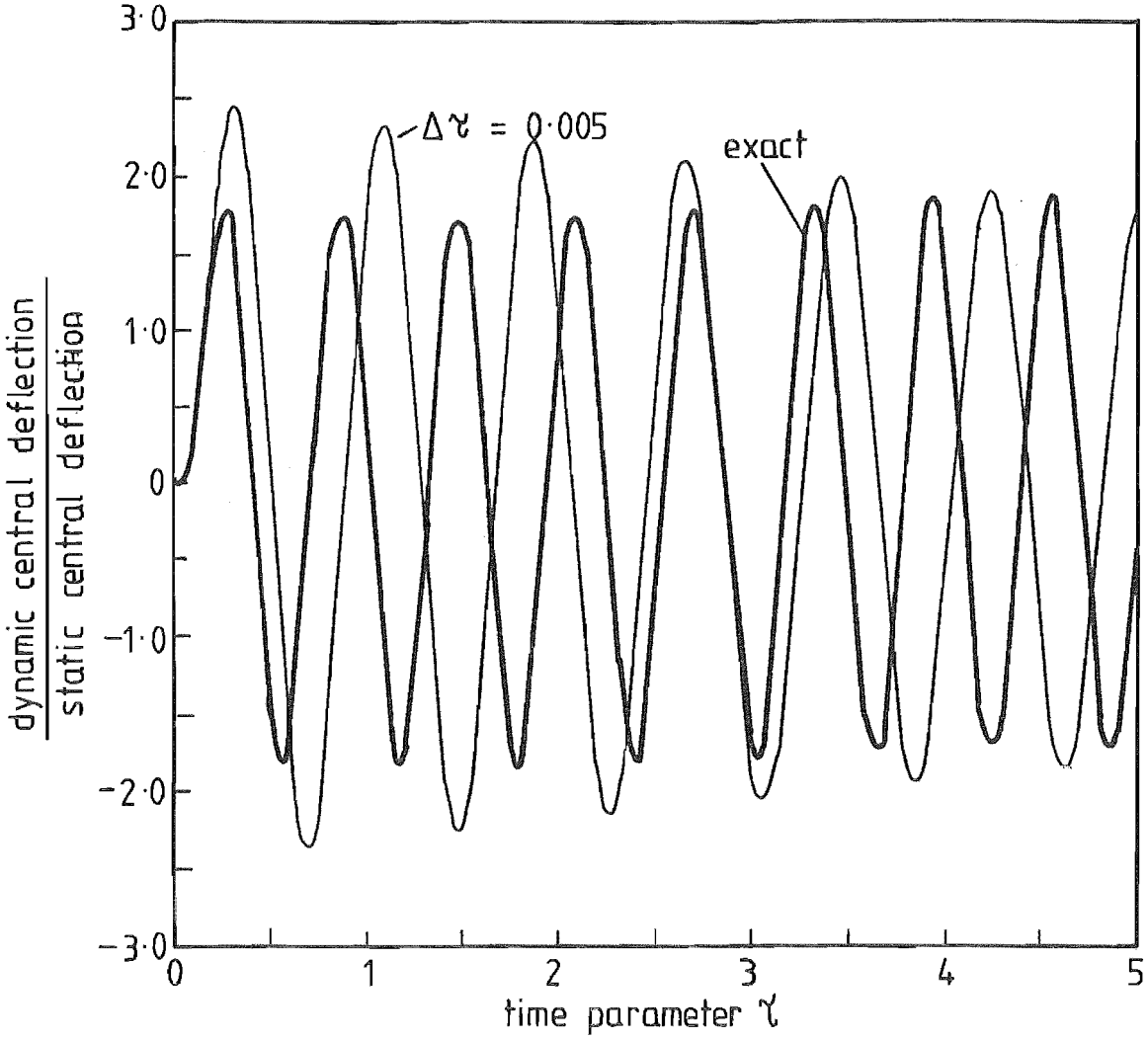

FIG 7·13 DEFLECTION vs TIME GALERKIN FOUR POINT RECURRENCE SCHEME $\eta = 702/35$, $\beta = 36/5$, $\gamma = 13/5$

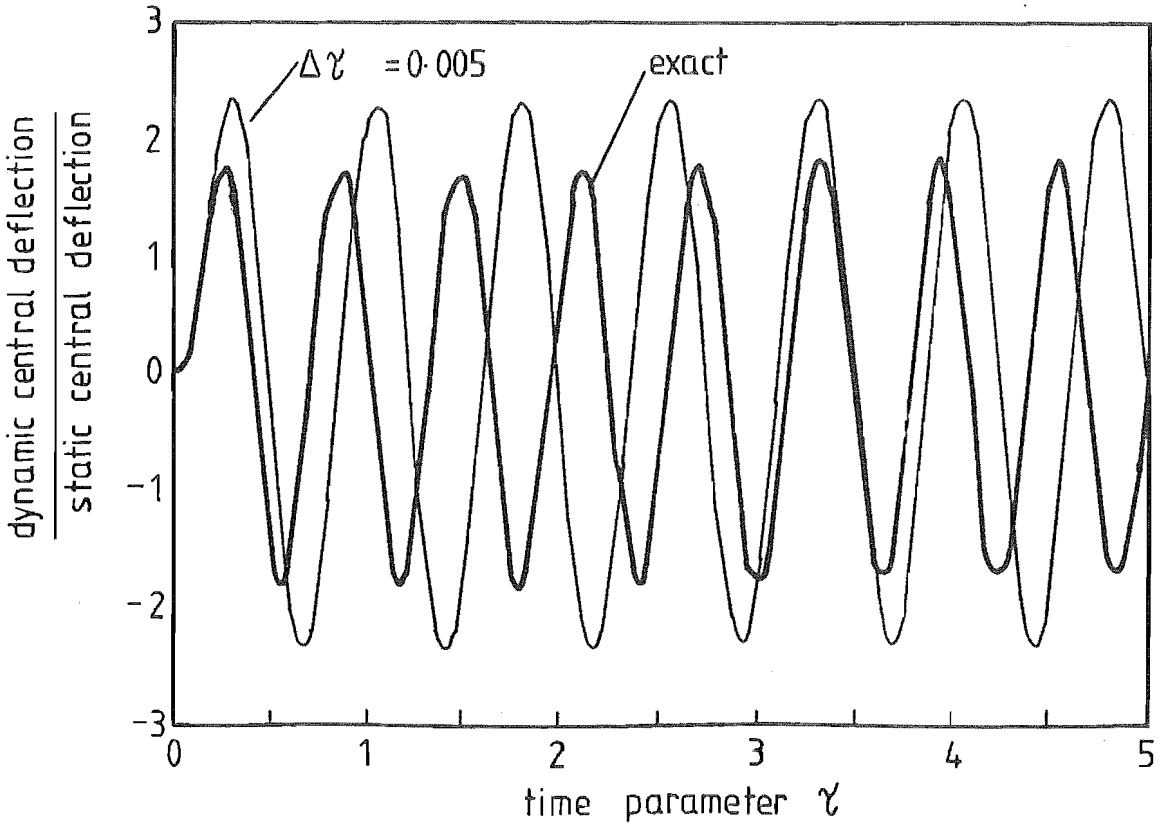

FIG 7·14 DEFLECTION vs TIME FOUR POINT RECURRENCE SCHEME

$\eta = 22, \beta = 8, \gamma = 3$

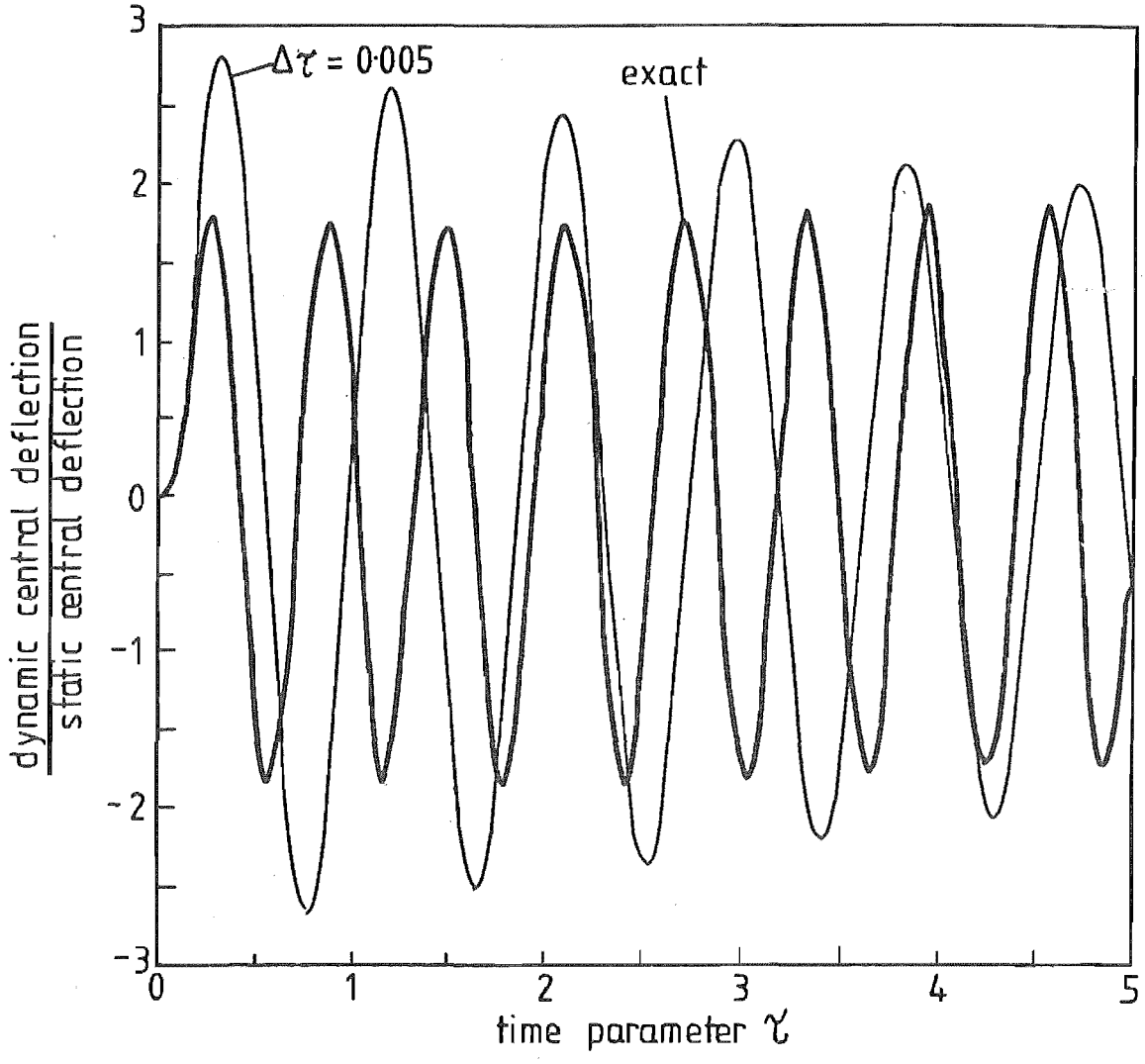

FIG 7·15 DEFLECTION vs TIME WILSON $\theta' = 1{\cdot}4$ FOUR POINT RECURRENCE SCHEME $\eta = 16{\cdot}24, \beta = 6{\cdot}58, \gamma = 2{\cdot}58$

was increased and for this procedure step sizes of less than $\Delta\tau$ = 0.0005 had to be employed for accurate plate analysis. The scheme = 24, β = 8, γ = 3, Fig. 7.12 displayed a similar error to the Houbolt relationship with the source of error being a function of the change in period and no apparent alogrithmic damping, as would be expected [6.23]. The Wilson technique θ' = 1.4, Fig. 7.15 for an equivalent step size $\Delta\tau$ = 0.005 exhibited both overshoot [6.24] and relative period error as well as alogrithmic damping, as did the Galerkin four point scheme, Fig. 7.13.

Finally for ζ = 22, β = 8, γ = 3, Fig. 7.14, the recurrence scheme exhibited a relative period error and overshoot but for a step size of $\Delta\tau$ = 0.005, there was no alogrithmic damping.

Therefore, while the Houbolt recurrence scheme was initially used with small step sizes of the order of $\Delta\tau$ = 0.0025 for the non-linear analysis, subsequent work was based upon the Newmark three point recurrence scheme. As can be seen from Fig. 7.6 and Fig. 7.11 these gave the most accurate representation for $\Delta\tau$ = 0.005 of the schemes considered.

7.2.3. VISCOUS DAMPING

From section 6.2.3.2.1. it can be appreciated that the viscous damping would modify the response of the algorithms used to describe the time domain and therefore the results from the numerical program were compared with those from the modal analysis for transient, dynamic deflection. The load cases considered were a rectangular pulse loading, a constant load and an exponentially decaying load condition using a range of non- dimensional viscous damping valves.

Comparison of the results for central deflection from the numerical solution of the plate subject to viscous damping, can be seen on Figs. 7.16 - 7.18, pages 228-9 for constant pressure loading, rectangular pulse pressure loading and exponentially decaying pressure respectively. For non-dimensional viscous damping values of 8, 16, 24 and 32 the two solution methods were identical for a step size of $\Delta\tau = 0.005$. Therefore the Newmark recurrence alogrithm adequately described the viscous damping, in agreement with section 6.2.3.2.1 page 196 and Sharpe's work [6.24].

The Houbolt recurrence scheme was also compared with the linear modal analysis for an identical step size and gave similar agreement. From these results it can be seen that for the plate, critical damping lies between $\chi = 16$ and $\chi = 24$ and for the fundamental first mode frequency was $\chi_{crit} = 20.43$.

7.2.4 WINKLER FOUNDATION

From Fig. 7.19, page 230 it can be seen that the increasing value of foundation constant raised the fundamental frequency of the system, as would be expected, according to the relationship

$$f_1 = (\lambda_1^4 + k^*)^{\frac{1}{2}}$$

Therefore the step size in the time domain had to be decreased to $\Delta\tau = 0.0025$ to avoid relative period error, particularly for stiffer foundations of $k^* > 100$. The numerical and modal analysis solutions for central deflection are shown in Fig. 7.20 for a constant load case and again are in agreement.

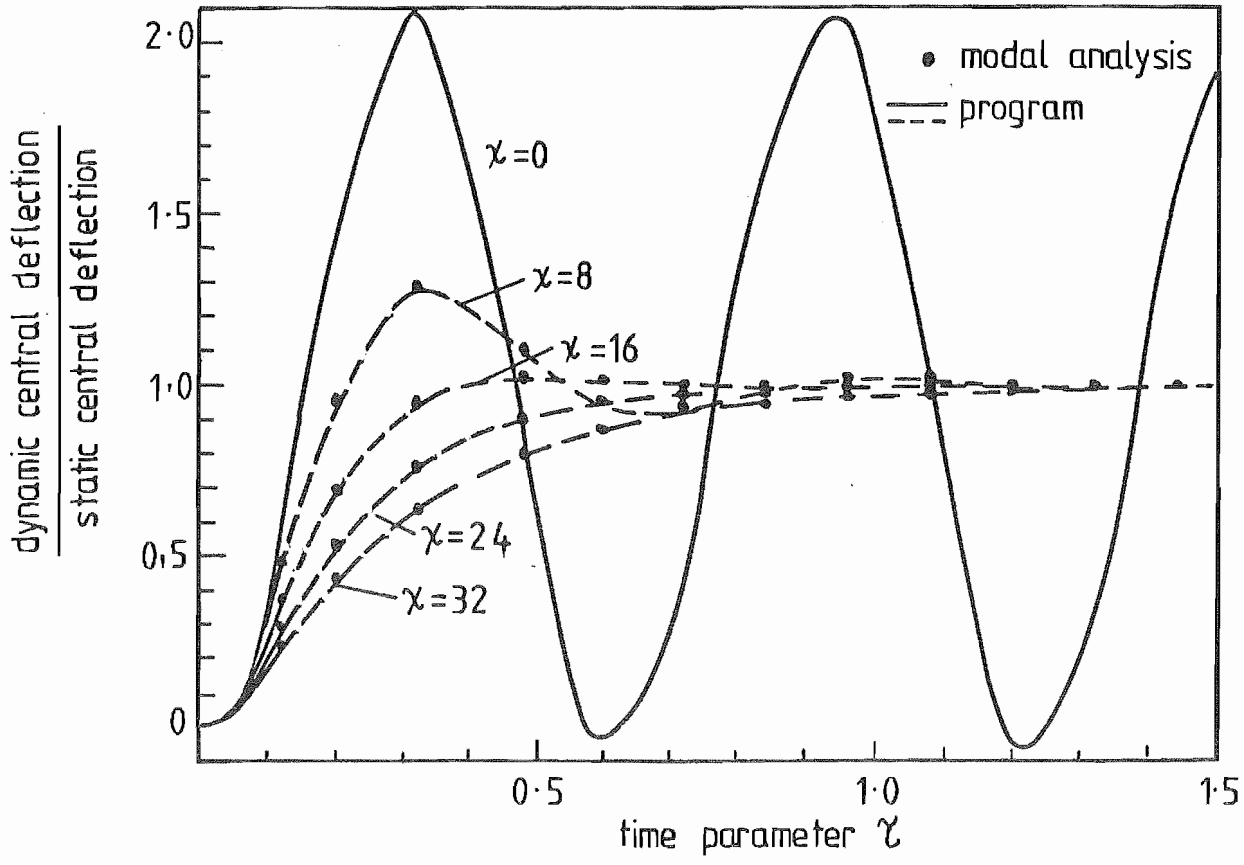

FIG 7·16 CENTRAL DEFLECTION vs TIME FOR VISCOUS DAMPING $\chi = 0{\cdot}8, 16, 24, 32$ WITH CONSTANT LOAD $\mathcal{E} = 10$, $a = 0{\cdot}3$

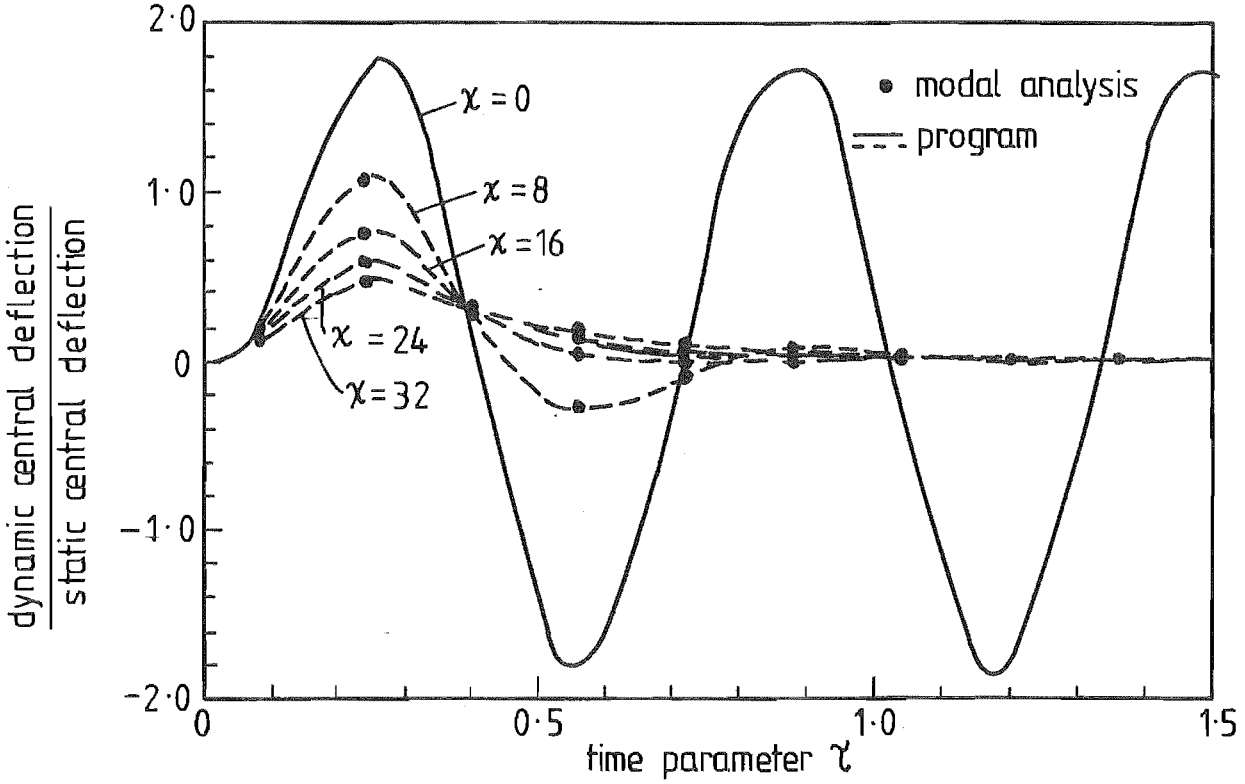

FIG 7·17 CENTRAL DEFLECTION vs TIME FOR VISCOUS DAMPING $\chi = 0, 8, 16, 24, 32$ WITH RECTANGULAR PULSE LOAD $\epsilon = 10, \tau_d = 0{\cdot}2, \lambda = 0{\cdot}3$

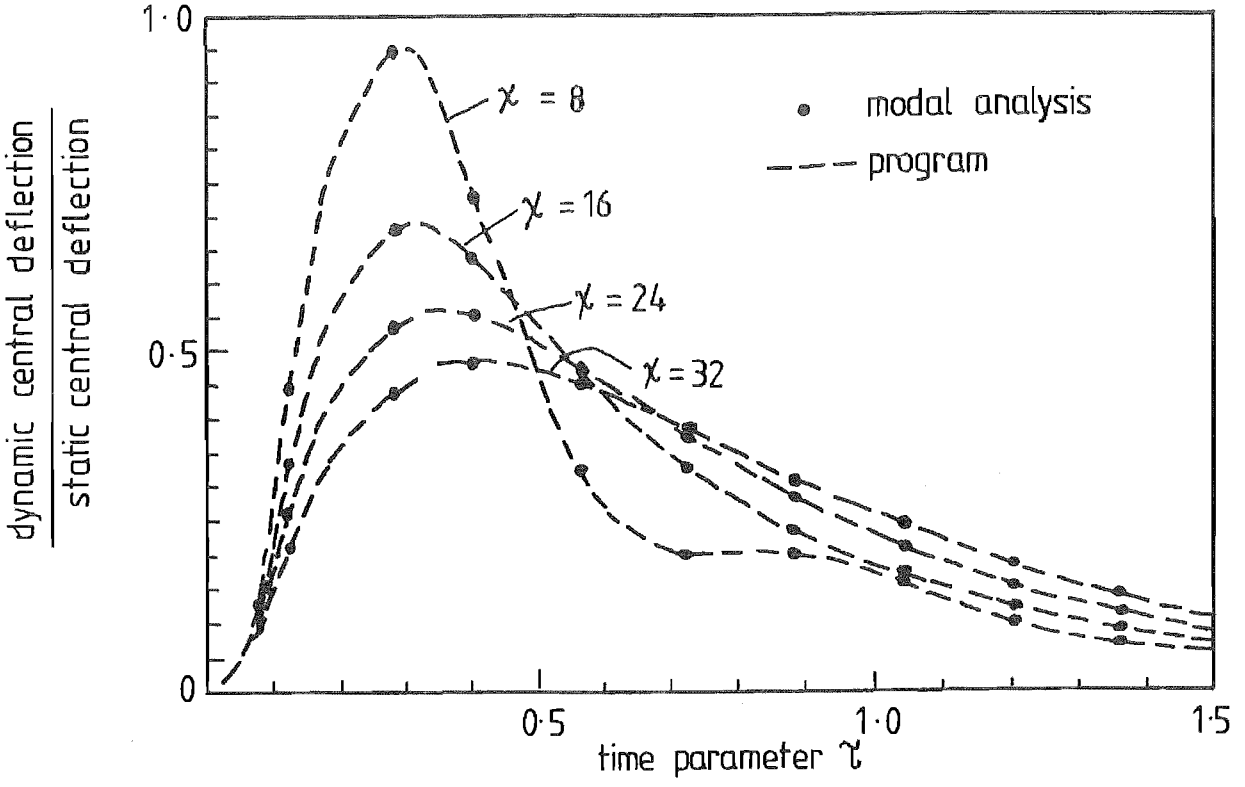

FIG 7·18 CENTRAL DEFLECTION vs TIME FOR VISCOUS DAMPING $\chi = 8, 16, 24, 32$ WITH EXPONENTIAL DECAYING LOAD $P_m = 10, \Theta = 0{\cdot}5, \lambda = 0{\cdot}3$

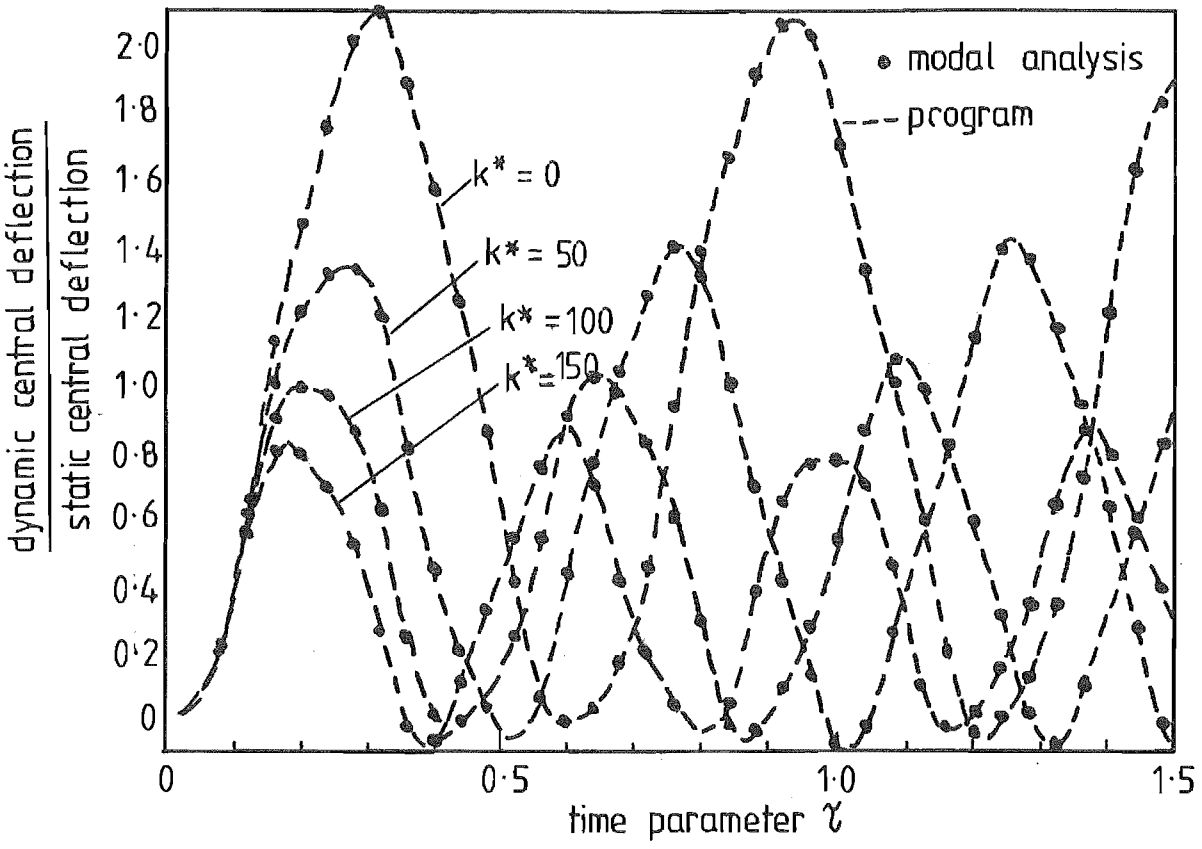

FIG 7·19 CENTRAL DEFLECTION vs TIME FOR PLATE / WINKLER FOUNDATION k^*= 0, 50, 100, WITH CONSTANT LOAD ξ=10, ν=0·3

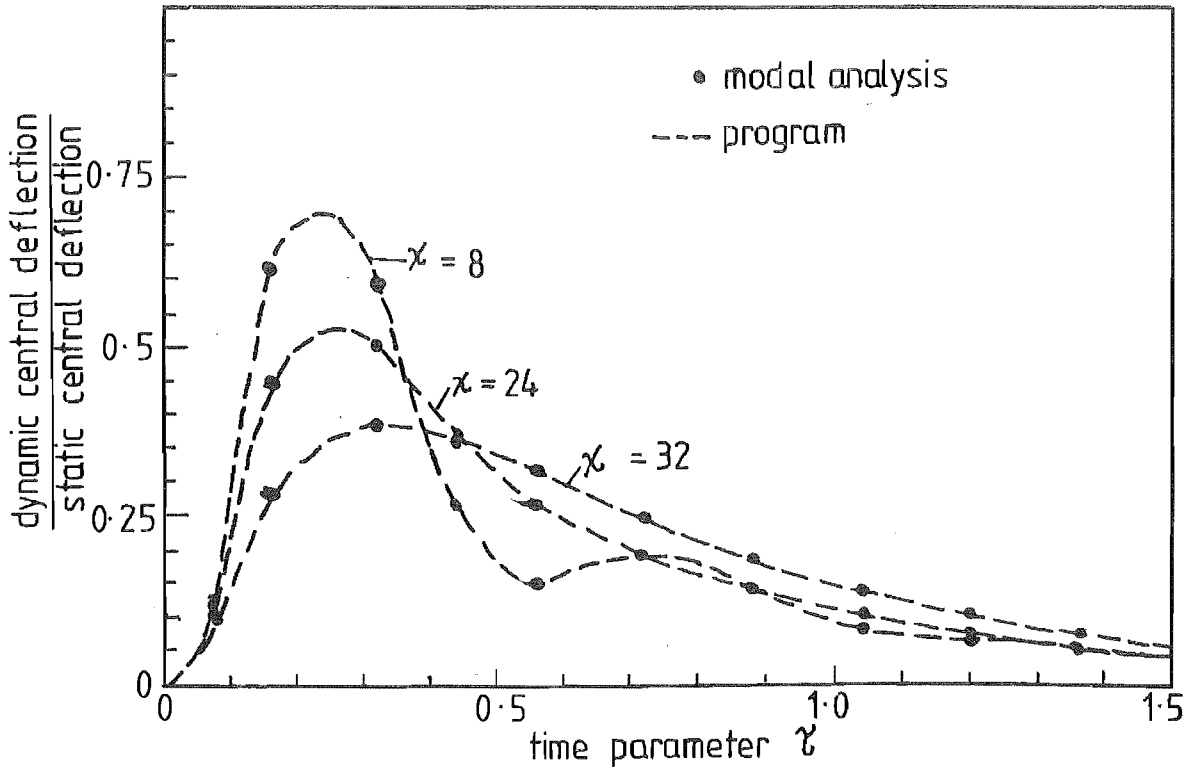

FIG 7·20 CENTRAL DEFLECTION vs TIME FOR A PLATE / WINKLER FOUNDATION k^*= 50 WITH VISCOUS DAMPING χ = 8, 24, 32 FOR EXPONENTIAL LOADING P_m = 10, θ = 0·5, ν = 0·3

An example of the central deflection history for a plate/Winkler foundation combination, subject to viscous damping, following the application of an exponentially decaying pressure, is given in Fig. 7.20, page 230. For the given time step $\Delta\tau = 0.0025$, the linear numerical and modal results are in agreement for viscous damping values of $\chi = 8$, 24 and 32.

7.2.5 PASTERNAK FOUNDATION

Fig. 7.21 shows the result for a plate/Pasternak foundation combination when subjected to a constant load of $\varepsilon = 10$ with $k = 50$ and for $G^* = 50$ and 100.

The linear numerical results for central dynamic deflection are in agreement with those from the modal analysis, section 5.2, page 142, and as for the Winkler foundation, the increasing fundamental frequency with increasing stiffness, as G^* increases in magnitude can be observed.

As for the previous case, a step size of $\Delta\tau = 0.0025$ was required to avoid relative period error in solutions approaching $\tau = 10$.

7.3 NON-LINEAR DYNAMIC RESULTS

The non-linear dynamic results for the rigidly clamped and simply supported immovable edge plate were obtained from the central difference program for a step load condition. These were plotted with the published results of Alwar et al[7.1] and Coleby et al[7.5] and discrepancies in the resultant form of the reponse discussed. Again viscous damping results were derived and compared with the

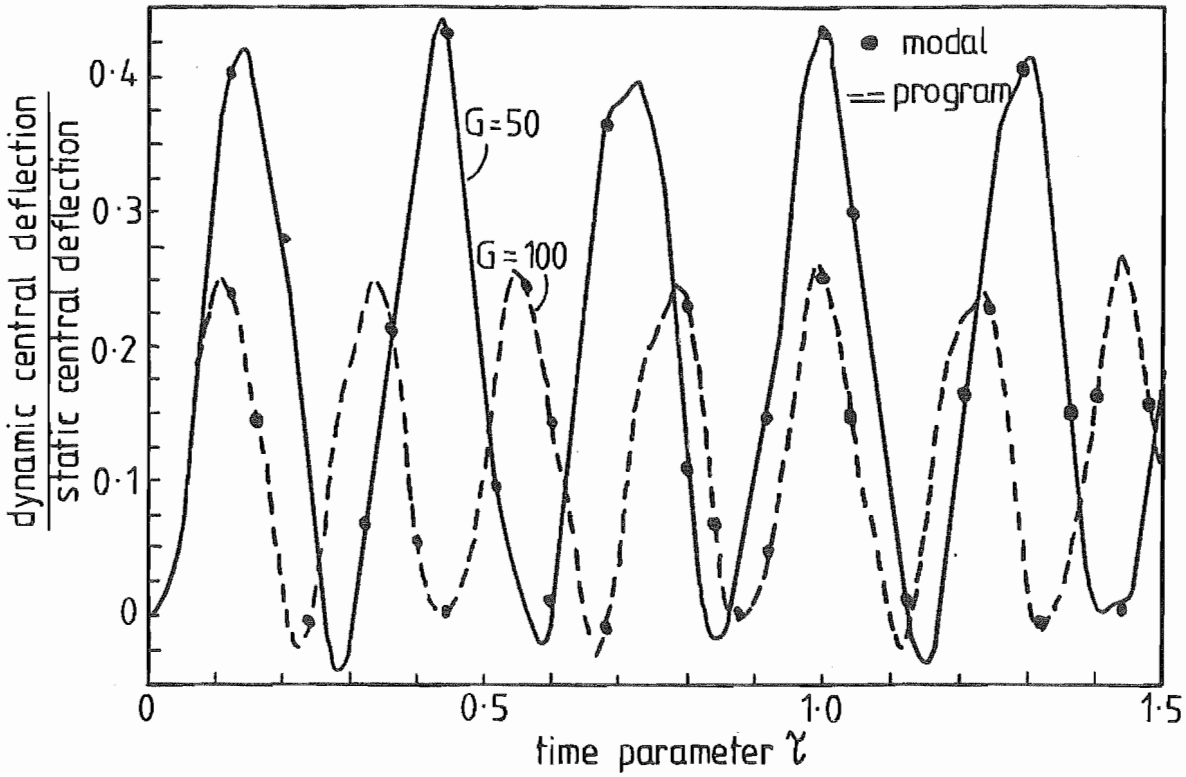

FIG 7·21 CENTRAL DEFLECTION vs TIME FOR A PLATE/PASTERNAK FOUNDATION $k^* = 50$, $G = 50, 100$ FOR CONSTANT LOAD $\varepsilon = 10$, $\nu = 0.3$

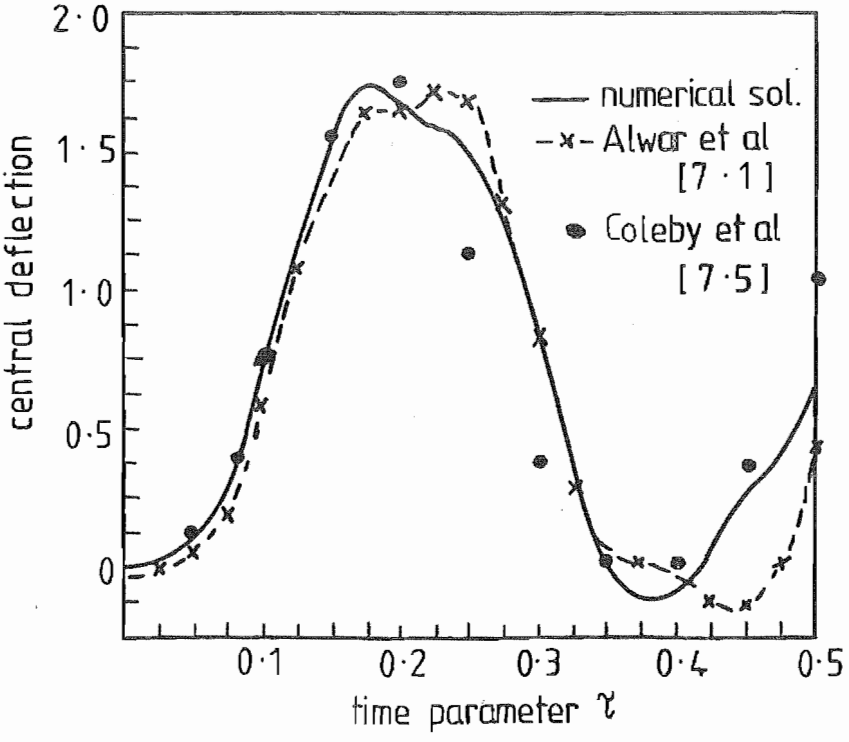

FIG 7·22 NON-LINEAR CENTRAL DEFLECTION vs TIME FOR RIGIDLY CLAMPED PLATE $\varepsilon = 10$, $\nu = 0.3$

results presented by Alwar et al.

The numerical results of the non-linear response of the plate/foundation combinations with Winkler and Pasternak foundation models for the above boundary conditions were presented and considered in relation to the work of Nath[7.7].

7.3.1 NON-LINEAR DYNAMIC TRANSIENT DEFLECTION

The results of Alwar et al [7.1] for the non-linear transient deflection of a fixed edge plate are compared, Fig. 7.22 page 232 with those from the program for an identical loading condition and it can be seen that there exists some differences in the central deflection history and the maximum deflections diverge by 2.9 .

This solution was based upon the use of Chebyshev polynomials to describe the spatial domain, in a technique developed by Alwar et al[7.2] for the static solution of the non-linear deflection of plates. The Houbolt four-point recurrence scheme was used in the time domain while a quasi-linearisation technique was implemented to allow the generation of a set of linear algebraic equations of the variable coefficients for the Chebyshev polynomials. The coefficient equations were a function of the governing equations and boundary conditions. This was solved at each nodal point in time and it would appear[7.3] that a time increment of $\Delta\tau = 0.001$ was required for an accurate solution.

The observed difference in deflection history was a function of the linearisation technique applied by Alwar et al for the non-linear terms in

using a Taylor series expansion of the form

$$(\bar{x})_i = (\bar{x})_{j-1} + (\frac{\partial \bar{x}}{\partial \tau})_{j-1} \Delta\tau + (\frac{\partial^2 \bar{x}}{\partial \tau^2})_{j-1} \Delta\tau^2$$

and the back substitution of a backward difference scheme for the first and second derivative with respect to time.

The first derivative, using backward difference, was given by [7.4]

$$\Delta\tau (\frac{\partial \bar{x}}{\partial \tau})_{j-1} = (\nabla + \tfrac{1}{2}\nabla^2 + \tfrac{1}{3}\nabla^3 .....)\bar{x}_{j-1}$$

where ∇ was the backward difference operator, j was the time nodal point while the second was

$$\Delta\tau^2 (\frac{\partial^2 \bar{x}}{\partial \tau^2})_{j-1} = (\nabla^2 + \nabla^3 + \frac{11}{12}\nabla^4 ....)\bar{x}_{j-1}$$

The substitution made by Alwar was

$$(\frac{\partial \bar{x}}{\partial \tau})_{j-1} = (\bar{x}_{j-1} - \bar{x}_{j-2})/\Delta\tau$$

and

$$(\frac{\partial^2 \bar{x}}{\partial \tau^2})_{j-1} = (\bar{x}_{j-1} - 2\bar{x}_{j-2} + \bar{x}_{j-3})/\Delta\tau^2$$

which gave

$$(\frac{\partial \alpha}{\partial \rho})_j (\frac{\partial \alpha}{\partial \rho})_{j-1} = (\frac{\partial \alpha}{\partial \rho})_j (2.5(\frac{\partial \alpha}{\partial \rho})_{j-1} - 2(\frac{\partial \alpha}{\partial \rho})_{j-2} - 0.5(\frac{\partial \alpha}{\partial \rho})_{j-3})$$

However, the derivation ignored the second order term for the first partial derivation with respect to time, which was of the same order of magnitude as the included second partial derivative with respect to time and if it had been included would have given the resultant quasi-linearisation

Therefore the errors in the quasi-linearisation were of the order of ∇^2 and when values of $\frac{\partial^2\alpha}{\partial\rho\partial\tau}$ and $\frac{\partial^3\alpha}{\partial\rho\partial\tau}$ increased, particularly as the maximum deflection was approached, this would have become significant, having the same influence as the second order partial derivative with respect to time. Figs. 7.23 and 7.24 page 236 show the variation of $\frac{\partial\alpha}{\partial\rho}$ and $\frac{\partial^2\alpha}{\partial\rho^2}$ as a function of time at locations $\rho = 0$ and $\rho = 0.33$ while Fig. 7.25 page 237 gave the derivatives $\frac{\partial^2\alpha}{\partial\rho\partial\tau}$ at those locations within the accuracy of numerical differentiation. From this figure it can be seen that the amplitude of $\frac{\partial^2\alpha}{\partial\rho\partial\tau}$ is significant and the rate of change is a maximum at the regions of discrepancy between the published results and those from the finite difference program.

The summation of the coefficients for both representations of the linearisation was unity and therefore the viscous damping case would give the static solution following decay of the oscillation irrespective of the accuracy of the dynamic deformation history. Therefore the check used by Alwar et al did not confirm the accuracy of the intermediate dynamic results, only those for the fully damped condition.

The spatial representation for the plate is also discussed in section 7.3.3 page 241 and the formulation considered.

To obtain a further comparison the numerical program was modified to allow solution for the immovable edge simply supported boundary condition i.e. at $\rho = 1$

$$\frac{\partial^2\alpha}{\partial\rho^2} + \frac{\nu}{\rho}\frac{\partial\alpha}{\partial\rho} = 0, \qquad \alpha = 0, \qquad \zeta = 0$$

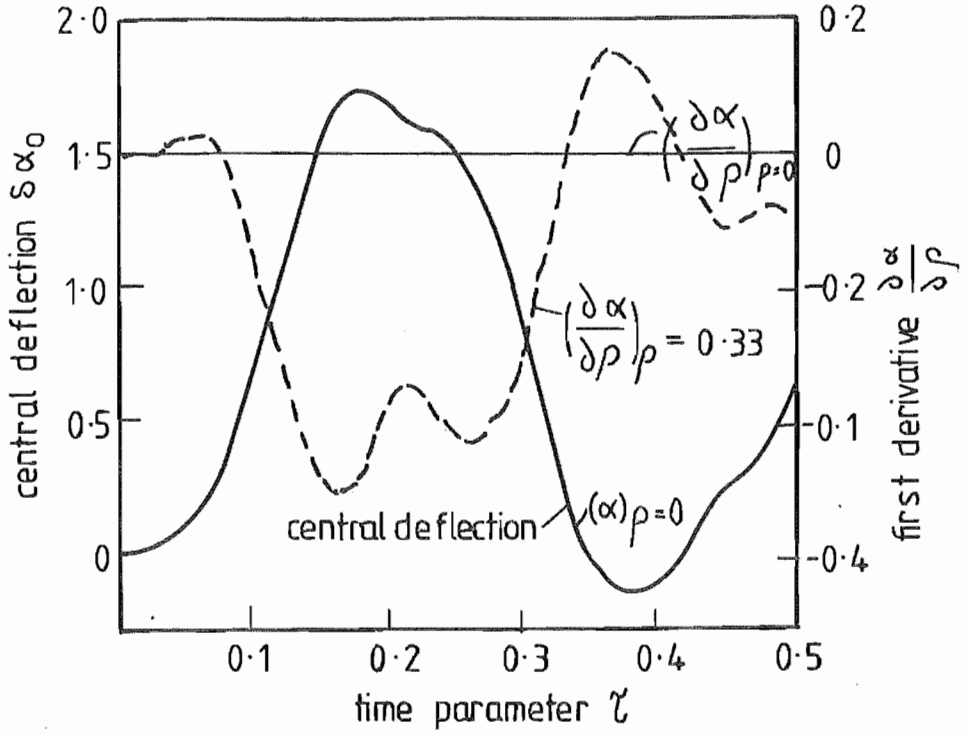

FIG 7·23 CENTRAL DEFLECTION AND FIRST DERIVATIVE vs TIME FOR RIGIDLY CLAMPED PLATE $\epsilon = 10$, $\nu = 0.3$

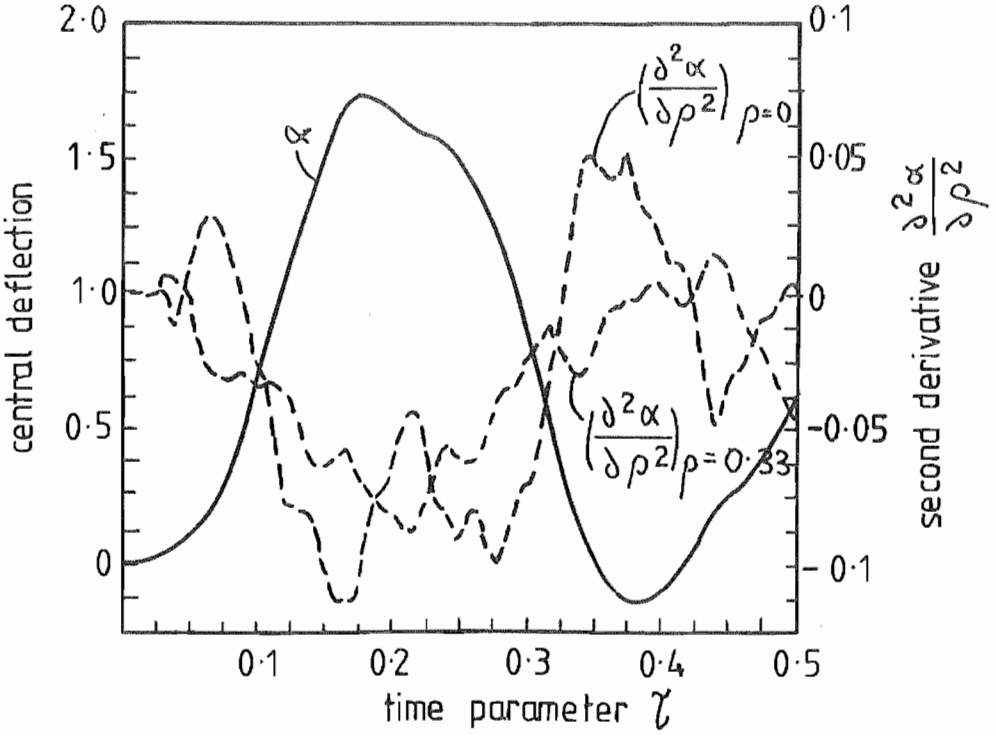

FIG 7·24 CENTRAL DEFLECTION AND SECOND DERIVATIVE vs TIME FOR RIGIDLY CLAMPED PLATE $\epsilon = 10$, $\nu = 0.3$

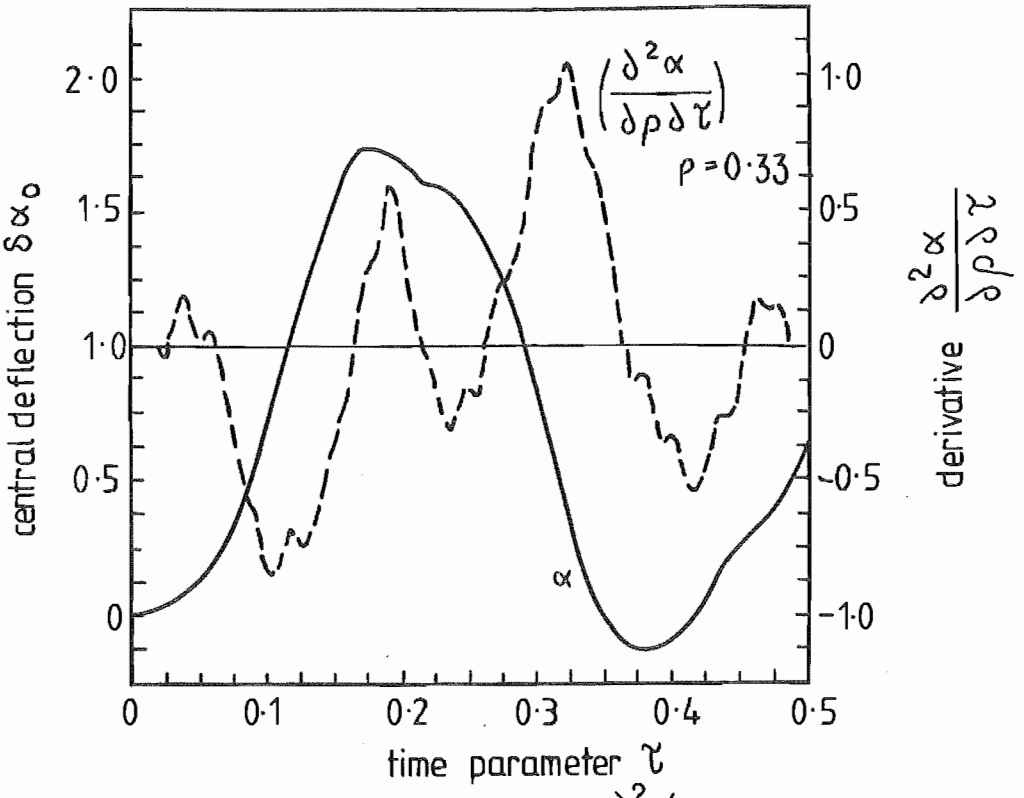

FIG 7·25 CENTRAL DEFLECTION AND $\frac{\partial^2\alpha}{\partial\alpha\partial\tau}$ vs TIME FOR RIGIDLY CLAMPED PLATE $\epsilon = 10$, $\nu = 0{\cdot}3$

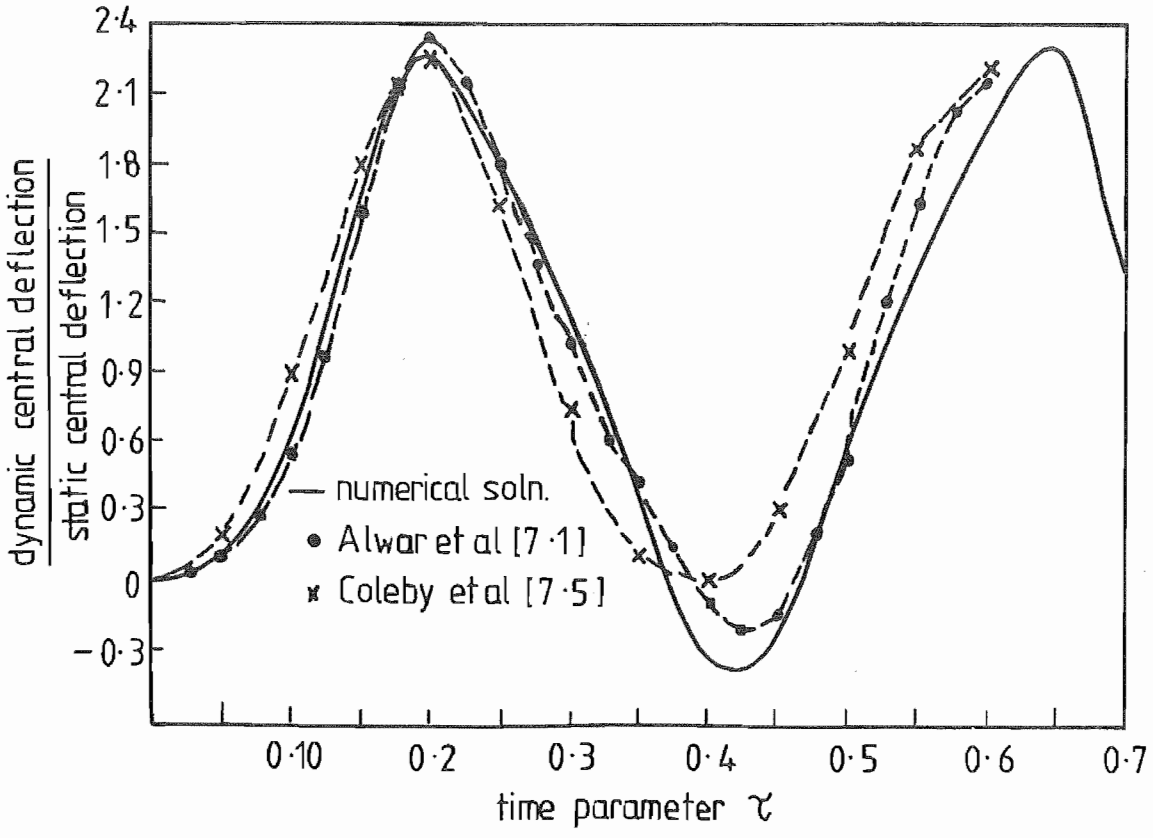

FIG 7·26 NON-LINEAR CENTRAL DEFLECTION vs TIME FOR SIMPLY SUPPORTED IMMOVABLE EDGE PLATE $\epsilon = 10$, $\nu = 0{\cdot}3$

Figure 7.26 page 237 shows the results of the program as well as those of Alwar.

An alternative solution presented by Coleby et al[7.5] was based upon the application of Berger's assumption to effectively decouple the governing equations and implementation of the iso-amplitude method of Mazumdar et al [7.6]. The resultant solutions for the circular plate with a rigidly clamped and simply supported immovable edge are presented in Fig 7.22 page 232 and Fig 7.26 page 237 , respectively. For the fixed edge condition the results of Coleby et al more closely followed the numerical program solution than those of Alwar et al. It has been established by Alwar et al [7.3] that Berger's assumption did not affect the accuracy of solution for $\varepsilon = 5$, however some discrepancy was apparent for loads of $\varepsilon = 10$. Therefore the difference exhibited between the numerical solution and that of Coleby et al was consistent with these results. The simply supported immovable edge boundary condition showed a similar difference in response.

7.3.2 VISCOUS DAMPING

The results of dynamic non-linear plate response, subject to viscous damping, were compared with those from Alwar et al [7.1]. As for the undamped plate behaviour, there was discrepancy in the deflection histories for the reasons discussed in the previous section.

Fig. 7.37 page 239 presents the results from the numerical program while Fig. 7.38 page 239 contains Alwar et al's graph for rigidly damped plate subject to a load of $\varepsilon = 10$ with a Poisson's ratio of $\nu = 0.3$. The maximum differentiation amplitude is 3.4% interpolating from the graphs. The results for the simply supported immovable edge plate are given in Figs. 7.29, 7.30, page 240 with the maximum difference in amplitude being 4.6%.

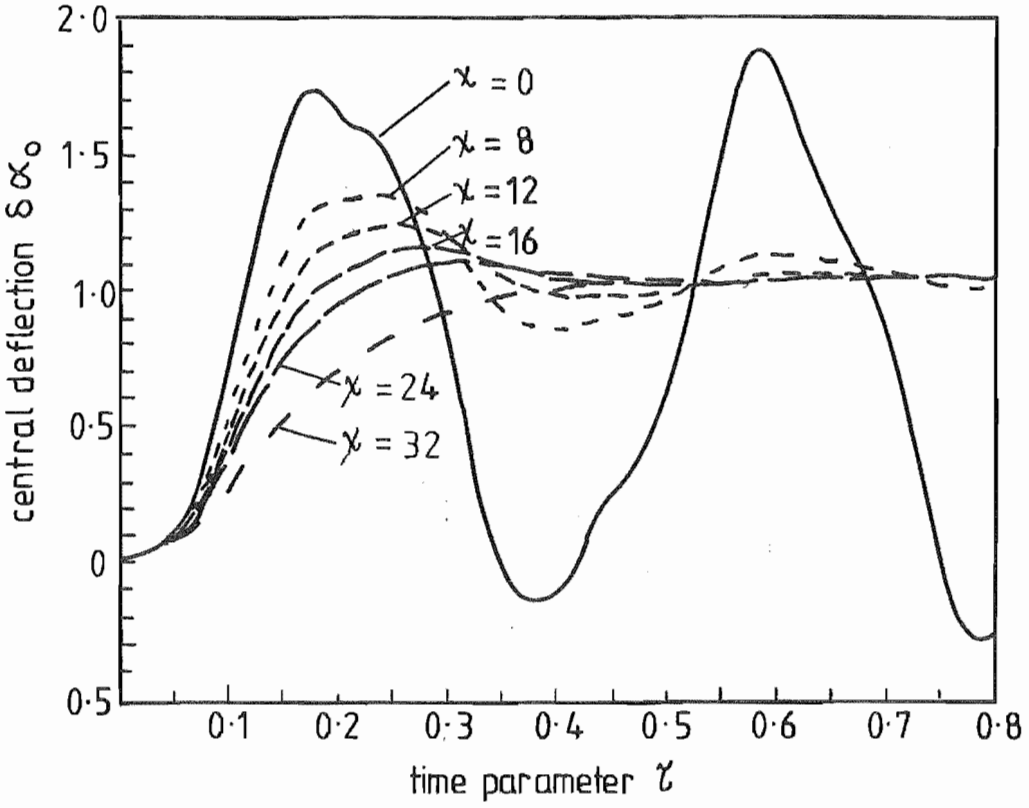

FIG 7·27 EFFECT OF DAMPING ON DYNAMIC RESPONSE FOR RIGIDLY CLAMPED PLATE $\epsilon = 10$, $\nu = 0{\cdot}3$

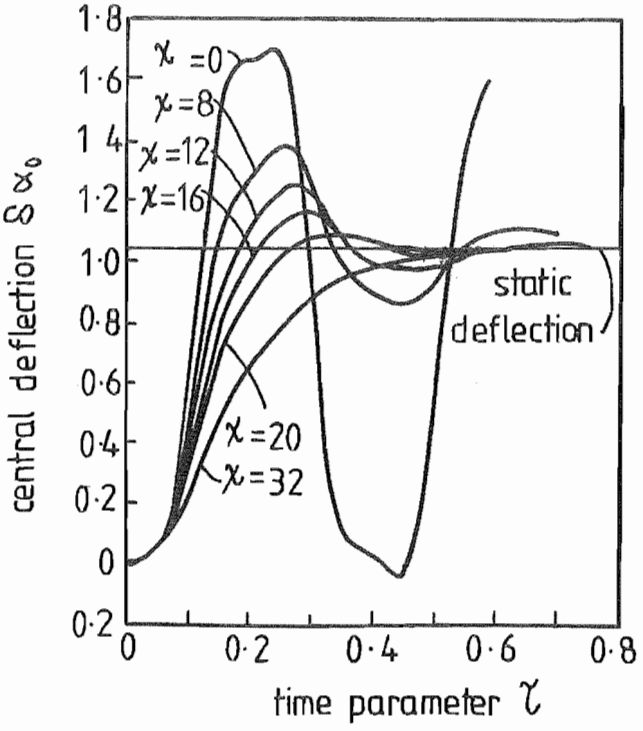

FIG 7·28 EFFECT OF DAMPING ON THE DYNAMIC RESPONSE ALWAR [7·1]

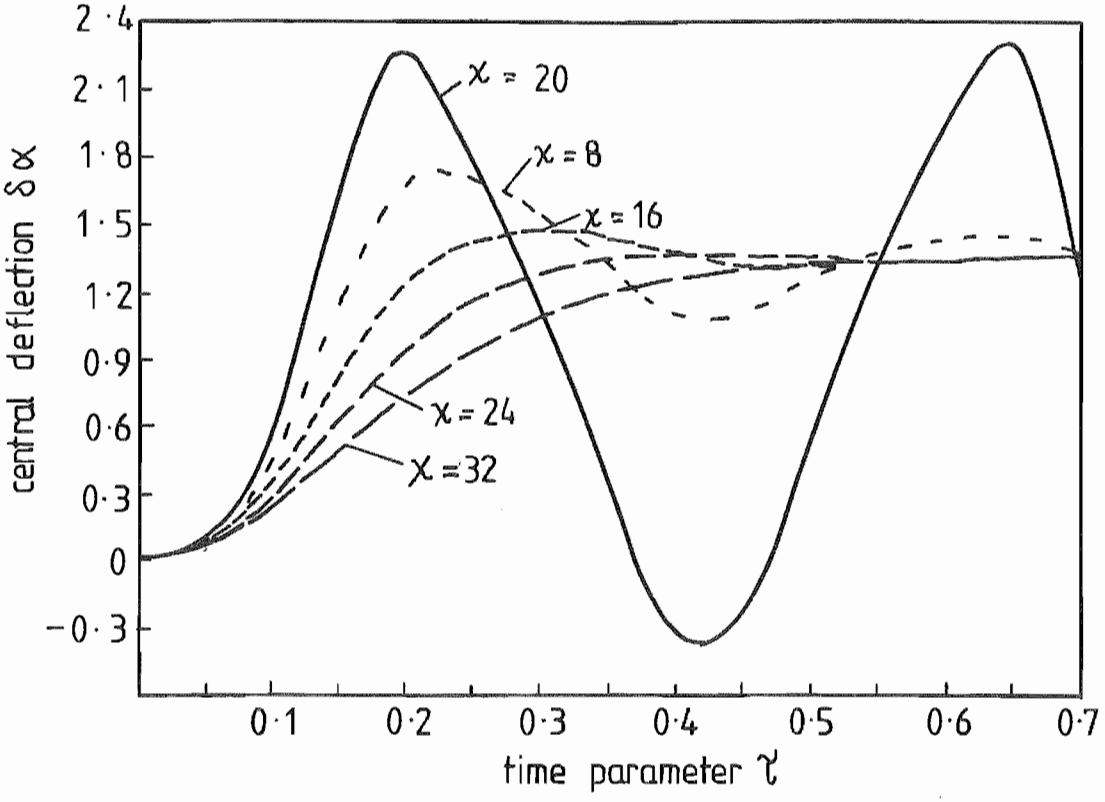

FIG 7·29 EFFECT OF DAMPING ON NON-LINEAR DYNAMIC RESPONSE FOR A SIMPLY SUPPORTED IMMOVABLE EDGE PLATE
$\epsilon = 10,\ \gamma = 0{\cdot}3$

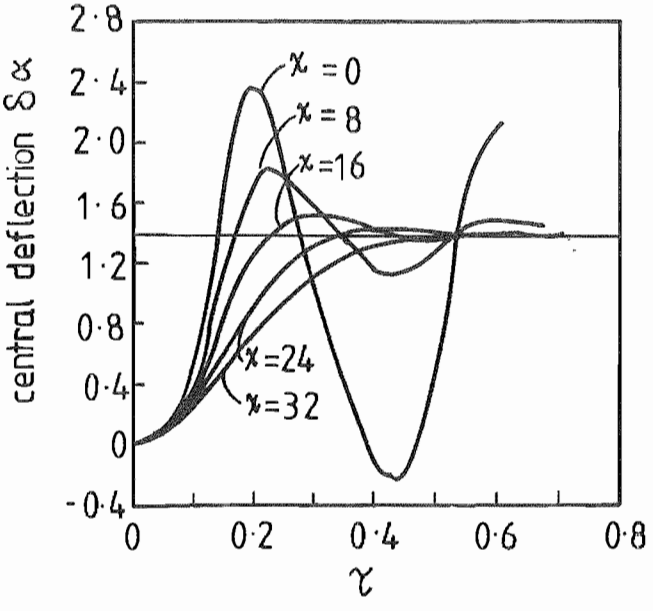

FIG 7·30 EFFECT OF DAMPING ON THE DYNAMIC RESPONSE FOR CONSTANT LOAD
$\epsilon = 10$, AFTER ALWAR [7·1]

As for the linear case it can be seen in Fig. 7.27 giving the response of a fixed edge plate, that the amplitude of the maximum deflection varies also.

7.3.3 WINKLER FOUNDATION

The results of static non-linear deflection for the plate/foundation combination were in agreement with Sinha [6.3], Fig. 6.12 page 191.

To verify the accuracy of the dynamic solution, constant loads were applied, with a viscous damping value of $\chi = 20$ to a clamped circular plate. The resultant central deflection was recorded, following cessation of oscillation, against the load for specific Winkler foundation constants $k^* = 80$ and $k^* = 120$, Fig. 7.31 page 242 . As for the static case the results coincided with those of Sinha.

The central deflection was plotted on a function of time for foundation constraints of $k^* = 50$, 100 and 150, Figure 7.32 page 242 while the results of Nath [7.7] for similar foundation and load case are presented in Fig. 7.33 page 243 . It can be seen that while the results from the program approximated those of Nath's, the published results had a lower value of maximum central deflection particularly for those with a large Winkler foundation constant. Fig. 7.34 page 243 shows superimposed results for $k^* = 50$ and $k^* = 100$ and illustrates the above point.

The resultant values from the dynamic damped cases, along with the appropriate Sinha results for the given foundation constraints were superimposed on those from Nath's paper and are presented on Fig. 7.35 page 244 . It can be seen that a discrepancy exists between the results presented by Nath, and those from Sinha and the numerical analysis. The results obtained by Nath were

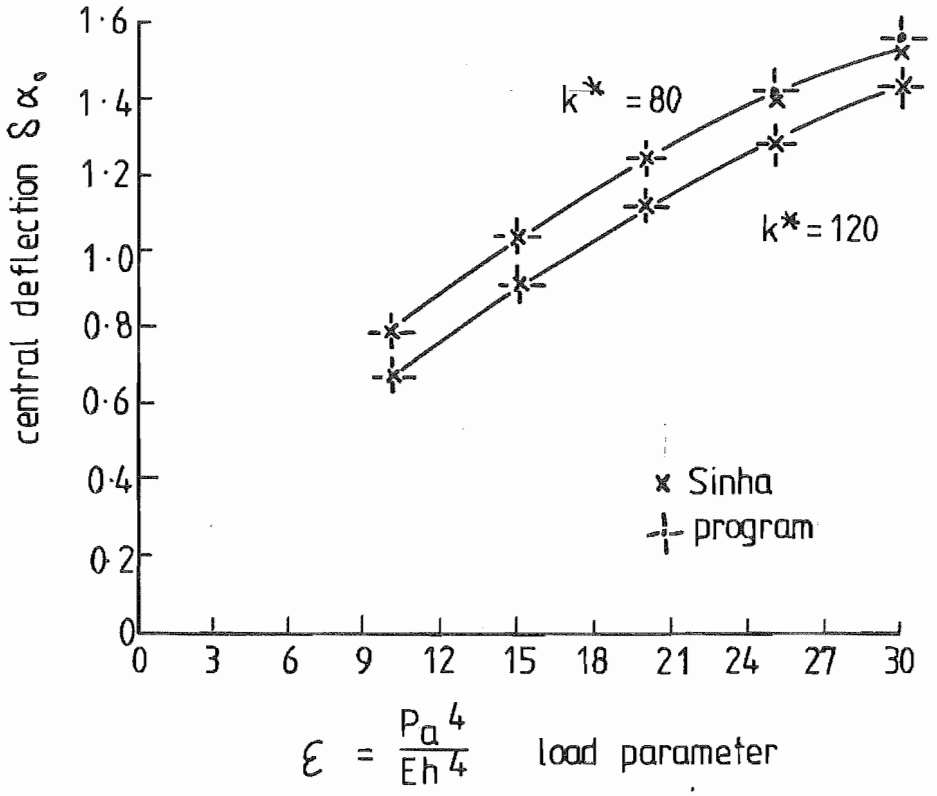

FIG 7·31 COMPARISON OF NUMERICAL RESULTS WITH SINHA [6·3] FOR CLAMPED PLATE/FOUNDATION $\nu = 0.3$

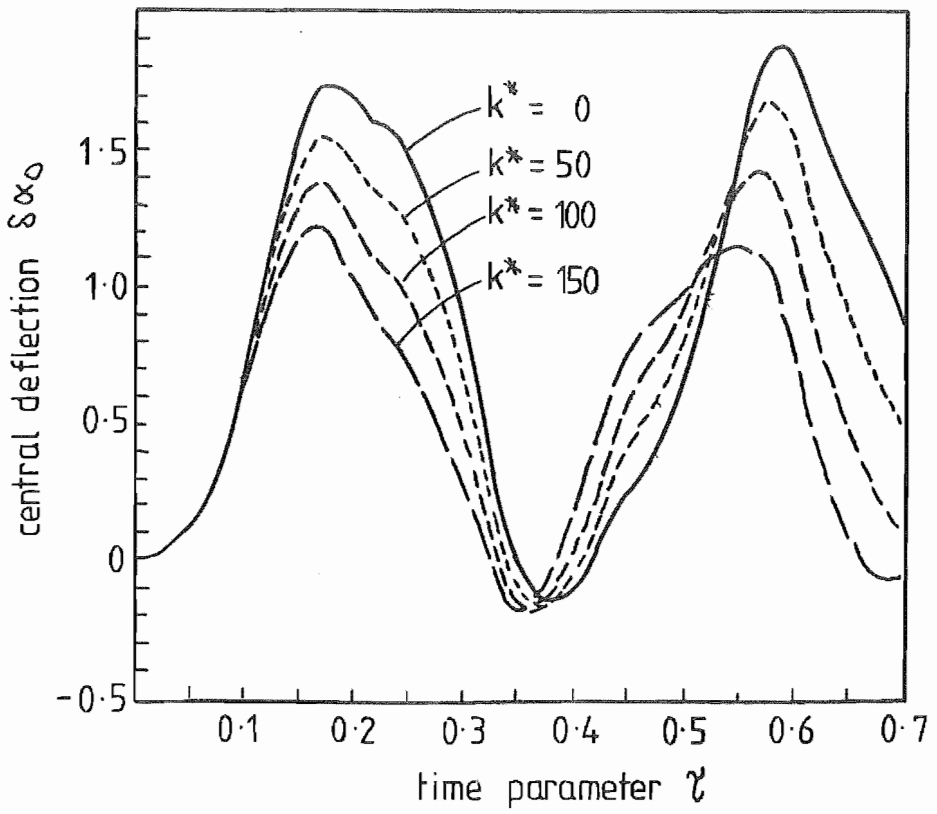

FIG 7·32 NON-LINEAR CENTRAL DEFLECTION vs TIME FOR CLAMPED PLATE/FOUNDATION COMBINATION WITH WINKLER CONSTANTS k* = 0, 50, 100 AND 150 FOR A LOAD ε = 10, ν = 0·3

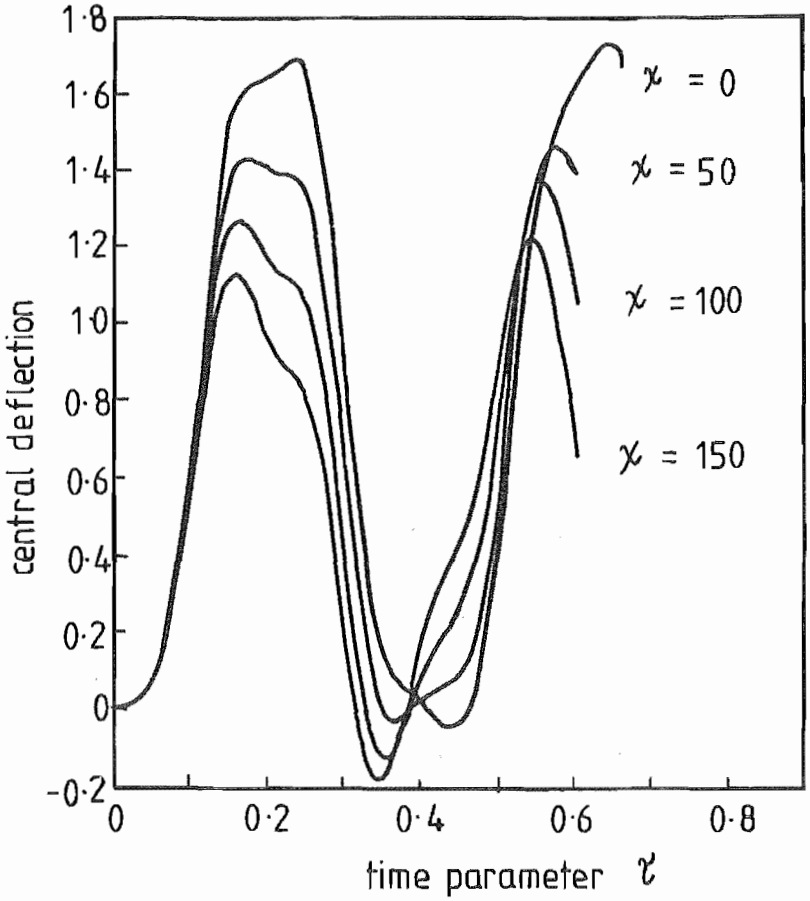

FIG 7·33 RESPONSE OF CLAMPED EDGE CIRCULAR PLATES ON WINKLER FOUNDATION FOR CONSTANT LOAD $\mathcal{E}$ = 10 AFTER NATH [7·7]

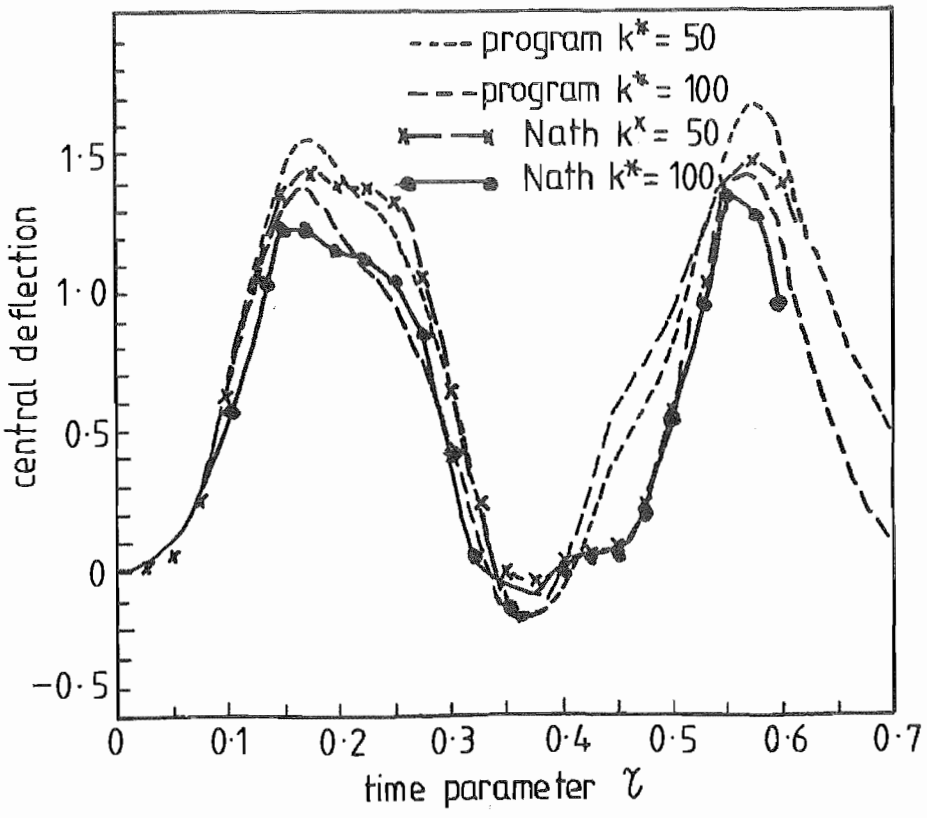

FIG 7·34 NON-LINEAR CENTRAL DEFLECTION vs TIME FOR RIGIDLY CLAMPED PLATE/FOUNDATION COMBINATION FOR WINKLER FOUNDATION k^* = 50, 100 AND $\mathcal{E}$=10, ν = 0·3 COMPARISON WITH NATH'S RESULTS [7·7]

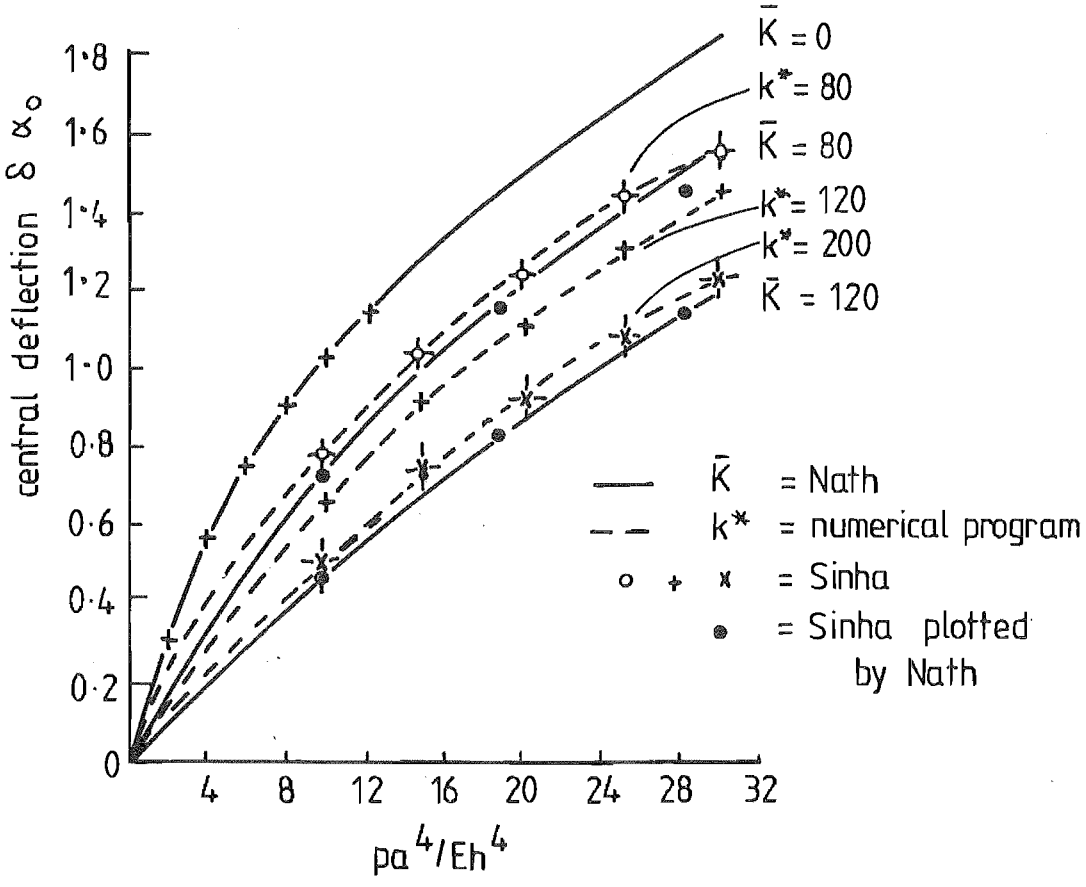

FIG 7·35 STATIC RESPONSE OF CLAMPED CIRCULAR PLATES ON WINKLER FOUNDATION AFTER NATH WITH SUPER-IMPOSED SINHA AND NUMERICAL RESULTS

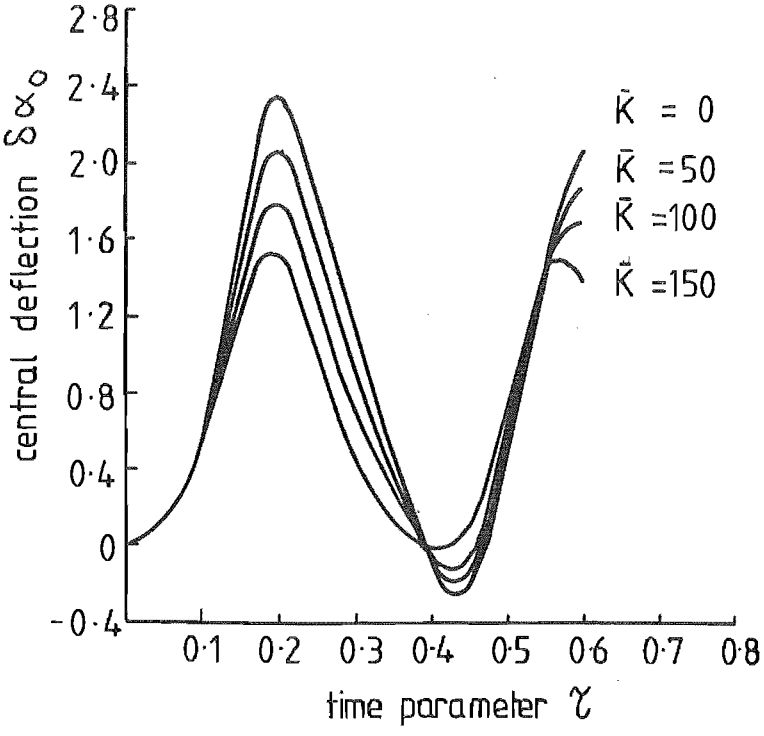

FIG 7·36 RESPONSE OF SIMPLY SUPPORTED EDGE CIRCULAR PLATES ON WINKLER FOUNDATION FOR CONSTANT LOAD $\bar{\epsilon}$=10 AFTER NATH [7·7]

stiffer than those from either Sinha or the numerical program.

Nath extended the work of Alwar et al [7.1] to describe the transient non-linear dynamic deflection of circular plate/ foundation combinations.

The governing equations used by Nath were

$$\rho^2(\nabla^2 - \frac{1}{\rho^2})\chi^* + \frac{1-\nu^2}{2}\rho(\frac{\partial\alpha}{\partial\rho})^2 = 0$$

$$\rho^3\nabla^4\alpha - 12\delta^2\rho^2\frac{\partial}{\partial\rho}(\chi^*\frac{\partial\alpha}{\partial\rho}) + \rho^3(k^*\alpha - G^*\nabla^2\alpha) - \rho^3(\varepsilon(\tau) - \chi\frac{\partial\alpha}{\partial\tau}\frac{\partial^2\alpha}{\partial\tau^2}) = 0$$

where the symbols were, as for Chapter Four, with the stress function being given by

$$\chi^* = [(1-\nu^2)/Eha].\bar{\chi}$$

and $$\bar{\chi} = rN_r$$

$$\frac{\partial\bar{\chi}}{\partial r} = N_\theta$$

This was a re-statement of equations 4.15 and 4.16.

Quasi-linerisation based upon the method discussed in section 7.3.1, of Alwar et al was used while the spatial integration of the governing equation was carried out using a finite Chebyshev polynomial series.

The deflection $\alpha(\rho,\tau)$, stress function $\chi^*(\rho,\tau)$ and their respective derivation with respect to p were defined by a Chebyshev series in the range $0 < \rho < 1$ as follows:

$$\alpha(\rho) = \frac{\alpha_o}{2} + \sum_{r=1}^{N} \alpha_r T_r^*(\rho) = \sum_{r=0}^{N}{}' \alpha_r T_r^*(\rho)$$

$$\frac{\partial \alpha(\rho)}{\partial \rho} = \frac{\alpha_o^{(1)}}{2} + \sum_{r=1}^{N-1} \alpha_r^{(1)} T_r^*(\rho) = \alpha^{(1)}$$

$$= \sum_{r=0}^{N-1}{}' \alpha_r^{(1)} T_r^*(\rho)$$

$$\frac{\partial^2 \alpha(\rho)}{\partial \rho^2} = \frac{\alpha_o^{(2)}}{2} + \sum_{r=1}^{N-2} \alpha_r^{(2)} T_r^*(\rho) = \alpha^{(2)}$$

$$= \sum_{r=0}^{N-2}{}' \alpha_r^{(2)} T_r^*(\rho)$$

$$\frac{\partial^3 \alpha(\rho)}{\partial \rho^3} = \frac{\alpha_o^{(3)}}{2} + \sum_{r=1}^{N-3} \alpha_r^{(3)} T_r^*(\rho) = \alpha^{(3)}$$

$$= \sum_{r=0}^{N-3}{}' \alpha_r^{(3)} T_r^*(\rho)$$

$$\frac{\partial^4 \alpha(\rho)}{\partial \rho^4} = \frac{\alpha_o^{(4)}}{2} + \sum_{r=1}^{n-4} \alpha_r^{(4)} T_r^*(\rho) = \alpha^{(4)}$$

$$= \sum_{r=0}^{N-4}{}' \alpha_r^{(4)} T_r^*(\rho)$$

$$\chi^*(\rho) = \frac{\chi_o^*}{2} + \sum_{r=1}^{N} \chi_r^* T_r^*(\rho)$$

$$= \sum_{r=0}^{N}{}' \chi_r^* T_r^*(\rho)$$

$$\frac{\partial \chi^*(\rho)}{\partial \rho} = \frac{\chi_o^{*(1)}}{2} + \sum_{r=1}^{N-1} \chi_r^{*(1)} T_r^*(\rho) = \chi^{*(1)}$$

$$= \sum_{r=0}^{N-1}{}' \chi_r^{*(1)} T_r^*(\rho)$$

$$\frac{\partial^2 \chi^*(\rho)}{\partial \rho^2} = \frac{\chi_o^{*(2)}}{2} + \sum_{r=1}^{N-1}{}' \chi_r^{*(2)} T_r^*(\rho) = \chi^{*(2)}$$

$$= \sum_{r=0}^{N-2}{}' \chi_r^{*(2)} T_r^*(\rho)$$

where subscripts (2) describe the order of the derivative with respect to ρ. Therefore the substitution of the vertical deflection, stress function and their respective derivatives was made allowing for the quasi-linearisation for the non-linear terms.

The derivatives when multiplied by powers of ρ were reduced to Chebyshev polynomials using product terms.

Consider for the j^{th} time step; the derivative

$$\rho^3 \frac{\partial^4 \alpha(\rho)}{\partial \rho^4} = \rho^3 \sum_{r=0}^{N-4}{}' \alpha_{r,j}^{(4)} T_r^*(\rho)$$

which on taking the radial term ρ^3 inside the summation gave

$$\rho^3 \frac{\partial^4 \alpha(\rho)}{\partial \rho^4} = \sum_{r=0}^{N-4}{}' \alpha_{r,j}^{(4)} \rho^3 T_r^*(\rho)$$

The product term, for the shifted Chebyshev polynomial of the first kind was given by [7.8]

$$\rho^s T_t^*(\rho) = \frac{1}{2^{2s}} \sum_{i=0}^{2t} \binom{2s}{i} T^*_{|t-s+i|}(\rho)$$

where

$$\binom{2s}{i} = \frac{2s!}{(2s-i)!\,i!}$$

Therefore the derivative term became on substitution for s and t

$$\rho^3 \frac{\partial^4 \alpha}{\partial \rho^4} = \sum_{r=0}^{N-4} \alpha_{r,j}^{(4)} \left(\frac{1}{64} T^*_{|r-3|}(\rho) + \frac{3}{32} T^*_{|r-2|}(\rho) + \frac{15}{64} T^*_{|r-1|}(\rho)\right.$$

$$\left. + \frac{5}{6} T_r^*(\rho) + \frac{15}{64} T^*_{r+1}(\rho) + \frac{3}{32} T^*_{r+2}(\rho) + \frac{1}{64} T^*_{r+3}(\rho)\right)$$

The recurrence relationship which could have been used to regroup the Chebyshev polynomials without introducing derivatives of the Chebyshev polynomials was

$$T^*_{r+1}(\rho) = 2(2\rho - 1)T^*_r(\rho) - T^*_{|r+1|}(\rho)$$

However the form of the above equation was not amenable to this regrouping without reverting to the original product term.

Considering the terms r = n-3 to r = n+3 by inspection, it could be seen that the coefficients for $T^*_r(\rho)$ were

$$\frac{1}{64}\alpha_{|n\pm3|} + \frac{3}{32}\alpha_{|n\pm2|} + \frac{15}{64}\alpha_{|n\pm1|} + \frac{5}{6}\alpha_n$$

Therefore terms for r > 3 and r > N-7 would satisfy the result given by Nath

$$\rho^3\left(\frac{\partial^4\alpha}{\partial\rho^4}\right) = \sum_{r=0}^{N-4}{}' \left\{\frac{1}{64}\alpha_{|n\pm3|} + \frac{3}{32}\alpha_{|n\pm2|} + \frac{15}{64}\alpha_{|n\pm1|} + \frac{5}{6}\alpha_n\right\}$$

and since $T^*_n(\rho) = 0$ if values of $|n - i| < 0$ result in $\alpha_{|n-i|} = 0$ the result given by Nath could be applied for the range r = 0 to r < N - 7.

$$\rho^3\left(\frac{\partial^4\alpha}{\partial\rho^4}\right) = \sum_{r=0}^{N-7}{}' \left\{\frac{1}{64}\alpha_{|n\pm3|} + \frac{3}{32}\alpha_{|n\pm2|} + \frac{15}{64}\alpha_{|n\pm1|} + \frac{5}{6}\alpha_n\right\}T^*_r(\rho)$$

+ additional terms in the range N - 7 <r < N - 4

and only if the condition $\alpha_r = 0$ where r > N - 4 does the description used by Nath apply over the range 0 < r < N - 4.

On substitution of the Chebyshev polynomials into the governing equations for the vertical deflection and stress function, Nath uses incorrect limits for the summation of the lower order derivatives. In the case of the lower derivatives the summation should have been from r = 0 to r = N - i where i was the order of the derivative.

Alternatively the derivatives could have been left in the form

$$\rho = \frac{\partial^3 \alpha(\rho)}{\partial \rho^3} = \sum_{r=0}^{N-3}{}' \alpha_{r,j}^{(3)} \left(\frac{1}{16} T^*_{|r\pm2|}(\rho) + \tfrac{1}{4} T^*_{|r\pm1|}(\rho) + \frac{3}{8} T^*_r(\rho)\right)$$

substituted into the governing equations, and the coefficients of the respective Chebyshev polynomials equated to zero. Again the recurrence relationship

$$\alpha_{|r-1|}^{(k+1)} \quad \alpha_{|r+1|}^{(k+1)} = 4r\, a_r^k$$

would be used to relate the coefficients of derivatives of differing orders.

The differences were consistent with those observed for the maximum central deflection histories in the published data [7.7] and the results derived from the numerical program.

The comparison with Way's results [4.4] was exact, within the accuracy of the presentation of the data; and therefore the source of error was considered to be in the implementation of the foundation response.

The simply supported immovable edge plate/foundation combination was also considered and the results can be seen in Fig. 7.36, page 244 from Nath's work and Fig. 7.37, page 244 for the central difference program. In this case there was a closer corrrespondence between the two sets of results with the difference in the first cycle maximum central deflection being -4%, -3.4% and -0.6% for k^* = 50, 100 and 150 respectively. This should be

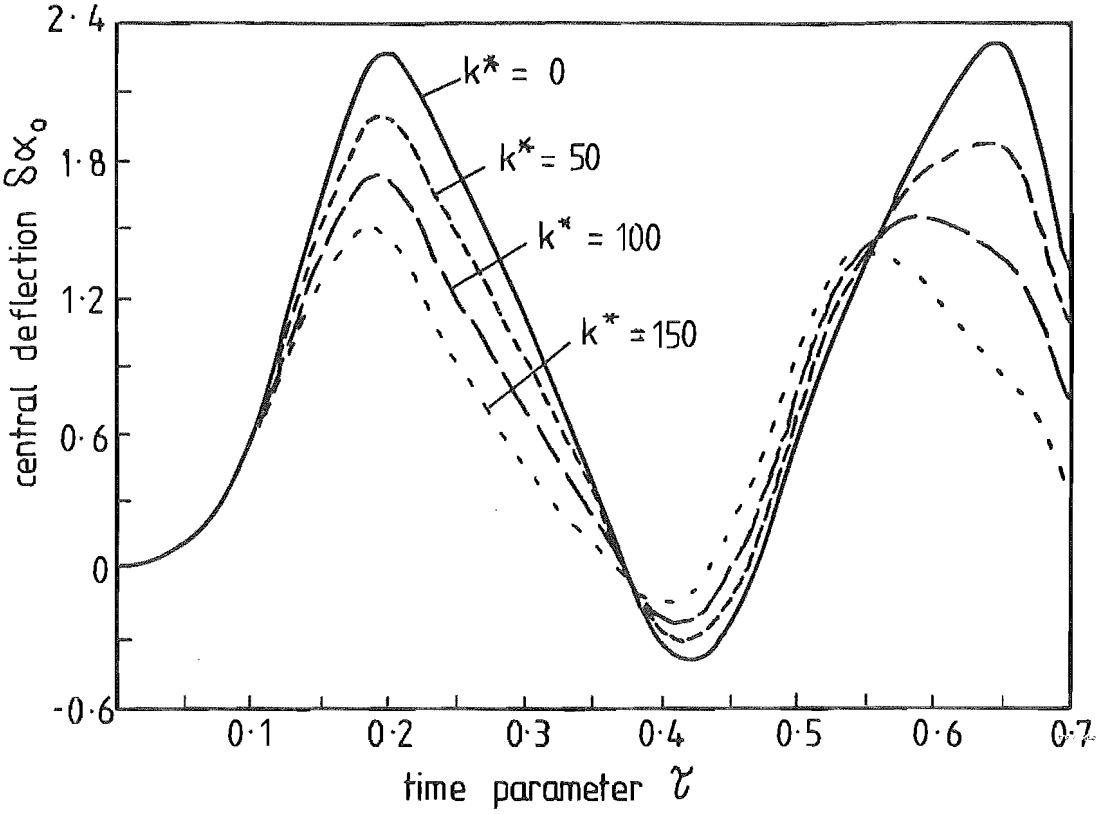

FIG 7·37 CENTRAL DEFLECTION vs TIME FOR SIMPLY SUPPORTED IMMOVABLE EDGE PLATE/FOUNDATION COMBINATION WINKLER FOUNDATION CONSTANTS k = 50, 100, 150, ε = 10, λ = 0·3

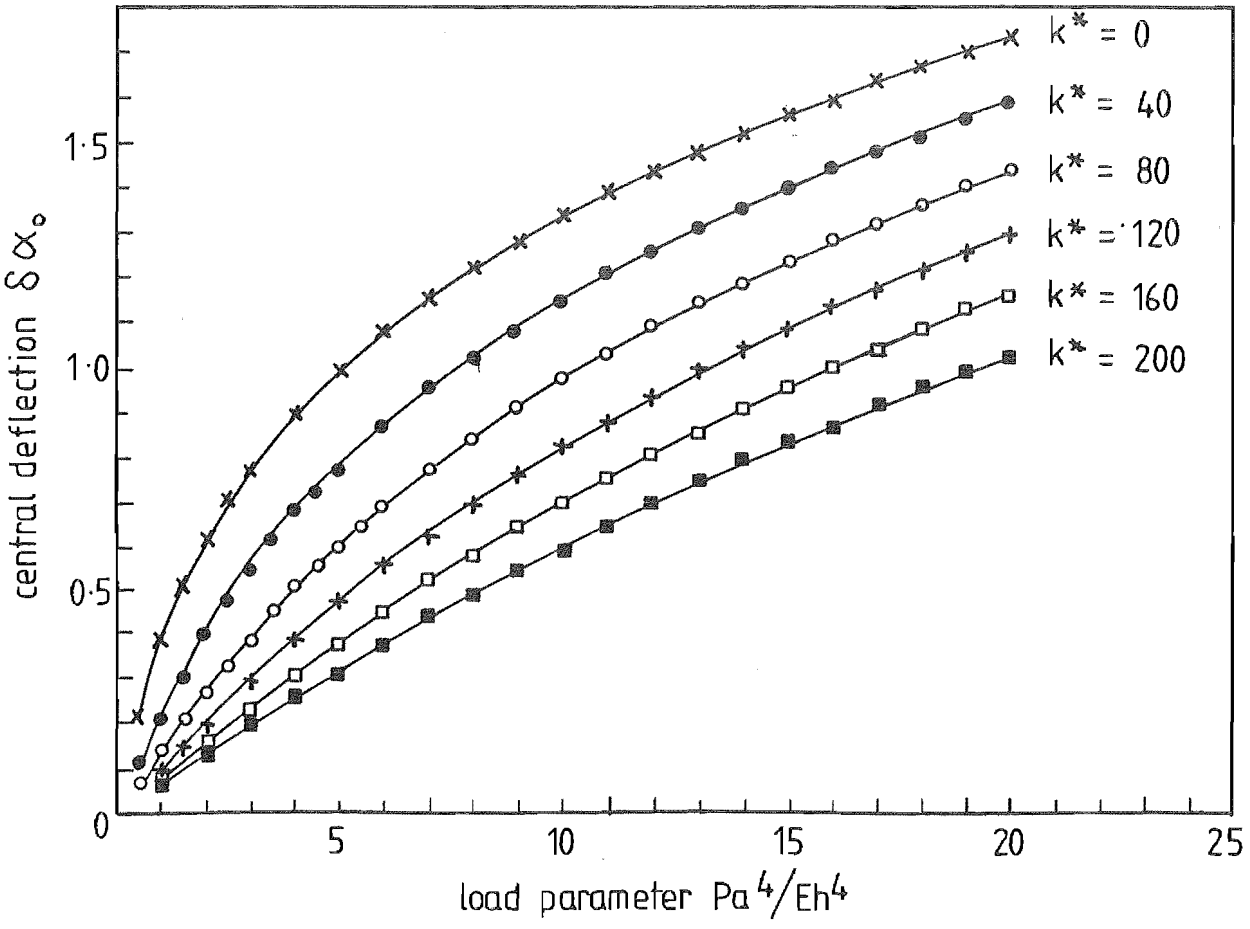

FIG 7·38 STATIC CENTRAL DEFLECTION FOR SIMPLY SUPPORTED IMMOVABLE EDGE PLATE ON WINKLER FOUNDATION λ = 0·3

compared with the fixed edge plate/ foundation combination where the differences for the same constants were -7.3%, -8.3% and -7.3% respectively.

Also static central deflection for the simply supported immovable edge case is presented in Fig. 7.38, page 250 for loads in the range $\varepsilon = 0 - 20$ and for Winkler foundation constants $k^* = 0$, 40, 80, 120, 160 and 200.

The representation of the Winkler foundation in the central difference program was identical for the linear and non-linear transient dynamic analysis while the geometrical non-linear contribution was not directly associated with the time domain model. In section 7.2.4, it was shown that the linear numerical solution was in agreement with the modal analysis while the static and damped dynamic solutions coincided with the published data on Sinha, Fig. 6.12, page 191. Therefore the numerical program was considered to describe the behaviour of the plate/foundation more accurately than the published results.

Since Nath's results were the only published information for the dynamic non-linear deflection of a clamped or simple supported immovable edge circular plate on a foundation no other comparison could be made and for the reasons given above, it was considered the finite difference numerical program would be an appropriate model on which to base transducer behaviour studies, when considering a dielectric with Winkler foundation characteristics.

Nath's paper was marred by typographical errors which made it difficult to determine if the discrepancy was a function of incorrect formulation or programming errors.

7.3.4. PASTERNAK FOUNDATION

The dynamic response for a fixed edge circular plate on a Pasternak foundation is shown in Fig. 7.39, page 253 and it can be seen that it was at variance with the corresponding results obtained by Nath [7.7], Fig. 7.40, page 253. For a fixed value of k^* the results from the finite difference program showed a decrease in deflection with increasing value of G^*. The referenced results exhibit a decrease in central deflection for $G^* = 50$, $k^* = 50$ by comparison with the Winkler foundation $k^* = 50$ while for $G^* = 100$, $k^* = 50$ the central deflection increases in relation to $G^* = 0$, $k^* = 50$.

Fig. 7.41 page 254 gives the influence of the Pasternak foundation module on maximum central deflection as obtained for a clamped circular plate by Nath. Since the maximum central deflection was not constant for each cycle, i.e. Fig.. 7.27, page 239, the plot of static central deflection for $k^* = 50$ and $k^* = 100$ as a function of Pasternak foundation module for $\varepsilon = 20$, $\nu = 0.3$ is presented in Fig. 7.42, page 254.

For the simply supported immovable edge plate the central deflection history is presented in Fig. 7.43, page 255 and it can be seen that in this case an increasing value of G^* results in an increase in the stiffness of the system. While the form of the response was similar to that derived by Nath, Fig. 7.44, page 255 the difference in the amplitudes of the first maximum for $G^* = 50$ and $G^* = 100$ were 9.2% and 10.2%. As for the fixed edge condition the plot of static central deflection for $k^* = 50$ and $k^* = 100$ as a function of the Pasternak foundation modulii for $\varepsilon = 20$, $\nu = 0.3$ is presented in Fig. 7.45, page 256.

The results from the central finite difference program were taken as being an accurate representation of the non-linear transient deflection of a rigidly damped plate for the Pasternak foundation.

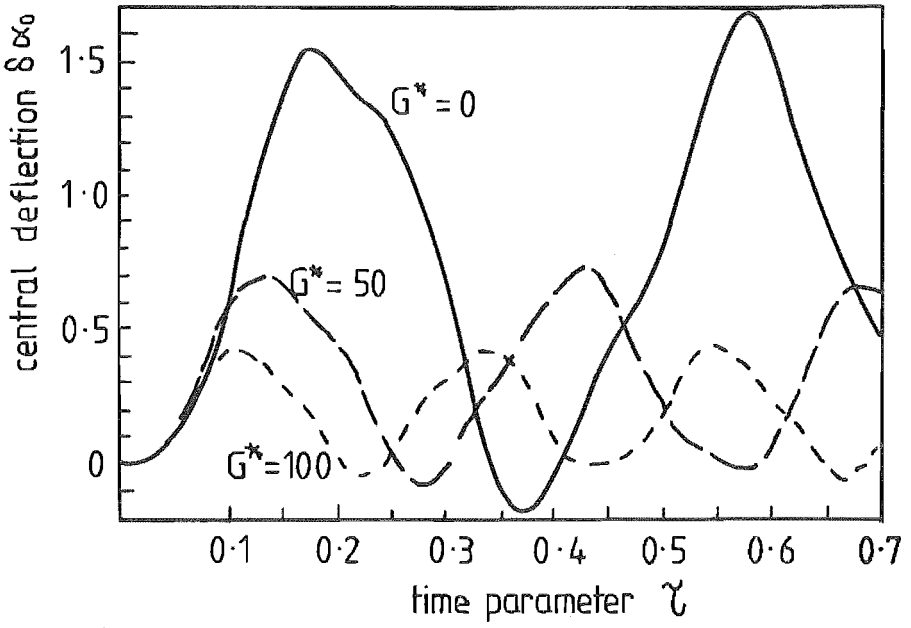

FIG 7·39 NON-LINEAR CENTRAL DEFLECTION vs TIME FOR RIGIDLY CLAMPED PLATE / PASTERNAK FOUNDATION $k^* = 50$, $G^* = 0, 50, 100$, FOR CONSTANT LOAD $\epsilon = 10$, $\nu = 0{\cdot}3$

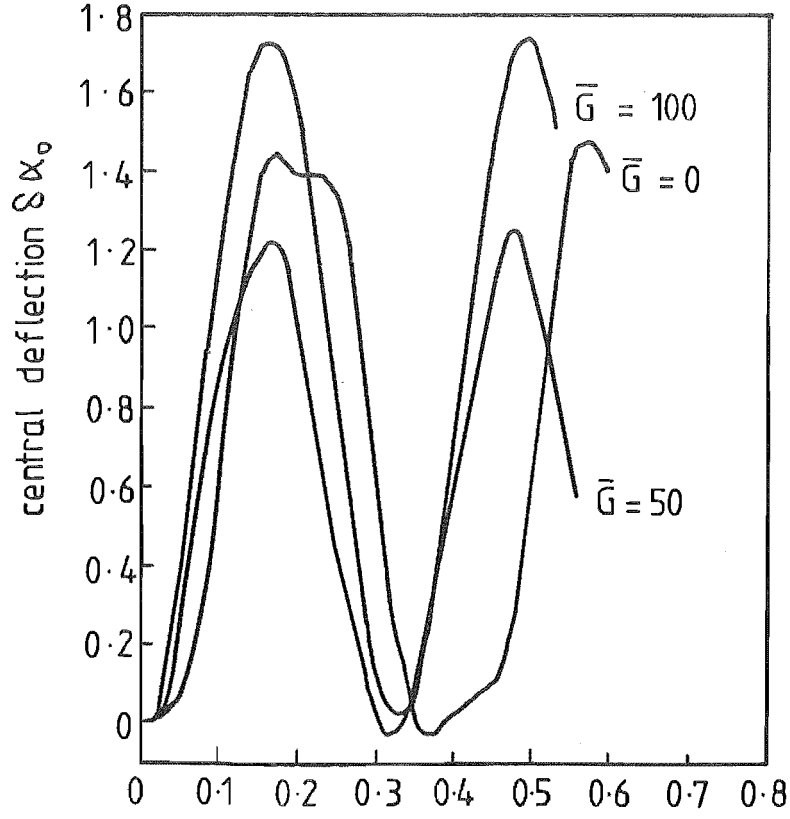

FIG 7·40 RESPONSE OF CLAMPED EDGE CIRCULAR PLATES ON PASTERNAK FOUNDATION FOR $\epsilon = 10$, $k^* = 50$, AFTER NATH [7·7]

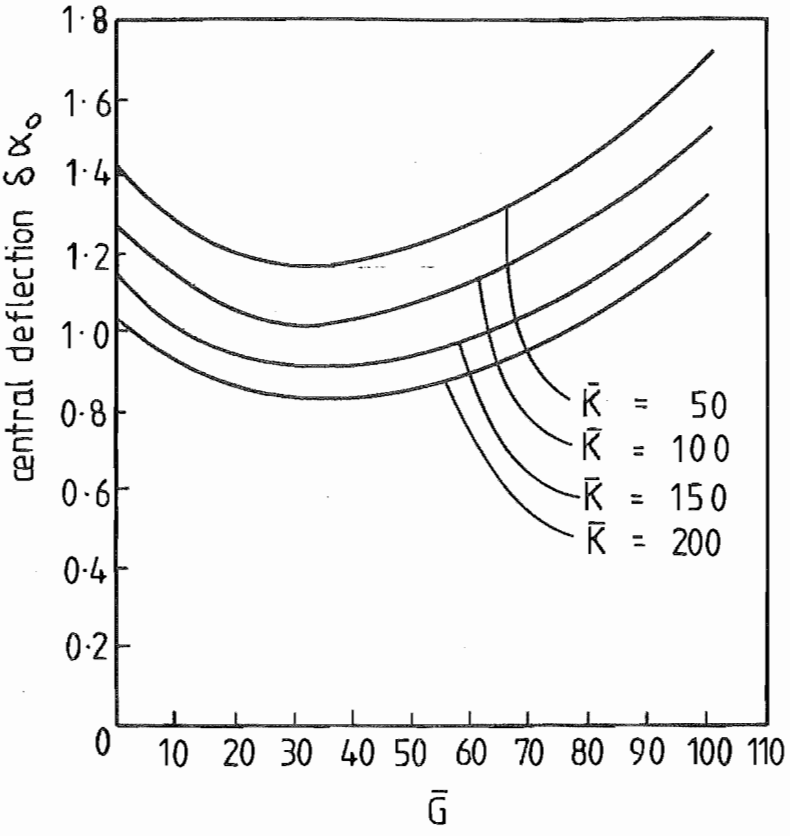

FIG 7·41 INFLUENCE OF PASTERNAK FOUNDATION MODULI ON THE CENTRAL DEFLECTION OF CLAMPED CIRCULAR PLATES ϵ = 10 AFTER NATH [7·7]

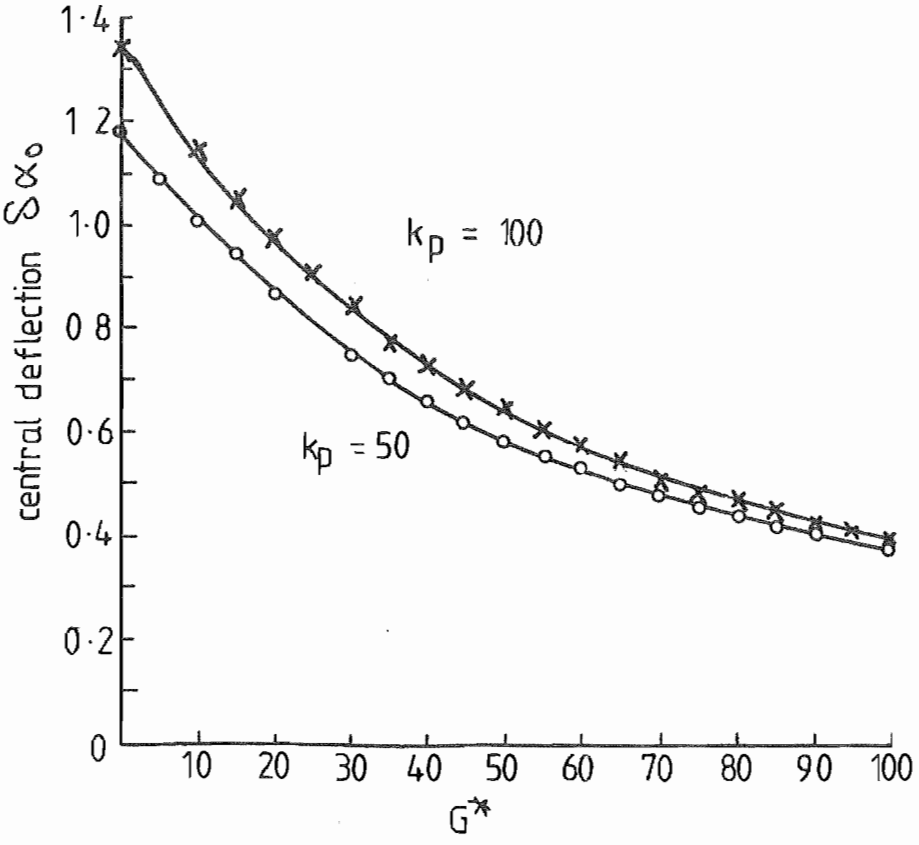

FIG 7·42 VARIATION OF CENTRAL DEFLECTION WITH G^* FOR STATIC NON-LINEAR DEFLECTION FOR RIGIDLY CLAMPED PLATE ϵ = 20, γ = 0·3

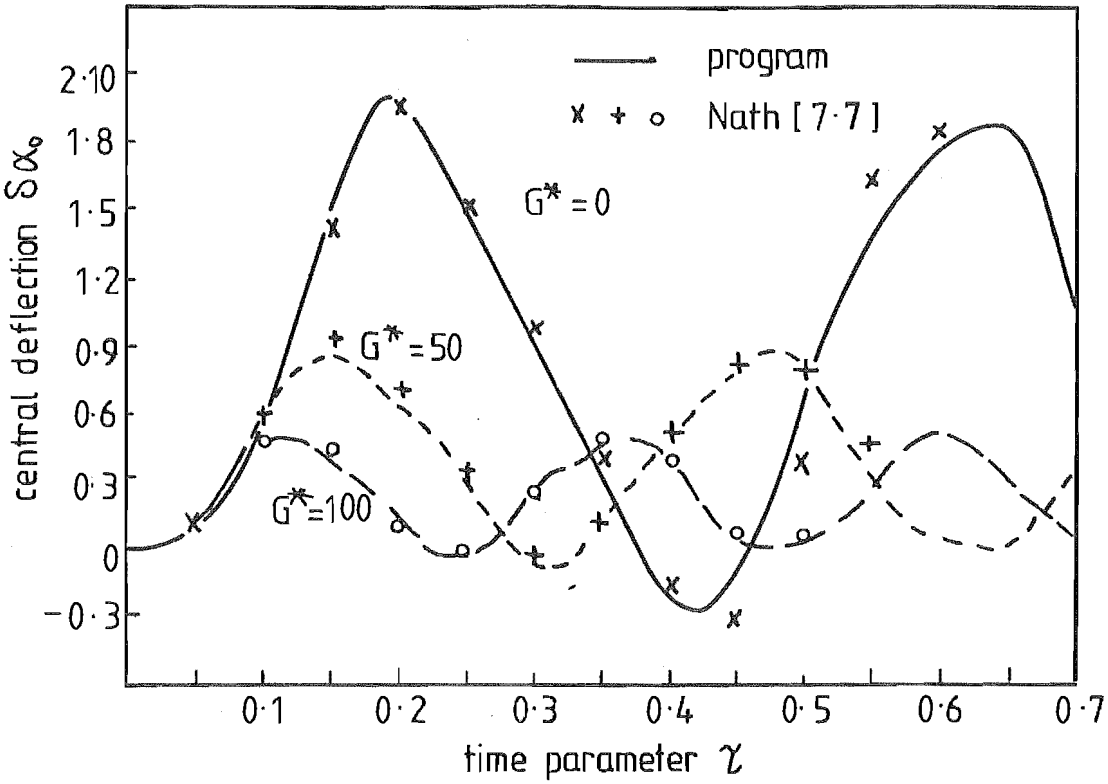

FIG 7·43 NON-LINEAR RESPONSE OF SIMPLY SUPPORTED IMMOVABLE EDGE CIRCULAR PLATES ON PASTERNAK FOUNDATION FROM NUMERICAL PROGRAM $\epsilon = 10$, $k^* = 50$, $\nu = 0{\cdot}3$

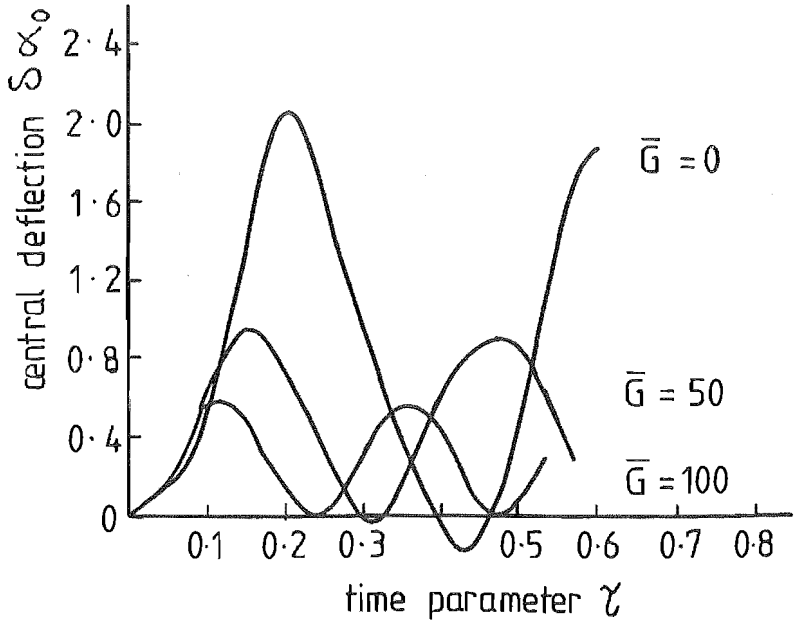

FIG 7·44 RESPONSE OF SIMPLY SUPPORTED EDGE CIRCULAR PLATES ON PASTERNAK FOUNDATION $\epsilon = 10$, $k^* = 50$, AFTER NATH [7·7]

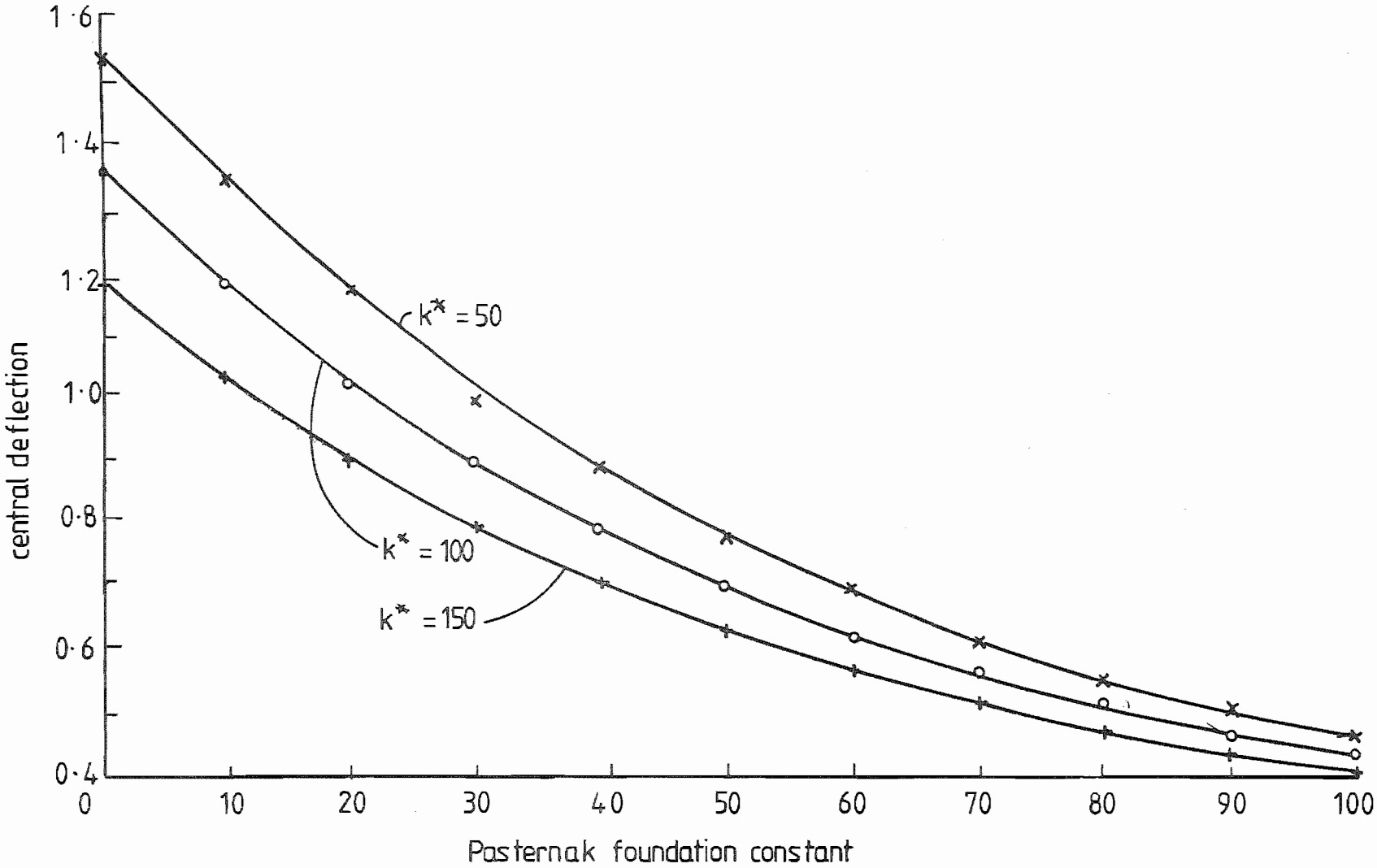

FIG 7·45 STATIC CENTRAL DEFLECTION vs PASTERNAK FOUNDATION CONSTANT FOR A SIMPLY SUPPORTED IMMOVABLE EDGE PLATE $\nu = 0{\cdot}3$ $\epsilon = 20$

The Pasternak foundation was based upon a shear interaction being superimposed on the spring model of Winkler equation.The spring elements, Fig. 7.46, page 258 were considered effectively connected to an isotropic layer of incompressible vertical elements which can only deform in transverse shear. The resultant equilibrium condition [7.9] gave

$$q(x,y) = k\,w(x,y) - G\,\nabla^2 w(x,y)$$

where G was the shear modulus for the incompressible layer.

Therefore for polar co-ordinates the relationship was

$$q(r) = k\,w(r) - G\,\nabla^2 w(r)$$

for axisymmetric deformation.

Selvadurai pointed out the similarity with the Filonenko-Borodich model, Fig. 7.47, page 258 where T = G which would give in polar co-ordinates

$$q(r) = k\,w(r) - G\,\nabla^2 w(r)$$

Since the equivalent model consisted of an elastic membrane, tensioned to T, on which the springs act, it can be visualised that if the values of T increased, the stiffness of the plate/foundation combination would increase.

Alternatively, considering an element in the shear layer acting in the Pasternak foundation it can be shown that the equilibrium condition was [7.9]

$$\frac{\partial \tau^*_{rz}}{\partial r} + \frac{\tau^*_{rz}}{r} + \rho - k(w) = 0$$

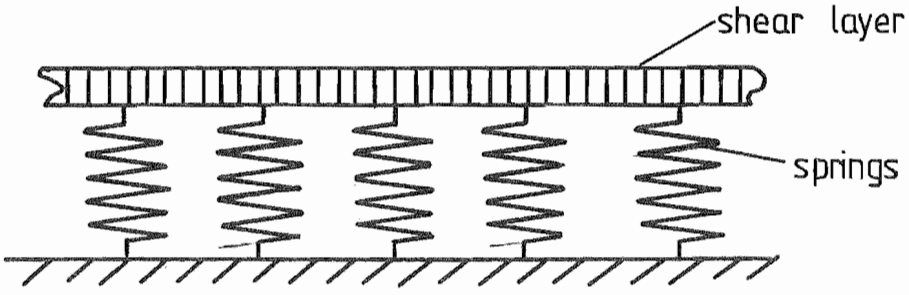

FIG 7·46 SCHEMATIC OF PASTERNAK FOUNDATION MODEL

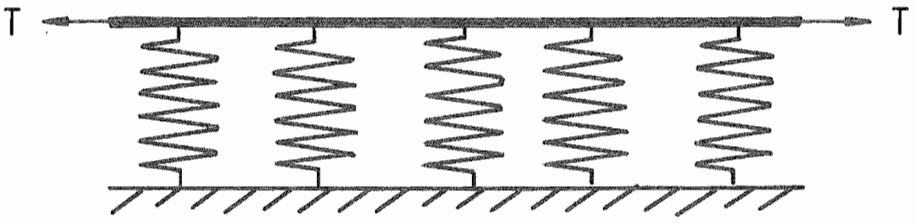

FIG 7·47 SCHEMATIC OF FILONENKO – BORODICH FOUNDATION MODEL

where τ^*_{rz} = transverse shear stress = $G \frac{\partial w}{\partial r}$

ρ = applied pressure

$k(w)$ = spring reaction

which gave the Pasternak foundation characteristic

$$G \nabla^2 w + \rho - k(w) = 0$$

and if the spring support was equated to zero, the resultant transverse shear would react against the applied loading. Therefore as the value of G increased the magnitude of $\tau^*_{r\zeta}$, for a given value of slope $\frac{\partial w}{\partial r}$ or linear deflection, would increase proportionately giving a greater reactive force to the plate. This implied that the effect of increasing G would be to stiffen the plate/foundation combination as observed in the results from the numerical program. The apparent reduction in stiffness with increasing magnitude of G* for the rigidly clamped plate, after Nath [7.7], Fig. 7.40, page 253 and Fig. 7.41, page 254 contradicted this consideration.

Further, as for the Winkler foundation, the linear dynamic control deflection of a rigidly clamped circular plate on a Pasternak foundation obtained by numerical and modal analysis showed agreement for $G^* = 50$, 100 and $k^* = 50$, Fig. 7.21, page 232 . The same alogorithm was used to implement the Pasternak foundation, in the programs for the linear and non-linear solution while the numerical technique used to describe the geometric non-linearity was common to all the non-linear programs. The geometric non-linearity alogorithm gave identical results to Way and Sinha for static non-linear deflection, Fig. 6.7, page 184 and Fig. 6.12, page 191 while for damped dynamic deflection the results again corresponded to the published data, Fig. 7.31, page 242. As mentioned above the Pasternak foundations alogorithm satisfied the dynamic linear deflection.

Also it would be anticipated that the change in response for the non-linear deflection, with increasing value of G^*, would be similar in form to that for the linear deflection but with reduced amplitude since the geometric non-linearity was a function of the vertical deflection.

In the comparison between the program results for the simply supported immovable edge plate and the fixed edge plate, Fig. 7.39, page 253 and Fig. 7.43, page 255, again the form of response was similar with variation of amplitude and frequency as was expected. Since the simply supported edge condition of the first case had a lower rigidity while the in-plane boundary condition was identical, the resultant deflection and frequency increased. From Nath's results, the maximum central deflection was of the order $\delta\alpha_o \simeq 1.7$ for the rigidly clamped plate given $G^* = 100$, $k^* = 50$, $\varepsilon = 10$, while for the same conditions for the simply supported plate, the central deflection was $\delta\alpha_o \simeq 0.6$.

In view of these results, the comments in the section 7.3.3. and the previous discussion, the central finite difference program was taken as describing the behaviour of a rigidly clamped plate/foundation system, particularly for the Pasternak foundation, while Nath's results were considered to be in error.

It would appear that the implementation of the rigidly clamped boundary condition had a more significant effect on the accuracy of Nath's results than the simply supported cases, particularly in the presence of foundations.

7.4 NON-LINEAR MODAL ANALYSIS

The result for central deflection from the non-linear modal analysis can be seen in Fig. 7.48, page 262 along with that from the numerical program for the fixed edge circular plate, subject to a uniform constant load at $\rho = 0$.

It could be seen that the modal analysis result approximated those from the central difference program for deflections in the range $\delta\alpha_o > 0.7$. However, for greater deflections the results of modal analysis were significantly lower, the error in the maximum deflection being -9.2%.

Therefore, the non-dimensional form of the Berger solution for static non-linear deflection was considered because the method of decoupling the equations governing vertical and in-plane deflection used the assumption that the first strain invariant was constant, after Berger, and was equated to the difference between the square of the roots $\lambda^2_2 - \lambda^2_1$ at a given point in time. Fig. 7.49, page 262 shows the relationship between γ^{*2} and the central deflection $\delta\alpha_o$ and it can be seen that it was non-linear. Therefore the requirement of linearity for superposition was not satisfied and the modes could not be effectively decoupled so that the higher order modes, in particular, were inaccurate in amplitude and frequency.

Although the instantaneous influence of the non-linearity in the values of $\lambda^2_2 - \lambda^2_1$ for the given mode was determined, the assumed independence of modes introduced errors in the values of $\lambda^2_2 - \lambda^2_1$ and hence, ω_n as well as the effective elapsed time. The relationship between $\lambda^2_2 - \lambda^2_1$ and $\delta\alpha$ (o) for the first order mode is shown in Figure 7.49 while the resultant frequency as a function of central deflection is compared with results from the literature [4.3] in Fig. 7.50, page 263. The values of $\lambda^2_2 - \lambda^2_1$ for the first mode and γ^{*2} did not coincide because of the time dependence of $\lambda^2_2 - \lambda^2_1$. Also the time dependence of the radial

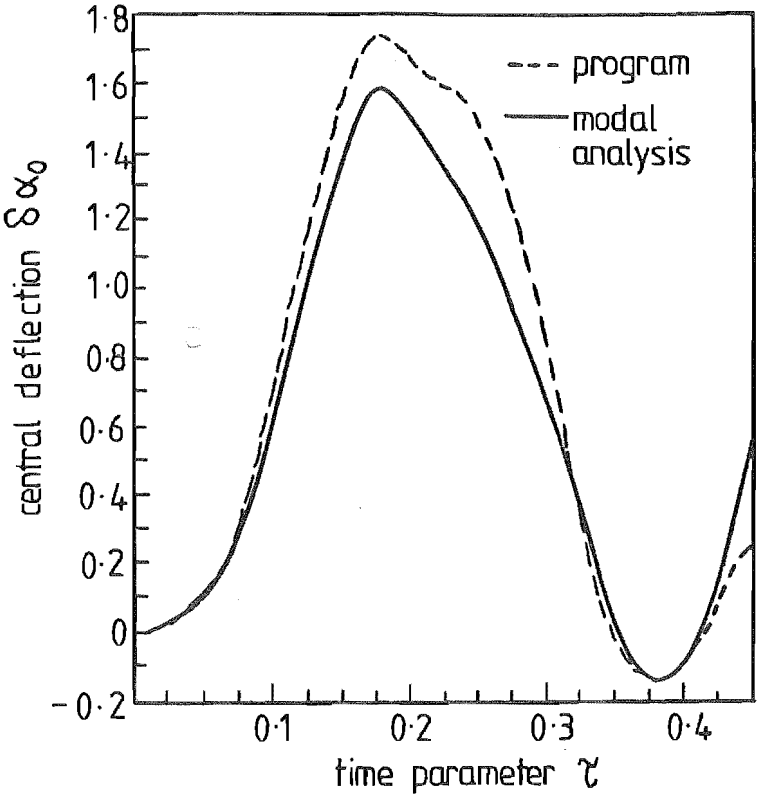

FIG 7·48 NON-LINEAR MODAL ANALYSIS FOR RIGIDLY CLAMPED PLATE $\epsilon = 10$

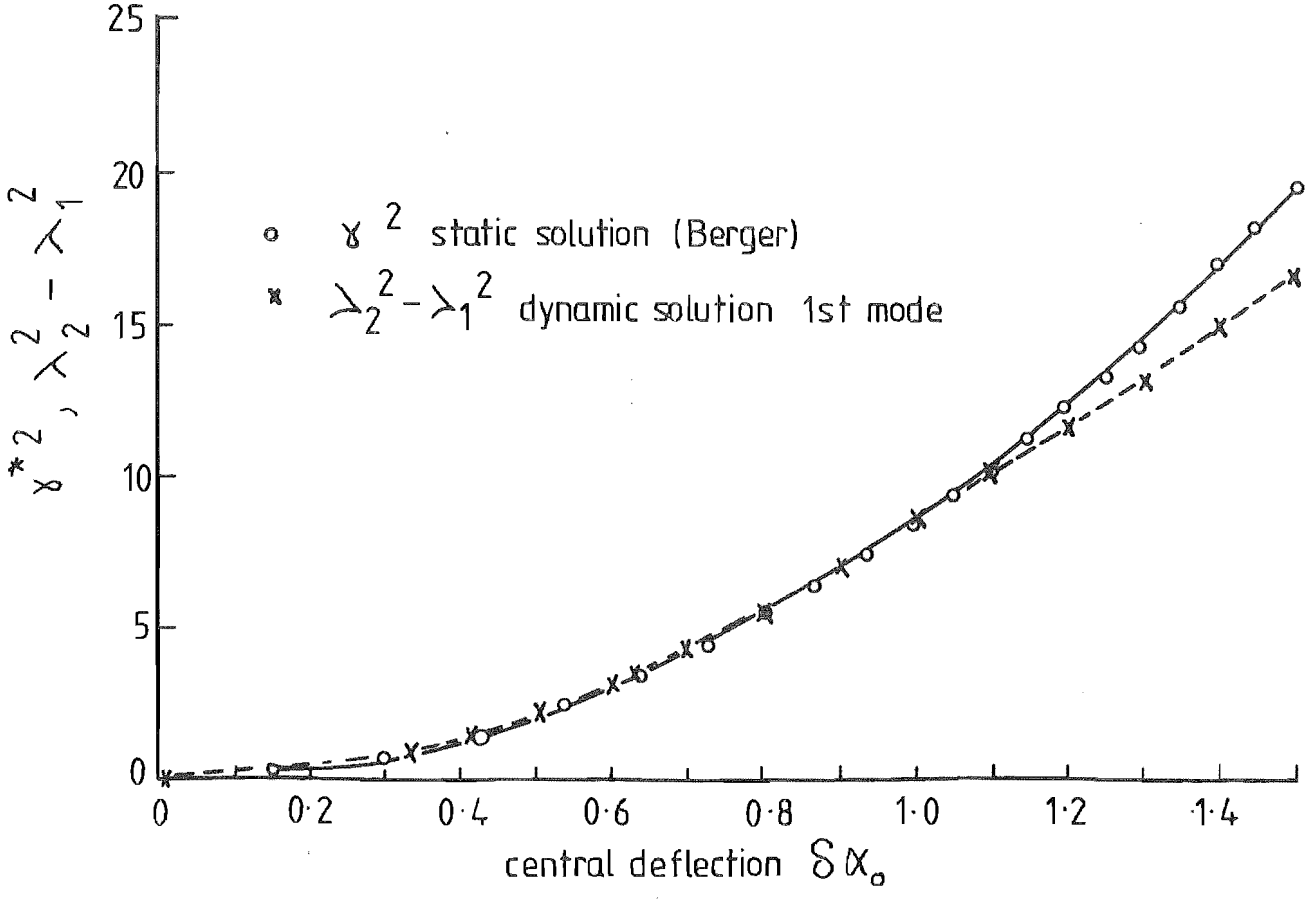

FIG 7·49 γ^2, $\lambda_2^2 - \lambda_1^2$ vs $\delta\alpha_{(0)}$ FOR RIGIDLY CLAMPED PLATE

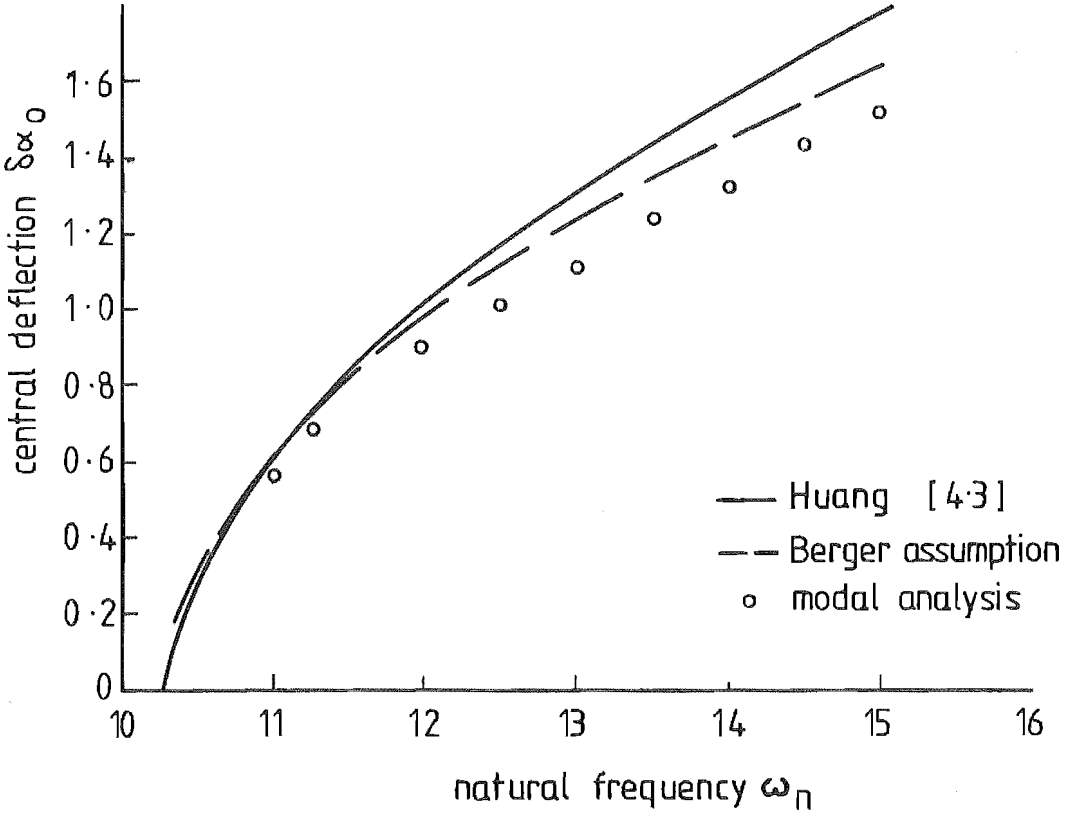

FIG 7·50 CENTRAL DEFLECTION vs FREQUENCY FOR FIRST MODE OF NON-LINEAR MODAL ANALYSIS FOR PLATE

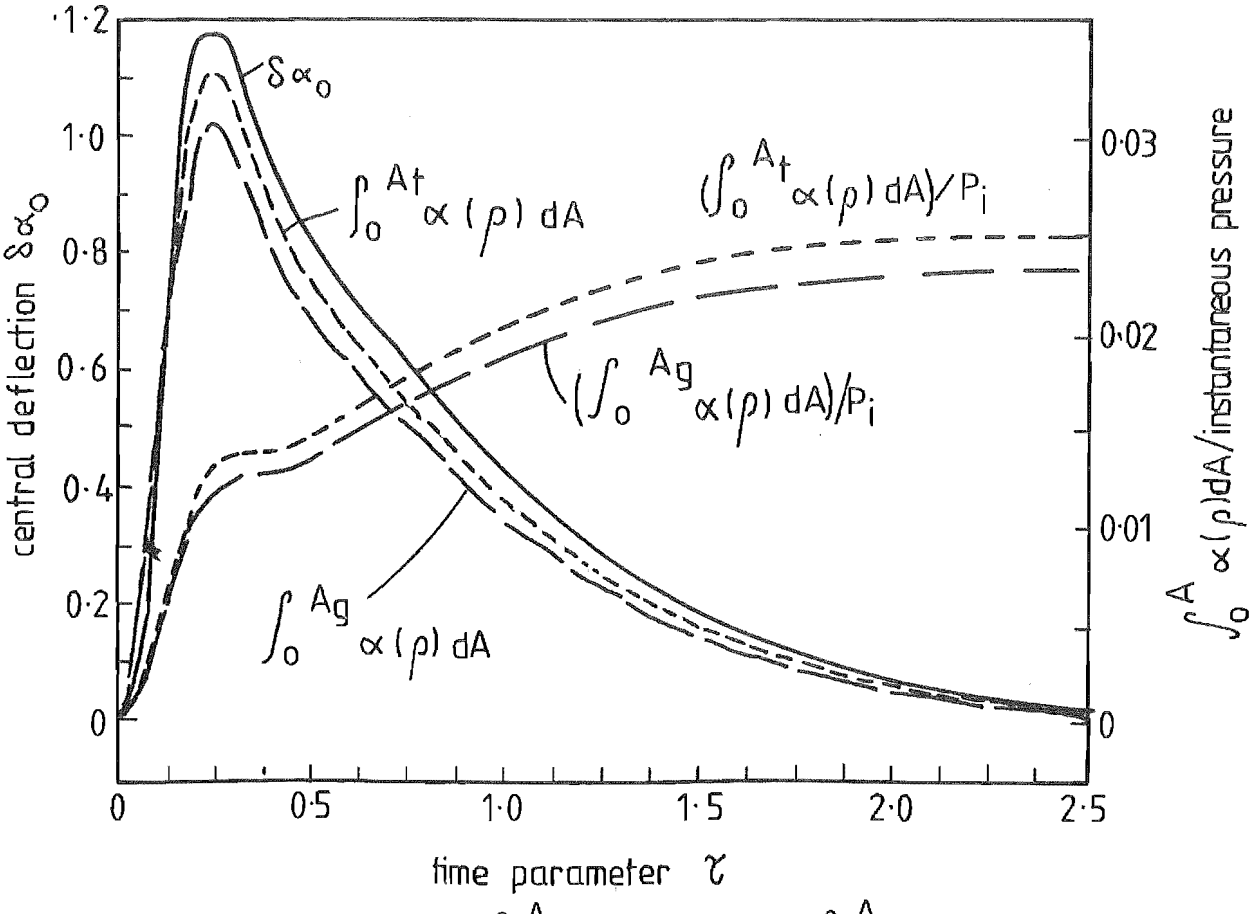

FIG 7·51 CENTRAL DEFLECTION $\int_0^A \alpha(\rho)\,dA$ AND $(\int_0^A \alpha(\rho)\,dA)$ INSTANTANEOUS PRESSURE vs TIME FOR PLATE SUBJECT TO AN EXPONENTIALLY DECAYING LOAD $\varepsilon = 15$, $\theta = 0{\cdot}5$, $\chi = 20$, $\lambda = 0{\cdot}3$

boundary condition resulted in the frequency for the apparent deflection being greater than that predicted by Huang[4.3].

Beyond $\tau = 0.33$ the divergence between results increased due to the influence of the non-linearity on the calculation of the effective elapsed time.

7.5 TRANSDUCER PERFORMANCE

Based upon section 3.5 page , for a capacitance transducer the change in voltage for a constant charge condition was given by

$$\Delta V = \frac{q_c}{\varepsilon_o \varepsilon_r} \frac{a}{A_t} \int^{A_t} \alpha(\rho) dA$$

where q_c = charge
ε_o = permittivity of free space
ε_r = relative permittivity
A_t = area over which capacitance measured
$\alpha(\rho)$ = vertical delection of plate,

while if a piezoelectric crystal foundation was used, then ignoring radial effects following York[3.21], to the first order of accuracy the resultant change due to the deflection would be proportional to the area integral.

Therefore Fig 7.51 page 263, plots the term $\int^{A_t} \alpha(\rho) dA$ for a plate subject to an exponentially decaying load $\varepsilon = 15$, $\theta = 0.5$, $\chi = 20$, $\nu = 0.3$ for A_t equals the area of the plate while the integral limit A_g was equal to an area of $0.64A_t$ for a capacitance transducer using a guard ring section 3.5 to ensure a uniform electrostatic field. The response of the transducer was considered by also

plotting $\int^{A_t} \alpha(\rho)dA$/instantaneous pressure against time on the same Fig 7.51.

Profiles of the vertical and radial deflection of the plate are presented for times τ = 0.12,0.16,0.19 and 0.235 in Figs 7.52,7.53 page 266 while the combined radial stress as well as the radial bending and radial membrane stresses are contained in Figs 7.54-7.56 pages 267-8 for the times τ = 0.12,0.16 and 0.235. Similarly tangential stress profiles are shown in Figs 7.57-7.59 pages 268-9 for the same times.

The vertical deflection profiles for a plate/foundation combination, k^* = 50, under identical loading conditions as well as the plot of the central deflection, $\int^{A_t} \alpha(\rho)dA$ and $\int^{A_t} \alpha(\rho)dA$/ instantaneous pressure are contained in the Figs 7.60, 7.61 page 270. Finally for a Winkler foundation constant of k^* = 100, results for vertical deflection profiles and central deflection and response are presented in Figs 7.62, 7.63 page 271.

It can be seen that the foundation modulii k^* = 100 gave the response most appropriate for the pressure transducer and therefore a compromise between sensitivity and dynamic response based upon the rigidity of the dielectric foundation was required.

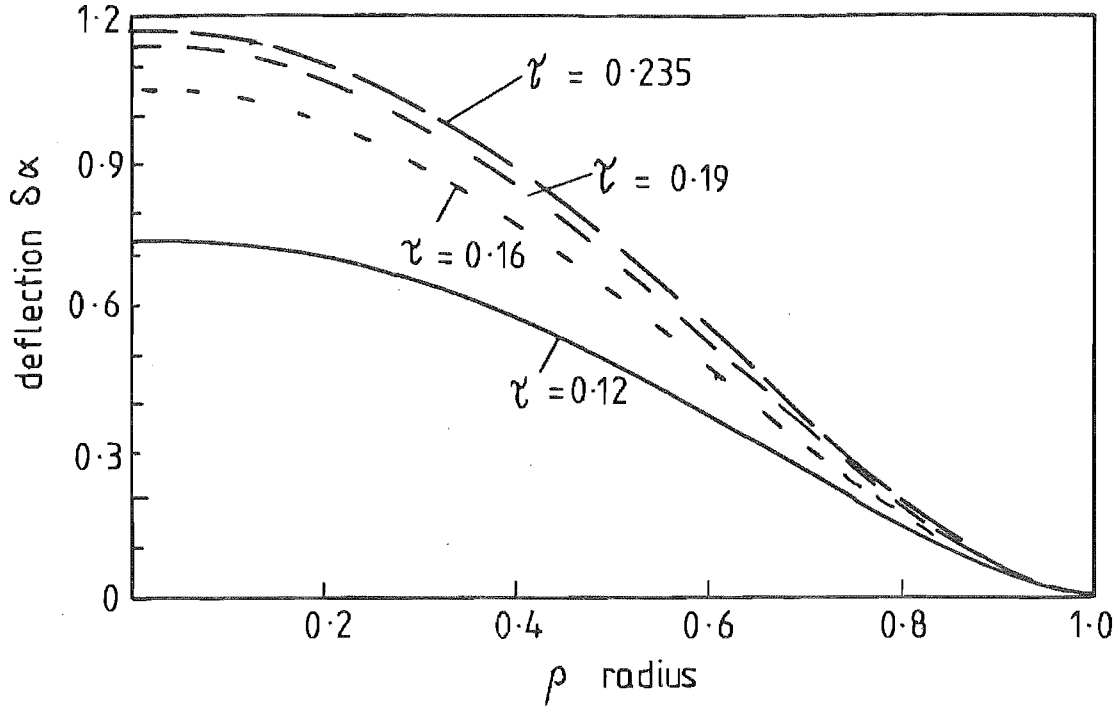

FIG 7·52 VERTICAL DEFLECTION PROFILES FOR PLATE SUBJECT TO AN EXPONENTIALLY DECAYING LOAD $\epsilon = 15$, $\Theta = 0{\cdot}5$, $\varkappa = 20$, $\lambda = 0{\cdot}3$

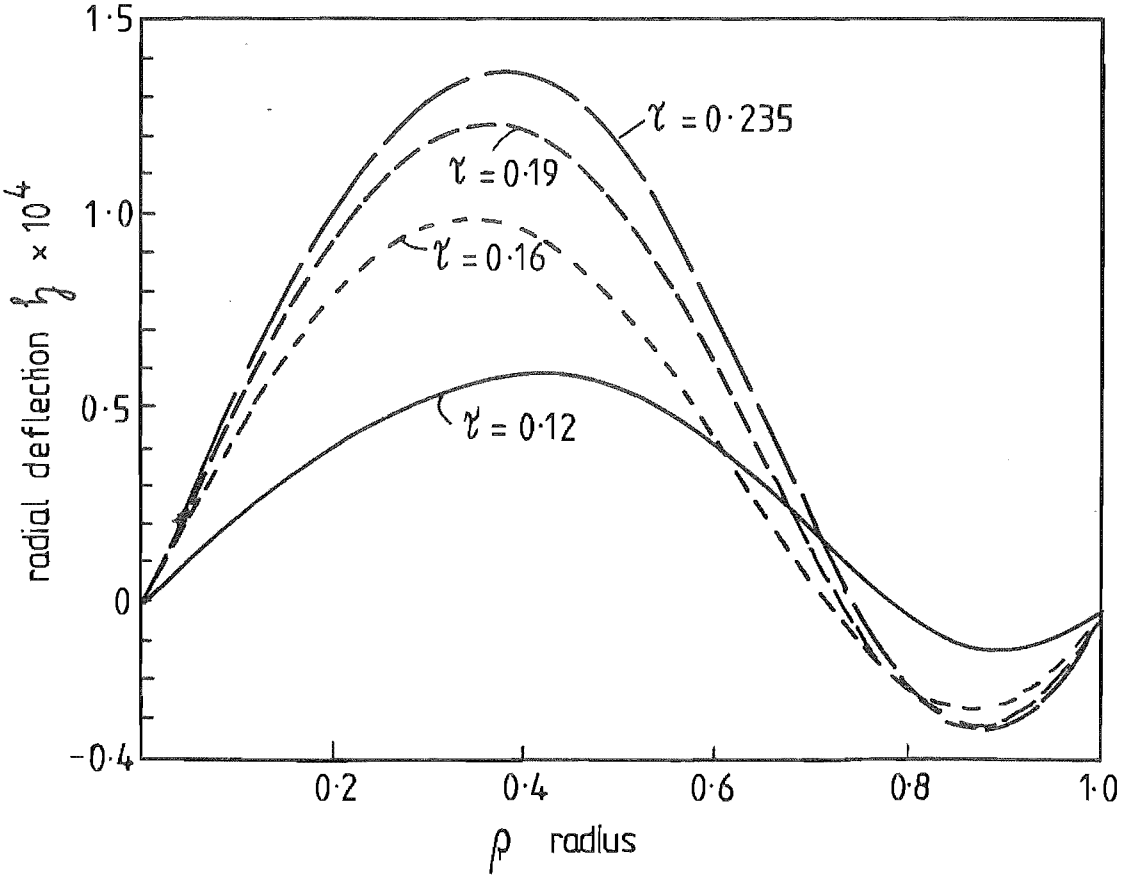

FIG 7·53 RADIAL DEFLECTION PROFILES FOR PLATE SUBJECT TO AN EXPONENTIALLY DECAYING LOAD $\epsilon = 15$, $\Theta = 0{\cdot}5$, $\varkappa = 20$ $\lambda = 0{\cdot}3$

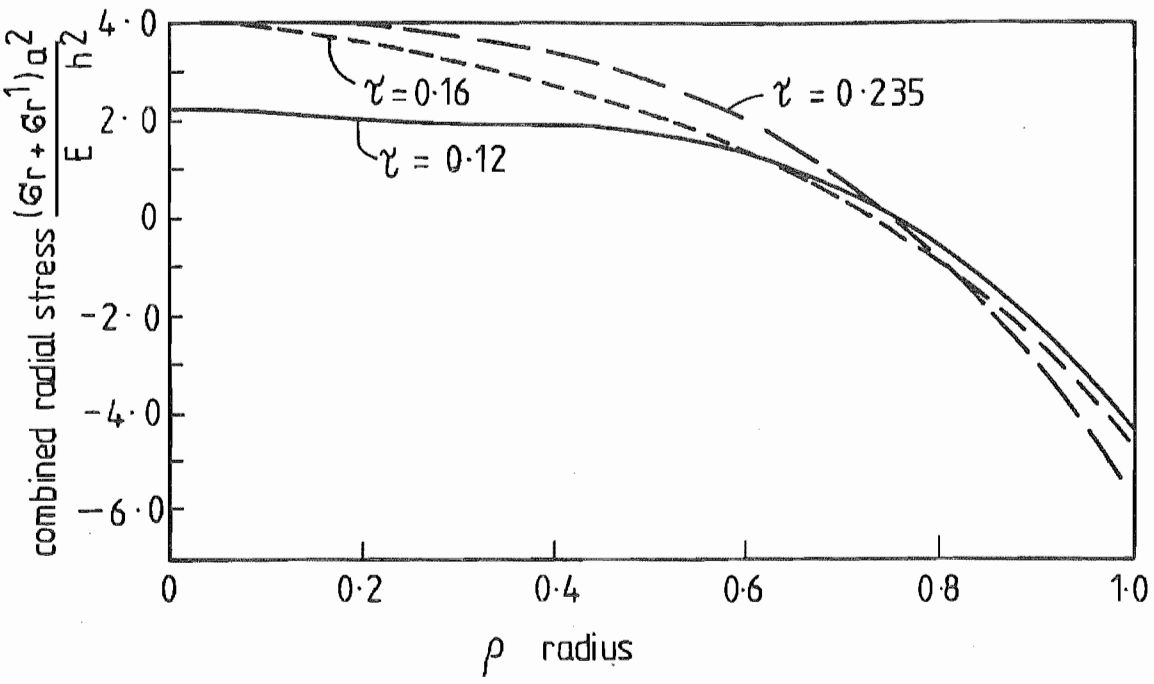

FIG 7·54· COMBINED RADIAL STRESS PARAMETER PROFILES FOR PLATE SUBJECT TO AN EXPONENTIALLY DECAYING LOAD
$\varepsilon = 15, \theta = 0{\cdot}5, \chi = 20, \lambda = 0{\cdot}3$

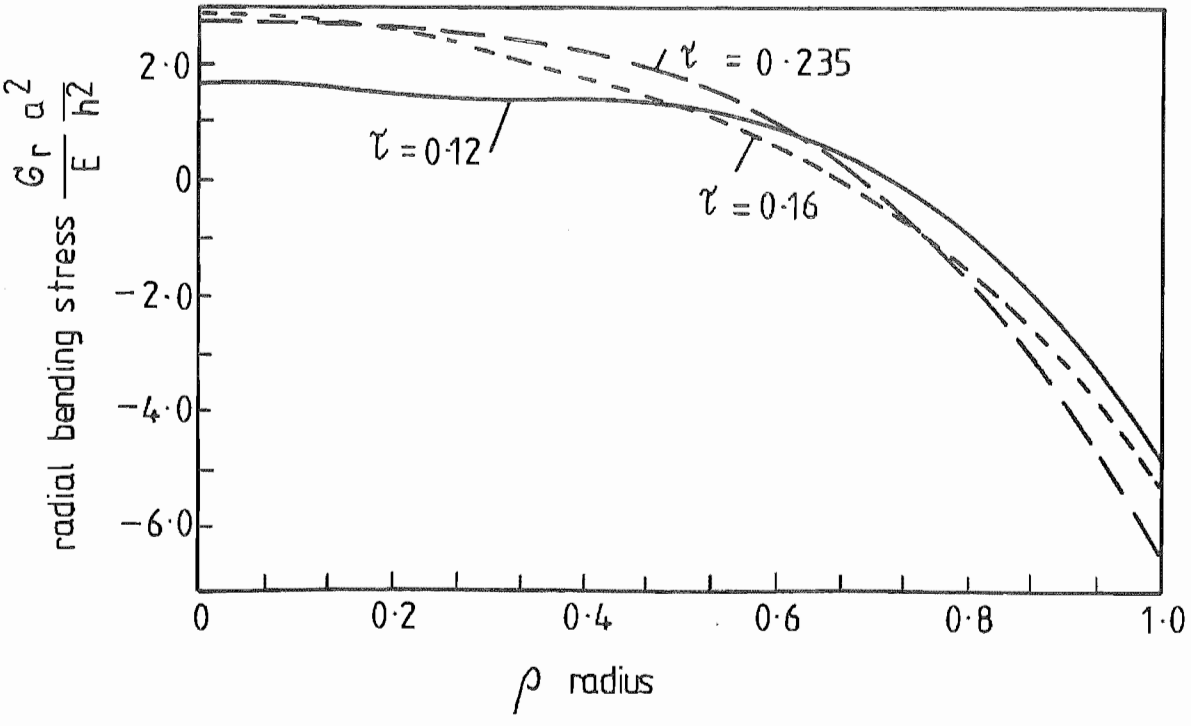

FIG 7·55 RADIAL BENDING STRESS PARAMETER PROFILES FOR PLATE SUBJECT TO AN EXPONENTIALLY DECAYING LOAD
$\varepsilon = 15, \theta = 0{\cdot}5, \chi = 20, \lambda = 0{\cdot}3$

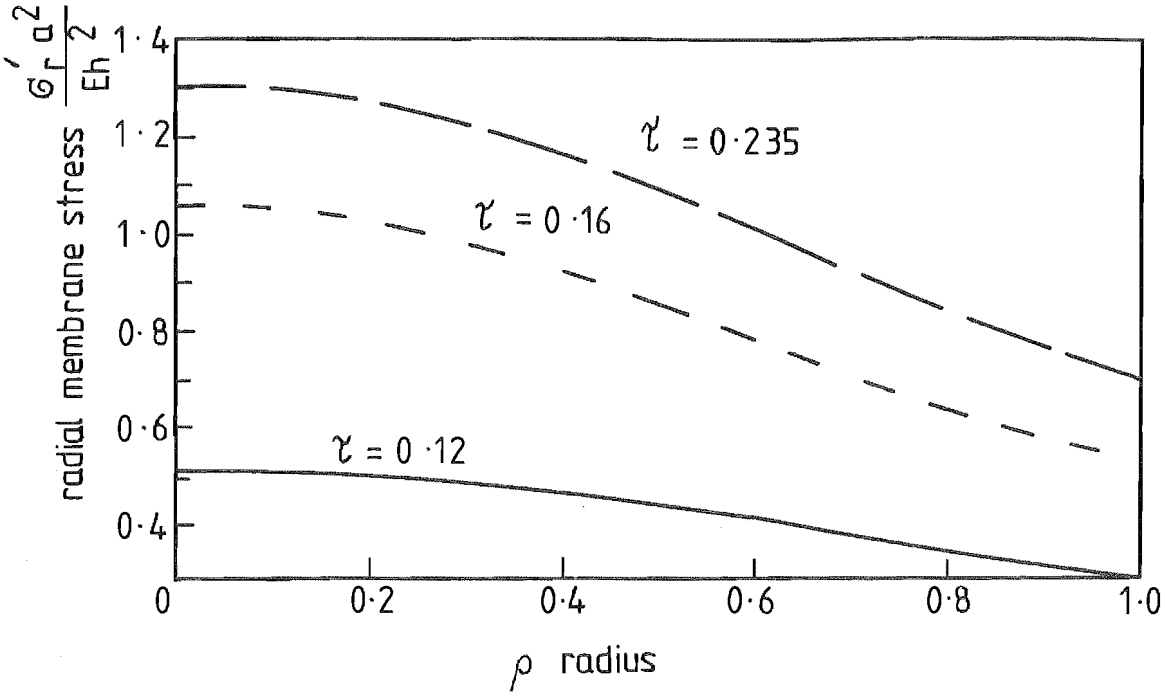

FIG 7·56 RADIAL MEMBRANE STRESS PARAMETER PROFILES FOR PLATE SUBJECT TO AN EXPONENTIALLY DECAYING LOAD

ε = 15, Θ = 0·5, χ = 20, λ = 0·3

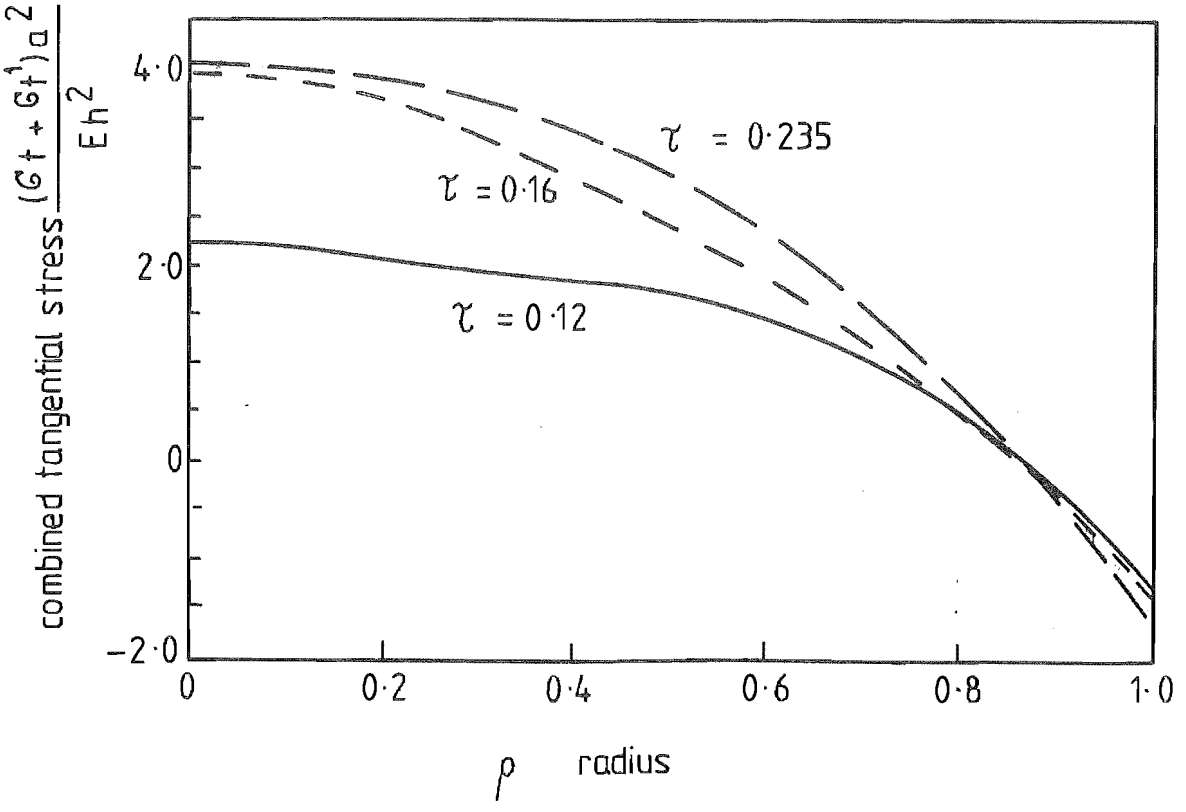

FIG 7·57 COMBINED TANGENTIAL STRESS PARAMETER PROFILES FOR PLATE SUBJECT TO AN EXPONENTIALLY DECAYING LOAD

ε = 15, Θ = 0·5, χ = 20, λ = 0·3

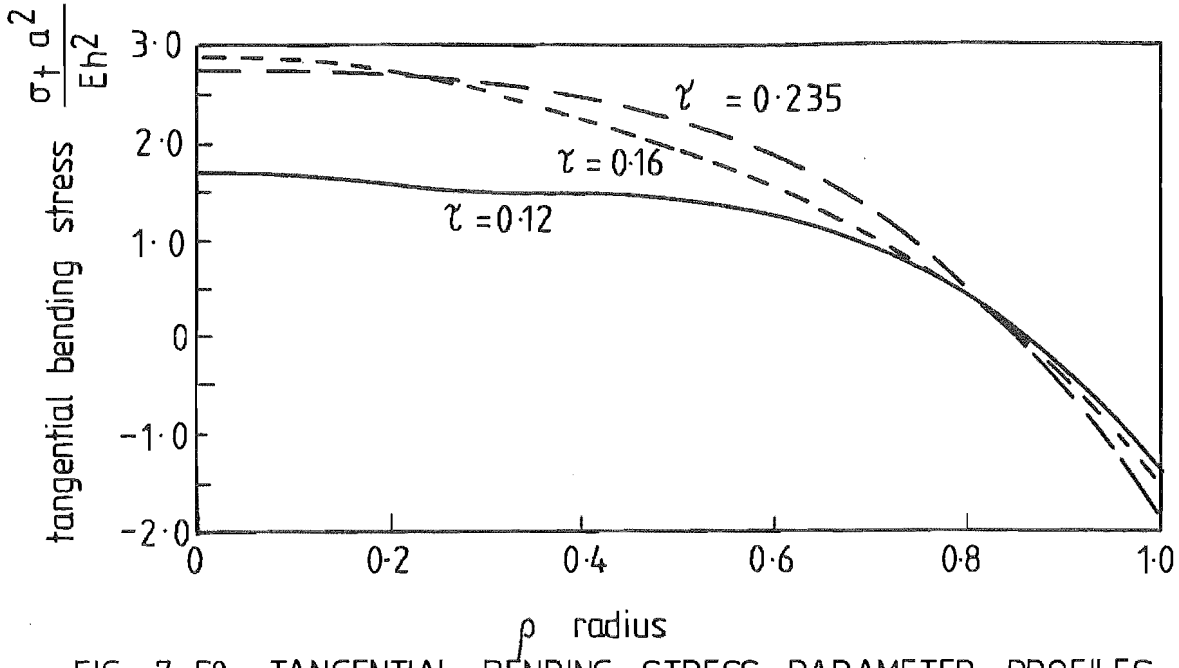

FIG 7·58 TANGENTIAL BENDING STRESS PARAMETER PROFILES FOR PLATE SUBJECT TO AN EXPONENTIALLY DECAYING LOAD ϵ =15, Θ = 0·5, χ = 20, λ = 0·3

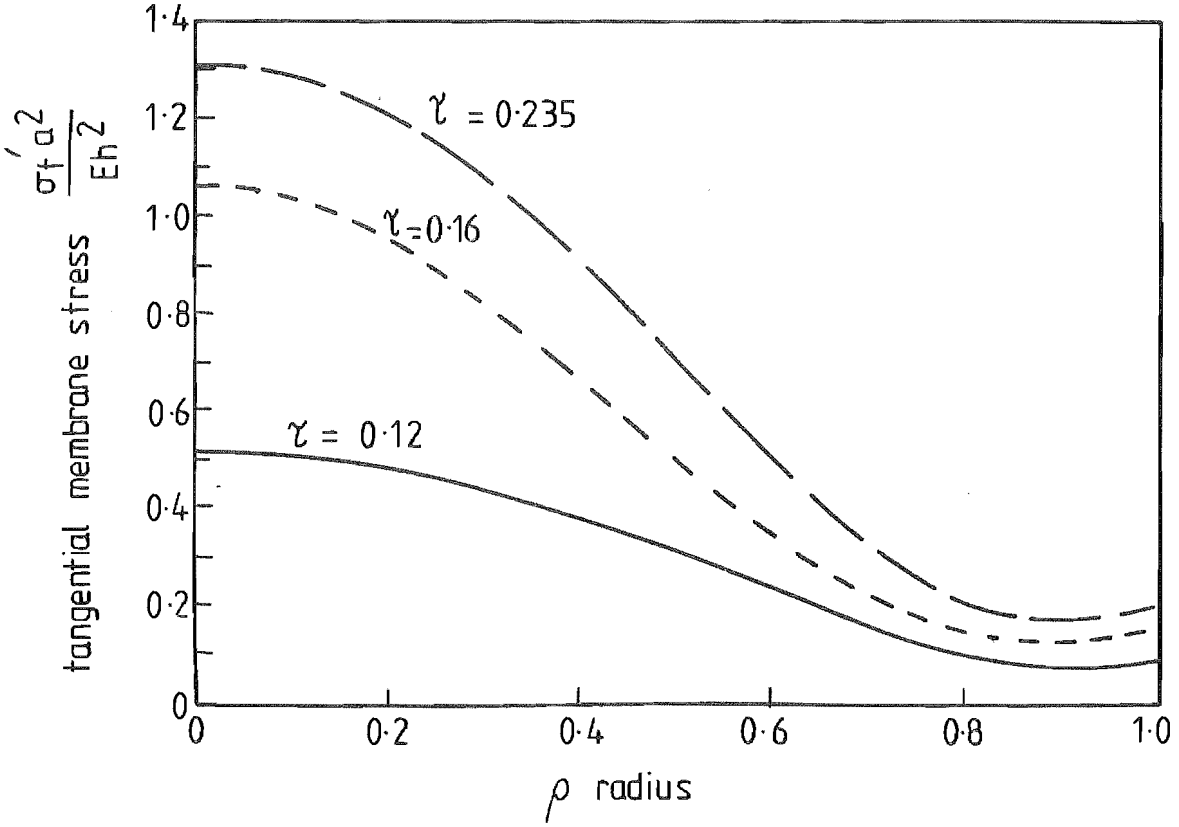

FIG 7·59 TANGENTIAL MEMBRANE STRESS PARAMETER FOR PLATE SUBJECT TO AN EXPONENTIALLY DECAYING LOAD

ϵ = 15, Θ = 0·5, χ = 20, λ = 0·3

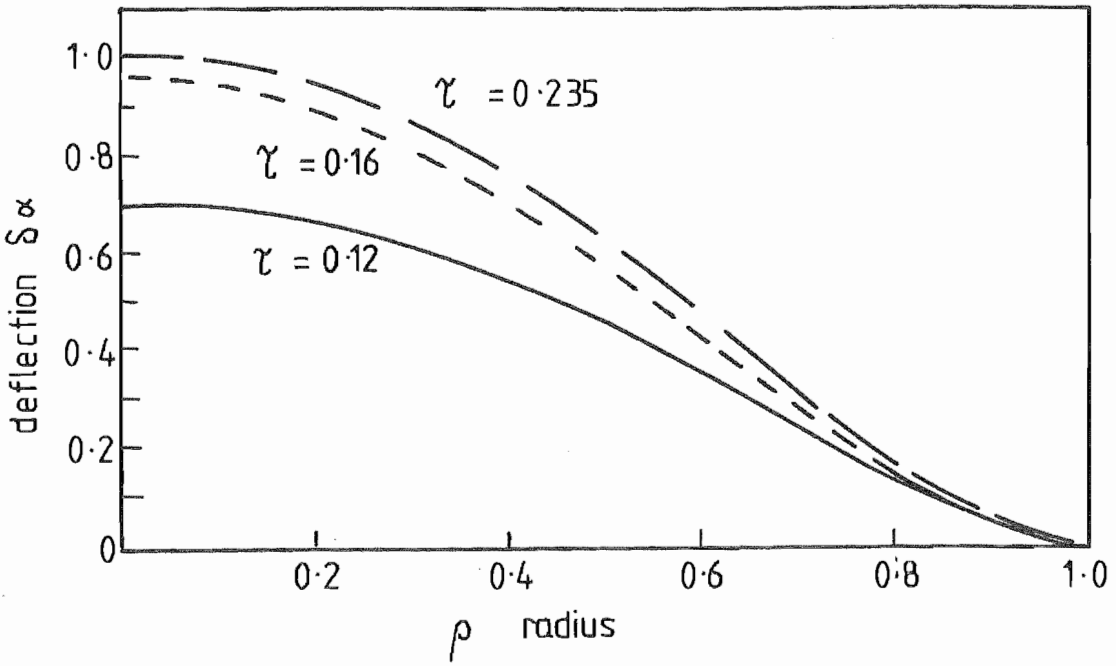

FIG 7·60 VERTICAL DEFLECTION PROFILES FOR PLATE/FOUNDATION $k^* = 50$ SUBJECT TO AN EXPONENTIALLY DECAYING LOAD $\varepsilon = 15$, $\Theta = 0{\cdot}5$, $\chi = 20$, $\eta = 0{\cdot}3$

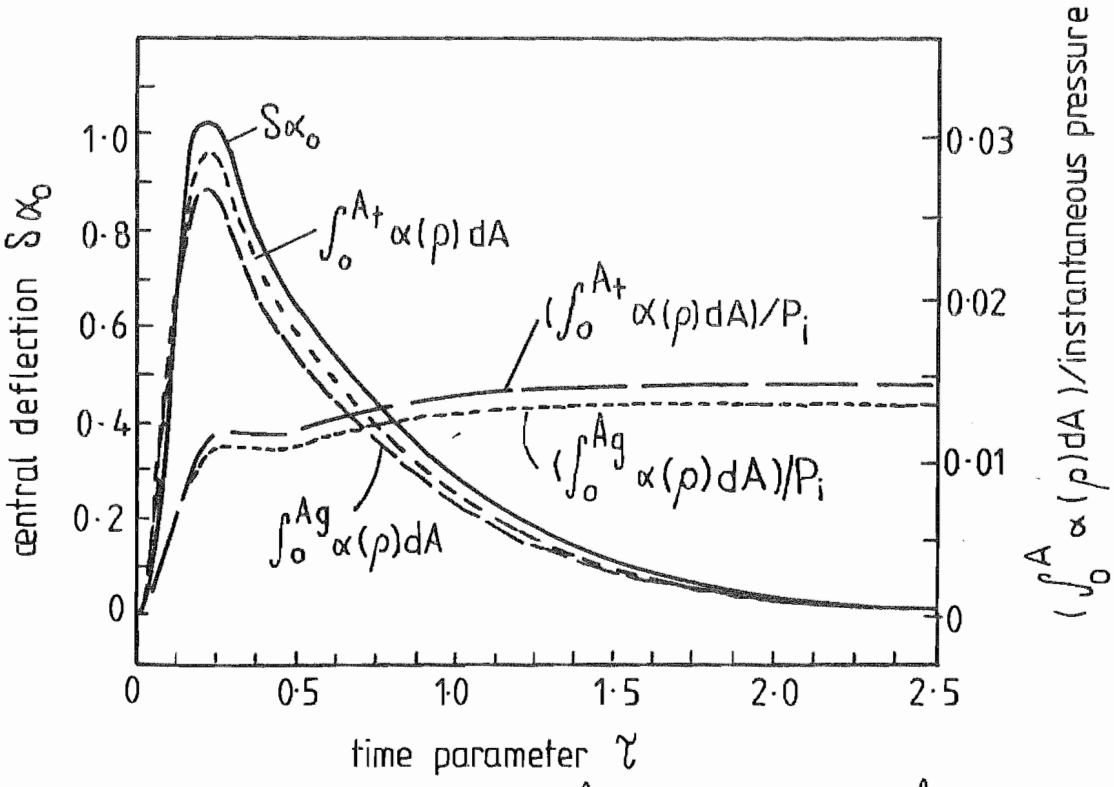

FIG 7·61 CENTRAL DEFLECTION $\int_0^A \alpha(\rho)\,dA$ AND $(\int_0^A \alpha(\rho)\,dA)/$ INSTANTANEOUS PRESSURE vs TIME FOR PLATE/FOUNDATION $k^* = 50$ SUBJECT TO AN EXPONENTIALLY DECAYING LOAD $\varepsilon = 15$, $\Theta = 0{\cdot}5$, $\chi = 20$, $\eta = 0{\cdot}3$

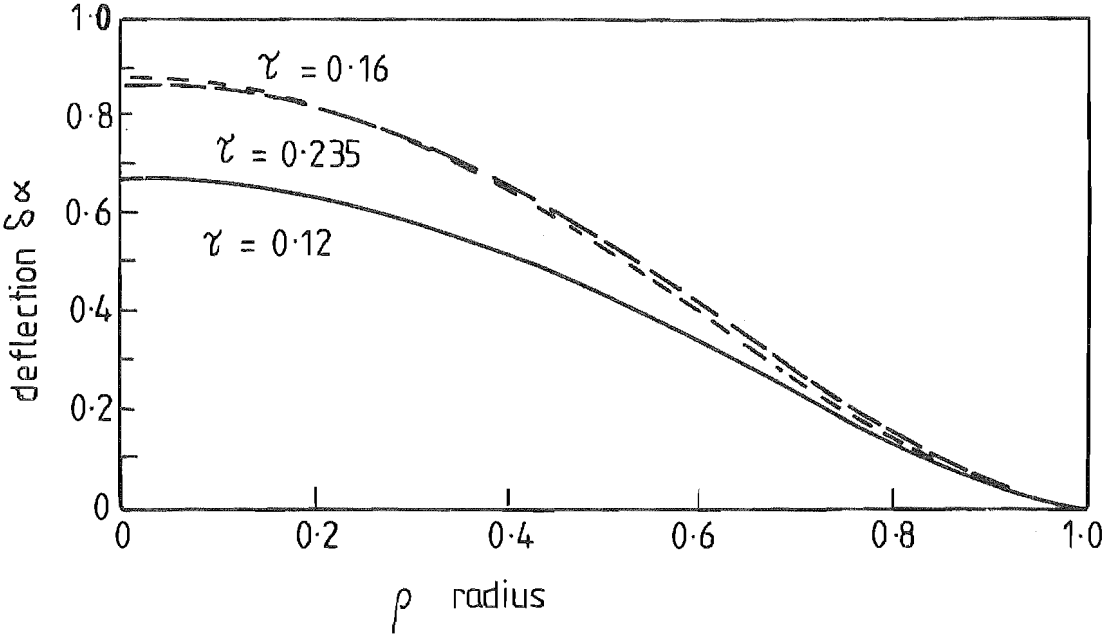

FIG 7·62 VERTICAL DEFLECTION PROFILES FOR PLATE/FOUNDATION $k^* = 100$ SUBJECT TO AN EXPONENTIALLY DECAYING LOAD $\varepsilon = 15, \Theta = 0{\cdot}5, \chi = 20, \lambda = 0{\cdot}3$

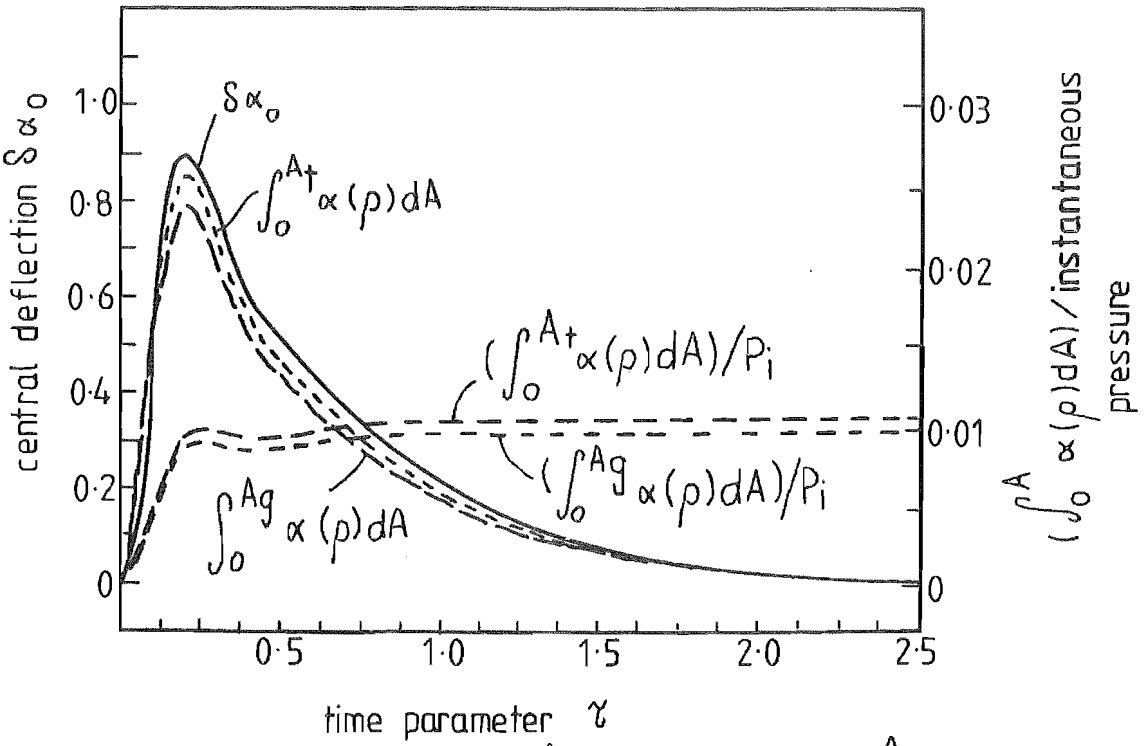

FIG 7·63 CENTRAL DEFLECTION $\int_0^A \alpha(\rho)\,dA$ AND $\left(\int_0^A \alpha(\rho)\,dA\right)$/INSTANTANEOUS PRESSURE vs TIME FOR PLATE/FOUNDATION $k^* = 100$ SUBJECT TO AN EXPONENTIALLY DECAYING LOAD $\varepsilon = 15, \Theta = 0{\cdot}5, \chi = 20, \lambda = 0{\cdot}3$

CHAPTER EIGHT

CONCLUSION AND RECOMMENDATIONS

Following a review of the literature on explosive forming it was apparent that information on the pressure history in the region of the blank/ transfer medium interface was required. This would be necessary to understand the reloading phase and the blank/transfer medium interaction as well as the initial loading phase due to the incident shock wave. Therefore, following the consideration of a capacitance or piezoelectric transducer the response of circular plates and plate/foundation combinations were analysed for transient loading conditions. For the fixed edge boundary condition the linear and non-linear response were determined, as was the non-linear response for the simply supported immovable edge boundary condition.

The extension of the existing linear model analysis of a plate subjected to transient loading [5.1], to include viscous damping and a foundation gave an exact solution. The Winkler and Pasternak foundation models were used while the selected boundary condition was the fixed edge case.

The central difference program accurately described the linear response of the plate and plate/foundation system. The comparison with the linear modal results showed that the representation of the vertical deflection, the Winkler and Pasternak foundations and the spatial boundary conditions were correct. The consideration of the time domain recurrence schemes resulted in the use of a three point scheme based upon Newmark's work for $\gamma = \frac{1}{2}$, $\beta = \frac{1}{4}$.

The program results for the non-linear response of the fixed edge and simply supported immovable edge plate compared favourably with the existing published work of Alwar [7.1] for maximum deflection while the difference in the form of the response was a function of the quasi-linearisation associated with Alwar's solution. For the Winkler model, the plate/foundation deflection derived from the numerical model, for both boundary conditions, was similar in form to that of Nath [7.7] although there was divergence in the results particularly as the foundation modulus was increased. The source of the error in Nath's results, for the Winkler foundation was due to both the quasi- linearisation and the representation of the spatial domain. The comparison of the static non-linear deflection results with those of Sinha [6.3] for the fixed edge condition established that the numerical modelling of the geometric non-linearity was correct confirming the results obtained for the plate [4.4].

For the Pasternak foundation, the calculated non-linear response based on the fixed edge condition was totally divergent from that of Nath. The results obtained by the program were consistent with those from the linear analysis in that increasing values of the Pasternak modulus resulted in increased stiffness for a fixed value of Winkler modulus. The results of Nath exhibited a decrease in stiffness for an increase in Pasternak modulus beyond a specific value.

For the simply supported immovable edge boundary condition the form of the numerical solution and Nath's results were in agreement on the influence of the Pasternak modulus although a difference in magnitude occurred.

The central difference program gave an accurate presentation of the dynamic non-linear response of the plate and plate/foundation systems in view of the comparison made for the linear dynamic and non-linear static solution. The comparisons were made with the published non-linear static solutions and the linear dynamic data from the modal analysis.

Therefore the response of the transducer based upon the program was calculated and it could be seen that the resultant sensitivity and frequency response was a compromise of foundation stiffness and plate thickness.

The only data available on the non-linear dynamic deflection of the plate/foundation combination was limited to Nath's analysis [7.7] and the results obtained from the central difference program were at variance with Nath's for the reasons discussed in section 7.3.1 and 7.3.3. Therefore it is recommended that an experimental study on plate and plate/foundation response to impulsive loading be conducted for the non-linear deflection regime. The only existing experimental data in the literature is associated with the determination of the frequency of plates [8.1] and plate/foundation combination [4.8] at large deflection. The plate experiment would use a capacitance measurement system while the plate/foundation system would be based upon the use of a dielectric foundation with capacitance measurement or a piezo electric foundation to determine the plate deflection.

Modification to the program to incorporate radial inertia and radial viscous damping as well as allowing the simply supported movable free edge would extend the range of the application beyond that required for the development of the transducer.

Since the central difference method was not easily modified to describe the material non-linearities associated with plastic deformation, the development of a finite element program to model the plate behaviour should be considered. This then could be extended to calculate the deflection of the workpiece during explosive free forming using the loading history determined by the pressure transducer. Also for the transducer the dielectric model could be extended to enable the description of the piezoelectric behaviour to incorporate the influence of radial deflection.

Consideration should be given to correcting the work of Alwar and Nath in conjunction with the discussion in section 7.3.1 and 7.3.3. This would take advantage of the Chebyshev polynomial technique which enables the derivatives of deflection to be determined directly with greater accuracy than numerical differentiation, particularly at the spatial boundaries. However, the criteria on convergence for this method would have to be based upon the highest derivative considered and hence sufficient coefficients would need to be determined to ensure convergence on that derivative.

The stress function representation of Nath

$$\Phi = r N_r$$

$$\frac{\partial \Phi}{\partial r} = N_t$$

where Φ = Airy stress function

would have the advantage of reducing the numerical differentiation required in the determination of both the contribution of the geometric non-linearity as well as the membrane stresses. While this would decrease the number of iterations required to converge on an accurate result, the stress function solution would not allow the direct inclusion of radial inertia and radial damping.

The main recommendation, in conjunction with the previously mentioned development, is that capacitance and piezoelectric transducers based upon the existing program should be developed and applied to the explosive free forming process to enable the loading history to be determined.

REFERENCES

Chapter One

1.1) WILSON, F.W. High velocity forming of metals. 1st Ed., American Society of Tool and Manufacturing Engineers, N.J. Prentice-Hall Inc., 1964.

1.2) BRUNO, E.J. High velocity forming of metals. Revised Edition, Dearborn, Michigan. American Society of Tool and Manufacturing Engineers, 1968.

1.3) PRICE, N.W., ANDA, M. and FAHY, F.W. Explosive forming MECH.ENG. REPORT MM/16/63, Mechanical Engineering Dept., University of Canterbury, 1963.

1.4) HUDSON, G.E. A theory of the dynamic plastic deformation of a thin diaphragm. J. of Appl. Phys., Vol. 213, No. 1. January, 1951, pp 1-11.

1.5) THURSTON, G.A. On the effect of edge pull-in on the explosive forming of domes. Proc. 7th Int. M.T.D.R. Conference, University of Birmingham, September 1966. Pergamon Press Inc., Oxford, 1967, pp 129-144.

1.6) EZRA, A.A. and PENNING, F.A. Development of scaling laws for explosive forming. Experimental Mechanics, Vol. 2, No. 8, August, 1962, pp 234-239.

1.7) BAGULEY, D.E. Explosive forming. P.E.L., D.S.I.R., N.Z. Tech. Note TN169.

1.8) BOSWELL, J.M. Some fundamental aspects of explosive forming using a designed-experiment approach. Masters Thesis, University of Auckland, 1965.

1.9) SMALE, G., McQUILKIN, P.H. and FAHY, F.W. Explosive forming. Mech. MM 25/64, Mechanical Engineering Department, University of Canterbury, 1964.

REFERENCES

Chapter Two

2.1) GIANNOCCULO, S. Explosive forming of 12 Foot diameter end closures for Sealab II. Proc. of 1st Int. Conf. of the Center for High Energy Forming, Estes Park, Colorado, June 1967, pp 3.6.1 - 3.6.44.

2.2) EZRA, A.A. and PETERSON, H.C. Interaction of an underwater shock wave with a deforming circular plate. Proc. of 2nd Int. Conf. of the Center for High Energy Forming, Estes Park, Colorado, June 1969, pp 3.1.1. - 3.1.12.

2.3) MUNROE, C.E. Modern explosives. Scribners Magazine (May, 1888).

2.4) EZRA, A.A. Principles and practices of explosives metalworking. 1st Ed., London. Industrial Newspaper Limited, 1973.

2.5) BRUNO, E.J. High velocity forming of metals. Revised Edition, Dearborn, Michigan. American Society of Tool and Manufacturing Engineers, 1968.

2.6) RINEHART, J.S. and PEARSON, J. Explosive working of metals. 1st Ed., New York. Pergamon Press, Distributed Macmillan Co., 1963.

2.7) DAVIES, R. and AUSTIN, E.R. Developments in high speed metal forming. 1st Ed., London. The Machinery Publishing Co. Ltd, London, 1970.

2.8) BORON, H.G. and COSTELLO, E. de L. Explosive forming. Met. Reviews, Vol. 8, 1963, pp 369-426.

2.9) PIETTEUR, J. Industrial applications of steel explosive forming - Belgium methods and development. Proc. of 1st Int. Conf. of the Center for High Energy Forming, Estes Park, Colorado, June 1967, pp 2.1.1. - 2.1.67.

2.10) FREY, A. Applications of high energy rate forming in France. Ibid. pp 2.2.1. - 2.2.17.

2.11) SIMMLER, W. High energy rate forming in Germany. Ibid. pp 2.3.1. - 2.3.14.

2.12) NEMITZ, P. Explosive forming of high strength steels. Ibid. pp 2.4.1. - 2.4.30.

2.13) KIYOTA, K. Application of high energy rate forming in Japan. Ibid. pp 2.5.1. - 2.5.29.

2.14) HAEGLAND, B. Applications of high energy rate forming in Norway. Ibid. pp 2.6.1. - 2.6.26.

2.15) BERMAN, I., KUNSAGI, L. and THAKAAR, B. Developments and use of explosive forming for commercial applications. Ibid. pp 3.1.1 - 3.1.45.

2.16) EZRA, A.A. and ADAMS, J.E. The explosive forming of 10 foot diameter aluminium domes. Ibid. pp 3.2.1. - 3.2.76.

2.17) BECK, W.A. and RUDY, J.F. Production of explosive formed five-foot diameter aluminium domes. Ibid. pp 3.4.1. - 3.4.24.

2.18) ALTING, L. Explosive forming of domes. Proc. of the 3rd Int. Conf. of the Center for High Energy Forming, Vail, Colorado, July 1971, pp 6.1.1. - 6.1.36.

2.19) CORRAL, J.S. Explosive forming of core segments. Proc. of the 1st Int. Conf. of the Center for High Energy Forming, Estes Park, Colorado, June 1967, pp 3.5.1. - 3.5.10.

2.20) UNDERWATER EXPLOSIVES RESEARCH

Vol. I The Pressure Pulse

Vol. II The Gas Globe

Vol. III The Damage Process

A compilation of papers.) Office of Naval Research, 1950.

2.21) SAG, N. Computer aided experimental study of deformation characteristics of explosively formed sheet metal dished ends. Conference on Stress and Strain in Engineering, Brisbane, 1973. (National Committee on Applied Mechanics, The Institute of Engineers, Australian National Conference Publication No. 73/5.) pp 233 - 240.

2.22) KENNARD, E.H. The effect of a pressure wave on a plate or diaphragm. Underwater Explosion Research, Vol. III. The Damage Process, Office of Naval Research, 1950, page 11.

2.23) RICHARDSON, J.H. and KIRKWOOD, J.G. Theory of the plastic deformation of thin plates by underwater explosions. Ibid. Page 305.

2.24) FYE, P.M. and ELDRIDGE, J.E. Diaphragm gauge studies of underwater explosions. Ibid. Page 517.

2.25) IDA, N.W. and EZRA, A.A. Die-less explosive forming of one-piece thin shells of revolution. Proc. of 3rd Int. M.T.D.R. Conf., University of Birmingham, September 1962. Pergamon Press Inc. Published 1963. pp 365..

2.26) JOHNSON, W., DUNCAN, J.L., KORMI, K., SOWERBY, R. and TRAVIS, F.W. Some contributions to high rate sheet metal forming. Proc. of 4th Int. M.T.D.R. Conf. The Manchester College of Science and Technology, September 1963. pp 257 - 317.

2.27) JOHNSON, W., KORMI, K. and TRAVIS, F.W. An investigation into the explosive deepdrawing of circular blanks using the plug-cushion technique. Int. Journ. Mech. Sci., Vol. 6, No. 4, August 1964. pp 287 - 301.

2.28) HOBSON, G. and AMINI, E. Fundamentals of an explosive forming machine. Int. J. Mech. Tool Design Res. Vol. 4, No. 2, December 1964. pp 73 - 90.

2.29) JOHNSON, W. and SOWERBY, R. Experiments on clamped circular blanks subject to an underwater explosive charge. Proc. Inst. Mech. Engrs. Vol. 179, Part I, No. 7, 1964-1965. pp 197 - 221.

2.30) JOHNSON, W. Experiments and efficiency considerations in high-rate forming. J. Australian Inst. Metals. Vol. 12, No. 2, May 1967. pp 139 - 154.

2.31) WATTS, A.F. and RARDIN, G.N. High energy rate metal forming. OTS - US Dept. of Commerce Report, PB161274, 1959.

2.32) JOHNSON, W., POYTON, A., SINGH, H. and TRAVIS, F.W. Experiments in the underwater explosive stretch forming of clamped circular blanks. Int. J. Mech. Sci., Vol. 8, No. 6, April 1966, pp 237 - 270.

2.33) HOBSON, G. and AMINI, E. Analysis of an explosive forming machine. Proc. of 5th Int. M.T.D.R. Conf., University of Birmingham, 1964. pp 339 - 352.

2.34) TOBIAS, S.A. Automation of high energy rate forming processes. Proc. of the 1st Int. Conf. of the Center for High Energy Forming, Estes Park, Colorado, June 1967. pp 4.1.1- 4.1.32.

2.35) POMFRET, K.R. Explosive forming experience at Birmingham University. Welding and Metal Fabrication, Vol. 34, No. 5, May 1966. pp 179-183.

2.36) HOBSON, G., AMINI, E. and TOBIAS, S.A. Development of an explosive sheet forming machine. Proc. of 4th Int. M.T.D.R. Conf. The Manchester College of Science and Technology, September 1963. pp 337 - 354.

2.37) CORBETT, S.E. Correlation of theory and experiment in the free forming of clamped circular diaphragms subject to explosive loading. Sheet Metal Industries. Vol. 41, June 1964. pp 485 - 491.

2.38) EZRA, A.A. and MALCOLM, M. An investigation of the effects of explosive stand off distance on the forming of metal blanks. Proc. of the 1st Int. Conf. of the Center for High Energy Forming, Estes Park, Colorado, June 1967, pp 6.4.1 - 6.4.20.

2.39) WITTROCK, E.P. Investigation of a dieless forming technique to form thick steel domes. Proc. of 4th Int. Conf. of the Center for High Energy Forming, July 1973. Vail, Colorado. pp 1.2.1-1.2.48.

2.40) COLTON, R.M. and JONES, A.F. Explosive autofrettage of canon. Proc. of 2nd Int. Conf. of the Center for High Energy Forming, Estes Park, Colorado, June 1969. pp 9.1.1 - 9.1.16.

2.41) MASAKI, S. Dynamic plastic deformation of thin cylindrical shells under radial impulsive pressure. Ibid. pp 3.4.1 - 3.4.19.

2.42) CHING, L.K.W. and WEESE, J.A. The explosive forming of rings. Ibid.pp 3.3.1 - 3.3.89.

2.43) AGRICOLA, K.R. and SNYDER, J.T. Springback control-key to accuracy in explosive forming. Tool and Manfg. Engr. Vol. 58, No. 3, March 1967. pp 28 - 31.

2.44) BOES, P.J.M. Forming with high explosives. Presented by J.L. Remmerswaal at the I.I.P.E.R. Conf. Czechoslavakia, September 1961.

2.45) HARDEE, P.C. Explosive forming with vented dies. Proc. of the 3rd Int. Conf. of the Center for High Energy Forming, July 1971, Vail, Colorado,pp 6.3.1 - 6.3.27.

2.46) BERMAN, I. and SCHROEDER, J.W. Development, use and evaluation of explosively formed components. Proc. of the 4th Int. Conf. of the Center for High Energy Forming, July 1973. Vail, Colorado,pp 1.4.1 - 1.4.15.

2.47) KULKARNI, S.B. and EZRA, A.A. The design and analysis of explosive forming thin shell dies. Proc. of the 13th Int.M.T.D.R. Conf., Birmingham, 1972, pp 403 - 408.

2.48) BOUMA, D.D. Strain measurements upon blank and die during explosive forming. Proc. of the 3rd Int. Conf. of the Center for High Energy Forming, Vail, Colorado, July 1971.pp 4.4.1 - 4.4.15.

2.49) LIEBERMAN, I. and ZERNOW, L. A new concept of low cost tooling for explosive forming - ice dies. ASTME Paper No. SP63-68 (1963).

2.50) ORAVA, N. and KHUNTIA, P. The relative effect of explosive and isostatic forming on Methanol cracking in Titanium. Proc. of the 3rd Int. Conf. of the Center for High Energy Forming, Vail, Colorado, July 1971,pp 4.1.1 - 4.1.21.

2.51) TRUEB, L.F. Lattice effects in explosion-shocked nickel after thermal recovery. Procs. of the 2nd Int. Conf. of the Center for High Energy Forming, Estes Park, Colorado, June 1969. pp 1.1.1 - 1.1.35.

2.52) STONE, L.R. Residual properties in explosively formed stainless tubes. Proc. of the 4th Int. Conf. of the Center for High Energy Forming, Vail, Colorado, July 1973,pp 1.1.1 - 1.1.24.

2.53) ORAVA, R.N. and OTTO, H.E. The effect of high energy rate forming on the terminal characteristics of metal - A Review. Journal of Metals, February 1970,pp 17 - 31.

2.54) VAN WELY, F.E. Comparison between the influence of cold-pressing and explosive-forming on material properties of steel. Proc. of the 4th Int. Conf. of the Center for High Energy Forming, Vail, Colorado, July 1973,pp 1.3.1 - 1.3.33.

2.55) VAN WELY, F.E. Material aspects of explosive working of metals. Proc. of the 1st Int. Conf. of the Center for High Energy Forming, Estes Park, Colorado, June 1967,pp 7.2.1 - 7.2.27.

2.56) HOLLINGUM, S.W. Research and development of high-rate forming techniques. J. Austr. Inst. Metals, Vol. 12, 1967, pp 199 - 214.

2.57) MAHAJAN, S. The imbition of shock twinning in prestrained Armco iron. Proc. of 1st Int. Conf. of the Center for High Energy Forming, Estes Park, Colorado, June 1967. pp 7.7.1 - 7.7.22.

2.58) OTTO, H.E. and MICKESELL, R. The shock hardening of structural metals. Ibid,pp 7.6.1 - 7.6.46.

2.59) HARDING, J. Mechanical properties of high rates of strain. Proc. of the Conf. on Mech. Properties of Materials at High Rates of Strain. Conference Series No. 21, Institute of Physics, Oxford, April 1974.

2.60) SHEWNON, P.G. and ZACKAY, V.F. Response of metals to high velocity deformation. Int-science, 1961.

2.61) OTTE, H.M. et al. Explosive forming of 2219 Aluminium. Martin Co. Report No. CT-65-41, (1965).

2.62) ORAVA, R.N. and OTTO, H.E. The effects of high energy rate forming on the terminal properties of aluminium alloys. Proc. of the 2nd Int. Conf. of the Center for High Energy Forming, Estes Park, Colorado, June 1969. pp 1.2.1 - 1.2.33.

2.63) CHATTERJEE, S. and TRAVIS, F.W. Effects of varying workpiece thickness on the efficiency of energy transfer and further considerations in the use of a vacuum chest in the explosive forming of metals. Proc. of the 11th Int. M.T.D.R. Conf., University of Birmingham, September 1970, pp 901 - 924.

2.64) COOK, M.A. The science of high explosives. Published Reinhold Publishing Corporation, New York, 1958.

2.65) ZELDONVICH, I.B. and KOMPANEETS, A.S. Theory of detonation. Published Aacademic Press, New York, 1960.

2.66) ————————, Proc. 4th Symposium (Int) on Detonation, 1965, ACR-126, Office of Naval Research.

2.67) BERGER, S.A. and HOLT, M. Spherical explosions in sea water. 6th Mid-Western Conference on Fluid Mechanics, University of Texas, 1959. p 118.

2.68) BERGER, S.A. and HOLT, M. Implosive phase of a spherical explosion in sea water. The Physics of Fluids, Vol. 5, No. 4, April 1962, pp 426 - 431.

2.69) SCHAUER, H.M. Pressures and impulses from underwater explosions. Proc. of the 1st Int. Conf. of the Center for High Energy Forming, Estes Park, Colorado, June 1967. pp 5.5.1 - 5.5.17.

2.70) COLE, R.H. Underwater explosions. Published Princeton University Press, New Jersey, 1948.

2.71) BEBB, A.H. Underwater explosion measurements from small charges at short ranges. Phil. Trans. of Roy. Soc. A Vol. 244, 1952, pp 153 - 175.

2.72) PENNEY, W.G. The pressure-time curve for underwater explosions, underwater explosion research, Vol. I, the shock wave. Office of Naval Research, 1950. p 273.

2.73) PENNEY, W.G. and DASGUPTA, H.K. Pressure - time curves for sub-marine explosions. Ibid. p 289.

2.74) BRINKLEY, S.R. and KIRKWOOD, J.G. Theory of the shock wave produced by an underwater explosion. Ibid. p 383.

2.75) JONES, N., DUMAS, J.W., GIANNOTTI, J.G. and GRASSIT, K.E. The dynamic plastic behaviour of shells. Dynamic Response of Structures Symposium, Stanford, 1971. Edited G. Harrmann and N. Perrona. Published Pergamon Press Inc., New York, 1972.

2.76) JONES, N. Impulsive loading of a simply supported circular rigid plastic plate. J. Appl. Mechs. Trans. A.S.M.E., Vol. 35, 1968. pp 59 - 65.

2.77) RAWLINGS, B. Response of structures to dynamic loads. Proc. of the Conf. on Mech. Properties of Materials at High Rates of Strain. Conference Series No. 21, Institute of Physics, Oxford, April 1974, pp 279-298.

2.78) BOYD, D.E. Dynamic deformation of circular membranes. Jour. of the Engineering Mechanics Division, ASCF, Vol. 92, EM3, June 1966, pp 1-16.

2.79) WOJNO, W. and WIERZBICKI, T. Perturbation solution for impulsively loaded viscoplastic plates, Int. J. Non-linear Mechanics, Vol. 15, 1980, pp 211-223.

2.80) HOPKINS, H.G. and PRAGER, W. On the dynamics of plastic circular plates, ZAMP (Journal of Applied Mathematics and Physics), Vol. 5, No. 4, 1954. pp 317-330.

2.81) WANG, A.J. The permanent deflection of a plastic plate under blast loading. Journ. of Appl. Mech., Vol. 22, No. 3, September 1955. pp 375 - 376.

2.82) THOMSON, R.G. Plastic behaviour of circular plates under transverse impulse loadings of Gaussian distribution, NASA TR R-279, January 1968.

2.83) CONROY, H.F. Rigid plastic analysis of a simply supported circular plate due to dynamic circular loading. Journal of the Franklin Institute, Vol. 288, No. 2, August 1969. pp 121-135.

2.84) MAZALOV, V.N. and NEMIROUSKII, Y.V. Dynamical bending of circular piece-wise non-homogeneous plates. Arch. Mech. Stds. Vol. 25, No. 3, 1973. pp 469-490.

2.85) FLORENCE, A.L. Circular plate under a uniformly distributed impulse load. Int. J. Solids & Struc., Vol. 2, 1966, pp 37-47.

2.86) WIERZBICKI, T. Impulive loading of rigid-viscoplastic plate. Int. J. Solids & Struc. Vol. 3, No. 4, July 1967. pp 635 - 646.

2.87) YOUNGDAHL, C.K. Influence of pulse shape on the final plastic deformation of a circular plate. Int. J. Solids & Struct., Vol. 7, No. 9, 1971. pp 1127-1142.

2.88) WANG, A.J. and HOPKINS, H.G. On the plastic deformation of built-in circular plates. Journ. of Mechanics and Physics of Solids, Vol. 3, No. 1, 1954. pp 22-37.

2.89) FLORENCE, A.L. Clamped circular rigid-plastic plates under blast loading. Trans. of the ASME J. Appl. Mech., Vol. 33, 1966. pp 256-260.

2.90) KRAJCINOVIC, D. Dynamic analysis of clamped plastic circular plates. Int. J. Mech. Sci., Vol. 14, 1972. pp 225-234.

2.91) WIERZBICKI, T. and FLORENCE, A.L. A theoretical and experimental investigation of impulsively loaded clamped circular viscoplastic plates. Int. J. Solids & Struct., Vol. 6, No. 5, 1970. pp 553-568.

2.92) WIERZBICKI, T. Large deflections of a strain rate sensitive plate loaded impulsively. Arch. Mech. Stds., Vol. 21, No. 1, 1969, pp 67-78.

2.93) BATRA, R.C. and DUBEY, R.N. Impulsively loaded circular plates. Int. J. Solids & Struct., Vol. 7, No. 1971. pp 965-978.

2.94) WU, R.W.H. and WITMER, E.A. Finite element analysis of large elastic-plastic transient deformations of simple structures. J. AIAA, Vol. 9, 1971, pp 1719-1724.

2.95) MONDKAR, D.P. and POWELL, G.H. Finite element analysis of non-linear static and dynamic response. Int. J. for Numerical Methods in Engineering, Vol. 11, 1977, pp 499-520.

2.96) BATHE, K-J., and OZDEMIR. Elastic-plastic large deformation of static and dynamic analysis. Computers and Structures, Vol. 6, 1976, pp 81-92.

2.97) WIERZBICKI, T. An analysis of final shapes in free forming problems. Proc. of Int. Conf. on Use of High Energy Rate Methods for Forming Welding and Compaction. Leeds, 1973, Paper 4.

2.98) WITMER, E.A., BALMER, H.A., LEECH, J.W. and PIAN, T.H.H. Large dynamic deformations of beams, rings, plates, and shells. AIAA, Vol. 1, No. 8, 1963. pp 1848-1857.

2.99) LEECH, J.W., WITMER, E.A. and PIAN, T.H.H. Numerical calculation technique for large elastic plastic transient deformations of thin shells. AIAA, Vol. 6, No. 12, 1968. pp 2352-2359.

2.100) MORINO, L., LEECH, J.W. and WITMER, E.A. An improved numerical calculation technique for large elastic-plastic transient deformations of thin shells. Part I - Background and theoretical formulation. Trans. of the A.S.M.E. J. Appl. Mechs., Vol. 38, No. 2, 1971. pp 423-428.

2.101) MORINO, L., LEECH, J.W. and WITMER, E.A. An improved numerical calculation technique for large elastic-plastic transient deformation of thin shells. Part II - Evaluation and Application. Ibid. pp 429-436.

2.102) DUFFY, T.A. and KEY, S.W. Experimental-theoretical calculations of impulsively loaded clamped circular plates. Experimental Mechanics, Vol. 9, No. 6, 1969. pp 241-249.

2.103) FORAL, R.F. An energy analysis of the explosive forming of domes. Proc. of the 1st Int. Conf. of the Center for High Energy Forming, Estes Park, Colorado, June 1967,pp 6.2.1.- 6.2.24.

2.104) NOBLE, C.F. and OXLEY, P.L.B. Estimating the charge size in explosive forming of sheet metal. Proc. of 5th Int. M.T.D.R. Conference, University of Birmingham, September 1964. Pergamon Press Inc., Oxford, 1965. pp 329 - 338.

2.105) JOHNSON, W. The forming efficiency and other calculations in some high rate forming processes. Ibid. pp 5.2.1.- 5.2.41.

2.106) HIRD, W.T. and FAHY, F.W. Instrumentation for the measurement of velocity of deformation of explosively formed materials. Mechanical Engineering Department, University of Canterbury, MECH MM 049/69, 1969.

2.107) CHONG, C.T., HO, K.V. and SMAILL, J.S. Instrumentation of explosive forming. Mechanical Engineering Department, University of Canterbury, MECH MM 024/72, 1972.

2.108) KIYOTA, K. Experiments on the plastic deformation of thin metal plates under blast type loading. Mem. Fac. Engng, Kumanisto, Vol. 9, 1962, p 1.

2.109) CORBETT, S.E. and BICKER, A.W. Some small-scale experiments in explosive forming. Sheet Metal Industries, Vol. 39, 1962. pp 555-562.

2.110) HUDSON, G.E. and JOHNSON, C.T. Time-displacement studies of diaphragms deformed by explosive loading. Underwater Explosion Research, Vol. III, The Damage Process, Office of Naval Research, 1950. pp 445-459.

2.111) BEDNARSKI, T. The dynamic deformation of a circular membrane. Int. J. Mech. Sci., Vol. 11, 1968, pp 949-959.

2.112) BEDNARSKI, T. Measurement of dynamic plastic deformation of circular membranes. Mechanika Tearetyczni i stosowona, Vol. 8, No. 3, 1970. pp 295-318.

2.113) JOHNSON, W., KORMI, K., TRAVIS, F.W. The explosive drawing of square and flat bottomed circular cups and bubble pulstation phenomena. Proc. of 5th Int. M.T.D.R. Conference, Birmingham, 1964. pp 293-328.

2.114) NISHIYOMAI, V. and INOUE, T. A study of the utilization of generated energies in hydro-spark forming and explosive forming. Int. J. Mech. Sci., Vol. 10, 1968. pp 479-486.

REFERENCES

Chapter Three

3.1) REDSHAW, S.C. A sensitive miniature pressure cell. J. Sci. Instr., Vol. 31, December 1954. pp 467-469.

3.2) BERT, C.W. and CRITES, N.A. Experimental mechanics in the development of a new miniature pressure transducer. Proc. of 1st Int. Cong. on Expt. Mechs, New York, November 1961. Pergamon Press, pp 307-322.

3.3) ANGELO, E.J. Pressure measurements for launch and re-entry vehicles. Proc. of 6th Int. Aerospace Instrumentation Symposium, 1970, Paper 5.

3.4) MILLIGAN, R.V. The effects of high pressure on foil strain gauges. Experimental Mechanics, Vol. 4, No. 2, February 1964, p 25-36.

3.5) MILLIGAN, R.V. The gross hydrostatic-pressure effect as related to foil and wire strain gauges. Experimental Mechanics, Vol. 7, No. 2, February 1967, p 67-74.

3.6) BRACE, W.F. Effect of pressure on electric-resistance strain gauges. Experimental Mechanics, Vol. 4, No. 7, July 1964, p. 212-216.

3.7) HARIDER,K., HOLTBECKER, H. and JORZIK, E. Pressure transducer for blast measurements. Journal of Physics E., Sci. Instr. Vol. 3, No. 11, November 1970. p 945-946.

3.8) GRABOWSKY, W.R. and DURRAN, D.A. Gaufe for measuring impulsive pressure in a container subjected to large time-varying applied voltages. Rev. Sci. Instr., Vol. 39, No. 1, January 1968, pp 35-39.

3.9) GRABOWSKY, W.R., DURRAN, D.A. and GERARD, M.E. Pressure gauge for plasma subjected to large dynamic electric and magnetic fields. Rev. Sci. Instr., Vol. 38, 1967. pp 1160-1161.

3.10) ANDEEN, C., FONTONELLA, J. and SCHUELE, D. A capacitance gauge for the accurate measurement of high pressure. Rev. Sci. Instr. Vol. 42, No. 4, 1971, pp 495-496.

3.11) BAGANOFF,D. Pressure gauge with one-tenth microsecond risetime for shock reflection studies. Rev. Sci. Instr., Vol. 35, No. 3, March 1964. pp 288-295.

3.12) HANSON, R.K. and BAGANOFF,D. Improved fast response pressure gauge for shock reflection studies in ionized gases. Vol. 43, No. 3, March 1972. pp 394-399.

3.13) GREY, J. Pressure transducers. Product Engineering, Vol. 25, No. 1, 1954. pp 174-179.

3.14) LION, K.S. Instrumentation in Scientific Research. McGraw-Hill Book Co. Inc., 1959.

3.15) BERNSTEIN, L. and GOODCHILD, R.O. High-sensitivity piezoelectric transducer for wave velocity measurements in shock tubes. Rev. Sci. Instr., Vol. 38, 1967, pp 971-972.

3.16) HEUSINKVELD, M., HOLZIC, F., MARKS, R. and SIESEMONE, C. Stress history measurements with piezoelectric crystals. Preliminary Report. Project Gnome PNE,

3.17) PAUL, D.E. Simple inexpensive pressure transducers for wave velocity measurement in shock tubes. Rev. Sci. Instr., Vol. 37, No. 9, September 1966. pp 1269-1270.

3.18) JONES, T.G. and VLASES, G.C. Pressure probes for research in plasma dynamics and detonations. Rev. Sci. Instr., Vol. 38, No. 8, August 1967, pp 1038-1042.

3.19) DE KLERK, J. and KELLY, E.F. Vapour-deposited thin-film piezoelectric transducers. Rev. Sci. Instr., Vol. 36, No. 4, April 1965. pp 506-510.

3.20) HOFLAND, R. and GLICK, H.S. A miniature transducer for measuring low transient pressures. Rev. Sci. Instr., Vol. 40, No. 9, September 1969. pp 1146-1151.

3.21) YORK, T.M. Stress dynamics in high speed piezoelectric pressure probes. Rev. Sci. Instr., Vol. 41, No. 4, April 1970. pp 519-521.

3.22) SCIBOR-RYLSKI, A. and GLOVER, D.D. The shock tube pressure transducer. Aircraft Engineering, Vol. 38, July 1966. pp 11-12.

3.23) HERTELENDY, P. and REYNARD, P. 'Thumbtack' accelerometer for the 1.5 - 150 kc range. Rev. Sci. Instr. 35,10, October 1964. pp 1305-1306.

3.24) JENKINS, R.C. and HOPKINS, H.B. Model surface pressure instrumentation for a hypersonic shock tunnel. Rev. Sci. Instr. 35,12, December 1964. pp 1684-1688.

3.25) O'BRIEN, J.F. and WASLEY, R.G. Quartz pressure transducer package. Rev. Sci. Instr. 37,4, April 1966, p. 531.

3.26) LANGENECKER, B. Piezoelectric device for measuring dynamic and static forces. Rev. Sci. Instr. 33,1, January 1962, pp 47-49.

3.27 TUCKER, D.G. and GAZEY, B.K. Applied underwater acoustics. Pergamon Press, London, 1966.

3.28 BRIDGMAN, P.W. The measurement of hydrostatic pressure to 30,000 kg/cm^2. Proc. Amer. Acad., 74:1, 1940, pp 1-10.

3.29 BRIDGMAN, P.W. Physics of high pressure. G. Bell and Sons, London, 1949.

3.30) WLODARSKI, W. and PINTARA, J. On the application of the gold-chromium (2.1%) alloy resistance transducer for measuring rapidly varying pressures in the range up to 500 atm. Bulletin D L'Académie Polonaise Des Sciences, Seŕie des sciences techniques. Vol. XXI, No. 7-8, 1973. pp 99-103.

3.31) BIRKS, A.W. Design and development of manganin and other wire tensors together with a resistance strain gauge transducer for use at pressures up to 200,000 lbf/m², (1.38 GN/m²), Strain, Vol. 9, No. 2, 1973. pp 60-65.

3.32) KICKS, J.C. Development and refinement of an ultraminiature pressure transducer and application to airplane model and airplane subsystem testing in wind tunnels. Proc. of 6th Int. Aerospace Instrumentation Symposium, 1970, Paper 9.

3.33) ZIAS, A.R. and HARE, W.F.J. Integration bringing a generation of low-cost transducers. Electronics, Vol. No. 1972, pp 83-88.

3.34) SAMAUN, WISE, K.D. and ANGELL, J.B. An IC piezoresistive sensor for biomedical instrumentation, IEEE Transactions in Biomedical Engineering, Vol. BME-20, No. 2, March 1973. pp 101-109.

3.35) HOPKINSON, B. A method of measuring the pressure produced in the detonation of high explosives or by the impact of bullets. Phil. Trans. of the Roy. Soc. 213, 1914, pp 437-456.

3.36) DAVIES, R.M. A critical study of the Hopkinson pressure bar. Trans. Roy. Soc., London, 240, 1948, pp 375-457.

3.37) CURTIS, C.W. Propagation of an elastic strain pulse in a semi-infinite bar. Int. Symposium on Stress Wave Propagation in Materials. Interscience Publishers Inc., New York, 1960. pp 15-43.

3.38) EDWARDS, D.H., DAVIES, L. and LAWRENCE, T.R. The application of a piezoelectric bar gauge to shock tube studies. J. Sci. Instrum., 41,10, Oct. 1964. pp 609-613.

3.39) EDWARDS, D.H. A piezoelectric pressure bar gauge. J.Sci. Instrum., 35,9, September 1958, pp 346-349.

3.40) JONES, I.R. Beryllium pressure bar having submicrosecond risetime. Rev. Sci. Instr., 37,8, August 1966, pp 1059-1061.

3.41) BLACKSTOCK, A.W., KRATZ, H.R. and FEENEY, M.B. Piezoelectric gauges for measuring rapidly varying pressures up to seven kilobars. Rev. Sci. Instr., 35,1, January 1964. pp 105-110.

3.42) SIKORSKI, M.E. and ANDREATCH, P. Tunnel diode hydrostatic pressure transducer. Rev. Sci. Instr. 33,2 February 1962, pp 155-160.

3.43) COHEN, M.M. and HORN, L. Tunnelling junction diode pressure gauge. Rev. Sci. Instr. 36,5, May 1965, pp 638-641.

3.44) WLODARSKI, W. and PINTARA, J. Application of the semi-conductor p-n junction to measurements of rapidly varying pressures. Bulletin De L'academie Polonaise Des Sciences, serie des sciences techniques, Vol. XXI, No. 5, 1973. pp 65-73.

3.45) SIKORSKI, M.E., ANDREATCH, P., GRIECO, A. and CHRISTENSEN, H. Transistor microphone. Rev. Sci. Instr. 33,10,October 1962, pp 1130-1131.

3.46) WATSON, R.W. Gauge for determining shock pressure. Rev. Sci. Instr. Vol. 38, 1967, pp 978-980.

3.47) MILLER, C.E., DEAN, J.W. and FLYNN, T.M. Commercial carbon composition resistors as pressure transducers. Rev. Sci. Instr. 36,2, February 1965, pp 231-232.

3.48) STANKIEWIEZ, J. and WHITE, R.L. Carbon resistors as pressure gauges. Rev. Sci. Instr., Vol. 42, No. 7, July 1971, pp 1067-1068.

3.49) CLARK, D.B. Pressure-sensitive material measures explosion forces ..... or footfall of a fly. Product Engineering September 1957.

3.50) MASSEY, B.S. and KAVRAK, I. A miniature pressure transducer. J.Sci.Instrum.,43,8, August 1966, pp 569-571.

3.51) KING, J.H. The production of a known high pressure. J.Sci. Instrum., Vol. 43, 1966, pp 320-322.

3.52) ————————, A Guide for the dynamic calibration of pressure transducers. American National Standard, ANSI B88.1 - 1972. Published ASME.

3.53) LEISSA, A.W. Vibration of plates. NASA SP-160, 1969.

3.54) NEUBERT, H.K.P. Instrument transducers. Oxford University Press, Great Britain, 1963.

REFERENCES

Chapter Four

4.1) KERR, A.D. Elastic and visco-elastic foundation. Trans. of A.S.M.E. J. Appl. Mech., Vol. E31, 1963, pp 491-498.

4.2) NOWINSKI, J.L. Non-linear transverse vibrations of circular elastic plates built-in at the boundary. Proc. 4th U.S. Nat. Cong. Appl. Mech., Vol. 1, 1962, p 325.

4.3) HUANG, C.L.D. and SANDMAN, B.E. Large amplitude vibrations of a rigidly clamped circular plate, Int. J. Non-linear Mechanics, Vol. 6, 1971, pp 451-468.

4.4) WAY, S. Bending of circular plates with large deflections, Trans. Am. Soc. Mech. Engrs, 56, pp 627-636, 1934.

4.5) REISSNER, E. On finite deflections of circular plates. Proc. Symposia Appl. Math., Vol. 1, 1949, pp 213-219.

4.6) SHARMA, S.P. and DAS GUPTA, S. The bending problem of axially constrained beams on non-linear elastic foundations, Int. J. Solids and Structures, Vol, 11, 1975, pp 853-859.

4.7) NASH, W.A. and KANEMATSU, H. Finite amplitude response of circular plates subject to dynamic loading. Instability of Continuous Systems, Herrenalb Symposium, Editor H. Leipholz, IUTAM, 1971, pp 311-316.

4.8) DATTA, S. Large amplitude free vibrations of irregular plates placed on an elastic foundation. Int. J. Non-linear Mechanics, Vol. 11, pp 337-345, 1976.

REFERENCES

Chapter Five

5.1) HRUDEY, T.M. Non-linear Transient Dynamics Analysis of Circular Plates. National Research Council of Canada, LTR-ST 740, 1974.

5.2) McLACHLAN, N.W. Bessel Functions for Engineers. Oxford University Press, 1st Edition, 1934.

5.3) KREYSZIG, E. Advanced Engineering Mathematics. John Wiley and Sons Inc., 1964.

5.4) WOOLDRIDGE, R. An Introduction to Computing. Oxford University Press, 1962.

5.5) BERGER, H.M. A new approach to the analysis of large deflection of plates. Trans. of A.S.M.E., J. Appl. Mech., Vol. 82, 1955, pp 465-472.

5.6) NOWINSKI, J.L. and OHNABE, H. On certain inconsistencies in Berger equations for large deflections of elastic plates. Int. Jo. Mech. Sci., Vol. 14, 1972, pp 165-170.

5.7) HUANG, C.L.D. and AlKHATLAT, I.M. Finite amplitude vibrations of a circular plate. Int. Jo. Non-linear Mechanics, Vol. 12, 1977, pp 297-306.

REFERENCES

Chapter Six

6.1) NADAI, A. Die elastische platten, Springer, Berlin, 1925, p. 288.

6.2) TIMOSHENKO, S. Vibration problems in engineering. D. Van Nostrand Co., New York, 1928, p. 317.

6.3) SINHA, S.N. Large deflection of plates on elastic foundations. J. Engng Mech. Div., A.S.C.F., Vol. 89, No. EMI, 1963, pp 1-24.

6.4) RAMACHANDRAN, J. Frequency analysis of plates vibrating at large amplitudes. Jn. of Sound and Vibration, Vol. 51, pp 1-5.

6.5) DATTA, S. Large amplitude free vibrations of irregular plates in an elastic foundation. Int. J. Non-linear Mechanics, Vol. 11, 1976, pp 337-345.

6.6) WAH, T. Vibration of circular plates at large amplitudes. J. Engn. Mech. Div., Proc. ASCE, Vol. 89, 1963, pp 1-15.

6.7) COLEBY, J.R. and MAZUMDAR, J. Non-linear vibration of elastic plates subjected to transient pressure loading. Journal of Sound and Vibration, Vol. 80, No. 2, 1982, pp 193-201.

6.8) BANERJEE, B. and DATTA, S. A new approach to an analysis of large deflections of thin elastic plates. Int. J. Non-linear Mechanics, Vol. 16, 1981, pp 47-52.

6.9) SCHMIDT, R. On Berger's method on the non-linear theory of plates. J. Appl. Mechs., Trans of A.S.M.E., Series E, Vol. 41, No. 2, 1974, pp 521-523.

6.10) SCHMIDT, R. and DeDEPPO, D.A. A new approach to the analysis of shells, plates and membranes with finite deflection. Int. J. Non-linear Mechanics, Vol. 9, 1974, pp 409-419.

6.11) HAISLER, W.E. and STRICKLIN, J.A. Computational methods for solving non-linear structural mechanical problems. Computer Methods in Non-Linear Mechanics; Proceedings of International Conference on Computer Methods, Austin, Texas, 1974, pp 393-403.

6.12) MURTHY, S.D.N. and SHERBOURNE, A.N. Non-linear bending of elastic plates of variable profile. J. of Eng. Mechs. Div. A.S.C.E. Vol. 100, No. EM2, 1974, pp 254-265.

6.13) HRUDEY, T.M. Non-linear transient dynamic analys of circular plates. National Research Council of Canada, LTR-ST740, 1974.

6.14) MONDKAR, D.P. and POWELL, G.H. Finite element analysis of non-linear static and dynamic response. Int. J. for Numerical Methods in Engineering, Vol. 11, 1977, pp 499-520.

6.15) MARTIN, J.A.C. and MOTA SEARES, C.A. Non-linear transient analysis of plate by mixed elements. A.S.M.E. paper 81-DET-146 for Meet Sept. 20-23, 1981.

6.16) KELLER, H.B. and REISS, E.L. Non-linear bending and buckling of circular plates. Proceedings of the Third U.S. National Congress of Applied Mechanics, June 11-14, 1958, pp 375-385.

6.17) MAH, G.B.J. Axisymmetric finite deflection of circular plates. J. Engr. Mechs. Div., A.S.C.E. Vol. 95, No. EM5, 1969, pp 1125-1143.

6.18) ARGYRIS, J.H., VAZ, L.E. and WILLIAM, K.J. Higher order methods for transient diffusion analysis. Computer Methods in Applied Mechanics and Engineering, Vol. 12, 1977, pp 243-278.

6.19) ZIENKIEWICZ, O.C. A new look at the Newmark, Houbolt and other time stepping formulas. A weighted residual approach. Earthquake Engineering and Structural Dynamics, Vol. 5, 1977, pp 413-418.

6.20) HILBER, H.M. and HUGHES, T.J.R. Collocation, dissipation and 'overshoot' for time integration schemes in structural dynamics. Earthquake Engineering and Structural Dynamics, Vol. 6, 1978, pp 99-117.

6.21) KRIEG, R.D. Unconditional stability in numerical time integration methods. J. Appl. Mech., Vol. 40, 1973. pp 417-421.

6.22) HOUBOLT, J.C. A recurrence matrix solution for the dynamic response of elastic aircraft. J. Aeron. Sci., Vol. 17, 1950, pp 540-550.

6.23) ZIENKIEWICZ, O.C. The finite element method. 3rd Edition, McGraw-Hill Book Company (UK) Ltd, 1977, p. 584.

6.24) SHARPE, R.D. The seismic response of inelastic structures. Ph.D. Thesis, Civil Engineering Department, University of Canterbury, 1974.

6.25) HILBER, H.M., HUGHES, T.J.R. and TAYLOR, R.L. Improved numerical dissipation for time integration algorithms in structural dynamics. Earthquake Engineering and Structural Dynamics, Vol. 5, 1977, pp 283-292.

6.26) WOOD, W.L. On the Zienkiewicz four-time-level scheme for the numerical integration of vibration problems. Int. J. for Numerical Methods in Engineering, Vol. 11, 1977, pp 1519-1528.

6.27) WOOD, N.L. Numerical integration of structural dynamics and periodic forging terms. Int. J. for Numerical Methods in Engineering, Vol. 17, 1981, pp 281-289.

REFERENCES

Chapter Seven

7.1) ALWAR, R.S. and YOGENDRA NATH. Non-linear dynamic response of circular plates subjected to transient loads. Jo. Franklin Inst. Vol. 303, 1977, pp 527-542.

7.2) ALWAR, R.S. and YOGENDRA NATH. Application of Chebyshev polynomials to the non-linear analysis of circular plates. Int. J. Mech. Sci., Vol. 18, 1976, pp 589-595.

7.3) ALWAR, R.S. and REDDY, B. Seklar. The dynamic analysis of circular plates and shallow spherical shells. Journal of Sound and Vibration, Vol. 70, No. 4, 1980, pp 467-473.

7.4) ————————. Modern Computing Methods. 2nd Edition. National Physical Laboratory, H.M.S.O. 1961.

7.5) COLEBY, J.R. and MAZUMDAR, J. Non-linear vibrations of elastic plates subjected to transient pressure loading. Journal of Sound and Vibration, Vol. 80, No. 2, 1982, pp 193-201.

7.6) MAZUMDAR, J. and JONES, R. A simplified approach to the large amplitude vibration of plates and membranes. Journal of Sound and Vibration, Vol. 50, No. 3, 1977, pp 389-397.

7.7) NATH, Y. Large amplitude response of circular plates on Elastic foundations. Int. J. Non-Linear Mechanics, Vol. 17, No. 4, 1982, pp 285-296.

7.8) FOX, L. and PARKER, I.B. Chebyshev Polynomials in Numerical Analysis. Reprint, Oxford University Press. 1977.

7.9) SELVADURAI, A.P.S. Elastic analysis of soil-foundation interaction. Elseview Scientific Publishing Co., 1979.

REFERENCES

Chapter Eight

8.1) YAMAKI, N., OTOMO, K. and CHIBA, M. Non-linear vibrations of a clamped circular plate with initial deflection and initial edge displacement, Part II: Experiment, Journal of Sound and Vibration, Vol. 79, 1981, pp 43-59.

APPENDIX A

DETERMINATION OF ORTHONORMAL EIGENFUNCTION

$$\bar{\alpha}_m(\rho) = G_m\{J_o(\lambda_{1m}\rho)I_o(\lambda_{2m}) - J_o(\lambda_{1m})I_o(\lambda_{2m}\rho)\}$$

Application of the orthogonality conditions with respect to the radius parameter β as a weight function gave

$$\int \rho\, \bar{\alpha}_m(\rho)\bar{\alpha}_n(\rho)d\rho = 0 \qquad m \neq n$$
$$= 1 \qquad m = n$$

Therefore

$$\int_o^1 \rho\,(G_m\{I_o(\lambda_{1m}\rho)I_o(\lambda_{2m}) - J_o(\lambda_{1m})I_o(\lambda_{2m}\rho)\})^2\, d\rho = 1$$

giving

$$G_m^2\,(I_o^2(\lambda_{2m}) \int_o^1 \rho\, J_o^2(\lambda_{1m}\rho)d\rho - 2J_o(\lambda_{1m})I_o(\lambda_{2m})$$
$$\int_o^1 \rho\, J_o(\lambda_{1m}\rho)I_o(\lambda_{2m}\rho)d\rho + J_o^2(\lambda_{1m}) \int_0^1 \rho\, I_o^2(\lambda_{2m}\rho)d\rho) = 1$$

But the standard forms of the integrals 7.3 were

$$\int_o^1 \rho\, J_o^2(\lambda_{1m}\rho)d\rho = \tfrac{1}{2}(J_o^2(\lambda_{1m}) + J_1^2(\lambda_{1m}))$$

$$\int_o^1 \rho\, J_o(\lambda_{1m}\rho)I_o(\lambda_{2m}\rho)d\rho$$
$$= \frac{1}{\lambda_{1m}^2 + \lambda_{2m}^2}(\lambda_{1m} J_1(\lambda_{1m})I_o(\lambda_{2m}) + \lambda_{2m}J_o(\lambda_{1m}) + I_1(\lambda_{2m}))$$

$$\int_o^1 \rho\, I_o^2(\lambda_{2m}\rho)d\rho = \tfrac{1}{2}(I_o^2(\lambda_{2m}) - I_1^2(\lambda_{2m}))$$

but from the frequency equation

$$\lambda_{1m}J_1(\lambda_{1m})I_o(\lambda_{2m}) + \lambda_{2m}J_o(\lambda_{1m})I_1(\lambda_{2m}) = 0$$

Therefore substitution in the original equation gives

$$\int_0^1 \rho\, \bar{\alpha}_m(\rho)\bar{\alpha}_n(\rho)d\rho$$

$$= G_m^2 \{\tfrac{1}{2}\ J_o^2(\lambda_{1m}) + J_1^2(\lambda_{1m})\ \times I_o^2(\lambda_{2m}) + \tfrac{1}{2}J_o^2(\lambda_{1m})\times$$

$$I_o^2(\lambda_{2m}) - I_1^2(\lambda_{2m})\ \}$$

$$= G_m^2\, J_o^2(\lambda_{1m}) I_o^2(\lambda_{2m}) (1 + \tfrac{1}{2} \frac{J_1^2(\lambda_{1m})}{J_o^2(\lambda_{1m})} - \tfrac{1}{2} \frac{I_1^2(\lambda_{2m})}{I_o^2(\lambda_{2m})}$$

Letting $E_m = 1 + \tfrac{1}{2} \dfrac{J_1^2(\lambda_{1m})}{J_o^2(\lambda_{1m})} - \tfrac{1}{2} \dfrac{I_1^2(\lambda_{2m})}{I_o^2(\lambda_{2m})}$

and applying the orthogonality condition

$$1 = G_m^2\, J_o^2\ (\lambda_{1m})\ I_o^2\ (\lambda_{2m})\ E_m$$

i.e.

$$G_m = \frac{1}{\sqrt{E_m}\, J_o(\lambda_{1m})\ I_o(\lambda_{2m})}$$

APPENDIX B

DETERMINATION OF CONSTANTS FOR GENERALISED FOURIER SERIES EXPANSION

The constants were given by [5.3]

$$a_m = \frac{1}{\int_0^1 \rho \alpha_m^2(\rho)\,d\rho} \int_0^1 \rho \bar{\alpha}_m(\rho)\,d\rho$$

and since $\bar{\alpha}_m(\beta)$ was orthonormal with respect to the weight function β the constants were obtained by the equation

$$a_m = \int_0^1 \rho \bar{\alpha}_m(\rho)\,d\rho$$

Therefore substituting for

$$\bar{\alpha}_m(\rho) = \frac{1}{\sqrt{E_m}} \left(\frac{J_o(\lambda_{1m}\rho)}{J_o(\lambda_{1m})} - \frac{I_o(\lambda_{2m}\rho)}{I_o(\lambda_{2m})}\right.$$

gave

$$a_m = \int_0^1 \frac{\rho}{\sqrt{E_m}} \left(\frac{J_o(\lambda_{1m}\rho)}{J_o(\lambda_{1m})} - \frac{I_o(\lambda_{2m}\rho)}{I_o(\lambda_{2m})}\right) d\rho$$

Consider the term

$$\int_0^1 \rho\, J_o(\lambda_{1m}\rho)\,d\rho$$

Using the relationship 5.2

$$\frac{d}{dz}\{z^\nu J_\nu(z)\} = z^\nu J_{\nu-1}(z)$$

it can be shown that

$$\int_0^a z\, J_o(kz)\,dz = \frac{a^2 J_1(ka)}{ka}$$

giving $$\int_0^1 \rho\, J_o(\lambda_{1m}\rho)\,d\rho = \frac{J_1(\lambda_{1m})}{\lambda_{1m}}$$

Next considering the term

$$\int_o^1 \beta \, I_o(\lambda_{2m}\beta)d\beta$$

The relationship

$$\frac{d}{dz}\{z^\nu I_\nu(z)\} = z^\nu I_{\nu-1}(z)$$

gave

$$\int_o^a z \, I_o(kz)dz = \frac{a^2 I_1(ka)}{ka}$$

giving

$$\int_o^1 \beta \, I_o(\lambda_{2m}\beta)d\beta = \frac{I_1(\lambda_{2m})}{\lambda_{2m}}$$

Therefore substitution in the original equation gave the constant

$$a_m = \frac{1}{\sqrt{E_m}}\left(\frac{J_1(\lambda_{1m})}{\lambda_{1m}J_o(\lambda_{1m})} - \frac{I_1(\lambda_{2m})}{\lambda_{2m}I_o(\lambda_{2m})}\right)$$

for $\lambda_{1m} \neq \lambda_{2m}$

while for $\lambda_{1m} = \lambda_{2m}$ it has been shown that $E_m = 1$ and the constant reverts to

$$a_m = \frac{1}{\lambda_m}\left(\frac{J_1(\lambda_{1m})}{J_o(\lambda_{1m})} - \frac{I_1(\lambda_{2m})}{I_o(\lambda_{2m})}\right).$$

APPENDIX C

ROOTS TO FREQUENCY EQUATION

$$J_o(\lambda)I_1(\lambda) + J_1(\lambda)I_o(\lambda) = 0$$

Mode	Value	Mode	Value	Mode	Value
1	3.1962	2	6.3064	3	9.4395
4	12.5771	5	15.7164	6	18.8565
7	21.9971	8	25.1379	9	28.2789
10	31.4200	11	34.5612	12	37.7025
13	40.8438	14	43.9852	15	47.1266
16	50.2680	17	53.4095	18	56.5509
19	59.6924	20	62.8339	21	65.9754
22	69.1169	23	72.2584	24	75.3999
25	78.5414	26	81.6830	27	84.8245
28	87.9660	29	91.1076	30	94.2491
31	97.3907				

APPENDIX D
ROOTS TO FREQUENCY EQUATION

$$\lambda_1 J_1(\lambda_1) I_o(\lambda_2) + \lambda_2 J_o(\lambda_1) I_1(\lambda_2) = 0$$

$$\lambda_2 = (G + \lambda_1^2)^{\frac{1}{2}}$$

$$G = 50$$

Mode	λ_1	λ_2	Mode	λ_1	λ_2
1	2.7532	7.5882	16	50.2631	50.7581
2	6.0990	9.3380	17	53.4051	53.8712
3	9.3268	11.7042	18	56.5470	56.9874
4	12.5080	14.3683	19	59.6889	60.1063
5	15.6701	17.1917	20	62.8307	63.2273
6	18.8236	20.1079	21	65.9725	66.3504
7	21.9725	23.0822	22	69.1143	69.4750
8	25.1189	26.0951	23	72.2560	72.6012
9	28.2637	29.1348	24	75.3977	75.7286
10	31.4077	32.1938	25	78.5394	78.8571
11	34.5510	35.2671	26	81.6811	81.9866
12	37.6939	38.3514	27	84.8228	85.1170
13	40.8365	41.4441	28	87.9644	88.2482
14	43.9788	44.5437	29	91.1061	91.3801
15	47.1210	47.6486	30	94.2477	94.5126
			31	97.3894	97.6457

APPENDIX E

ROOTS TO FREQUENCY EQUATION

$$\lambda_1 J_1(\lambda_1) I_o(\lambda_2) + \lambda_2 J_o(\lambda_1) I_1(\lambda_2) = 0$$

$$\lambda_2 = (G + \lambda_1^2)^{\frac{1}{2}}$$

$$G = 100$$

Mode	λ_1	λ_2	Mode	λ_1	λ_2
1	2.6562	10.3468	17	53.4008	54.3291
2	5.9952	11.6594	18	56.5432	57.4207
3	9.2504	13.6224	19	59.6855	60.5174
4	12.4539	15.9718	20	62.8276	63.6185
5	15.6310	18.5561	21	65.9697	66.7233
6	18.7944	21.2892	22	69.1117	69.8314
7	21.9500	24.1206	23	72.2536	72.9424
8	25.1011	27.0197	24	75.3955	76.0558
9	28.2494	29.9671	25	78.5374	79.1715
10	31.3959	32.9500	26	81.6792	82.2891
11	34.5411	35.9595	27	84.8210	85.4085
12	37.6855	38.9897	28	87.9628	88.5294
13	40.8293	42.0953	29	91.1046	91.6518
14	43.9726	45.0953	30	94.2463	94.7754
15	47.1156	48.1651	31	97.3880	97.9001
16	50.2583	51.2435			

APPENDIX F

RADIAL DEFLECTION

For a fixed point in time, once radial inertia and radial damping were ignored, the radial deflection, after Berger [5.5], could be represented by,

$$\left(\frac{d\zeta(\rho)}{d\rho}\right)_\tau + \tfrac{1}{2}\left(\frac{d\alpha(\rho\tau)}{d\rho}\right)_\tau^2 + \left(\frac{\zeta(\rho)}{\rho}\right)_\tau = \frac{\lambda_{2m}^2 - \lambda_{1m}^2}{12\delta^2}$$

Therefore for the mth mode

$$\alpha_m = a_m A_m(\tau)\bar{\alpha}_m(\rho)$$

giving

$$\frac{d(\rho\zeta_m(\rho))}{d\rho} = \frac{\rho(\lambda_{2m}^2 - \lambda_{1m}^2)}{12\delta^2} - \frac{\rho}{2}\left(\frac{d\alpha_m}{d\rho}\right)^2$$

Integrating once gave

$$\rho\zeta_m(\rho) = \frac{\rho^2(\lambda_{2m}^2 - \lambda_{1m}^2)}{24\delta^2} - \int\frac{\rho}{2}\left(\frac{d\alpha_m}{d\rho}\right)^2 d\rho + A$$

Consider the term

$$\int\frac{\rho}{2}\left(\frac{d\alpha_m(\rho)}{d\rho}\right)^2 d\rho = a_m^2 A_m^2(\tau)\ \frac{\rho}{2}\left(\frac{d(\bar{\alpha}_m(\rho))}{d\rho}\right)^2 d\rho$$

Since $\bar{\alpha}_m(\rho) = \frac{1}{\sqrt{E_m}}\left(\frac{J_o(\lambda_{1m}\rho)}{J_o(\lambda_{1m})} - \frac{I_o(\lambda_{2m}\rho)}{I_o(\lambda_{2m})}\right)$

$$\frac{d\bar{\alpha}_m(\rho)}{d\rho} = \frac{1}{\sqrt{E_m}}\left(\frac{1}{J_o(\lambda_{1m})}\ \frac{dJ_o(\lambda_{1m}\rho)}{d\rho} - \frac{1}{I_o(\lambda_{2m})}\ \frac{d(I_o(\lambda_{2m}\rho))}{d\rho}\right)$$

and from the recurrence relationships

$$\frac{d\,J_o(\lambda_{1m}\rho)}{d\rho} = \frac{-J_1(\lambda_{1m}\rho)}{\lambda_{1m}}$$

$$\frac{d\,I_o(\lambda_{2m}\rho)}{d\rho} = \frac{I_1(\lambda_{2m}\rho)}{\lambda_{2m}}$$

therefore

$$\frac{d\bar{\alpha}_m(\rho)}{d\rho} = \frac{-1}{\sqrt{E_m}} \left(\frac{J_1(\lambda_{1m})}{\lambda_{1m} J_o(\lambda_{1m})} + \frac{I_1(\lambda_{2m}\rho)}{\lambda_{2m} I_o(\lambda_{2m})}\right)$$

so the term

$$\int \frac{\rho}{2}\left(\frac{d(\alpha_m(\rho))}{d\rho}\right)^2 d\rho$$

$$= \frac{1}{E_m} \int \frac{\rho}{2}\left(\frac{J_1(\lambda_{1m}\rho)}{\lambda_{1m} J_o(\lambda_{1m})} + \frac{I_1(\lambda_{2m}\rho)}{\lambda_{2m} I_o(\lambda_{2m}\rho)}\right)^2 d\rho$$

$$= \frac{1}{E_m} \int \frac{\rho}{2}\left(\frac{J_1^2(\lambda_{1m}\rho)}{\lambda_{1m}^2 J_o^2(\lambda_{1m})} + \frac{2J_1(\lambda_{1m}\rho) I_1(\lambda_{2m}\rho)}{\lambda_{1m}\lambda_{2m} J_o(\lambda_{1m}) I_o(\lambda_{2m})}\right.$$

$$\left. + \frac{I_1^2(\lambda_{2m}\rho)}{\lambda_{2m}^2 I_o^2(\lambda_{2m}\rho)}\right) d\rho$$

Consider the first term

$$\int \rho J_1^2(\lambda_{1m}\rho) d\rho = \tfrac{1}{2}\rho^2 \left\{\frac{1}{\lambda_{1m}^2}\left(\frac{dJ_1(\lambda_{1m}\rho)}{d\rho}\right)^2\right.$$

$$\left. + \left(1 - \frac{1}{\lambda_{1m}^2\rho^2}\right) J_1^2(\lambda_{1m}\rho)\right\}$$

using a standard integral [5.2] on regrouping gave

$$\int \rho J_1^2(\lambda_{1m}\rho) d\rho = \tfrac{1}{2}\rho^2 \left\{J_1^2(\lambda_{1m}\rho) + \left(\frac{1}{\lambda_{1m}} \frac{dJ_1(\lambda_{1m}\rho)}{d\rho}\right.\right.$$

$$\left.\left. - \frac{1}{\lambda_{1m}\rho} J_1(\lambda_{1m}\rho)\right) \times \left(\frac{1}{\lambda_{1m}} \frac{dJ_1(\lambda_{1m}\rho)}{d\rho} + \frac{1}{\lambda_{1m}\rho} J_1(\lambda_{1m}\rho)\right)\right\}$$

From the recurrence relationships

$$\frac{1}{\lambda_{1m}} \frac{dJ_1(\lambda_{1m}\rho)}{d\rho} - \frac{1}{\lambda_{1m}\rho} J_1(\lambda_{1m}\rho) = -J_2(\lambda_{1m}\rho)$$

$$\frac{1}{\lambda_{1m}} \frac{dJ_1(\lambda_{1m}\rho)}{d\rho} + \frac{1}{\lambda_{1m}\rho} J_1(\lambda_{1m}\rho) = J_o(\lambda_{1m}\rho)$$

giving

$$\int \rho J_1^2(\lambda_{1m}\rho)d\rho = \tfrac{1}{2}\rho^2\{J_1^2(\lambda_{1m}\rho) - J_o(\lambda_{1m}\rho).J_2(\lambda_{1m}\rho)\}$$

Consider the second term

$$\int \rho J_1(\lambda_{1m}\rho)\ I_1(\lambda_{2m}\rho)d\rho = \frac{\rho}{\lambda_{1m}^2 + \lambda_{2m}^2}\{\lambda_{2m}\ J_1(\lambda_{1m}\rho)I_2(\lambda_{2m}\rho)$$

$$+ \lambda_{1m}J_2(\lambda_{1m}\rho)\ I_1(\lambda_{2m}\rho)\}$$

from the standard integral form.

Similarly the third term gave

$$\int \rho I_1^2(\lambda_{2m}\rho)d\rho = \tfrac{1}{2}\rho\{-\frac{1}{\lambda_{2m}^2}(\frac{dI_1(\lambda_{2m}\rho)}{d\rho})^2 + I_1^2(\lambda_{2m}\rho)$$

$$+ \frac{1}{\lambda_{2m}^2\rho^2}\ I_1^2(\lambda_{2m}\rho))\}$$

using the standard integral form [5.2]

$$= \tfrac{1}{2}\rho\{I_1^2(\lambda_{2m}\rho) + (\frac{1}{\lambda_{2m}\rho}\ I_1(\lambda_{2m}\rho) - \frac{1}{\lambda_{2m}}\frac{dI_1(\lambda_{2m}\rho)}{d\rho}) \times (\frac{1}{\lambda_{2m}\rho}\ I_1(\lambda_{2m}\rho)$$

$$+ \frac{1}{\lambda_{2m}}\frac{dI_1(\lambda_{2m}\rho)}{d\rho})\}$$

From the recurrence relationships

$$\frac{1}{\lambda_{2m}\rho}\ I_1(\lambda_{2m}\rho) - \frac{1}{\lambda_{2m}}\ \frac{dI_1(\lambda_{2m}\rho)}{d\rho} = -I_2(\lambda_{2m}\rho)$$

$$\frac{1}{\lambda_{2m}\rho}\ I_1(\lambda_{2m}\rho) + \frac{1}{\lambda_{2m}}\ \frac{dI_1(\lambda_{2m}\rho)}{d\rho} = +I_o(\lambda_{2m}\rho)$$

giving

$$\int \rho I_1^2(\lambda_{2m}\rho)d\rho = \tfrac{1}{2}\rho^2\{I_1^2(\lambda_{2m}\rho) - I_o(\lambda_{2m}\rho)\ I_2(\lambda_{2m}\rho)\}$$

Therefore substituting into the original equation and dividing through by ρ the description of the radial deflection associated with the mth mode at time τ was given by

$$\zeta_m(\rho) = \rho \frac{(\lambda_{2m}^2 - \lambda_{1m}^2)}{24\delta^2} - \frac{\rho}{4}\left\{\frac{1}{E_m}\frac{\lambda_{1m}^2}{J_o^2(\lambda_{1m})}\left[J_1^2(\lambda_{1m}\rho) - J_o(\lambda_{1m}\rho)J_2(\lambda_{1m}\rho)\right]\right.$$

$$- \frac{1}{E_m}\frac{\lambda_{1m}\lambda_{2m}}{\lambda_{1m}^2 + \lambda_{2m}^2}\frac{1}{J_o(\lambda_{1m})I_o(\lambda_{2m})}\left[\lambda_{1m}J_2(\lambda_{1m}\rho)I_1(\lambda_{2m}\rho) - \lambda_{2m}J_1(\lambda_{1m}\rho)\right.$$

$$\left.\left.\times I_2(\lambda_{2m}\rho)\right] + \frac{\rho}{4}\frac{1}{E_m}\frac{\lambda_{2m}^2}{I_o^2(\lambda_{2m})}\left[I_1^2(\lambda_{2m}\rho) - I_o(\lambda_{2m}\rho)I_2(\lambda_{2m}\rho)\right]a_m^2 A_m(\tau)^2\right]\Big\}$$

since the value of $\zeta(o) = 0$ at the centre of the plate and the resultant value for the constant of integration was $A = 0$.

APPENDIX G

DERIVATIVES OF FREQUENCY EQUATION

Given the equation for function F_1

$$F_1(\lambda_{1m}, \lambda_{2m}) = \lambda_{1m}J_1(\lambda_{1m})I_o(\lambda_{2m}) + \lambda_{2m}J_o(\lambda_{1m})I_2(\lambda_{2m})$$

the partial derivative with respect to the root $_{1m}$ was

$$\frac{\partial F_1(\lambda_{1m}, \lambda_{2m})}{\partial \lambda_{1m}} = J_1(\lambda_{1m})I_o(\lambda_{2m}) + \lambda_{1m}\frac{\partial J_1(\lambda_{1m})}{\partial \lambda_{1m}} I_o(\lambda_{2m})$$

$$+ \lambda_{2m}\frac{\partial J_o(\lambda_{1m})}{\partial \lambda_{1m}} I_1(\lambda_{2m})$$

But from the recurrence relationships

$$\frac{\partial J_1(\lambda_{1m})}{\partial \lambda_{1m}} = \tfrac{1}{2}(J_o(\lambda_{1m}) - J_2(\lambda_{1m}))$$

$$\frac{\partial J_o(\lambda_{1m})}{\partial \lambda_{1m}} = -J_1(\lambda_{1m})$$

giving

$$\frac{\partial F_1(\lambda_{1m},\lambda_{2m})}{\partial \lambda_{1m}} = J_1(\lambda_{1m})I_o(\lambda_{2m}) + \tfrac{1}{2}\lambda_{1m}J_o(\lambda_{1m})I_o(\lambda_{2m})$$

$$- \tfrac{1}{2}\lambda_{1m}J_2(\lambda_{1m})I_o(\lambda_{2m}) - \lambda_{2m}J_1(\lambda_{1m})I_1(\lambda_{2m})$$

while the partial derivative with respect to the root λ_{2m} was given by

$$\frac{F_1(\lambda_{1m},\lambda_{2m})}{\partial \lambda_{2m}} = \lambda_{1m}J_1(\lambda_{1m})\frac{\partial I_o(\lambda_{2m})}{\partial \lambda_{2m}} + J_o(\lambda_{1m})I_1(\lambda_{2m})$$

$$+ \lambda_{2m}J_o(\lambda_{1m})\frac{\partial I_1(\lambda_{2m})}{\partial \lambda_{2m}}$$

But from the recurrence relationships

$$\frac{\partial I_1(\lambda_{2m})}{\partial \lambda_{2m}} = \tfrac{1}{2}(I_o(\lambda_{2m}) + I_2(\lambda_{2m}))$$

$$\frac{\partial I_o(\lambda_{2m})}{\partial \lambda_{2m}} = I_1(\lambda_{2m})$$

giving

$$\frac{\partial F_1(\lambda_{1m},\lambda_{2m})}{\partial \lambda_{2m}} = \lambda_{1m} J_1(\lambda_{1m}) I_1(\lambda_{2m}) + J_o(\lambda_{1m}) I_1(\lambda_{2m})$$

$$+ \tfrac{1}{2}\lambda_{2m} J_o(\lambda_{1m}) I_o(\lambda_{2m}) + \tfrac{1}{2}\lambda_{2m} J_o(\lambda_{1m}) I_2(\lambda_{2m})$$

APPENDIX H

DERIVATIVE OF RADIAL BOUNDARY CONDITION EQUATION

Given the equation for function F_2 was

$$F_2(\lambda_{1m},\lambda_{2m}) = \frac{\lambda_{2m}^2 - \lambda_{1m}^2}{24\delta^2} - \frac{1}{E_m} a_m^2 A_m^2(\tau)\{\tfrac{1}{4}\frac{\lambda_{1m}^2}{J_o^2(\lambda_{1m})}(J_1^2(\lambda_{1m}) - J_o(\lambda_{1m})J_2(\lambda_{1m})$$

$$+ \tfrac{1}{4}\frac{\lambda_{2m}^2}{I_o^2(\lambda_{2m})}(I_1^2(\lambda_{2m}) - I_o(\lambda_{2m})I_2(\lambda_{2m}))$$

$$+ \frac{\lambda_{1m}\lambda_{2m}}{\lambda_{1m}^2+\lambda_{2m}^2}\frac{1}{J_o(\lambda_{1m})I_o(\lambda_{2m})}(\lambda_{1m}J_2(\lambda_{1m})I_1(\lambda_{2m})$$

$$+ \lambda_{2m}J_1(\lambda_{1m})I_2(\lambda_{2m}))\}$$

if $$X_m = \tfrac{1}{4}\frac{\lambda_{1m}^2}{J_o^2(\lambda_{1m})}(J_1^2(\lambda_{1m}) - J_o(\lambda_{1m})J_2(\lambda_{1m}))$$

$$Y_m = \tfrac{1}{4}\frac{\lambda_{2m}^2}{I_o^2(\lambda_{2m})}(I_1^2(\lambda_{2m}) - I_o(\lambda_{2m})I_2(\lambda_{2m}))$$

$$Z_m = \frac{\lambda_{1m}\lambda_{2m}}{\lambda_{1m}^2 + \lambda_{2m}^2}\frac{1}{J_o(\lambda_{1m})I_o(\lambda_{2m})}(\lambda_{1m}J_2(\lambda_{1m})I_1(\lambda_{2m})$$

$$+ \lambda_{2m}J_1(\lambda_{1m})I_2(\lambda_{2m}))$$

$$F_2(\lambda_{1m},\lambda_{2m}) = \frac{\lambda_{2m}^2 - \lambda_{1m}^2}{24\delta^2} - \frac{1}{E_m} a_m^2 A_m^2(\tau)(X_m + Y_m + Z_m)$$

The partial derivative with respect to the root λ_{1m} was

$$\frac{\partial F_2(\lambda_{1m},\lambda_{2m})}{\partial\lambda_{1m}} = -\frac{\lambda_{1m}}{12\delta^2} + \frac{1}{E_m^2} a_m^2 A_m^2(\tau)(X_m + Y_m + Z_m)\frac{\partial E_m}{\partial\lambda_{1m}}$$

$$- \frac{1}{E_m} 2a_m A_m^2(\tau)(X_m + Y_m + Z_m)\frac{\partial a_n}{\partial\lambda_{1m}} - \frac{1}{E_m} 2a_m^2 A_m(\tau)(X_m + Y_m + Z_m)\frac{\partial A_m(\tau)}{\partial\lambda_{1m}}$$

$$- \frac{1}{E_m} a_m^2 A_m^2(\tau)\left(\frac{\partial X_m}{\partial\lambda_{1m}} + \frac{\partial Y_m}{\partial\lambda_{1m}} + \frac{\partial Z_m}{\partial\lambda_{1m}}\right)$$

while the partial derivative with respect to the root λ_{2m} was

$$\frac{\partial F_2(\lambda_{1m},\lambda_{2m})}{\partial \lambda_{2m}} = \frac{\lambda_{2m}}{12\delta^2} + \frac{1}{E_m^2} a_m^2 A_m^2(\tau)(X_m + Y_m + Z_m) \frac{\partial E_m}{\partial \lambda_{2m}}$$

$$- \frac{1}{E_m} 2.a_m A_m^2(\tau)(X_m + Y_m + Z_m) \frac{\partial a_m}{\partial \lambda_{2m}} - \frac{1}{E_m} 2a_m^2 A_m(\tau)(X_m + Y_m + Z_m) \frac{\partial A_m(\tau)}{\partial \lambda_{2m}}$$

$$- \frac{1}{E_m} a_m^2 A_m^2(\tau) \left(\frac{\partial X_m}{\partial \lambda_{2m}} + \frac{\partial Y_m}{\partial \lambda_{2m}} + \frac{\partial Z_m}{\partial \lambda_{2m}}\right)$$

*Considering individual terms in the equations

$$E_m = 1 + \tfrac{1}{2} \frac{J_1^2(\lambda_{1m})}{J_o^2(\lambda_{1m})} - \tfrac{1}{2} \frac{I_1^2(\lambda_{2m})}{I_o^2(\lambda_{2m})}$$

$$\frac{\partial E_m}{\partial \lambda_{1m}} = \frac{J_1(\lambda_{1m})}{J_o^2(\lambda_{1m})} \frac{J_1(\lambda_{1m})}{\partial \lambda_{1m}} - \frac{J_1^2(\lambda_{1m})}{J_o^3(\lambda_{1m})} \cdot \frac{J_o(\lambda_{1m})}{\partial \lambda_{1m}}$$

But $$\frac{\partial J_1(\lambda_{1m})}{\partial \lambda_{1m}} = \tfrac{1}{2}(J_o(\lambda_{1m}) - J_2(\lambda_{1m}))$$

$$\frac{\partial J_o(\lambda_{1m})}{\partial \lambda_{1m}} = - J_1(\lambda_{1m})$$

Therefore

$$\frac{\partial E_m}{\partial \lambda_{1m}} = \tfrac{1}{2} \frac{J_1(\lambda_{1m})}{J_o(\lambda_{1m})} - \tfrac{1}{2} \frac{J_1(\lambda_{1m}) I_2(\lambda_{1m})}{J_o^2(\lambda_{1m})} + \frac{J_1^3(\lambda_{1m})}{J_o^3(\lambda_{1m})}$$

---

*Footnote: While the derivative could be rearranged into alternative forms with possibly less terms, using recurrence relationships, they were programmed as shown in the interest of time.

while

$$\frac{\partial E_m}{\partial \lambda_{2m}} = -\frac{I_1(\lambda_{2m})}{I_o^2(\lambda_{2m})}\frac{I_1(\lambda_{2m})}{\partial \lambda_{2m}} + \frac{I_1^2(\lambda_{2m})}{I_o^3(\lambda_{2m})}\frac{I_o(\lambda_{2m})}{\partial \lambda_{2m}}$$

From recurrence relationships [5.2]

$$\frac{\partial I_1(\lambda_{2m})}{\partial \lambda_{2m}} = \tfrac{1}{2}(I_o(\lambda_{2m}) + I_2(\lambda_{2m}))$$

$$\frac{\partial I_o(\lambda_{2m})}{\partial \lambda_{2m}} = I_1(\lambda_{2m})$$

$$\frac{\partial E_m}{\partial \lambda_{2m}} = -\tfrac{1}{2}\frac{I_1(\lambda_{2m})}{I_o(\lambda_{2m})} + \tfrac{1}{2}\frac{I_1(\lambda_{2m})I_2(\lambda_{2m})}{I_o^2(\lambda_{2m})} + \frac{I_1^3(\lambda_{2m})}{I_o^3(\lambda_{2m})}$$

$$a_m = \left(\frac{J_1(\lambda_{1m})}{\lambda_{1m} J_o(\lambda_{1m})} - \frac{I_1(\lambda_{2m})}{\lambda_{2m} I_o(\lambda_{2m})}\right)$$

$$\frac{\partial a_m}{\partial \lambda_{1m}} = \left(\frac{1}{\lambda_{1m} J_o(\lambda_{1m})}\frac{\partial J_1(\lambda_{1m})}{\partial \lambda_{1m}} - \frac{J_1(\lambda_{1m})}{\lambda_{1m}^2 J_o(\lambda_{1m})} - \frac{J_1(\lambda_{1m})}{\lambda_{1m} J_o^2(\lambda_{1m})}\frac{\partial J_o(\lambda_{1m})}{\partial \lambda_{1m}}\right)$$

$$= \left(\tfrac{1}{2}\cdot\frac{1}{\lambda_{1m}} - \tfrac{1}{2}\frac{1}{\lambda_{1m}}\frac{J_2(\lambda_{1m})}{J_o(\lambda_{1m})} - \frac{1}{\lambda_{1m}^2}\frac{J_1(\lambda_{1m})}{J_o(\lambda_{1m})} + \frac{1}{\lambda_{1m}}\frac{J_1^2(\lambda_{1m})}{J_o^2(\lambda_{1m})}\right)$$

$$\frac{\partial a_m}{\partial \lambda_{2m}} = -\frac{1}{\lambda_{2m} I_o(\lambda_{2m})}\frac{\partial I_1(\lambda_{2m})}{\partial \lambda_{2m}} + \frac{I_1(\lambda_{2m})}{\lambda_{2m}^2 I_o(\lambda_{2m})} + \frac{I_1(\lambda_{2m})}{\lambda_{2m} I_o^2(\lambda_{2m})}\frac{\partial I_o(\lambda_{2m})}{\partial \lambda_{2m}}$$

$$= -\tfrac{1}{2}\frac{1}{\lambda_{2m}} - \tfrac{1}{2}\frac{1}{\lambda_{2m}}\frac{I_2(\lambda_{2m})}{I_o(\lambda_{2m})} + \frac{I_1(\lambda_{2m})}{\lambda_{2m}^2 I_o(\lambda_{2m})} - \frac{I_1^2(\lambda_{2m})}{\lambda_{2m} I_o^2(\lambda_{2m})}$$

$$X_m = \tfrac{1}{4}\frac{\lambda_{1m}^2}{J_o^2(\lambda_{1m})}(J_1^2(\lambda_{1m}) - J_o(\lambda_{1m})J_2(\lambda_{1m}))$$

$$\frac{\partial X_m}{\partial \lambda_{1m}} = \tfrac{1}{2} \frac{\lambda_{1m}}{J_o^2(\lambda_{1m})} (J_1^2(\lambda_{1m}) - J_o(\lambda_{1m})J_2(\lambda_{1m})) - \tfrac{1}{2} \frac{\lambda_{1m}^2}{J_o^3(\lambda_{1m})}(J_1^2(\lambda_{1m})$$

$$- J_o(\lambda_{1m})J_2(\lambda_{1m})) \frac{J_o(\lambda_{1m})}{\partial \lambda_{1m}} + \tfrac{1}{4} \frac{\lambda_{1m}^2}{J_o^2(\lambda_{1m})}(2J_1(\lambda_{1m}) \frac{\partial J_1(\lambda_{1m})}{\partial \lambda_{1m}}$$

$$- \frac{\partial J_o(\lambda_{1m})}{\partial \lambda_{1m}} J_2(\lambda_{1m}) - J_o(\lambda_{1m}) \frac{\partial J_2(\lambda_{1m})}{\partial \lambda_{1m}}$$

But

$$\frac{\partial J_2(\lambda_{1m})}{\partial \lambda_{1m}} = \frac{1}{\lambda_{1m}} (-2J_2(\lambda_{1m}) + \lambda_{1m} J_1(\lambda_{1m}))$$

$$\frac{\partial X_m}{\partial \lambda_{1m}} = (J_1^2(\lambda_{1m}) - J_o(\lambda_{1m})J_2(\lambda_{1m})) (\tfrac{1}{2} \frac{\lambda_{1m}}{J_o^2(\lambda_{1m})} + \tfrac{1}{2} \frac{\lambda_{1m}^2 J_1(\lambda_{1m})}{J_o^3(\lambda_{1m})}$$

$$+ \tfrac{1}{4} \frac{\lambda_{1m}^2}{J_o^2(\lambda_{1m})} (J_1(\lambda_{1m})J_o(\lambda_{1m}) - J_1(\lambda_{1m})I_2(\lambda_{1m}) - I_1(\lambda_{1m})I_2(\lambda_{1m})$$

$$- J_o(\lambda_{1m})J_1(\lambda_{1m}) + \frac{2J_2}{\lambda_{1m}} (\lambda_{1m})J_o(\lambda_{1m})) = \tfrac{1}{2}(J_1^2(\lambda_{1m}) - J_o(\lambda_{1m})J_2(\lambda_{1m}))$$

$$(\frac{\lambda_{1m}}{J_o^2(\lambda_{1m})} + \frac{\lambda_{1m}^2 J_1(\lambda_{1m})}{J_o^3(\lambda_{1m})}) + \tfrac{1}{2} \frac{\lambda_{1m}^2}{J_o^2(\lambda_{1m})}(\frac{J_2(\lambda_{1m})J_o(\lambda_{1m})}{\lambda_{1m}} - J_1(\lambda_{1m})J_2(\lambda_{1m}))$$

$$\frac{\partial X_m}{\partial \lambda_{2m}} = 0$$

$$Y_m = \tfrac{1}{2} \frac{\lambda_{2m}^2}{I_o^2(\lambda_{2m})} (I_1^2(\lambda_{2m}) - I_o(\lambda_{2m})I_2(\lambda_{2m}))$$

$$\frac{\partial Y_m}{\partial \lambda_{1m}} = 0$$

$$\frac{\partial Y_m}{\partial \lambda_{2m}} = \left(\tfrac{1}{2}\frac{\lambda_{2m}}{I_o^2(\lambda_{2m})} - \tfrac{1}{2}\frac{\lambda_{2m}^2}{J_o^3(\lambda_{2m})}\frac{\partial I_o(\lambda_{2m})}{\partial \lambda_{2m}}\right)\left(I_1^2(\lambda_{2m}) - I_o(\lambda_{2m})I_2(\lambda_{2m})\right)$$

$$+ \tfrac{1}{4}\frac{\lambda_{2m}^2}{I_o^2(\lambda_{2m})}\left(2I_1(\lambda_{2m})\frac{\partial I_1(\lambda_{2m})}{\partial \lambda_{2m}} - \frac{\partial I_o(\lambda_{2m})}{\partial \lambda_{2m}} I_2(\lambda_{2m}) + I_o(\lambda_{2m})\frac{I_2(\lambda_{2m})}{\partial \lambda_{2m}}\right)$$

But

$$\frac{\partial I_2(\lambda_{2m})}{\partial \lambda_{2m}} = \frac{1}{\lambda_{2m}}\left(-2I_2(\lambda_{2m}) + \lambda_{2m}I_1(\lambda_{2m})\right)$$

$$\frac{\partial Y_m}{\partial \lambda_{2m}} = \left(\tfrac{1}{2}\frac{\lambda_{2m}}{I_o^2(\lambda_{2m})} - \tfrac{1}{2}\frac{\lambda_{2m}^2 I_1(\lambda_{2m})}{I_o^3(\lambda_{2m})}\right)\left(J_1^2(\lambda_{2m}) - I_o(\lambda_{2m})I_2(\lambda_{2m})\right)$$

$$+ \tfrac{1}{4}\frac{\lambda_{2m}^2}{I_o^2(\lambda_{2m})}\left(I_1(\lambda_{2m})I_o(\lambda_{2m}) + I_1(\lambda_{2m})I_2(\lambda_{2m}) - I_1(\lambda_{2m})I_2(\lambda_{2m})\right.$$

$$\left. + \tfrac{1}{2}\frac{\lambda_{2m}^2}{I_o^2(\lambda_{2m})}\left(I_1(\lambda_{2m})I_o(\lambda_{2m}) - \frac{I_o(\lambda_{2m})I_2(\lambda_{2m})}{\lambda_{2m}}\right)\right.$$

$$Z_m = \frac{\lambda_{1m}\lambda_{2m}}{\lambda_{1m}^2 + \lambda_{2m}^2}\frac{1}{J_o(\lambda_{1m})I_o(\lambda_{2m})}\left(\lambda_{1m}J_2(\lambda_{1m})I_1(\lambda_{2m})\right.$$

$$\left. + \lambda_{2m}J_1(\lambda_{1m})I_2(\lambda_{2m})\right)$$

$$\frac{\partial Z_m}{\partial \lambda_{1m}} = \left(\frac{\lambda_{2m}}{\lambda_{1m}^2 + \lambda_{2m}^2}\frac{1}{J_o(\lambda_{1m})I_o(\lambda_{2m})} - \frac{\lambda_{1m}\lambda_{2m}}{(\lambda_{1m}^2 + \lambda_{2m}^2)^2}\frac{2\lambda_{1m}}{J_o(\lambda_{1m})I_o(\lambda_{2m})}\right.$$

$$\left. - \frac{\lambda_{1m}\lambda_{2m}}{\lambda_{1m}^2 + \lambda_{2m}^2}\frac{1}{J_o^2(\lambda_{1m})I_o(\lambda_{2m})}\frac{\partial J_o(\lambda_{1m})}{\lambda_{1m}}\right)\left(\lambda_{1m}J_2(\lambda_{1m})I_1(\lambda_{2m})\right.$$

$$\left. + \lambda_{2m}J_1(\lambda_{1m})I_2(\lambda_{2m})\right)\frac{\lambda_{1m}\lambda_{2m}}{\lambda_{1m}^2 + \lambda_{2m}^2}\frac{1}{J_o(\lambda_{1m})I_o(\lambda_{2m})}\left(I_2(\lambda_{1m})I_1(\lambda_{2m})\right.$$

$$\left. + \lambda_{1m}\frac{J_2(\lambda_{1m})I_1(\lambda_{2m})}{\partial \lambda_{1m}} + \lambda_{2m}\frac{\partial J_1(\lambda_{1m})}{\partial \lambda_{1m}}J_2(\lambda_{2m})\right)$$

$$\frac{\partial Z_m}{\partial \lambda_{1m}} = \left(\frac{\lambda_{2m}}{\lambda_{1m}^2+\lambda_{2m}^2}\ \frac{1}{J_o(\lambda_{1m})I_o(\lambda_{2m})} - \frac{2\lambda_{1m}^2\ \lambda_{2m}}{(\lambda_{1m}^2+\lambda_{2m}^2)^2}\ \frac{1}{J_o(\lambda_{1m})I_o(\lambda_{2m})}\right.$$

$$\left. + \frac{\lambda_{1m}\ \lambda_{2m}}{\lambda_{1m}^2+\lambda_{2m}^2}\ \frac{J_1(\lambda_{1m})}{J_o^2(\lambda_{1m})I_o(\lambda_{2m})}\right)(\lambda_{1m}J_2(\lambda_{1m})I_1(\lambda_{2m}) + \ _{2m}J_1(\lambda_{1m})I_2(\lambda_{2m}))$$

$$+ \frac{\lambda_{1m}\ \lambda_{2m}}{\lambda_{1m}^2+\lambda_{2m}^2}\ \frac{1}{J_o(\lambda_{1m})I_o(\lambda_{2m})}\ (J_2(\lambda_{1m})I_1(\lambda_{2m}) + J_1(\lambda_{2m})(-2J_2(\lambda_{1m})$$

$$+ \lambda_{2m}\cdot\tfrac{1}{2}(J_o(\lambda_{1m}) - J_2(\lambda_{1m}))I_2(\lambda_{2m})) = \frac{1}{\lambda_{1m}^2+\lambda_{2m}^2}\ \frac{1}{J_o(\lambda_{1m})I_o(\lambda_{2m})}$$

$$\left((\lambda_{2m} - \frac{2\lambda_{1m}^2\ \lambda_{2m}}{\lambda_{1m}^2+\lambda_{2m}^2} + \frac{J_1(\lambda_{1m})}{J_o(\lambda_{1m})}\right) \times \lambda_{1m}\ \lambda_{2m}(\lambda_{1m}J_1(\lambda_{1m})J_1(\lambda_{2m}) - J_2(\lambda_{1m})$$

$$I_1(\lambda_{2m}) + \frac{\lambda_{2m}}{2}\ J_o(\lambda_{1m})J_2(\lambda_{2m}) - \frac{\lambda_{2m}}{2} - J_2(\lambda_{1m})I_2(\lambda_{2m}))$$

$$\frac{\partial Z_m}{\partial \lambda_{2m}} = \left(\left(\frac{\lambda_{1m}}{\lambda_{1m}^2+\lambda_{2m}^2} - \frac{2\lambda_{1m}\ \lambda_{2m}^2}{(\lambda_{1m}^2+\lambda_{2m}^2)^2}\right)\frac{1}{J_o(\lambda_{1m})I_o(\lambda_{2m})}\right.$$

$$\left. - \frac{\lambda_{1m}\ \lambda_{2m}}{\lambda_{1m}^2+\lambda_{2m}^2}\cdot\ \frac{1}{J_o(\lambda_{1m})I_o^2(\lambda_{2m})}\ \frac{\partial I_o(\lambda_{2m})}{\partial \lambda_{2m}}\right)(\lambda_{1m}J_2(\lambda_{1m})I_1(\lambda_{2m}) + \ _{2m}J_1(\lambda_{1m})$$

$$I_2(\lambda_{2m})) + \frac{\lambda_{1m}\ \lambda_{2m}}{\lambda_{1m}^2+\lambda_{2m}^2}\ \frac{1}{J_o(\lambda_{1m})I_o(\lambda_{2m})}\ (\lambda_{1m}J_2(\lambda_{1m})\ \frac{\partial I_1(\lambda_{2m})}{\partial \lambda_{2m}} + J_1(\lambda_{1m})I_2(\lambda_{2m})$$

$$+ \ _{2m}J_1(\ _{1m})\ \frac{I_2(\ _{2m})}{2m}) = \frac{_{1m}\ \ _{2m}}{^2_{1m}+\ ^2_{2m}}\ \frac{1}{J_o(\ _{1m})J_o(\ _{2m})}\left(\left(\frac{_{1m}}{2m} - 2\ _{1m}\ \ ^2_{2m}\right.\right.$$

$$\left.\left. - \frac{I_1(\lambda_{2m})}{I_o(\lambda_{2m})}\right) \times (\lambda_{1m}J_2(\lambda_{1m})I_1(\lambda_{2m}) + \lambda_{2m}J_1(\lambda_{1m})I_2(\lambda_{2m})) + \left(\frac{\lambda_{1m}}{2}\ J_2(\lambda_{1m})\right.\right.$$

$$\left.\left.(I_o(\lambda_{2m}) + I_2(\lambda_{2m})) + J_1(\lambda_{1m})J_2(\lambda_{2m}) + J_1(\lambda_{1m})(\lambda_{2m}J_1(\lambda_{2m}) - 2J_2(\lambda_{2m}))\right)\right.$$

$$= \frac{\lambda_{1m}\lambda_{2m}}{\lambda_{1m}^2+\lambda_{2m}^2} \frac{1}{J_o(\lambda_{1m})I_o(\lambda_{2m})} \left(\left(\frac{\lambda_{1m}}{\lambda_{2m}} - 2\lambda_{1m}\lambda_{2m}^2 - \frac{I_1(\lambda_{2m})}{I_o(\lambda_{2m})}\right)\right.$$

$$\times \left(\lambda_{1m}J_2(\lambda_{1m})I_1(\lambda_{2m}) + \lambda_{2m}J_1(\lambda_{1m})I_2(\lambda_{2m})\right) + \frac{\lambda_{1m}}{2} J_2(\lambda_{1m})I_o(\lambda_{2m})$$

$$\left. + \frac{\lambda_{1m}}{2} J_2(\lambda_{1m})I_2(\lambda_{2m})\lambda_{2m}J_1(\lambda_{1m})I_1(\lambda_{2m}) - J_1(\lambda_{1m})I_2(\lambda_{2m})\right)$$

Loading Case Step Load

For the step loading case where

$$\varepsilon(\tau) = \varepsilon(H(\tau))$$

Underdamped Condition $\chi_m < 1$

Equation of coefficient

$$A_m(\tau) = \frac{a_m}{\omega_m^2}\left(1 - e^{-\chi_m\omega_m\tau}\cos\Omega'_m\tau - \frac{2\chi_m\omega_m}{\Omega'_m} e^{-\chi_m\omega_m\tau}\sin\Omega'_m\tau\right)$$

Since $\chi_m = \frac{\chi}{2\omega_m}$ the partial differential form $\frac{\partial A_m(\tau)}{\partial\lambda_m}$ where $\lambda_m = \lambda_{1m}$ or λ_{2m} was given by

$$\frac{\partial A_m(\tau)}{\partial\lambda_m} = \left(\frac{\varepsilon\frac{\partial a_m}{\partial\lambda}}{\omega_m^2} - \frac{2\varepsilon a_m}{\omega_m^3}\frac{\partial\omega_m}{\partial\lambda_m}\right)\left(1 - e^{-\chi_m\omega_m\tau}\cos\Omega'_m\tau - \frac{2\chi_m\omega_m}{\Omega'_m}\right.$$

$$e^{-\chi_m\Omega_m\tau}\sin\Omega'_m\tau) + \frac{\varepsilon a_m}{\omega_m^2} e^{-\chi_m\omega_m\tau}\left(\tau\sin\Omega'_m\tau + \frac{2\chi_m\omega_m}{\Omega'^2_m}\sin\Omega'_m\tau\right.$$

$$\left. - \frac{2\chi_m\omega_m}{\Omega'_m}\tau\cos\Omega'_m\tau\right)\frac{\partial\Omega'_m}{\partial\lambda_m}$$

where

$$a_m = \left(\frac{J_1(\lambda_{1m})}{\lambda_{1m}J_o(\lambda_{1m})} - \frac{I_1(\lambda_{2m})}{\lambda_{2m}I_o(\lambda_{2m})}\right)$$

giving the partial derivative with respect to λ_{1m} of

$$\frac{\partial a_m}{\partial \lambda_{1m}} = \frac{1}{\lambda_{1m} J_o(\lambda_{1m})} \frac{\partial J_1(\lambda_{1m})}{\partial \lambda_{1m}} - \frac{J_1(\lambda_{1m})}{\lambda_{1m}^2 J_o(\lambda_{1m})} - \frac{J_1(\lambda_{1m})}{\lambda_{1m} J_o^2(\lambda_{1m})} \frac{\partial J_o(\lambda_{1m})}{\partial \lambda_{1m}}$$

$$\frac{\partial a_m}{\partial \lambda_{1m}} = \frac{1}{2\lambda_{1m} J_o(\lambda_{1m})} (J_o(\lambda_{1m}) - J_2(\lambda_{1m}) - \frac{J_1(\lambda_{1m})}{\lambda_{1m}^2 J_o(\lambda_{1m})} + \frac{1}{\lambda_{1m}} \frac{J_1^2(\lambda_{1m})}{J_o^2(\lambda_{1m})}$$

$$= \frac{1}{2\lambda_{1m}} - \frac{1}{2\lambda_{1m}} \frac{J_2(\lambda_{1m})}{J_o(\lambda_{1m})} - \frac{J_1(\lambda_{1m})}{\lambda_{1m}^2 J_o(\lambda_{1m})} + \frac{1}{\lambda_{1m}} \frac{J_1^2(\lambda_{1m})}{J_o^2(\lambda_{1m})}$$

while the partial derivative with respect to λ_{2m} was

$$\frac{\partial a_m}{\partial \lambda_{2m}} = - \frac{1}{\lambda_{2m} I_o(\lambda_{2m})} \frac{\partial I_1(\lambda_{2m})}{\partial \lambda_{2m}} + \frac{1}{\lambda_{2m}^2} \frac{I_1(\lambda_{2m})}{I_o(\lambda_{2m})} + \frac{1}{\lambda_{2m}} \frac{I_1(\lambda_{2m})}{I_o^2(\lambda_{2m})} \cdot \frac{\partial I_o(\lambda_{2m})}{\partial \lambda_{2m}}$$

$$= - \frac{1}{2\lambda_{2m}} I_o(\lambda_{2m}) (I_o(\lambda_{2m}) + I_2(\lambda_{2m})) + \frac{1}{\lambda_{2m}^2} \frac{I_1(\lambda_{2m})}{I_o(\lambda_{2m})} + \frac{1}{2m} \frac{I_1^2(\lambda_{2m})}{I_o^2(\lambda_{2m})}$$

$$= - \frac{1}{2\lambda_{2m}} - \frac{1}{2\lambda_{1m}} \frac{I_2(\lambda_{2m})}{I_o(\lambda_{2m})} + \frac{1}{\lambda_{2m}^2} \frac{I_1(\lambda_{2m})}{I_o(\lambda_{2m})} + \frac{1}{\lambda_{2m}} \frac{I_1^2(\lambda_{2m})}{I_o^2(\lambda_{2m})}$$

where

$$\omega_m^2 = \lambda_{1m}^2 \lambda_{2m}^2 + K$$

giving the partial derivative with respect to λ_{1m} of

$$2\omega_m \frac{\partial \omega_m}{\partial \lambda_{1m}} = \lambda_{1m} \lambda_{2m}^2$$

$$\frac{\partial \omega_m}{\partial \lambda_{1m}} = \frac{\lambda_{1m} \lambda_{2m}^2}{\omega_m}$$

and the partial derivative with respect to λ_{2m} of

$$\frac{\partial \omega_m}{\partial \lambda_{2m}} = \frac{\lambda_{1m}^2 \lambda_{2m}}{\omega_m}$$

when

$$\Omega_m = \omega_m^2 (1 - \chi_m^2)$$

$$= (\omega_m^2 - \tfrac{1}{4}\chi^2)$$

giving the partial derivative with respect to λ_{1m} of

$$2\Omega_m \frac{\partial_m \Omega_m}{\partial \lambda_{1m}} = 2\omega_m \frac{\partial \omega_m}{\partial \lambda_{1m}} = 2\,\lambda_{1m}\,\lambda_{2m}^2$$

$$\frac{\partial \Omega_m}{\partial \lambda_{1m}} = \frac{\lambda_{1m}\,\lambda_{2m}^2}{\Omega_m}$$

and hence the partial derivative with respect to λ_{2m} of

$$\frac{\partial\ \Omega_m}{\partial \lambda_{2m}} = \frac{\lambda_{1m}^2\,\lambda_{2m}}{\Omega_m}$$

It should be noted that the undamped condition $\chi_m = 0$ was the limiting cause for this condition, giving

$$\frac{\partial A_m(\tau)}{\partial \lambda_m} = \left(\frac{\varepsilon \frac{\partial a_m}{\partial \lambda_m}}{\omega_m^2} - \frac{2\varepsilon a_m}{\omega_m^3}\frac{\partial \omega_m}{\partial \lambda_m}\right)(1 - \cos \omega_m \tau') + \frac{\varepsilon a_m}{\omega_m^2}\,\tau \sin \omega_m \tau \frac{\partial \omega_m}{\partial \lambda_m}$$

Critically Damped Condition $\chi_m = 1$

Equations of coefficients

$$A_m(\tau) = \frac{\varepsilon a_m}{\omega_m^2}\left(1 - e^{-\omega_m \tau} - \tau e^{-\omega_m \tau}\right)$$

The partial differential form $\frac{\partial A_m(\tau)}{\partial \lambda_m}$ where $\lambda_m = \lambda_{1m}$ or λ_{2m} was given by

$$\frac{\partial A_m(\tau)}{m} = \left(\frac{\varepsilon \frac{\partial a_m}{\partial \lambda_m}}{\omega_m^2} - \frac{2\varepsilon a_m}{\omega_m^3}\frac{\partial \omega_m}{\partial \lambda_m}\right)\left(1 - e^{-\omega_m \tau} - \tau\, e^{-\omega_m \tau}\right)$$

$$+ \frac{2a_m}{\omega_m^2}(\tau + \tau^2)\, e^{-\omega_m \tau} \frac{\partial \omega_m}{\partial \lambda}$$

where $\frac{\partial a_m}{\partial \lambda_m}$, $\frac{\partial \omega_m}{\partial \lambda_m}$ have been previously defined.

Overdamped Condition $\chi_m > 1$

Equations of coefficients.

$$A_m(\tau) = \frac{\varepsilon a_m}{\omega_m^2}\left(1 - e^{-\chi_m\omega_m\tau}\cosh\Omega'_m\tau - \frac{2\chi_m\omega_m}{\Omega'_m}\, e^{-\chi_m\omega_m\tau}\sinh\Omega_m\tau\right)$$

Since $\chi_m = \frac{\chi}{2\omega_m}$ the partial differential form $\frac{\partial A_m(\tau)}{\partial\lambda_m}$ where

$\lambda_m = \lambda_{1m}$ or λ_{2m} was given by

$$\frac{\partial A_m(\tau)}{\partial\lambda_m} = \left(\frac{\varepsilon\frac{\partial a_m}{\partial\lambda_m}}{\omega_m^2} - \frac{2\varepsilon a_m}{\omega_m^3}\frac{\partial\omega_m}{\partial\lambda_m}\right)\left(1 - e^{-\chi_m\omega_m\tau}\left(\cosh\Omega'\tau - \frac{2\chi_m\omega_m}{\Omega'_m}\sinh\Omega'_m\tau\right)\right)$$

$$- \frac{\varepsilon a_m}{\omega_m^2}\, e^{-\chi_m\omega_m\tau}\left(\sinh\Omega'_m\tau - \frac{2\chi_m\omega_m}{\Omega'^2_m}\sinh\Omega'_m\tau + \frac{2\chi_m\omega_m}{\Omega'_m}\cosh\Omega'_m\tau\right)\frac{\partial\Omega_m}{\partial\lambda_m}$$

where

$$\Omega'^2_m = \omega_m^2(\chi_m^2 - 1)$$

$$= \tfrac{1}{4}\chi_m^2 - \omega_m^2$$

giving the partial derivative with respect to λ_{1m} of

$$2\Omega'_m\frac{\partial_m\Omega'_m}{\partial\lambda_{1m}} = -2\omega_m\frac{\partial\omega_m}{\partial\lambda_{1m}} = -2\lambda_{1m}\lambda_{2m}^2$$

$$\frac{\partial\Omega'_m}{\partial\lambda_{1m}} = -\frac{\lambda_{1m}\lambda_{2m}^2}{\Omega'_m}$$

and hence the partial derivative with respect to λ_{2m} of

$$\frac{\partial\Omega_m}{\partial\lambda_{2m}} = -\frac{\lambda_{1m}^2\lambda_{2m}}{\Omega'_m}$$

and $\frac{\partial a_m}{\partial\lambda_m}$, $\frac{\partial\omega_m}{\partial\lambda_{1m}}$ have been previously defined.

APPENDIX I

DEFERRED CORRECTION METHOD

Consider the equation

$$\underline{K}\,\underset{\sim}{\alpha} = \underline{L} + \underline{F}_1 + \underline{D} \tag{1}$$

where $\underline{K}$ = Matrix of coefficients

$\underline{L}$ = Load vector

$\underline{F}_1$ = Vector of equivalent pseudo-loads, containing the non-linear terms

$\underline{D}$ = Vector of errors

$= \underline{c}\,\underset{\sim}{\alpha}$

$\underline{c}$ = Matrix for differences greater than the fourth order term.

Initially the solution was obtained for:

$$\underset{\sim}{\alpha}_a = \underline{K}^{-1}(\underline{L} + \underline{F}_1) \tag{2}$$

was obtained by ignoring terms of greater than the fourth order.

The error for ignoring these terms was taken as $\underline{e}$ and gave

$$\underset{\sim}{\alpha} = \underset{\sim}{\alpha}_a + \underline{e} \tag{3}$$

Substitution in the original equation

$$\underline{K}(\underset{\sim}{\alpha}_a + \underline{e}) = \underline{L} + \underline{F}_1 + \underline{c}(\underset{\sim}{\alpha}_a + \underline{e}) \tag{4}$$

Therefore ignoring the higher order terms of the error, gave

$$\underline{K}\,\underline{e} \doteqdot \underline{c}\,\underset{\sim}{\alpha}_a$$

allowing the value of deflection to be corrected:

$$\underset{\sim}{\alpha} = \underset{\sim}{\alpha}_a + \underline{K}^{-1}\,\underline{c}\,\underset{\sim}{\alpha}_a \tag{5}$$

Therefore iterations were carried out until $|\underline{e}|$ was within the accepted convergence criteria.

APPENDIX J

CENTRAL FINITE DIFFERENCES

Since the derivative $\frac{\partial^4 \alpha}{\partial \rho^4}$ was necessarily represented by a fourth order difference term, the representation of all other derivatives include up to a third or fourth order difference term depending on whether they were on odd or even derivative.

Using standard difference operator symbols 7.4
the derivatives were obtained as following.

$$\rho_s \left(\frac{\partial \alpha}{\partial \rho}\right)_i = (\mu\delta - \frac{1}{6}\mu\delta^3 + \frac{1}{30}\mu\delta^5 \ldots.)\alpha_i$$

$$= (\tfrac{1}{2}(\alpha_{i+1} - \alpha_i) - \frac{1}{12}(\alpha_{i+2} - 2\alpha_{i+1} + 2\alpha_{i-1} - \alpha_{i-2})) + (\frac{1}{30}\mu\delta^5 + \ldots..)\alpha_i$$

$$\rho_s^2 \left(\frac{\partial^2 \alpha}{\partial \rho}\right)_i = (\delta^2 - \frac{1}{12}\delta^4 + \frac{1}{90}\delta^6 - \ldots.)\alpha_i$$

$$= (\alpha_{i+1} - 2\alpha_i + \alpha_{i-1} - \frac{1}{12}(\alpha_{i+2} - 4\alpha_{i+1} + 6\alpha_i - 4\alpha_{i-1} + \alpha_{i-2})) + (\frac{1}{90}\alpha^2 \ldots)\alpha_i$$

$$\rho_s^3 \left(\frac{\partial^3 \alpha}{\partial \rho^3}\right)_i = (\mu\delta^3 - \tfrac{1}{4}\mu\delta^5 + \ldots)\alpha_i$$

$$= \tfrac{1}{2}(\alpha_{i+2} - 2\alpha_{i+1} + 2\alpha_{i-1} - \alpha_{i-2})$$

$$(-\tfrac{1}{4}\mu\delta^5 + \ldots.)\alpha_i$$

$$\rho_s^4 \left(\frac{\partial^4 \alpha}{\partial \rho^4}\right)_i = (\delta^4 - \frac{1}{6}\delta^6 \ldots)\alpha_i = (\alpha_{i+2} - 4\alpha_{i+1} + 6\alpha_i - 4\alpha_{i-1} + \alpha_{i-2}) + (-\frac{1}{6}\delta^6 \ldots)\alpha_i$$

where δ = Central difference operator

μ = Averaging operator

ρ_s = Step size

APPENDIX K

STABILITY CRITERIA

A condition for a bounded oscillatory solution was the roots of the characteristic equation*

$$\lambda^*_{1,2} = \frac{(2 - g) \pm \sqrt{(2 - g)^2 - 4(1 + \ell)}}{2}$$

were complex.

Substituting for

$$q_i = 2\chi_i\theta^*$$

$$p_i = \theta^{*2}$$

where $\theta^* = \Delta\tau\omega_i$

into the definitions of g and ℓ gave

$$(2 - g) = \frac{2 + 2\chi_i\theta^*(2\gamma - 1) + (2\beta - \tfrac{1}{2} - \gamma)\theta^{*2}}{1 + 2\chi_i\gamma\theta^* + \beta\theta^{*2}}$$

$$(1 + \ell) = \frac{1 + 2\chi_i\theta^*(\gamma - 1) + (\tfrac{1}{2} - \gamma + \beta)\theta^{*2}}{1 + 2\chi_i\gamma\theta^* + \beta\theta^{*2}}$$

Therefore the condition for complex roots

$$4(1 + \ell) > (2 - g)^2$$

gave the inequality

$$4(1 + 2\chi_i\theta^*(\gamma-1) + (\tfrac{1}{2}-\gamma+\beta)\theta^{*2})(1 + 2\chi_i\ \gamma\theta^* + \beta\theta^{*2})$$

$$> (2 + 2\chi_i\theta^*(2\gamma-1) + \theta^{*2}(2\beta-\tfrac{1}{2}-\gamma))$$

which reduced to:

$$4(1 - \chi_i^2) + \theta^*2\chi_i(2\gamma - 1) + \theta^{*2}(4\beta - (\gamma + \tfrac{1}{2})^2) > 0$$

---

* Footnote: Symbols defined in Chapter 6.